New Light on Earth's Energy Budget and Its Implication for Solar Energy Potential

by

Yun Hang

A dissertation submitted in partial fulfillment of

the requirements for the degree of

Doctor of Philosophy

(Environment & Resources)

at the

University of Wisconsin-Madison

2020

Date of final oral examination: 04/06/2020

The dissertation is approved by the following members of the Final Oral Committee:
Tristan L'Ecuyer, Associate Professor, Atmospheric and Oceanic Sciences
Brad Pierce, Professor, Atmospheric and Oceanic Sciences
Stephanie Henderson, Assistant Professor, Atmospheric and Oceanic Sciences
Xiaodong Du, Associate Professor, Agricultural and Applied Economics
Song Gao, Assistant Professor, Geography

Abstract

New Light on Earth's Energy Budget and Its Implication for Solar Energy Potential

by

Yun Hang

The Earth is a solar powered system that maintains a balance between solar energy reaching the Earth and energy emitted from the Earth back to space. If an energy imbalance situation occurs, the Earth's temperature will change correspondingly to restore an energy balance. Thus, keeping an eye on Earth's energy budget is important for understanding the link between climate change and global warming. To provide observational benchmarks for global Earth's energy budget in climate models, this dissertation quantifies radiative influences of nine cloud types distinguished based on their vertical structure defined by spaceborne active observations from CloudSat and CALIPSO satellites. With accurate cloud base information provided by active sensors, this study goes beyond the top of atmosphere to establish how clouds influence the partitioning of the earth's energy imbalance between the atmosphere and surface that is poorly resolved by passive sensors and models. In addition, radiative contributions from multilayered cloud systems that are often misclassified as thick mid-level clouds in approaches that use passive sensors alone are explicitly diagnosed. The compositions and origins of these multilayered cloud systems are further investigated. This dissertation also explores regional energy budget to evaluate the radiative impacts of clouds and aerosols on solar energy potential. Rapid variations in local cloud and aerosol radiative effects directly influence solar energy generations from solar farms. This problem is particularly severe in Asia that has the world's largest solar farms but faces atmospheric dimming

from aerosols associated with fuel combustion and industrial activities. Thus, this dissertation assesses aerosol radiative impacts on solar energy potential in Asia with CloudSat and CALIPSO observations and MERRA-2 aerosol reanalysis. Hourly variations of aerosol optical depth at selected solar farms in India and Thailand are particularly discussed to better understand solar energy intermittency. These work offers new thoughts on saving base load energy resources and decreasing the rejection risk of solar power in electricity market.

Acknowledgements

I would like to thank many people who have helped me through the completion of this dissertation. First and foremost, I would like to express my sincere gratitude to Tristan L'Ecuyer, whose expertise, kindness, and patience has enriched my graduate experience very much. His guidance has helped me develop into a better scientific writer, researcher, and critical thinker. I could not imagine a better advisor and mentor for my graduate studies.

In conjunction with the mentorship of my advisor, I am very grateful to work with dynamic and intelligent committee members and appreciate their ideas, inquiries, and insights very much. I would like to thank Brad Pierce who brings me to the fascinating aerosol research and thank Xiaodong Du for his seasoned guidance on energy economics. Also, many thanks to Song Gao and Stephanie Henderson for their valuable feedbacks not only on my research but also on my career planning.

I would like to extend my gratitude to Tracey Holloway for her guidance on courses, research, and career opportunities at the interface of atmospheric science and energy systems analysis. I am very grateful for the support from Alex Matus, David Henderson, and Kai-Wei Chang, who have helped me solve many problems at work and in life over the years. I would like to thank AOS and Nelson faculties, administrators, students, staffs. I appreciate all their help through this process very much. I would like to thank my friends and research group that have been wonderfully supportive. I appreciate their companions that make my Ph.D. journey so delightful.

Last but not least, I would like to thank my family for their constant encouragement and love. I consider myself incredible lucky to have the best parents in the world. For the past 27 years, they always respect my own life choices and deeply trust the path that I have chosen. During my graduate school, I feel so fortunate to meet my husband, who is a very open-minded person that has been with me for every step of this journey.

Contents

List of Figures

List of Tables

Chapter 1

Introduction

1.1 Overview of Earth's Energy Budget

The Earth's climate is a solar powered system that maintains a balance between solar energy reaching the Earth and energy emitted from the Earth back to space. The Earth distributes the energy received from the sun into five components of our planet including water, ice, atmosphere, rocky crust, and all living things. Therefore, understanding the energy change in each component is critical to quantify the changing climate (Stephens et al., 2012a). However, Earth's energy balance depends on many factors, such as the spatial and temporal variations of cloud and aerosol that regulate incoming and outgoing radiations. As shown in Figure 1.1, some clouds and aerosols substantially prevent sunlight (shortwave radiation) from arriving at the Earth's surface that results in a cooling effect. At the same time, clouds can also block the energy emitted from the Earth (longwave radiation) below cloud bottom

that warm the Earth's surface. Since aerosol effects on longwave radiation is weak, in most scenarios only shortwave radiation is considered.

The Earth system is constantly trying to maintain the energy balance that the incoming solar energy is balanced by an equal energy flow emitting from Earth to space, namely, radiative equilibrium. Globally, the Earth system absorbs about 340 W m^{-2} solar power from the sun and radiates the same energy amount back to space annually. If an energy imbalance situation occurs, the Earth's temperature will change correspondingly to restore a new energy balance. Thus, keeping an eye on Earth's energy budget is important to understand the link between climate change and global warming. To monitor how the Earth's climate system balances the energy budget, processes occurring at three levels need to be considered, including the top of the atmosphere, where solar radiation enters the Earth's system; the surface of the Earth, where most solar heating takes place; and the atmosphere between the surface and the top of the atmosphere.

In the last three decades, Earth's energy budget has been directly measured by several satellites that are designed to quantify both solar-reflected and Earth-emitted radiation (Wielicki et al., 1995). In fact, more than 90% of the excess energy in the climate system due to increased greenhouse gas concentrations is absorbed at the surface where cloud and aerosol play a critical role in modulating radiative fluxes (Trenberth et al., 2014, 2009). However, current estimates of surface energy budget are poorly resolved because passive sensors lack the ability to penetrate optically thick clouds and provide information about the vertical structures of cloud and aerosols. Models also exhibit large biases in radiative fluxes at the surface relative to ground-based measurements (Garratt, 2001, Li et al., 2013,

Wild, 2005, 2008, Wild et al., 2013, 2001).

1.2 Clouds

Clouds are masses of liquid water, ice, or mixtures of both phases suspended in the atmosphere. Interactions among temperature, wind, and condensation nuclei form different types of clouds with distinct cloud shape, size, and phase. Figures 1.2 a-h show photos of eight single-layered cloud types. Cumulus, stratus, and stratocumulus clouds are low-level clouds with cloud bases lower than 3 km (Figure 1.2 a-c). Cumulus clouds appear relatively big and fluffy, like giant cotton balls in the sky. Stratus clouds appear uniformly gray in color and look like fog but do not reach the surface. Stratocumulus clouds are relatively lumpy with large horizontal scale around 5-50 km. Altostratus, altocumulus, and nimbostratus clouds are mid-level clouds with cloud bases lower than 7 km but higher than 2-3 km (Figures 1.2 d-f). Altostratus clouds float like parallel strips of clouds that sometimes thin enough to reveal the sun. Altocumulus clouds are white or gray and generally layered with one part darker than the other. Nimbostratus clouds are thick and continuous clouds that appear dark gray. Cirrus clouds are thin and light clouds with cloud bases higher than 7 km (Figure 1.2g). Deep convective clouds are many kilometers thick with cloud tops that always higher than 10 km. In a real world, we also have multilayered cloud systems such as the one shown in Figure 1.2I, a multilayered cloud system that consists of a layer of low-thick liquid cloud beneath a layer of high-thin cirrus cloud.

1.2.1 Cloud Feedback

Clouds substantially affect climate through a variety of ways. They are produced by and are host to a wide variety of microphysical and hydrological processes, including most latent heat release and precipitation. They also play an important role in regulating Earth's energy budget by modulating the amount of energy reflected, emitted and absorbed at the surface and in the atmosphere (L'Ecuyer et al., 2019). The redistribution of energy within the atmosphere by clouds can further help drive the large-scale circulation and vertical motions. Cloud feedback occurs when one or more of these cloud-related processes changes systematically in response to some external forcing such as global warming. Because clouds interact so strongly with climate, small changes in cloudiness can have a potent effect on the climate system (Myhre et al., 2001). However, measuring cloud feedback is extremely difficult because variations in cloud phase, height, thickness, and vertical structure all modulate the way clouds influence climate.

The role of clouds in modifying Earth's radiation balance is remained as one of the largest uncertainties in predicting future climate change (IPCC AR5). Different types of clouds regulate Earth's energy balance in different ways. Figure 1.3 compares radiative impacts of three common single-layered cloud types. It is shown that low-thick liquid clouds near the surface substantially reflect sunlight back to space, imposing a net cooling effect. In contrast, high-thin clouds let most shortwave solar radiation pass through them but trap the upwelling longwave radiation emitted by the Earth's surface, warming the planet like greenhouse gases. Between these two extremes, high-thick clouds largely block sunlight but also trap longwave heating from the surface, exerting neutral or slight cooling radiative

effects. Except single-layered clouds, multilayered cloud systems are frequently observed cover the Earth and influence energy balance. The most common type multilayered cloud system is consisting of low-thick cloud and high-thin cloud. As shown in Figure 1.3, adding a low-thick cloud below a high-thin cloud reflects more shortwave radiation and mutes the warming effect of the upper-level cloud. As a result, both accurate specification of cloud characters and separation of single- and multilayered cloud scenes are critical for quantifying cloud radiative effects (Hang et al., 2019, Oreopoulos et al., 2017).

Accurately modeling the sensitivity of climate to external forcing, therefore, requires a precise accounting of the radiative feedbacks owing to cloud changes. Yet it is not sufficient to merely tune models to represent the global net cloud effects since feedbacks depend critically on cloud characteristics, their location, and their environment (Stephens, 2005) and thus models must correctly represent radiative effects of distinct cloud types, their spatial distributions, and their temporal variability instead of relying on tuning the global-mean radiative energy to be balanced for the present-day climate. However, uncertainty remains concerning how different cloud types regulate radiative fluxes on global scales that impedes progress toward constraining the processes that govern spatial and temporal variability in cloud radiative effects. This is related to the fact that global models continue to exhibit significant cloud biases, such as insufficient boundary-layer clouds and a poor representation of multilayered cloud systems, that may significantly impact their ability to simulate cloud feedbacks (Calisto et al., 2014, Su et al., 2013, Zhang et al., 2005).

1.2.2 Upper Tropospheric Cloud Feedback

Clouds substantially affect climate through their influence on Earth's energy balance (Daloz et al., 2018, L'Ecuyer et al., 2015, Ramanathan, 1987, Ramanathan et al., 1989, Stephens et al., 2012a). This cloud impact has been recognized as an natural measure of climate change since the 1970s (Arakawa, 1975, Bony et al., 2015, Cess et al., 1990, Dufresne and Bony, 2008, Houghton et al., 1996, Norris et al., 2016, Ramanathan and Collins, 1991, Schneider, 1972, Senior and Mitchell, 1993, Stephens, 2005, Su et al., 2017, Webster and Stephens, 1984, Yue et al., 2019, Zelinka and Hartmann, 2011). In particular, high clouds affect the atmospheric general circulation and play an important role in cloud feedbacks (Bony et al., 2016, Boucher et al., 2013, Kay et al., 2012, Kubar et al., 2007, Randall et al., 1989a, Sherwood et al., 1994, Su et al., 2017, Voigt and Shaw, 2015). They impact climate through both albedo and greenhouse effects. If the cloud albedo increase (decrease), the energy received at the surface from the sun will decrease (increase) because more (less) sunlight will be reflected. The actual solar energy received by the Earth system is $F_{\odot}$ (1-α), $F_{\odot}$ is incident flux from the sun, α is albedo. High clouds also act as a blanket that make the atmosphere opaque. According to the Stephan-Boltzmann law, the amount of heat radiated from the Earth into space is $T_E\ \sigma^4$, T_E is the effective temperature of Earth's surface and atmosphere, and σ is the Stefan–Boltzmann constant. However, our understanding of the relationship between convection, detrained cirrus, and isolated cirrus in the upper troposphere is limited leading to large inter-model differences in the influence of upper tropospheric clouds (UTCs) on Earth's radiation budget (Lee et al., 2001). Such deficiencies present a severe obstacle for assessing future global and regional climate changes (Bony et al., 2015).

Over the years, three distinct hypotheses have been proposed to describe the role that UTCs play in climate system. In the early 1990s, Ramanathan and Collins (1991) hypothesized an ocean-atmosphere feedback mechanism in which an increase in 'highly reflective cirrus clouds' acts as a thermostat opposing the increased greenhouse effect as sea surface temperatures (SSTs) warm. This relation is illustrated in Figure 1.4a. Increased cirrus results in increased α and further increases the amount of heat radiated from the Earth into space. The reduced heat intake finally offsets the initial climate warming. However, this viewpoint has been challenged by a number of studies that highlighted the roles of evaporation, large-scale circulation, and ocean dynamics in regulating tropical SST. Pierrehumbert (1995) argued that clouds cannot serve as regulators for heating because their greenhouse and albedo effects cancel each other. Fu et al. (1992) used satellite radiance data to test this hypothesis and found that changes in the properties of cirrus clouds do not seem to be related to changes in SSTs. Wallace (1992) and Hartmann and Michelsen (1993) highlighted that large-scale dynamical processes will act to maintain uniform tropical tropospheric temperatures. Sun and Liu (1996) pointed out that the dynamic coupling between the atmosphere and ocean may limit the SST in the absence of cloud feedbacks.

Ten years later, the iris hypothesis, proposed by Lindzen et al. (2001), suggested cirrus clouds pose a strong negative feedback to global warming (Figure 1.4b). In a warmer climate, enhanced precipitation efficiency will lead to less cloud being detrained into the troposphere from deep convective cores. Then with less cloud cover, more infrared radiation can escape to space (T_E increases), thereby creating a strong climate-stabilizing negative cloud feedback that prevents significant warming from increasing greenhouse gases. This

iris hypothesis appeared to be supported by satellite-based measurements from passive instruments combined with radiation budget instruments including Earth Radiation Budget Experiment (ERBE), the Clouds and the Earth's Radiant Energy System (CERES), and Moderate Resolution Imaging Spectroradiometer (MODIS) (Choi et al., 2017, Lindzen and Choi, 2011, Spencer et al., 2007) but other studies have pointed to significant flaws with these analysis that cast doubt on the robustness of the results (Hartmann and Michelsen, 2002, Su et al., 2008). In addition to satellite studies, a modeling study Mauritsen and Stevens (2015) revisits the iris hypothesis by testing the model's convective parameterization. The result is that even though cloud cover is reduced as the climate warms, it does not generate a strong negative cloud feedback. Because reducing cloud cover not only lets more infrared energy out but also lets more sunlight in. Another argument against the iris comes from Dessler (2013) testing the cloud feedback in response to short-term climate variability by using observations. However, they found no response to short-term climate fluctuations.

In contrast, another seminal hypothesis, the proportionally higher anvil temperature (PHAT ,Figure 1.4c), suggested a positive feedback that warmer climate would lead anvil clouds to shift upward but emission temperatures remain nearly fixed or exhibit only a slight warming (Hartmann and Larson, 2002, Zelinka and Hartmann, 2010). PHAT has been shown to be consistent with a variety of observational data, as well as with highly resolved numerical simulations. Kuang and Hartmann (2007) used a cloud-resolving simulations of tropical radiative–convective equilibrium supported the hypothesis. Zelinka and Hartmann (2011) accessed PHAT with a suite of satellite instruments to assess the sensitivity of tropical high clouds to interannual tropical mean surface temperature anomalies. Harrop and Hartmann (2012) proved additional support for the PHAT by testing the temperature of tropical anvil

clouds through a cloud-resolving model. While subsequent studies questioned the methods and interpretation of the results in these early studies, there is evidence of alternate dynamic feedback in global warming simulations from general circulation models (GCMs) and of radiative-convective equilibrium (RCE) simulations from cloud-resolving models (CRMs) in which convective clouds aggregate into small regions limiting associated cold cloud cover (Harrop and Hartmann, 2012, Khairoutdinov and Emanuel, 2013, Tompkins and Craig, 1999, Wing and Cronin, 2016).

1.2.3 Cloud Radiative Effect and Heating

To access cloud feedback process in the period of global warming, Cloud Radiative Effect (CRE) is defined as the perturbation of net radiative flux due to the presence of clouds:

$$< CRE >= (F^{\downarrow} - F^{\uparrow})_{all-sky} - (F^{\downarrow} - F^{\uparrow})_{clear-sky} \tag{1.1}$$

where $F^{\downarrow}$ and $F^{\uparrow}$ are downward and upward fluxes under clear-sky and all-sky conditions in Earth's atmosphere, respectively (Hartmann et al., 1986, Henderson et al., 2013, Oreopoulos et al., 2011, Ramanathan et al., 1989).

In general, a positive CRE denotes a warming effect on Earth while a negative CRE denotes a cooling effect. Low clouds like stratus and stratocumulus decks tend to cool the planet because they block most solar energy reach the Earth's surface and reflect the energy back to space. But high clouds such as high-thin cirrus clouds act to warm the planet because they are highly transparent to solar radiation and trap longwave radiation at the surface. In contrast to cirrus and low clouds, high-thick deep convective clouds tend to have a neutral radiative effect on Earth. Because their cold cloud tops trap longwave radiation at the

surface, and at the same time, their thick cloud thicknesses reflect most solar radiation back to space.

CRE of distinct cloud types exert distinct influences on large scale circulations (Mace and Wrenn, 2013). For example, many studies have investigated the relationship between extratropical circulation and CRE (Ceppi et al., 2012, Li et al., 2015). The response of cloud fraction to global warming is that high clouds shift upward at all latitudes. The tropical cloud rise is consistent with the hypothesis of proportionally higher anvil temperature (PHAT), suggested a positive feedback that warmer climate would lead anvil clouds to shift upward but emission temperatures remain nearly fixed or exhibits only a slight warming (Hartmann and Larson, 2002, Zelinka and Hartmann, 2010). In the midlatitudes, cloud fraction decreases around 35° throughout the free troposphere. This is consistent with the widening of the tropical belt in a changing climate (Seidel et al., 2008). In the high latitudes, low-level cloud fraction changes are more complex because representing high-latitude low-level mixed-phase clouds in global climate models is challenging.

Cloud radiative heating is the cloud impact on atmospheric heating that can be derived as the difference in heating rates between clear-sky and all-sky conditions. The atmospheric heating rate Q is defined as:

$$Q\ (p) = \frac{dT}{dt} = -\frac{g}{c_p}\frac{\Delta F_{net}}{\Delta p} = -\frac{g}{c_p}\frac{\Delta F^{\downarrow} - \Delta F^{\uparrow}}{\Delta p} \tag{1.2}$$

where T is temperature, t is time, g is the gravitational constant, c_p is the specific heat capacity of dry air, F_{net} is net radiative flux defined as the difference between downward and upward fluxes, and p is pressure. It is straight-forward to show that cloud radiative

heating is equivalent to differencing the TOA and surface cloud radiative effect:

$$
\begin{aligned}
Q_{cld} &= Q_{all} - Q_{clr} \\
&= \frac{g}{c_p\ \Delta p}\ \left[[(F^{\downarrow}_{toa} - F^{\downarrow}_{sfc}) - (F^{\uparrow}_{toa} - F^{\uparrow}_{sfc})]_{all} - [(F^{\downarrow}_{toa} - F^{\downarrow}_{sfc}) - (F^{\uparrow}_{toa} - F^{\uparrow}_{sfc})]_{clr}\right] \\
&= \frac{g}{c_p\ \Delta p}\ \left[[(F^{\downarrow}_{toa} - F^{\uparrow}_{toa})_{all} - (F^{\downarrow}_{toa} - F^{\uparrow}_{toa})_{clear}] - [(F^{\downarrow}_{sfc} - F^{\uparrow}_{sfc})_{all} - (F^{\downarrow}_{sfc} - F^{\uparrow}_{sfc})_{clr}]\right] \\
&= \frac{g}{c_p\ \Delta p}\ (CRE_{toa} - CRE_{sfc}) \qquad (1.3)
\end{aligned}
$$

Previously, cloud radiative heating has been shown to be the primary way that clouds impact atmospheric circulations (Fueglistaler et al., 2009, Hartmann and Short, 1980, McFarlane et al., 2007, Randall et al., 1989b), the Madden-Julian oscillation (MJO), monsoons, and tropical rain belts (Jiang et al., 2015, Johansson et al., 2015, L'Ecuyer and Stephens, 2003, Li et al., 2015, Winker et al., 2017). However, there are comparatively few observational constraints on how the vertical characteristics of clouds influence atmospheric heating and, in turn, affect global atmospheric energy transport. Yet there is evidence that climate models likely fail to quantitatively reproduce this influence (Cesana et al., 2019, McFarlane et al., 2007) since cloud heating depends critically on the vertical distributions of cloud properties, their frequency, and their environment which are challenging to simulate accurately (Jakub and Mayer, 2015, Su et al., 2013, Zelinka et al., 2013).

1.2.4 Cloud Measurement Capability

In situ and ground-based cloud measurements provide high-quality observations at specific locations, but lack global coverage compared to satellites (Ackerman and Stokes, 2003, Comstock et al., 2002, Hahn and Warren, 1999, Kiehl, 1994, Wang and Sassen, 2001). Also,

ground-based active sensors may miss some high clouds due to attenuation (lidar) or loss of sensitivity (radar) (Protat et al., 2014). Satellite-based cloud detection from passive instruments combined with radiation budget instruments like Earth Radiation Budget Experiment (ERBE) vastly improved our understanding of cloud distributions and their global radiative impacts (Harrison et al., 1990, Ramanathan et al., 1989, Rossow and Lacis, 1990, Rossow and Schiffer, 1999, Wielicki et al., 1996a). Among the early studies to document the radiative properties of clouds from spaceborne passive observations were those of Ockert-Bell and Hartmann (1992) and Hartmann et al. (1992) who used C1 cloud data from the International Satellite Cloud Climatology Project (ISCCP) (Rossow and Schiffer, 1999) and radiative fluxes data from ERBE (Hartmann et al., 1992). The results provided valuable insights into the factors that govern the distributions of cloud radiative effects and their seasonal variation and served as important benchmarks for evaluating the global models at that time but they were, of course, subject to some limitations. The passive sensors and methods used lacked information for discriminating cloud types at night or distinguishing overlapping cloud fields (Chen et al., 2000, Rossow et al., 1985). Also, the lack of information concerning cloud vertical structure introduces large uncertainties when estimating cloud influences on surface radiation.

Building on ERBE measurements, the Clouds and the Earth's Radiant Energy System (CERES) instruments aboard the Tropical Rainfall Measurement Mission (TRMM), Terra and Aqua satellites have significantly improved radiative flux data (Wielicki et al., 1996a). The ISCCP D1 cloud product coupled new cloud retrieval methods to radiative transfer models to further estimate the radiative impacts of cloud types at the surface (SFC) (Chen et al., 2000). Likewise, the CERES Surface Radiation Budget (SRB) product has been

developed to derive the shortwave and longwave surface radiative fluxes on a global scale (Gupta et al., 1999). These datasets have been extensively validated against surface flux observations from the Baseline Surface Radiation Network (BSRN) to ensure that they yield accurate estimates of downwelling longwave and shortwave fluxes on monthly scales (Zhang et al., 2013). However, the limited information concerning cloud base or the presence of multiple cloud layers in the passive observations used by both ISCCP and SRB continues to hamper our ability to quantifying the radiative impacts of some complex cloud types (Gupta et al., 1999, Loeb et al., 2009, Rossow and Zhang, 1995, Wild et al., 2013, Zhang et al., 2005, 1995). But since 2006, the active sensors aboard CloudSat and Cloud Aerosol Lidar and Infrared Pathfinder Satellite Observation (CALIPSO) have provided new profiling capabilities offer potential for refining the analysis to include detailed near-global observations of cloud vertical structures and explicit cloud boundary information not available through conventional means (Stephens et al., 2018, 2002).

1.3 Aerosols

Aerosols are suspended solid particles or liquid droplets in Earth's atmosphere. They can be generated from both natural and anthropogenic sources. For example, dust and sea salt are natural aerosols while black carbon and sulfate generated from biomass burning and urban emission are anthropogenic aerosols. Aerosols perturb the atmosphere by two main pathways: direct effect and indirect effect. The direct effect is the net perturbation of the top of the atmosphere radiative balance owing to the presence of aerosols (Atwater, 1970). In this process, aerosols directly interact with solar radiation. As displayed in Figure 1.5, scattering aerosols like sulfate generally act to cool the atmosphere (Kiehl and Briegleb,

1993), whereas strongly absorbing aerosol particles like black carbon warm the atmosphere and possibly reduce the incidence of cloud formation through semi-direct effect (Ackerman et al., 2000, Koren et al., 2004). The indirect radiative effect describes how aerosol impact cloud microphysical properties through the cloud albedo effect and lifetime effect. The cloud albedo effect refers to that increased aerosol concentration increases clouds' albedo by enhancing the amount of water droplets (Twomey, 1977). The lifetime effect is due to certain types of aerosols (for example, sulfate aerosols) acting as cloud condensation nuclei (CCN) and possibly modifying microphysical properties of clouds and further affect cloud lifetime and thickness (Albrecht, 1989). These aerosol–cloud interactions have been found to impact large-scale shifts in rainfall (Chung and Soden, 2017), enhance the occurrence and strength of severe weather systems (Bell et al., 2008, Saide et al., 2015, Yang and Li, 2014), alter large-scale circulations (Ming and Ramaswamy, 2011), and drive climate variability (Booth et al., 2012).

1.3.1 Aerosol Direct Radiative Effect

Similar to cloud radiative effect, aerosol direct radiative effect (DRE) is defined as flux difference between clear-sky (no clouds) and clear, clean-sky conditions (no aerosols or clouds). Since aerosol effects on longwave radiation is weak, in most scenarios only shortwave radiation is considered.

$$< DRE >= (F^{\downarrow} - F^{\uparrow})_{clear-sky} - (F^{\downarrow} - F^{\uparrow})_{clean-sky} \tag{1.4}$$

where $F^{\downarrow}$ and $F^{\uparrow}$ are downward and upward fluxes under clear-sky and clean-sky conditions in Earth's atmosphere, respectively.

Aerosols can be natural or anthropogenic. The anthropogenic component of aerosol direct radiative effect is direct radiative forcing (DRF). Quantifying this human-made radiative forcing attracts more and more researchers in recent years because it is closely related to urbanization and industrialization. However, a consensus of global annual mean DRF is -0.35 W m^{-2} with large uncertainties from -0.85 W m^{-2} to +0.15 W m^{-2} that could even cancel this effect (IPCC AR5). This estimate is based on observational estimate (-0.3 W m^{-2}) from Myhre (2009) and model reanalysis estimate (-0.4 W m^{-2}) from Bellouin et al. (2013). Compared with the estimate of -0.5 W m^{-2} (-0.90 to +0.10) from IPCC AR4, the value of AR5 is weaker due to a modified sensitivity to black carbon aerosol (Ma et al., 2012). In a most recent paper (Matus et al., 2019), DRF is estimated as -0.50 W m^{-2} $\pm$ 0.3 W m^{-2} from collocated CloudSat and CALIPSO active observations, and the DRF comes mainly from sulfate pollution (-0.54 W m^{-2}) partially offset by absorption from smoke (0.03 W m^{-2}) (Matus et al., 2019). It has been suggested that DRF is likely comparable to greenhouse gases forcing and estimated to have offset a considerable fraction of global warming (Boucher et al., 2013, Forster et al., 2007). But the uncertainty is large because aerosols are very variable in space and time due to complicated species and their diverse interactions with clouds.

1.3.2 Aerosol Direct Forcing of Distinct Aerosol Species

Anthropogenic aerosols includes individual aerosol types as shown in Figure 1.6. It is important to determine each DRF component in Earth's radiation budget. On global annual average, sulfate formed from fuel combustion, industrial activities, biomass burning and volcanic eruptions strongly cool the atmosphere by –0.4 (–0.6 to –0.2) W m^{-2} while black carbon from fossil fuel and biofuel strongly warm the atmosphere by +0.4 (+0.05 to +0.8)

W m^{-2}. Primary organic aerosols from fossil fuel and biofuel, nitrate, and mineral contribute small cooling effects by –0.09 (–0.16 to –0.03) W m^{-2}, –0.11 (–0.3 to –0.03) W m^{-2}, and –0.1 (–0.3 to +0.1) W m^{-2}, respectively. Biomass burning aerosols and secondary organic aerosols (SOA) contribute almost neutral influence by +0.0 (–0.2 to +0.2) W m^{-2} and –0.03 (–0.27 to +0.20) W m^{-2}. One reason for large uncertainties in estimating DRF is that separating natural and anthropogenic sources of aerosols is difficult (Balkanski et al., 2007; Ginoux et al., 2012). Another reason is the limited ability of current models to accurate portray surface reflection and albedo. Multiple reflections between the surface and aerosols cause a non-linear surface influence. Over the ocean, the surface albedo depends primarily on wavelength and on solar and viewing angles, but over land the surface is highly heterogeneous, having highly anisotropic and wavelength-dependent optical properties. Most satellite measurements have a better estimate of DRF over ocean than over land because dark ocean surface reflection is easier to characterize. As such, adequate characterization of surface reflection is needed for both models and observations. Accurate representation of diurnal variability of aerosol direct forcing is also important to assess aerosol impacts on radiation. From the perspective of satellite remote sensing, the diurnal variation of aerosols can be better characterized by geostationary satellites (e.g. Geostationary Operational Environmental Satellite (GOES)), but geostationary satellites usually cover limited regions. To decrease uncertainties in estimating DRF, complementary information from observations and models are needed to represent aerosols on various spatial and temporal scales.

Although global annual mean DRF is small and with large uncertainties, the magnitude of regional DRF is much larger and has obvious spatial variations. Figure 1.7 shows model mean global distribution of annual mean DRF from 16 global aerosol models and their

standard deviation (Myhre et al., 2013). DRFs are most commonly observed over land. Strongly negative DRF is estimated in industrialized regions of eastern China, the US, Southeast Asia, the Indian subcontinent, Europe, central South America, and central-south Africa. The maximum is around -3 W m^{-2} over west Europe and east Asia. A warming effect is observed over Greenland and Antarctica ice sheet because high surface albedo enhances aerosol absorption. Large uncertainties appear in the region of high DRF such as Southeast Asia.

Figure 1.8 further shows global maps of model mean component DRF from Myhre et al. (2013). The most striking feature is that sulfate and black carbon from fossil fuel and biofuel are the two aerosol components with strongest absolute DRF that cancel each other in Southeast Asia. Nitrate and SOA also contribute significant cooling effects over eastern China, eastern US, and Europe. Over regions with high surface albedo such as the Sahara and Arctic the DRF is mostly quite weak, but DRF of biomass burning is relatively strong. The geographical pattern of biomass burning DRF is very different from the other aerosol components, and the cause of these differences vary by region. In some areas like southeast US it is caused by reduction in biomass burning emissions. In other regions like southern Africa the negative DRF is caused by low albedo over land, and positive DRF over ocean to the west of the coast is caused by large coverage of low lying clouds (Chand et al., 2009, Keil and Haywood, 2003). Also, the magnitude of biomass burning DRF varies over different time scales. Sena et al. (2013) assessed the direct impact of biomass burning aerosols over the Amazon Basin using satellite data. Over the 10-year study period, the estimated radiative forcing is about -5.6 W m^{-2}. But on short timescales, Observed maximum daily biomass burning DRF can reach -20 W m^{-2} at the top-of-atmosphere locally in Amazonia during

biomass burning seasons (Sena et al., 2013).

Comparing Figure 1.8 to Figure 1.7, sulphate make the most contribution to anthropogenic aerosol radiative forcing. Sulfate is mainly formed in the atmosphere from the oxidation of sulfur dioxide, which is emitted dominantly from fuel combustion and industrial activities. Among various types of tropospheric aerosols, sulfate has probably the largest fraction of anthropogenic contribution. Sulfate aerosol affects the Earth's radiative balance directly by scattering solar radiation and indirectly by forming new clouds as CCN and modifying cloud properties. Sulfate can also interact with other types of aerosols, such as dust and carbonaceous aerosols, to modify their hygroscopic properties when internally mixed with them. It is evident that South Asian emissions of sulfate results in large atmospheric concentrations of black carbon and other aerosols, also causing strong negative trends of surface solar radiation (Ramanathan et al., 2005). An increase in sulfate aerosols in the atmosphere due to human activity has been thought to link with atmospheric dimming, especially over anthropogenically polluted regions like Eastern China (Norris and Wild, 2009).

1.3.3 Aerosol Measurement Capability

Measuring aerosol distributions and optical properties in observations has been the subject of vigorous research for over 20 years. In situ and ground-based aerosol measurements provides high-quality observations at specific locations. The largest ground-based aerosol observation network with long-term data records in the world is AEROsol Robotic Network (AERONET) program, which provides spectral measurements of sun and sky radiance for cloud-free conditions over 200 sites globally (Holben et al., 1998, Smirnov et al., 2000). A variety of optical properties such as aerosol optical depth (AOD) (the magnitude of

aerosol extinction integrated in the vertical column), single-scattering albedo (the ratio of the scattering coefficient to the extinction coefficient), and phase function (the angular distribution of scattering radiation) are available over a wide spectral range from visible to near-infrared channels (0.34–1.02μm) with a high temporal resolution of 15 min and a low bias of 0.01–0.02 (Dubovik et al., 2002, 2000). These measurements have been widely used for aerosol studies including evaluation and validation of model simulation and satellite remote sensing applications. In addition, intensive field experiments offer detailed observations of aerosol physical, chemical, and optical properties to understand regional aerosol regimes. For example, ORACLES (ObseRvations of Aerosols above CLouds and their intEractionS) experiment has been designed to study African biomass burning aerosols, providing multi-year airborne observations of aerosol-cloud interactions. This can also be used to assess inter-model differences in aerosol forcing and verify observation methods.

While ground based networks offer detailed observations of aerosol composition and properties, satellites characterize large spatial and temporal heterogeneity of aerosol optical properties (King et al., 1999). For the last few decades, satellite instruments have been launched with increasing capability for remote sensing of aerosol measurements, which have provided wide spatial coverage. Advanced Very High Resolution Radiometer (AVHRR) and Total Ozone Mapping Spectrometer (TOMS) were first used to monitor aerosol from space, though they were originally designed for other properties. The AVHRR provides radiance observations in the visible and near infrared wavelengths that are sensitive to aerosol properties over the ocean with a spatial resolution of roughly 4 km. Because of the highly variable land surface reflectance of the visible wavelengths, the AVHRR retrieval cannot derive aerosol information over the land. In contrast, the retrieval products from the TOMS

measurements cover both land and ocean, since the TOMS instrument measures backscattering at the UV wavelengths, which have low and nearly constant reflectance at most surfaces (Herman et al., 1997). The UV channels are sensitive to aerosol absorption and successfully monitoring biomass burning smoke and dust (Herman et al., 1997). These two instruments have provided multi-decadal climatology of aerosol optical properties that has significantly advanced the understanding of aerosol distributions and their global impacts.

At the end of last century, multi-angle Imaging SpectroRadiometer (MISR) aboard the sun-synchronous polar orbiting satellite Terra measuring upwelling solar radiance in four spectral bands (0.446 μm, 0.558 μm, 0.672 μm and 0.866 μm) and at nine view angles (0°, ±26.1°, ±45.6°, ±60°, ±70.5°) over a 360 km swath (Diner et al., 1998). These wide range of along-track view angles accurately evaluate the surface contribution to the TOA radiances and hence retrieve aerosols over both ocean and land surfaces (Kahn et al., 2005). But MISR has a global coverage of 9 days at the equator and 2 days at the poles due to its polar orbit limitation. Fortunately, MODerate resolution Imaging Spectroradiometer (MODIS) aboard NASA's twin satellites Terra and Aqua has 36 channels ranging from 0.44 to 15 μm that performs near global daily observations of atmospheric aerosols over both land and ocean (Remer et al., 2005). A recent paper Wei et al. (2019) shows that MODIS products perform best in capturing the global temporal variations in aerosols and agree very well with AERONET-based AOD values on different spatial scales. The CERES also measures broadband solar and terrestrial radiances at three channels with a footprint at 20km (Wielicki et al., 1996b). CERES is collocated with MODIS and MISR aboard Terra and with MODIS on Aqua. Thus CERES estimates of TOA solar flux in clear-sky conditions can be in conjunction with measurements of aerosol optical depth from MODIS

and MISR to derive the aerosol direct effect (Zhang and Christopher, 2003). Other recent spaceborne passive sensors such as Visible Infrared Imaging Radiometer Suite (VIIRS) (Cao et al., 2013), Advanced Himawari Imager (AHI) (Lee et al., 2017), and Advanced Baseline Imager (ABI) (Schmit et al., 2005) are also capable to detect aerosol to retrieve aerosol optical properties.

Accurate discrimination of aerosol over cloud have, however, been challenging in conventional passive sensor approaches given their limitation to measure aerosol vertical structure (Yu et al., 2006). These lack of information introduces large uncertainties when estimating aerosol optical properties and hamper our ability to quantifying the radiative impacts of aerosols on Earth's radiation budget. Profiling capabilities afforded by spaceborne active sensors Cloud-Aerosol Lidar with Orthogonal Polarization (CALIOP) aboard CALIPSO satellite (Winker et al., 2003) and Cloud Profiling Radar (CPR) aboard CloudSat (Stephens et al., 2002) offer potential for refining to include explicit aerosol and cloud vertical dimension not available through conventional means (Stephens et al., 2018). These two collocated active sensors provide unprecedented measurements for absorbing aerosols over underlying clouds (Winker et al., 2010). But CALIPSO may suffer from uncertainty in the classification of aerosol types (Omar et al., 2013), can misclassify dense aerosol layers as clouds (Schuster et al., 2012), and may fail to detect aerosols with low AOD, especially in the presence of clouds (Kacenelenbogen et al., 2014).

1.4 Influence of Clouds and Aerosols on Solar Energy Potential

Renewable energy plays an important role in providing energy services in a sustainable manner. Across the world, solar energy capacity has increased dramatically due to falling prices, policies favoring renewable energy, and concerns over greenhouse gas emissions from fossil fuel generators. However, the solar energy received at a particular place is intermittent: solar generators only produce energy when the sun is shining. Therefore, rapid variations in local cloud amount and type play an important role in generating solar energy (Prasad et al., 2015, Troccoli and Morcrette, 2014). Clouds reduce the amount of irradiance reaching the surface due to their varying optical depth. For example, opaque clouds over photovoltaic (PV) arrays reduce output solar power production by as much as 50–80% (Hoff et al., 2009). It has been shown that intermittent cloud cover over a concentrated solar power (CSP) plant causes dramatic fluctuations in the power output (Powell and Edgar, 2012). Similarly, aerosols are associated with attenuation in the atmosphere by scattering and absorbing sunlight. Li et al. (2017a) evaluates the impact of aerosols on PV generation in China and find aerosol-related annual average reductions have comparable impacts to clouds over eastern provinces in winter. Thus, the ability to monitor global radiative effects of cloud and aerosol at fine resolution has emerged as a challenge to make solar energy reliable.

Assessing radiative impacts of cloud and aerosol has been the subject of vigorous research for the last half century. In-situ and ground-based measurements provide high-quality observations at specific locations, but lack global coverage compared to satellites. Satellite-based detection from passive instruments have vastly improved our understanding of cloud and

aerosol distributions and their global radiative impacts. Precise delineation of cloud top and base altitudes have, however, been challenging in conventional passive sensor approaches given their limited ability to measure cloud vertical structure (Mace and Wrenn, 2013). Since 2006, the active sensors aboard CloudSat and CALIPSO have provided near-global vertically resolved estimates of cloud and aerosol properties (Stephens et al., 2002, Winker et al., 2007). But the spatial resolutions of satellite images from CloudSat is coarser than required resolution for monitoring insolation variations. CloudSat's 94-GHz nadir-looking CPR cross-track resolution is only approximately 1.4×1.7 km^2 and with a vertical resolution of 240 m (Tanelli et al., 2008). But for a typical 1 MW solar farm, the area required is about 0.16 km^2. Another weakness of CloudSat and CALIPSO is their measurements are always collected at 01:30 and 13:30 local time due to orbit limitation. The estimated shortwave fluxes need to be normalized to the diurnally-averaged insolation to approximate the full diurnal cycle. Also, it takes CloudSat 16 days to repeat granule track that means observations for cloud movement are not possible. Fortunately, some limitations of polar-orbit satellites can be offset by geostationary satellite observations that monitor clouds and aerosols at high temporal resolution, such as the NOAA GOES network for North and South America that can combine sequential satellite images to track cloud and aerosol movements. Overall, not a single ground-based or satellite measurements can provide enough information to detect clouds, estimate cloud radiative impacts, and calculate cloud motion.

1.5 Research Questions and Dissertation Structure

The goal of this study is to revisit the role of cloud and aerosol in Earth's energy budget within the context of the complementary satellite observations provided by CloudSat and

CALIPSO. The results of this study are expected to advance current understanding of cloud radiative effects and heating to reduce uncertainties in representing these effects in climate models. Beyond that, this study will also estimate the influence of aerosols on solar energy potential in Asia to offer new thoughts for future energy planning from an atmospheric science perspective.

This dissertation presents research conducted by the author in four separate analysis. The results of these analysis are featured in Chapter 3 (Effect of Cloud Type on Earth's Energy Balance Part I: Top-of-Atmosphere and Surface (L'Ecuyer et al., 2019)), Chapter 4 (Effect of Cloud Type on Earth's Energy Balance Part II: Atmospheric Heating (Hang et al., 2019)), Chapter 5 (Effect of Upper Tropospheric Clouds on Earth's Energy Balance), and Chapter 6 (Influence of Aerosol on Solar Energy Potential). Versions of Chapters 3 and 4 have been published in *Journal of Climate*. A version of Chapter 5 will be submitted to *Journal of Climate*. Chapter 6 includes ongoing analyses presented with the intention of being published in the near future. A synthesis of the results and implications therein is covered in Chapter 7.

Cloud Class	Cloud Features	
High Cloud	Base	> 7.0 km
	Rain	no
	Horiz. Dim.	1 to 10^3 km
	Vert. Dim.	moderate
	LWP	= 0.
As	Base	2.0-7.0 km
	Rain	none
	Horiz. Dim.	10^3 km, homogeneous
	Vert. Dim.	moderate
	LWP	~ 0, dominated by ice
Ac	Base	2.0-7.0 km
	Rain	virga possible
	Horiz. Dim.	10^3 km, inhomogeneous
	Vert. Dim.	shallow or moderate
	LWP	> 0
St	Base	0-2.0 km
	Rain	none or slight
	Horiz. Dim.	10^2 km, homogeneous
	Vert. Dim.	shallow
	LWP	> 0.
Sc	Base	0.-2.0 km
	Rain	drizzle or snow possible
	Horiz. Dim.	10^3 km, inhomogeneous
	Vert. Dim.	shallow
	LWP	> 0.
Cu	Base	0-3.0 km
	Rain	drizzle or snow possible
	Horiz. Dim.	1 km or larger, isolated
	Vert. Dim.	shallow or moderate
	LWP	> 0.
Nb	Base	0-4.0 km
	Rain	prolonged rain or snow
	Horiz. Dim.	50 -1000 km
	Vert. Dim.	thick
	LWP	> 0.
Deep convective clouds	Base	0-3.0 km
	Rain	intense shower of rain or hail possible
	Horiz. Dim.	10 km or large
	Vert. Dim.	thick
	LWP	> 0.

TABLE 1.1: Cloud features of eight single-layered cloud types, modified from Wang et al. (2012).

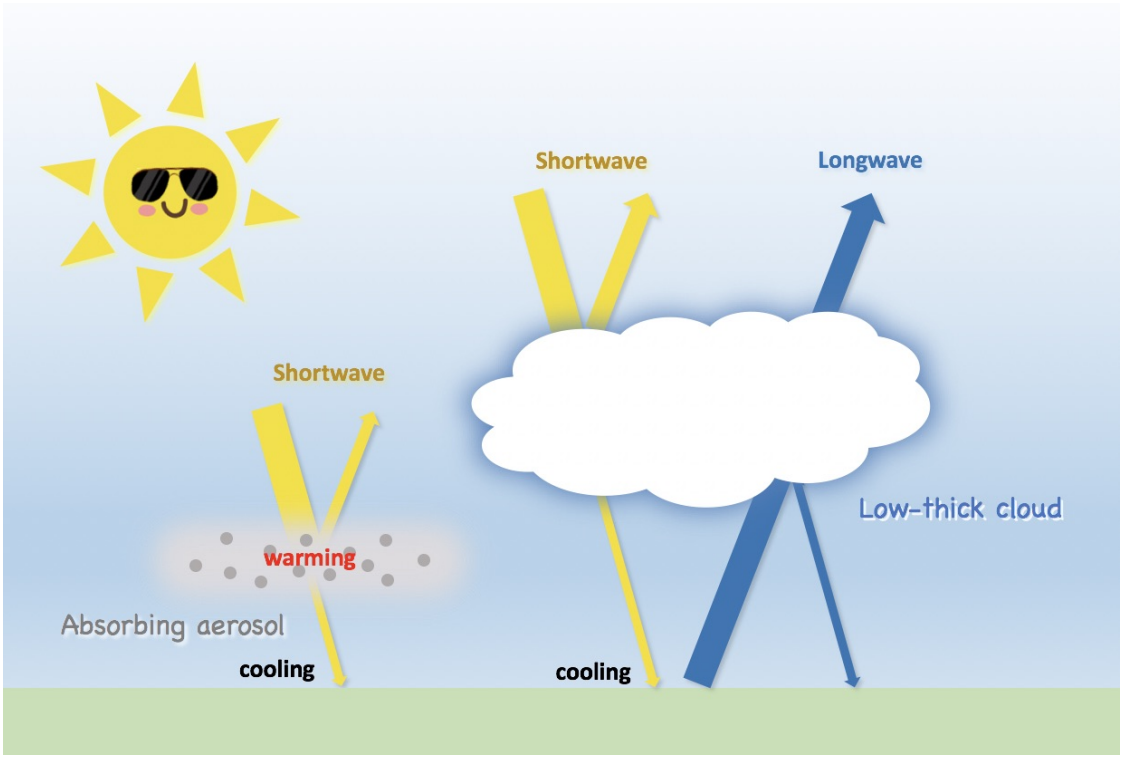

FIGURE 1.1: The role of low-thick cloud and absorbing aerosol in regulating Earth's energy budget.

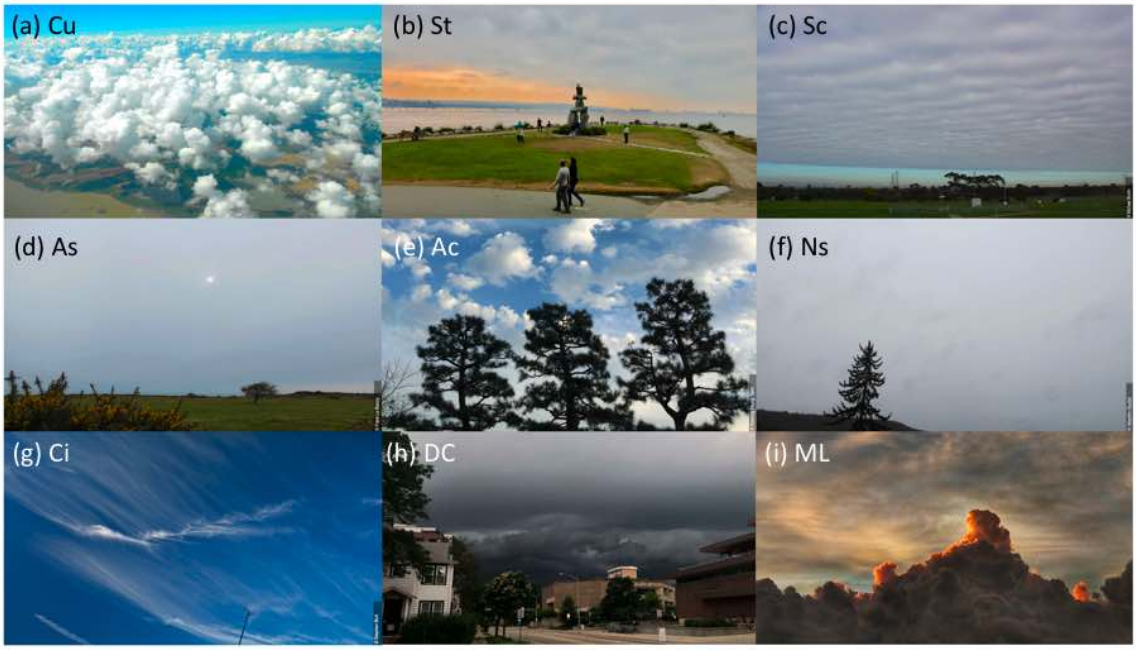

FIGURE 1.2: Photos of nine cloud types: (a) cumulus (©Yun Hang), (b) stratus (©Yun Hang), (c) stratocumulus (©Michael Bruhn), (d) altostratus (©Frank Le Blancq), (e) altocumulus (©Kwong Hung Tam), (f) nimbostratus (©Martin Gudd), (g) cirrus (©Stephen Burt), (h) deep convective clouds (©Yun Hang), (i) multilayered cloud systems (©Zhu Chen).

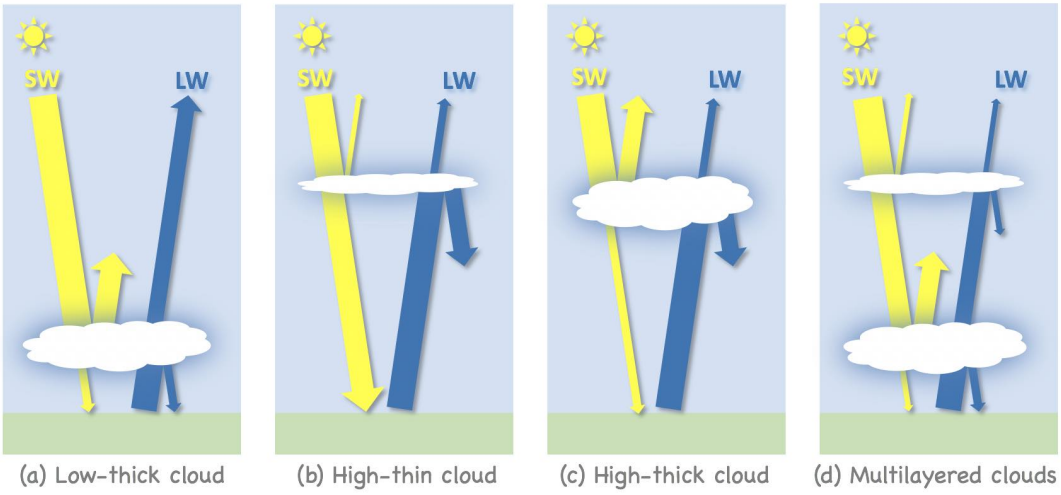

FIGURE 1.3: Cloud radiative impact of four common cloud types.

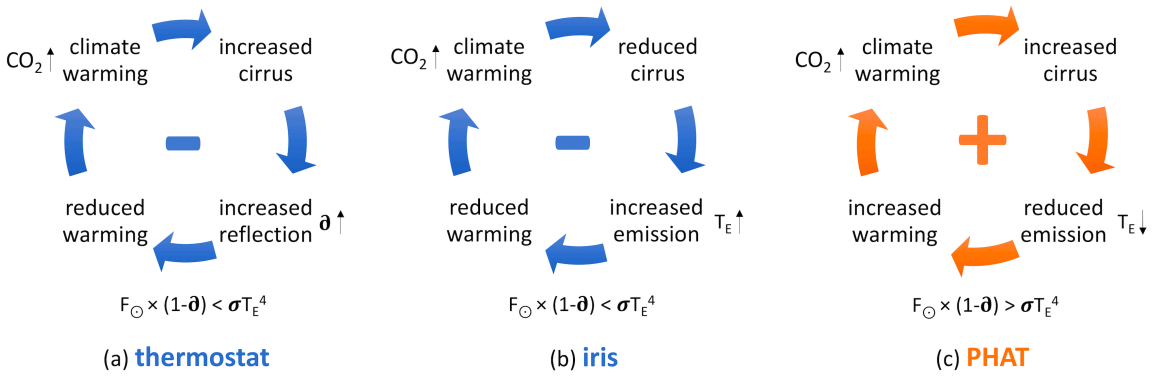

FIGURE 1.4: Diagram of three cold cloud feedback hypotheses: (a) 'thermostat' from Ramanathan and Collins (1991), (b) iris from Lindzen et al. (2001), and PHAT from Zelinka and Hartmann (2010).

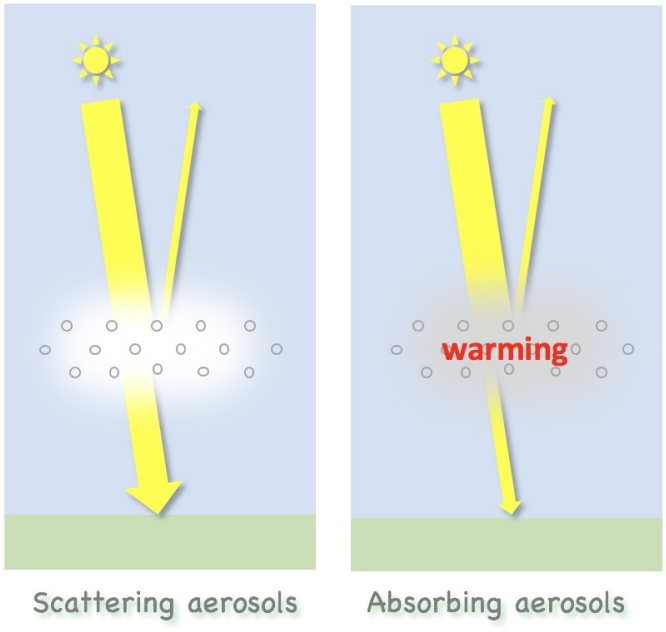

FIGURE 1.5: Aerosol direct radiative effect of scattering and absorbing aerosols.

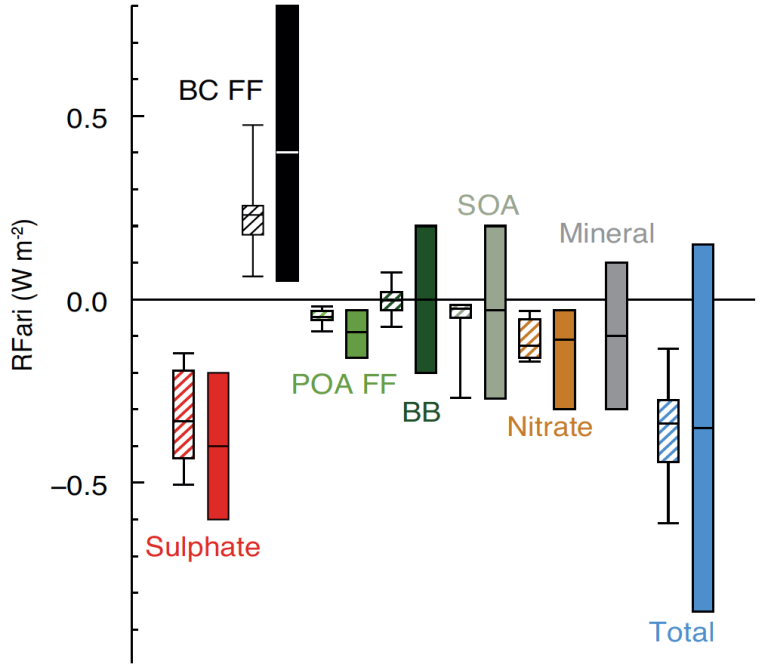

FIGURE 1.6: Annual mean top of the atmosphere radiative forcing due to aerosol–radiation interactions (RFari, in W m^{-2}) due to different anthropogenic aerosol types, for the 1750–2010 period. Hatched whisker boxes show median (line), 5th to 95th percentile ranges (box) and min/max values (whiskers) from AeroCom II models (Myhre et al., 2013) corrected for the 1750–2010 period. Solid coloured boxes show the AR5 best estimates and 90% uncertainty ranges. BC FF is for black carbon from fossil fuel and biofuel, POA FF is for primary organic aerosol from fossil fuel and biofuel, BB is for biomass burning aerosols and SOA is for secondary organic aerosols (IPCC AR5).

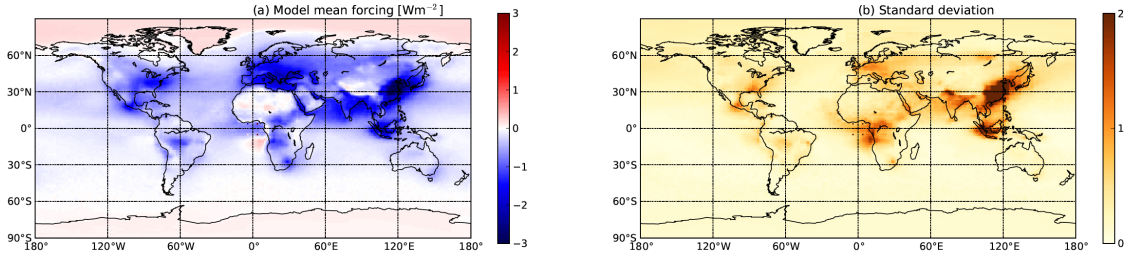

FIGURE 1.7: Model mean DRF (left) and standard deviation (right) Myhre et al. (2013).

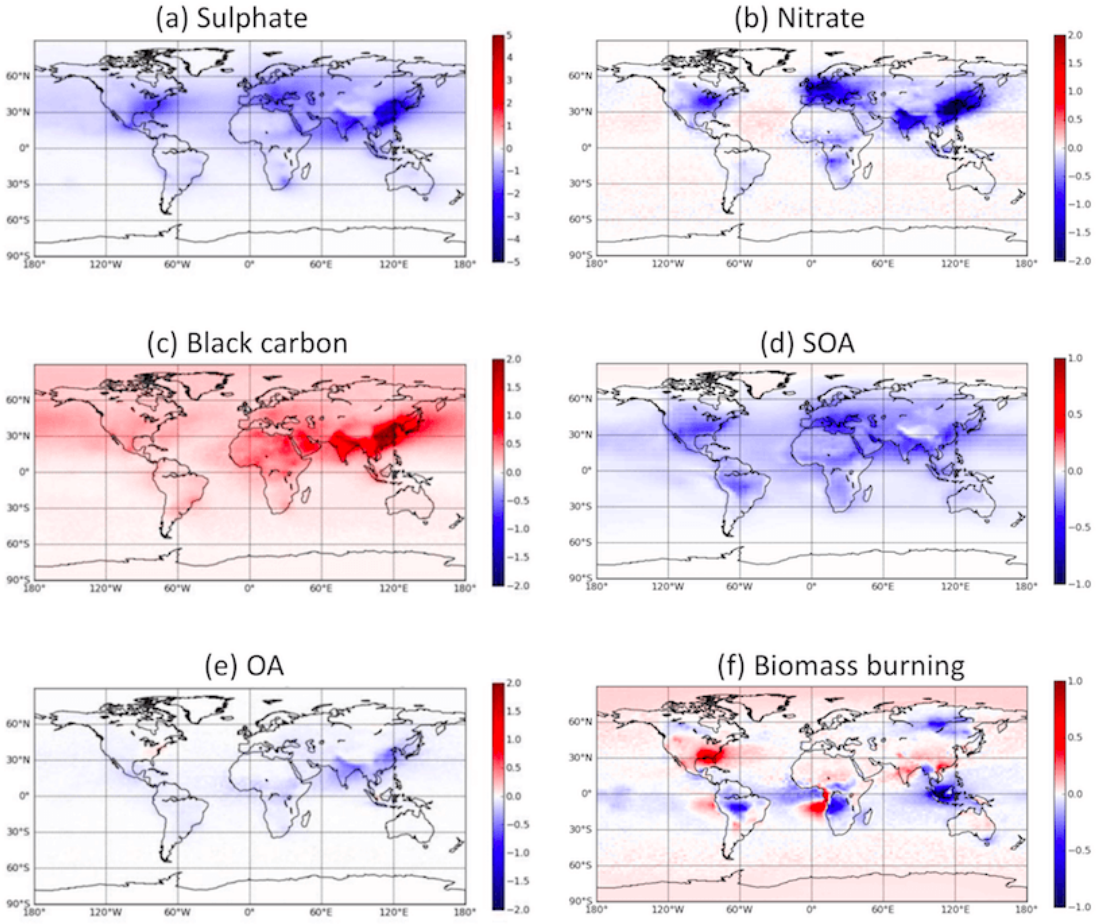

FIGURE 1.8: Model mean component DRF from Myhre et al. (2013). Top row: SO4 and NO3. Middle row: BC and SOA. Bottom row: OA and BB.

Chapter 2

Datasets

2.1 CloudSat and CALIPSO

Since 2006, the active sensors aboard CloudSat and CALIPSO have provided detailed near-global observations of cloud vertical structures (Stephens et al., 2002). This information is concisely summarized in CloudSat's level 2 cloud scenario classification (2B-CLDCLASS-LIDAR, hereafter, 2BCLD) product (Sassen and Wang, 2012) that combines radar and lidar measurements to distinguish canonical cloud types based on explicitly constrained cloud boundaries, two-dimensional cloud structure, cloud phase and precipitation features through a neural network approach. CloudSat's level 2 radiative flux and heating rate (2B-FLXHR-LIDAR, hereafter, 2BFLX) algorithm combines this information with cloud properties and scene characteristics from CloudSat, CALIPSO, and the MODIS to compute vertical profiles of shortwave (SW) and longwave (LW) radiative fluxes for each CloudSat

field of view. Together the 2BCLD and 2BFLX datasets provide the basis needed to reassess the effect of cloud type on Earth's energy balance in the modern satellite era.

2.1.1 2B-CLDCLASS-LIDAR

While classifying clouds by their cloud top pressure and optical depth has led to important breakthroughs in our understanding of cloud feedbacks, active sensors offer potential for further refining constraints on cloud vertical structure (L'Ecuyer and Jiang, 2010). CloudSat's 2BCLD product utilizes collocated CloudSat, CALIPSO, and MODIS measurements to explicitly incorporate two-dimensional cloud characteristics into a vertical and spatial-structure based cloud classification scheme (Sassen and Wang, 2012, Sassen et al., 2008). CloudSat's 94-GHz nadir-looking CPR has a minimum sensitivity of approximately -30 dBZ (at launch and for the time period considered here). The radar cross-track resolution is approximately 1.4×1.7 km^2 and with a vertical resolution of 480 m which is further over-sampled to 240 m (Tanelli et al., 2008). Since CloudSat's CPR is relatively less sensitive to small particles, the CALIOP on board CALIPSO provides complementary measurements of sub-visual cirrus and low-lying liquid clouds that go undetected by the CPR (Henderson et al., 2013, McGill et al., 2007, Winker et al., 2007). Together, these sensors provide the most accurate depiction of the vertical distribution of clouds currently available (Mace et al., 2009). Furthermore, combined CPR and CALIOP measurements provide reliable cloud phase (liquid, ice, or mixed-phase) discrimination for each cloud layer (Zhang et al., 2010). In addition, MODIS provides complementary measurements of cloud effective radius and integrated optical thickness that further constrain cloud radiative properties (Ackerman et al., 2008, Chan and Comiso, 2011, Platnick et al., 2003).

Compared to ISCCP and other similar cloud type schemes, the CloudSat 2BCLD product not only provides information for cloud type characterization more faithfully but also helps fill gaps in understanding multilayered clouds. The 2BCLD product groups cloud scenes into different layers, then classifies cloud clusters into stratus (St), stratocumulus (Sc), cumulus (Cu) (including Cu congestus), nimbostratus (Ns), altocumulus (Ac), altostratus (As), deep convective clouds (D.C.), or high clouds (cirrus and cirrostratus) based on cloud height and phase, maximum effective radar reflectivity factor and temperature, as well as the presence of precipitation reaching the surface. For boundary layer clouds, St and Sc are mainly separated by horizontal homogeneity based on cloud top height and radar reflectivity. Cu includes fair weather cumulus and deep cumulus congestus. Fair weather cumulus clouds are separated from St and Sc with cloud fraction. Specific definitions for each cloud category can be found in Sassen and Wang (2008). If more than one cloud type is identified in multiple distinct cloud layers separated by at least one CPR vertical range bin, then that pixel is classified as a multilayered (M.L.) cloud. Note that this definition of M.L. cloud is not only limited to multilayered clouds consisting of distinct liquid and ice layers (Matus and L'Ecuyer, 2017), but also includes mixed phase clouds. Together, CloudSat and CALIPSO likely observe the majority of all multilayered clouds with one exception. They can miss very low clouds that lie below optically thick overlying high or mixed-phase clouds where the lidar attenuates in the upper cloud and the radar misses the lower cloud layer due to ground-clutter (Protat et al., 2014). In this case, the missing clouds have negligible impact on TOA cloud radiative effect and weak impact on surface LW cloud forcing. The other missing clouds from combined CloudSat and CALIPSO do happen, but at a relatively low frequency. With the low occurrence, I do not expect the missing clouds to noticeably impact

the statistical results reported.

2.1.2 2B-FLXHR-LIDAR

The CloudSat 2BFLX algorithm derives estimates of broadband fluxes consistent with retrievals of atmospheric, cloud, and surface properties from CloudSat, CALIPSO, and MODIS (L'Ecuyer et al., 2008). This study uses the fifth release (R05) of the 2BFLX dataset that features improvements in mixed-phase and ice cloud properties (Matus and L'Ecuyer, 2017). Compared with the previous version (R04) of 2BFLX (Henderson et al., 2013), the R05 implements ice cloud properties from CloudSat 2C-ICE product which provides more rigorous treatment of thin ice clouds that includes explicit retrievals of ice water content (IWC) and effective radii (Deng et al., 2013, Ham et al., 2017, Matus and L'Ecuyer, 2017). The R05 2BFLX product remains sensitive to retrieval errors and sampling biases introduced by the limited spatial and temporal sampling characteristics of CloudSat and CALIPSO, especially on the scale of individual cloud system. Nevertheless, the algorithm has been demonstrated to provide a robust statistical representation of CERES top of the atmosphere fluxes when integrated over monthly and longer scales. The CERES instrument aboard Aqua provides a unique opportunity for evaluating 2BFLX, because of the small temporal gap between the orbits of Aqua satellite and CloudSat (Kato et al., 2010).

While the vertical structure information provided by spaceborne active sensors provides significant new insights into the role of distinct cloud types in the global energy budget, these data are not without their limitations. The spatial and temporal characteristics of CloudSat and CALIPSO may introduce sampling biases in the results. For example, the diurnal variations in cloud cover are not properly accounted for by the limited twice-daily

sampling of the A-Train. Also, these datasets do not provide full global coverage, omitting regions of 82.5°-90°. Uncertainties may also be present in the radiative effects estimated from 2B-FLXHR-LIDAR owing to cloud detection and cloud microphysical property retrievals. Liquid water content, surface temperature, and lower-troposphere humidity, in particular, exert strong influences on surface flux estimates that drive the error bars presented here (Henderson et al., 2013). In addition, Mülmenstädt et al. (2018) recently reported that significant regional errors may exist in downwelling LW fluxes due to uncertainty in cloud base heights. All uncertainty estimates reported in this study derive from the comparisons found in Matus and L'Ecuyer (2017) and a comprehensive set of sensitivity studies are reported in Henderson et al. (2013). Additional details concerning 2BFLX performance can be found in those studies.

An example profile from R05 2BFLX is shown in Figure 2.1, which shows the reflectivity and cloud mask as well as the corresponding cloud radiative effect estimated from 2BFLX at the TOA and SFC. According to 2BCLD, clouds are categorized as cirrus, altostratus, and multilayered clouds. The multilayered clouds cases have strong SW effects that dominate net CRE while the altostratus-only portion show small net CRE.

2.2 MERRA-2 Aerosol Reanalysis

The second Modern-Era Retrospective analysis for Research and Applications (MERRA-2) aerosol reanalysis (Randles et al., 2017) uses an upgraded version of the Goddard Earth Observing System Model, Version 5 (GEOS-5) data assimilation system that include additional meteorological observations and includes assimilation of AOD from various ground- and space-based remote sensing platforms at a spatial resolution of $0.625° \times 0.5°$ with 72

vertical layers and a temporal resolution of 1 hour (Randles et al., 2017). MERRA-2 has a global coverage and its temporal coverage is 1980-2019 that includes nearly 40 years data. MERRA-2 aerosol reanalysis is an excellent tool for calculating and providing the spatial distribution of direct radiative forcing of aerosols. The unique strength of MERRA-2 is that its assimilated aerosol data comes from several instruments that includes AERONET, AVHRR, MISR, and MODIS (Randles et al., 2017). The vertical structure of aerosol optical properties in MERRA-2 generally shows good agreement compared to both CALIOP and aircraft observations (Randles et al., 2017).

Another strength of MERRA-2 is that the GEOS-5 atmospheric general circulation model is radiatively coupled with the Georgia Tech/Goddard Global Ozone Chemistry Aerosol Radiation and Transport (GOCART) model (Chin et al., 2002). The GOCART model is driven by assimilated meteorological fields from the Goddard Earth Observing System Data Assimilation System (GEOS DAS) that includes winds, temperature, pressure, specific humidity, convective cloud mass flux, cloud fraction, precipitation, boundary layer depth, surface winds, and surface wetness (Chin et al., 2000, Ginoux et al., 2001, Schubert et al., 1993). This type of model is therefore appropriate for interpreting measurements for a specific period of time. The GOCART model has a resolution of $0.625^\circ \times 0.5^\circ$ and includes major tropospheric aerosol types of sulfate, dust, organic carbon, black carbon, and sea salt aerosols, providing global distributions of aerosol concentrations, vertical profiles, and optical thickness of individual as well as total aerosols. The model reproduces most of the prominent features in the satellite data and have good agreement with satellite retrieval products from Total Ozone Mapping Spectrometer (TOMS) over both land and ocean and

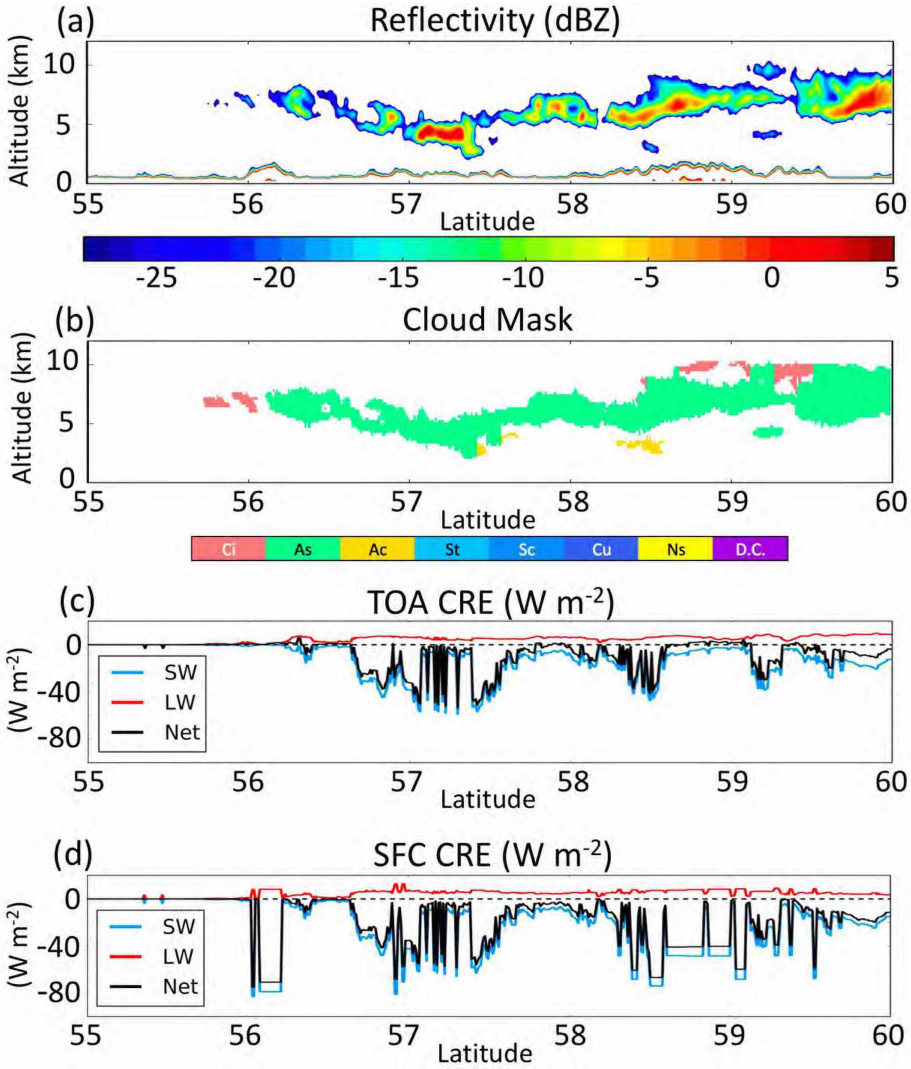

FIGURE 2.1: Selected inputs and outputs of 2BFLX from a portion of granule 05806 between 55°N and 60°N. Observed (a) reflectivity is shown in the upper panel, the (b) cloud mask is shown in the second panel, while the lower two show calculated cloud radiative effect (CRE) at the top-of-atmosphere (TOA) and surface (SFC) (c and d).

from AVHRR over the ocean (Chin et al., 2002). The comparison with AERONET measurements shows that the model can reproduce the seasonal variations, especially for biomass burning and dust aerosol (Ginoux et al., 2001).

Chapter 3

The Effect of Cloud Type on Earth's Energy Budget (EEB) Part I: Top-of-Atmosphere and Surface

This work is motivated by Ockert-Bell and Hartmann (1992) and Hartmann et al. (1992) who used C1 cloud data from the ISCCP (Rossow and Schiffer, 1999) and radiative fluxes data from ERBE (Hartmann et al., 1992) to document the radiative properties of distinct cloud types from spaceborne passive observations. The ISCCP C1 product classified clouds into five types (see Figure 3.1) according to observed cloud height and optical depth. (Ockert-Bell and Hartmann, 1992) and Hartmann et al. (1992) documented the impact of each of

these type on top-of-atmosphere longwave and shortwave radiation contrasting the effects of low, mid-level, and high clouds around the globe. The results provided valuable insights into the factors that govern the distributions of cloud radiative effects and their seasonal variation and served as important benchmarks for evaluating the global models at that time but they were, of course, subject to some limitations. The passive sensors and methods used lacked information for discriminating cloud types at night or distinguishing overlapping cloud fields (Chen et al., 2000, Rossow et al., 1985). Also, the lack of information concerning cloud vertical structure introduces large uncertainties when estimating cloud influences on surface radiation. But since 2006, the active sensors aboard CloudSat and CALIPSO have provided detailed near-global observations of cloud vertical structures (Stephens et al., 2002). In the following sections, the global distribution of radiative effect by individual cloud type at the TOA and the surface are accessed separately with CloudSat and CALIPSO satellite data. Chapter 4 further examines the implications of cloud type for radiative heating and cooling within the atmosphere. This study is published in Journal of Climate as L'Ecuyer et al. (2019).

3.1 Methodology

This study documents the radiative effects of nine vertical structure-based cloud types on radiant energy balance. The analysis uses data from the pre-anomaly phase of the CloudSat mission from January 2007 to December 2010 and covers the complete, near-global sampling provided by CloudSat and CALIPSO from 82.5°S to 82.5°N. All data are gridded to 2.5°×2.5° spatial resolution to ensure adequate sampling on monthly timescales. Since CloudSat and CALIPSO measurements are always collected at 01:30 and 13:30 local time,

the estimated SW fluxes are normalized to the diurnally-averaged insolation to approximate the full diurnal cycle. Here this is achieved by multiplying the shortwave fluxes for each CloudSat pixel by the albedo with the diurnally-averaged insolation for that day and location. This does not account for diurnal variations in cloud cover other than those directly observed at the two sampling times at 1:30 am/pm.

With this limitation in mind, the global annual mean net CRE at the TOA ($C_{Net,\ TOA}$) in this dataset is estimated to be -17.1±4.2 W m^{-2}, with -44.2±2 W m^{-2} in the shortwave ($C_{SW,\ TOA}$) and 27.1±3.7 W m^{-2} in the longwave ($C_{LW,\ TOA}$) (Matus and L'Ecuyer, 2017). The spatial distribution of $C_{Net,\ TOA}$ is shown in Figure 3.2. Clouds are observed to exert a net cooling effect over much of the globe peaking over the mid-latitude oceans. Smaller net warming effects are evident over tropical land regions, most notably equatorial Africa, and in polar regions. The resulting net TOA CRE is somewhat weaker than previous estimates from ISCCP (-25 W m^{-2}) (Raschke et al., 2016), possibly due to biases in assigning optical properties in some regions (Allan, 2011; Stackhouse Jr et al., 2011; Zhang et al., 2004), but agrees well with the latest estimates from CERES (-17.9 W m^{-2}) (Loeb et al., 2018).

In addition to estimating radiative effects at the TOA, cloud boundary information from CloudSat and CALIPSO allows surface cloud radiative effects to be estimated more accurately than from passive sensors. In general, SW CRE at the surface is larger than the TOA due to atmospheric absorption. The global annual average net CRE at the surface ($C_{Net,\ SFC}$) is estimated to be -24.8±8.7 W m^{-2}, with contributions of -51.1±7.8 W m^{-2} in the shortwave ($C_{SW,\ SFC}$) and 26.3±3.8 W m^{-2} in the longwave ($C_{SW,\ SFC}$) (Figure 3.2). The uncertainties in the surface fluxes are derived based on the sensitivity studies reported

in Henderson et al. (2013). Note that in the Henderson et al. (2013) the uncertainty in cloud base height was assumed to be 240 m but recent work of Mülmenstädt et al. (2018) suggest that 480 m is a more appropriate measure of cloud base error. The uncertainties in surface fluxes due to cloud base height errors reported in Table 6 of Henderson et al. (2013) are, therefore, doubled in this study. These estimates of surface cloud radiative effects agree well with derived from Surface Radiation Budget (SRB) dataset (Allan, 2011). Compared with previous results from passive sensors, the differences are significant because there is additional complexity involved in computing surface fluxes (in both 2BFLX and CERES) that contributes to additional uncertainty in flux calculations. To estimate surface fluxes based on TOA fluxes, assumptions need to be made regarding cloud base height, trace gases, aerosols, and radiative transfer. There are clearly discrepancies in the treatment of diurnal cycle between 2BFLX and CERES. Given the complexity involved, it is fairly challenging to attribute the source of this discrepancy. In fact, the global mean $C_{SW,\ SFC}$ from SRB (-53 W m^{-2}) is very similar to that reported here. $C_{LW,\ SFC}$ derived from SRB is somewhat larger (32 W m^{-2}) but still likely within the error bars of both estimates (Stackhouse Jr et al., 2011).

The difference between $C_{Net,\ TOA}$ and $C_{Net,\ SFC}$ implies 7.7$\pm$4.5 W m^{-2} of cloud-induced atmospheric absorption. Note that this atmospheric absorption is defined as the difference between TOA and SFC CRE, as a result, small errors in TOA or SFC can be amplified in the atmospheric absorption estimate since it is computed as a difference. This global mean cloud-induced atmospheric radiative heating derives almost entirely from enhanced SW absorption in the presence of clouds (6.9 W m^{-2}). However, unlike the spatial patterns of SW CRE (C_{SW}) which are almost identical at the TOA and SFC, there are substantial

differences in the spatial structure of LW CRE (C_{LW}) between the surface and the TOA, that demonstrate that clouds exert significant zonal variations in atmospheric radiative heating. Thus SW absorption controls global mean cloud atmospheric heating while strong regional gradients in the strength of cloud LW emission govern its spatial distribution.

3.2 Radiative Effects of Cloud Types

Figure 3.3 shows the global distribution of annual mean cloud fraction from CloudSat and CALIPSO observations that corresponds to the CRE estimates in Figure 3.2. Covering approximately 71% of Earth's surface, clouds are most commonly observed in the inter-tropical convergence zone (ITCZ) and mid-latitude storm tracks, and least frequently over remote subtropical oceans and deserts. A casual comparison of Figures 3.2 and 3.3 clearly demonstrates that total cloud fraction is insufficient for explaining the spatial distribution of net CRE. For example, despite the high net cloud fraction in the ITCZ (80%), $C_{Net,\ TOA}$ (Figure 3.2) in this region nearly vanishes owing to competing LW and SW radiative effects (Kiehl, 1994).

To understand the distribution of cloud radiative effects, cloudy scenes must be partitioned into distinct cloud types. The global distributions of the nine vertical structure-based cloud types identified in the 2BCLD cloud classification are shown in Figure 3.4. Here, an explicit distinction is made between pixels containing a single cloud layer and those that contain multiple layers whose radiative characteristics can differ substantially from those of any of the component layers in isolation. Single-layer clouds have further been separated into eight distinct types according to the 2BCLD classification. Note, however, that the more nuanced topic of further discriminating distinct multilayered cloud scenes (as in Oreopoulos et al.

(2017)) is left as a subject for future study. Instead, we focus on simply distinguishing this complex category of clouds that are often challenging to discriminate using passive sensors. As a result, the frequency and radiative effects of this more diverse category are enhanced relative to their single-layer counterparts but this is done intentionally to illustrate the importance of accurately characterizing such scenes in both observations and models when assessing global cloud radiative effects.

In general, the distributions in Figure 3.4 conform to our qualitative understanding of global cloud distributions: high clouds (cirrus, deep convective clouds, and multilayered cloud systems) are most frequently observed near the equator and over tropical continents resulting from the large transport of water vapor into upper levels by persistent convection. Mid-level clouds (altostratus, altocumulus, and nimbostratus clouds) are predominantly observed over storm track regions. Marine boundary layer clouds (stratus, stratocumulus, and cumulus) are prevalent in subsidence regions over mid-latitude oceans and subtropical eastern ocean margins. However, Figure 3.4 reveals two important distinctions that are generally not captured in passive cloud classifications. First, the ability to distinguish single- and multilayered cloud systems reveals that scenes consisting of more than one overlapping cloud layer cover nearly 30% of the globe. By comparison, the fractional coverage of all categories of single-layered cloud combined is 41%, with stratocumulus the most commonly observed single-layer cloud type at 15.5%. Note that the stratocumulus cloud fraction may be overestimated relative to stratus owing to CloudSat radar detection limits, that favor larger cloud and drizzle droplets and low cloud horizontal homogeneity (Wang et al., 2012). Second, the ability of active sensors to delineate convective cores at high spatial resolution demonstrates

that deep convection represents less than 1% of the cloudy scenes on Earth. From a radiative perspective, it is important to distinguish these convective profiles from the associated cirrus and multilayered clouds even though they may derive from the same storm system in many instances.

3.3 Top-of-Atmosphere

Cloud radiative effects depend not only on their geographic locations but also on their physical and optical properties (Hartmann et al., 1992, Rossow and Lacis, 1990). To quantify this radiative impact at the TOA, the conditional mean CRE of each cloud type, i, is defined as:

$$< C_i >= (F_i^{\downarrow} - F_i^{\uparrow})_{all-sky} - (F_i^{\downarrow} - F_i^{\uparrow})_{clear-sky} \tag{3.1}$$

where $F^{\downarrow}$ and $F^{\uparrow}$ are downward and upward fluxes under clear-sky and all-sky conditions in Earth's atmosphere, respectively (Hartmann et al., 1986, Henderson et al., 2013, Oreopoulos et al., 2011, Ramanathan et al., 1989). Clear-sky fluxes are obtained through plane-parallel radiative transfer calculations in which all condensed water is removed from the atmosphere, while all-sky fluxes represents the standard 2BFLX calculations described above. The subscript, i, denotes each of the nine cloud types in 2BCLD product. Each individual C_i is weighted by the global cloud fraction of each cloud type (shown in Figure 3.4) to determine its contribution to the total CRE:

$$C_i =< C_i > \times CF_i \tag{3.2}$$

where $< C_i >$ is the conditional mean CRE when cloud type i and CF_i is the corresponding cloud fraction. Figure 3.5 highlights examples of this calculation for cirrus and stratocumulus clouds. C_i shows the contributions of cloud type i to the total CRE. C_i exhibits more variability than $< C_i >$ which only accounts for variation in cloud effects induced by background or environmental conditions and cloud properties. This suggests that, once segregated by type, the spatial distribution of each cloud type plays a bigger role in determining its effect on climate than variations in cloud microphysical structure or environment. However, regional variations in conditional mean CRE are evident such as smaller net C_{Ci} over Tibetan Plateau, polar regions, and Rocky Mountains where the temperature contrast between cirrus and the colder underlying surfaces is smaller. Figure 3.5 also reveals that $< C_{Sc} >$ is more variable than $< C_{Ci} >$ because in the former case there is greater contribution to the net CRE from SW CRE which is more sensitive to internal cloud property (optical depth) variability within the cloud type, and also depends on systematic variations in solar geometry. The goal of this work is to contrast the radiative effects of each cloud type in CLDCLASS-LIDAR, C_i.

3.3.1 Global Distribution of Radiative Effect by Individual Cloud Types

Figures 3.6, 3.7, and 3.8 display global maps of annual mean $C_{Net,\ TOA}$, $C_{SW,\ TOA}$, and $C_{LW,\ TOA}$ of nine cloud types based on 2BFLX estimates. As shown in Figure 3.6, cirrus and stratocumulus clouds exert the strongest net radiative impacts globally of the single-layer cloud types. Cirrus clouds are found to warm the atmosphere and surface by 2 W m^{-2}, on the global annual mean, especially over relatively warm surfaces including the Tropical Warm Pool and Sahel region. Stratocumulus clouds, by contrast, exert a large cooling effect of -8.2 W m^{-2}. The most pronounced influences of stratocumulus occur over subtropical

oceans where they can exceed -20 W m^{-2}. Altocumulus, stratus, and cumulus clouds also exert significant cooling influences on the planet but these effects seldom exceed 10 W m^{-2} in any given location (Figure 3.6).

Multilayered cloud systems are found to significantly cool the planet by an average of -6.1 W m^{-2}, contributing nearly 44% of the global total $C_{SW,\ TOA}$ and nearly 49% of the global total $C_{LW,\ TOA}$. However, these effects vary substantially with geographic location. Multilayered cloud systems exert a strong cooling effect over the Pacific ITCZ, a warming effect over equatorial Africa, and a negligible effect over eastern India and Indonesia. This is a consequence of the fact that multilayered cloud pixels, as defined here, can consist of various combinations of high and low cloud whose frequency depends strongly on local environment. Nevertheless of the 9 cloud types considered here, the spatial distribution of total $C_{Net,\ TOA}$ most closely resembles that from multilayered cloud systems that are likely the most challenging to capture in both passive observations and global models.

The net effect of clouds on TOA radiation is determined by the relative magnitude of the LW and SW effects. The radiative impacts of the single-layer cloud types are governed by a combination of their frequency and geometric and optical properties. Optically thin high clouds exert a net warming effect while optically thick, shallow clouds contribute a net cooling effect. The transition between these regimes depends on both cloud height and optical depth but is decidedly skewed toward an albedo effect for most cloud types owing to the asymptotic behavior C_{LW} which saturates at relatively low optical depth. Only high, thin cirrus clouds and, to a much lesser extent, altostratus, exert positive net radiative effects globally.

The SW and LW radiative effects of each of cloud type are presented in Figures 3.7 and 3.8, respectively. Single-layer cirrus are found to reduce SW absorption by only 0.8 W m^{-2} but decrease outgoing LW by 2.8 W m^{-2} resulting in a net warming effect of 2 W m^{-2}. In contrast, stratocumulus clouds reduce SW absorption by 10.4 W m^{-2} on the global annual mean, an effect nearly five times stronger than their greenhouse effect noted above. While single-layer nimbostratus, altostratus, and deep convective clouds exert significant effects in both SW and LW radiation individually, these effects largely cancel over the mid-latitudes and tropics resulting in comparatively weak global mean net radiative effects. Cloud shortwave effects at the TOA are dominated by the grid box mean cloud optical depth which peaks in areas of frequent stratocumulus a few 100 km off the west coasts of North America, South America, Africa, and Australia. Stratus exert significant C_{SW} but in smaller regions confined closer to the coasts while altostratus and nimbostratus exert strong C_{SW} in the higher latitude storm-tracks. Once again, infrequent single-layer deep convective clouds lead to a relatively small net SW radiative effect that is confined to the ITCZ and west Pacific.

Cloud longwave effects are generally dominated by the distribution of cloud top height within each grid box peaking in regions where cirrus and altostratus are prevalent such as the Inter-Tropical and South Pacific convergence zones. At higher latitudes, frequent, relatively deep nimbostratus exert a significant longwave radiative effect that sums to a global impact comparable in magnitude to that of cirrus and altostratus. Perhaps less intuitively, clouds identified as stratocumulus in 2BCLD are also found to exert a substantial longwave radiative effect, owing to their large populations in storm tracks in north Atlantic and Pacific and over the Southern Oceans. While it may be debated whether it might be

more appropriate to classify these clouds as cumulus, these results clearly indicate that, in sufficient numbers, purely liquid bearing clouds with high emissivities and tops warmer than 273 K exert a significant global LW radiative effect at the TOA. At the fine resolution of individual CloudSat fields of view, single-layer deep convective clouds are observed relatively infrequently leading to a muted impact on TOA radiation that is largely confined to the ITCZ and west Pacific.

While these findings generally follow basic physical principles governing cloud radiative effects that have been understood for several decades (Gleckler et al., 1995, Harrison et al., 1990, Manabe and Strickler, 1964, Ramanathan et al., 1989, Stephens and Greenwald, 1991, Stephens and Webster, 1981), the active sensors aboard CloudSat and CALIPSO allow these effects to be quantified for individual cloud types defined based on explicit measures of their vertical structure. More importantly, CloudSat and CALIPSO provide unprecedented ability to identify pixels containing overlapping cloud layers revealing that multilayered cloud systems dominate both $C_{SW,\ TOA}$ and $C_{LW,\ TOA}$, exerting albedo and greenhouse effects of -19.4 W m^{-2} and 13.2 W m^{-2}, respectively. These radiative effects of multilayered cloud systems bear a strong resemblance to those of deep convective clouds in the tropics and stratocumulus clouds over mid-latitude oceans, partially explaining the reduced influence of deep convection globally relative to other studies (Oreopoulos et al., 2011). At the pixel level, these observations reveal that systems that are traditionally generalized as 'deep convection' really consist of a relatively small fraction of contiguous deep cores and a much larger fraction of multi-layer clouds that often consist of cirrus overlying liquid clouds (Stephens and Wood, 2007). While this distinction may seem inconsequential for TOA radiation balance, it has important implications for the structure of radiative heating in the atmosphere

that can significantly influence atmospheric general circulation. Thus accurate estimates of the relative frequency of single- and multilayered clouds within convective systems has the potential to improve the accuracy of climate models (Chepfer et al., 2008, Naud et al., 2010).

3.3.2 Seasonal Variation of Cloud Radiative Effects

Cloud cover, environmental characteristics, and solar insolation all vary substantially over the course of the year imparting a strong seasonality on net cloud radiative effects. For historical context, wherever possible the seasonal variability in cloud radiative effects are loosely grouped into cloud types that parallel those adopted more than 25 years ago by Ockert-Bell and Hartmann (1992) and Hartmann et al. (1992) to illustrate the evolution of the perspective provided by earlier passive instruments into that from modern radar-lidar observations. The most logical grouping is illustrated in Figure 3.1 that highlights the new information provided by space-borne active sensors. The five cloud types on the left correspond to the cloud top pressure and visible optical depth-based cloud type definitions used by Hartmann et al. (1992). Those on the right, illustrate where each of the nine 2BCLD CloudSat and CALIPSO vertical structure-based classes reside on this diagram. Given that there is no 1:1 relationship between physical height and pressure and the optical depths of the 2BCLD cloud types are variable, the axes on the right-hand chart have been replaced with qualitative indicators of increasing cloud height and optical thickness. Nevertheless, Figure 3.9 illustrates how active sensors allow further distinctions to be made based on quantitative cloud top and base information and explicit detection of multiple cloud layers. Lacking such information, ISCCP cloud types were primarily based on estimates of cloud top height and total optical thickness and made no distinction between single and multilayered

cloud systems, often mis-interpreting the latter as mid-level clouds (Mace et al., 2009). More modern clustering techniques make use of spatial structure information to better distinguish cumuliform and stratiform cloud types but have not fully resolved issues associated with mis-interpreting multilayered cloud systems (Oreopoulos et al., 2011, Tselioudis and Jakob, 2002). By contrast, vertically resolved measurements from CloudSat and CALIPSO are able to distinguish multilayered cloud systems from deep convective and mid-thick clouds as well as to sub-divide mid- and low-level cloud types into alto-cumulus, alto-stratus, cumulus, stratocumulus, and stratus based on their vertical and horizontal extents, as shown in Figure 3.1b.

Figure 3.9 compares zonal mean distributions of TOA SW, LW, and net CRE in Northern Hemisphere winter and summer defined as December-February (DJF) and June-August (JJA), respectively. Total zonal mean SW CRE (Figures 3.9a and 3.9b) is approximately mirrored about the equator in DJF compared to JJA, owing to the shift in solar illumination between the hemispheres as expected. However, significant asymmetries exist at higher latitudes where shortwave effects are considerably more pronounced in the southern hemisphere in DJF due to enhanced solar reflection from ubiquitous marine clouds in the Southern Ocean. This asymmetry can be largely attributed to increased effects of stratocumulus clouds that exert nearly three times as much SW CRE over the Southern Oceans than at similar latitudes in the Northern Hemisphere owing to the substantial difference in land fraction between the hemispheres.

By contrast, Figures 3.9c and 3.9d show that the LW CRE is far more symmetric between the hemispheres with a maximum tracking the migration of the ITCZ and a distinct minimum in

the subsidence regions at approximately 20 degrees latitude in the winter hemisphere. This results in a hemispheric imbalance in net CRE. Not surprisingly, deep convective clouds and isolated cirrus dominate single-layered clouds effects on $C_{LW,\,TOA}$ in the tropics while mid-level cloud types contribute significantly at mid-latitudes. The LW CRE of single-layer high clouds are, however, confined to tropical regions and considerably reduced relative to estimates from passive sensors owing to the explicit distinction between single- and multilayered systems enabled by active sensors. This is in contrast to the perspective from passive sensors that suggest nearly equal contributions are made by high-thin clouds and high-thick clouds (e.g. Hartmann et al. (1992), Oreopoulos et al. (2011)).

Figures 3.9e and 3.9f demonstrate that SW radiative effects dominate net cloud radiative effects at the TOA at most latitudes in both hemispheres with the exception of the polar regions in the winter hemisphere where nimbostratus and multilayered cloud systems induce a net heating over the ice caps. While it is well-understood that clouds exert a positive net CRE in polar night, the magnitude of this effect has been very difficult to quantify with passive sensors, let alone isolating the effects of different cloud types. Here we find that cloud heating reaches a peak of more than 20 W m^{-2} over the southern hemisphere sea ice at 65°S before decreasing substantially over the interior of the Antarctic ice sheet. Conversely, clouds are found to warm the Arctic in winter by a more uniform 15 W m^{-2} poleward of 60°N.

Globally, stratocumulus and multilayered clouds contribute nearly equally to net CRE at the TOA, each imparting a large net cooling to Earth's energy budget. This can be contrasted with previous work that suggested that low clouds dominate the net radiative effect, with mid-level clouds providing the second-largest contribution. This emphasizes the value of

spaceborne active sensors for resolving the ambiguity introduced in assigning multilayered systems by cloud top pressure and optical depth (Mace et al., 2006a, 2009). Scenes that contain a combination of high and low cloud are frequently mis-classified as optically-thick mid-level cloud by passive sensors (Mace and Wrenn, 2013, Marchand et al., 2010). This has important implications for evaluating cloud distributions and their resultant radiative effects in global models. Vertically-resolved measurements from CloudSat and CALIPSO offer new capability to resolve such ambiguities enabling new methods of cloud partitioning that may provide a robust understanding of the radiative effects of complex multilayered cloud types.

3.4 Surface

Clouds also strongly impact the surface energy balance by modulating radiative heat exchanges between the atmosphere, land surface, and the ocean (Bony et al., 1997, Wild et al., 2013, Zhang et al., 1995). In fact, more than 90% of the excess energy in the climate system due to increased greenhouse gas concentrations is absorbed at the surface where clouds play a critical role in modulating radiative fluxes (Trenberth et al., 2014, 2009). However, current estimates of surface energy budget are poorly resolved because passive sensors lack the ability to penetrate optically thick clouds and quantify cloud base height. Models also exhibit large biases in radiative fluxes at the surface relative to ground-based measurements, some of which may be associated with cloud base heights (Garratt, 2001, Li et al., 2013, Wild, 2005, 2008, Wild et al., 2013, 2001). The accurate cloud base information provided by CloudSat and CALIPSO allows more robust estimates of how clouds influence the surface energy balance (L'Ecuyer et al., 2009, Stephens et al., 2012a).

Figures 3.10, 3.11, and 3.12 show the global distributions of $C_{Net,\ SFC}$, $C_{SW,\ SFC}$, and $C_{LW,\ SFC}$ derived from 2BFLX from each cloud type over 2007-2010. Most clouds exert larger net cooling effects at the surface (Figure 3.10) compared to the TOA (Figure 3.6). The exception is stratus and stratocumulus clouds that enhance LW emission to the surface offsetting a significant fraction of their SW cooling effect. On the global annual mean, multilayered cloud systems represent the single largest source of cooling in Earth's surface energy budget with an estimated surface net CRE of -11.9 W m^{-2}. Stratocumulus clouds exert the second strongest net cooling at the surface (-4.1 W m^{-2}), only half as strong as their net effect at the TOA. All cloud types, especially, stratiform clouds and multilayered cloud systems, are found to exert a net warming effect over polar regions where enhanced longwave emission exceeds impacts on SW absorption owing to the reflective snow and ice surfaces and reduced annual mean solar insolation (Pavolonis and Key, 2003).

It is clear from Figures 3.11 and 3.12 that longwave heating dominates the difference in CRE between the TOA and surface. Figure 3.11 shows that the spatial patterns of $C_{SW,\ SFC}$ and $C_{SW,\ TOA}$ are very similar even though each cloud type exerts larger shortwave cooling effect at the surface than the TOA owing to additional absorption of SW radiation. The greatest contributions to $C_{SW,\ SFC}$ are, therefore, once again from multilayered cloud systems (-22.3 W m^{-2}) and stratocumulus clouds (-11.6 W m^{-2}) as at the TOA. $C_{LW,\ SFC}$ (Figure 3.12), on the other hand, exhibits distinctly different patterns from the TOA (Figure 3.8). For example, cirrus clouds, deep convective clouds, and multilayered cloud systems exert much greater longwave radiative effects at the TOA than at the surface. Stratocumulus, stratus, and cumulus clouds, on the other hand, exert significant LW warming at the surface especially over subtropical and mid-latitude oceans where they enhance longwave emission

to the surface at warm temperatures that correspond to their low cloud bases and large optical thicknesses (Mülmenstädt et al., 2018).

Global estimates of the zonal mean CRE at the surface are displayed in Figure 3.13. Overall, there is closer symmetry between the CRE in DJF and in JJA at the surface than at the TOA. The zonal distribution of $C_{SW,\ SFC}$ (Figures 3.13a and 3.13b) is similar to $C_{SW,\ TOA}$ (Figures 3.9a and 3.9b), but with a larger magnitude. $C_{SW,\ SFC}$ peaks in DJF over the Southern Ocean where it approaches -140 W m^{-2} on the seasonal mean. The zonal distribution of $C_{LW,\ SFC}$ is substantially different from $C_{LW,\ TOA}$ exhibiting a pronounced minimum in the tropics owing to both a relatively low fraction of optically-thick low clouds and the effects of water vapor that mask cloud emission to the surface. LW CRE increases at the surface over mid-latitudes especially over the Southern Oceans where clouds enhance LW emission to the surface by nearly 60 W m^{-2} in both summer and winter causing a substantial seasonal oscillation in net cloud radiative effects at the surface (Figures 3.13c and 3.13d).

Figures 3.13e and 3.13f indicate that clouds strongly cool the surface in the summer hemisphere while exerting somewhat smaller warming effects in the winter hemisphere. Thus the seasonal contrast in solar insolation between the hemispheres is muted at the surface (Rossow and Zhang, 1995). The largest annual cycle of net CRE at the surface occurs over the Southern Oceans where clouds exert substantial warming in JJA and exert the strongest seasonal-mean net cooling observed anywhere on Earth in DJF. This results in a 125 W m^{-2} variation in net radiation absorbed at the surface over the annual cycle. When integrated

over each hemisphere, this alternating cloud heating and cooling between winter and summer leads to about 100 W m^{-2} of relative cooling in the summer hemisphere offsetting a substantial fraction of the seasonal hemispheric imbalance in solar insolation.

3.5 Chapter Summary

This work updates global observational estimates of cloud impacts on the global radiation balance in light of the new vertically-resolved cloud information from CloudSat and CALIPSO. While this topic far from new, these active sensors provide more robust information for separating single-layered and multilayered cloud systems according to their spatial and vertical structure than previous available. We calculate the radiative effects of nine distinct cloud types using the fifth release 2B-FLXHR-LIDAR product, which yields high horizontal and vertical resolution (1.4×1.7 km^2 and 240 m, respectively) radiative flux and heating rate profiles consistent with CloudSat, CALIPSO, MODIS, and AMSR-E observations. On the annual mean, clouds are found to exert a net cooling of -17.1±4.2 W m^{-2}. This results from -44.2±2 W m^{-2} of SW reflection and 27.1±3.7 W m^{-2} of enhanced LW heating, globally. Contrary to classical analyses, the greatest contributions to global CRE are found to come from multilayered clouds that are often misclassified as thick mid-level clouds in approaches that use passive sensors alone. Since multilayered cloud systems are often represented through crude overlap parameterizations in atmospheric general circulation models, these results reinforce the significant challenges involved in accurately modeling the impact of clouds on atmospheric circulations (Mace et al., 2009, Naud et al., 2008, Pincus et al., 2006, Shonk et al., 2012). The decomposition of cloud radiative effects into vertically resolved cloud types and multilayered cloud systems presented here, may offer a potential

pathway for evaluating the distribution of cloud radiative effects and column heating rates within AGCMs in light of the new vertical structure information provided by spaceborne active sensors in much the same way as ISCCP and ERBE did three decades ago (Cess et al., 1990, 1989, Harrison et al., 1990, Webb et al., 2001, Wyant et al., 2006, Zhang et al., 2005).

This work also leverages CloudSat and CALIPSO cloud boundary information to discern the influence of cloud-type variations on radiation balance at the Earth's surface, a critical factor in modulating the disposition of excess energy in the climate system. The global annual net cloud radiative effect at the surface is estimated to be -24.8±8.7 W m^{-2}. SFC SW CRE exhibits a very similar spatial pattern as TOA SW CRE but is enhanced by 7 W m^{-2} to -51.1±7.8 W m^{-2} owing to increased atmospheric absorption by clouds. On the other hand, the global mean LW CRE at the surface (26.3±3.8 W m^{-2}) is almost identical to that at the TOA but exhibits a markedly different spatial pattern reflecting the fact that SFC LW CRE derives from enhanced emission from liquid water near the surface. This implies that, while cloud SW effects govern cloud impacts on total atmospheric heating, LW effects govern its redistribution. This result is explored in much greater detail in Chapter 4.

It is further shown that multilayered clouds also dominate CRE at the surface, enhancing surface longwave radiation by 10.4 W m^{-2} and reducing surface shortwave radiation by 22.3 W m^{-2}. Stratocumulus clouds also strongly reduce surface shortwave radiation by 11.6 W m^{-2} but nearly 60% of this is offset by enhanced LW emission. These results provide valuable constraints on TOA and surface energy balance and hint at the different roles distinct cloud types may play in atmospheric heating. They clearly confirm that clouds with similar TOA

radiative signatures can have very different impacts at the surface. This is consistent with the fact that distinct cloud types exhibit distinct vertical heating profiles in the atmosphere and, by extension, exert distinct influences on large scale circulations (Mace and Wrenn, 2013). Though it is beyond the scope of the current study, CloudSat and CALIPSO provide the vertical resolution required to examine the influence of cloud morphology on the spatial and vertical distribution of heating within the atmosphere (Ham et al., 2017, Mather and McFarlane, 2009, Protat et al., 2014).

Consistent with other recent work, a hemispheric asymmetry in CRE is observed. This is illustrated in Figure 3.14 that summarizes all of the numerical findings from this work and reports the radiative impacts of each vertical structure-based cloud type at the TOA and SFC for each hemisphere separately. At the TOA, clouds cool the Northern Hemisphere by -12.8 W m^{-2} while cooling the Southern Hemisphere by -21.4 W m^{-2}. This asymmetry is primarily caused by the strong radiative cooling from stratocumulus over the Southern Ocean during local summer (Fasullo and Trenberth, 2008, Stephens et al., 2016). Stratocumulus clouds exert almost twice as much SW cooling at the TOA (-13.5 W m^{-2}) in the Southern Hemisphere as they do in the Northern Hemisphere (-7.5 W m^{-2}).

Possibly more striking, however, is the fact that there is no accompanying hemispheric imbalance in cloud radiative effects at the surface. On the annual mean, the stronger summertime surface SW cooling from stratocumulus is canceled by enhanced LW heating from low clouds year-round. This suggests that the asymmetry in cloud radiative effects is primarily realized in the atmosphere, influencing atmospheric heat transport across the equator much more so than in the oceans. As noted by many others, understanding and modeling this hemispheric

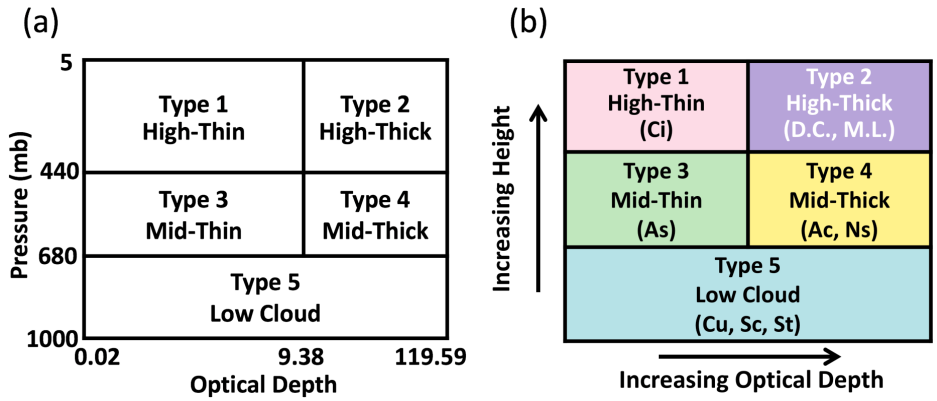

FIGURE 3.1: Five classes of cloud defined according to the ISCCP radiance classification (Hartmann et al., 1992) (left), and equivalent classification based on true cloud height and cloud thickness according to the CloudSat and CALIPSO 2BCLD (right).

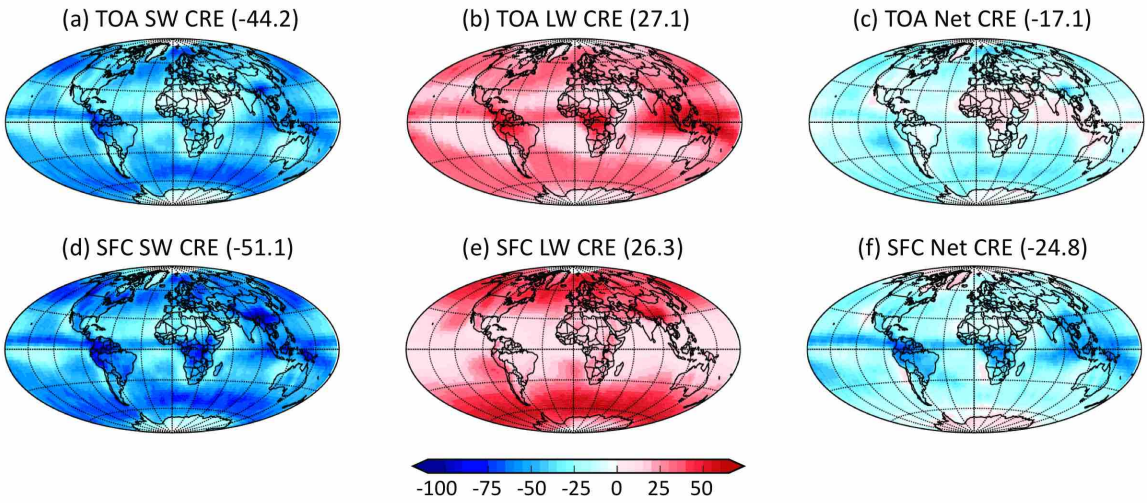

FIGURE 3.2: Annual mean SW, LW, and net cloud radiative effects at the top of atmosphere (top) and surface (bottom) (W m^{-2}). All fluxes data presented are from 2BFLX, 2007-2010. The area-weighted global average (in W m^{-2}) is shown in parentheses.

asymmetry is critical for accurately representing atmospheric circulations in global models (Frierson et al., 2013, Loeb et al., 2016, Stephens et al., 2016). The results presented here reinforce the need to resolve model low cloud biases in the Southern Oceans and add an imperative to assess and improve the representation of multilayered cloud systems using active sensors.

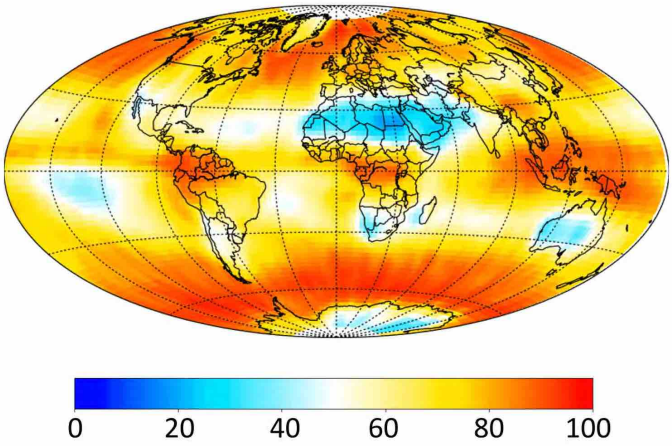

FIGURE 3.3: Annual mean cloud fraction using CloudSat and CALIPSO observations from 2007 to 2010 (%). The global average is 70.8%.

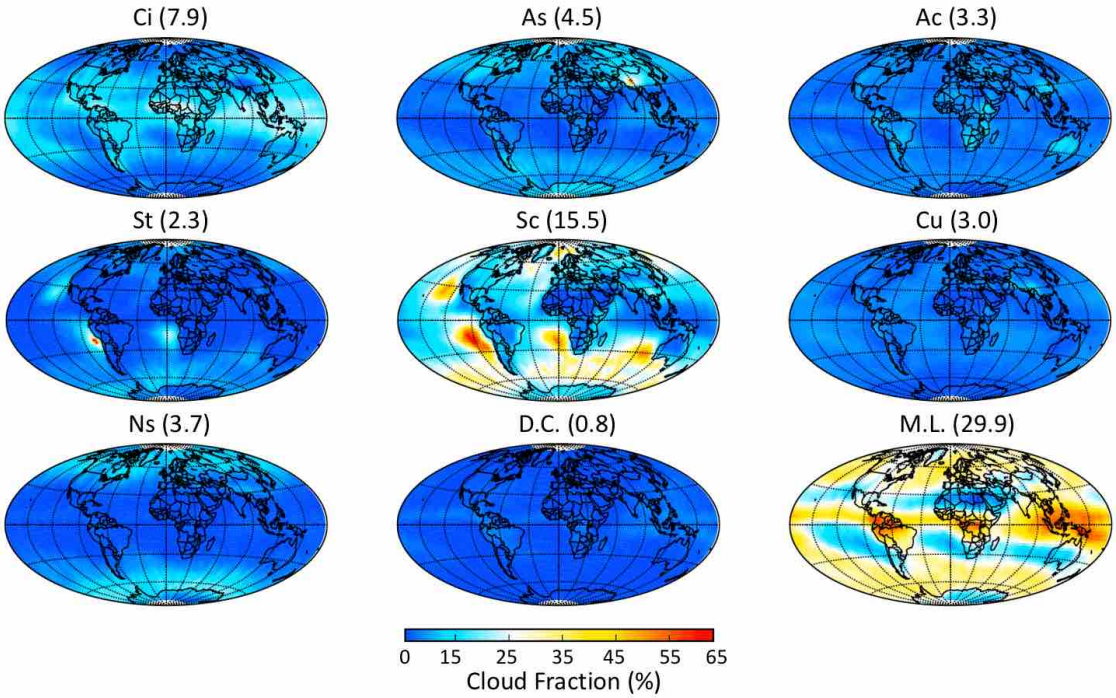

FIGURE 3.4: Breakdown of annual mean cloud fraction (Figure 3.3) by cloud type determined based on 2BCLD classification, 2007-2010 (%). The area-weighted global average (in %) is shown in parentheses. Ci=cirrus, As=altostratus, Ac=altocumulus, St=stratus, Sc=stratocumulus, Cu=cumulus, Ns= nimbostratus, D.C.=deep convection and M.L.=multilayered cloud system.

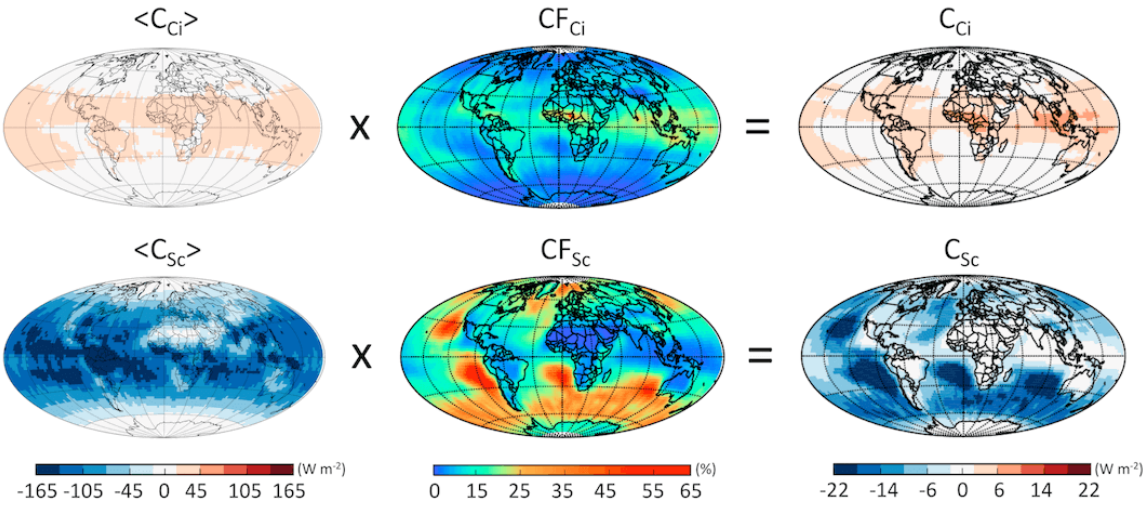

FIGURE 3.5: Selected global maps of $< C_i > \times CF_i = C_i$ (for cirrus, Ci, and stratocumulus, Sc, clouds). $< C_i >$ is the total net CRE at TOA when cloud type i is observed, CF_i is the cloud fraction of cloud type i, C_i shows the contribution of cloud type i to the global CRE.

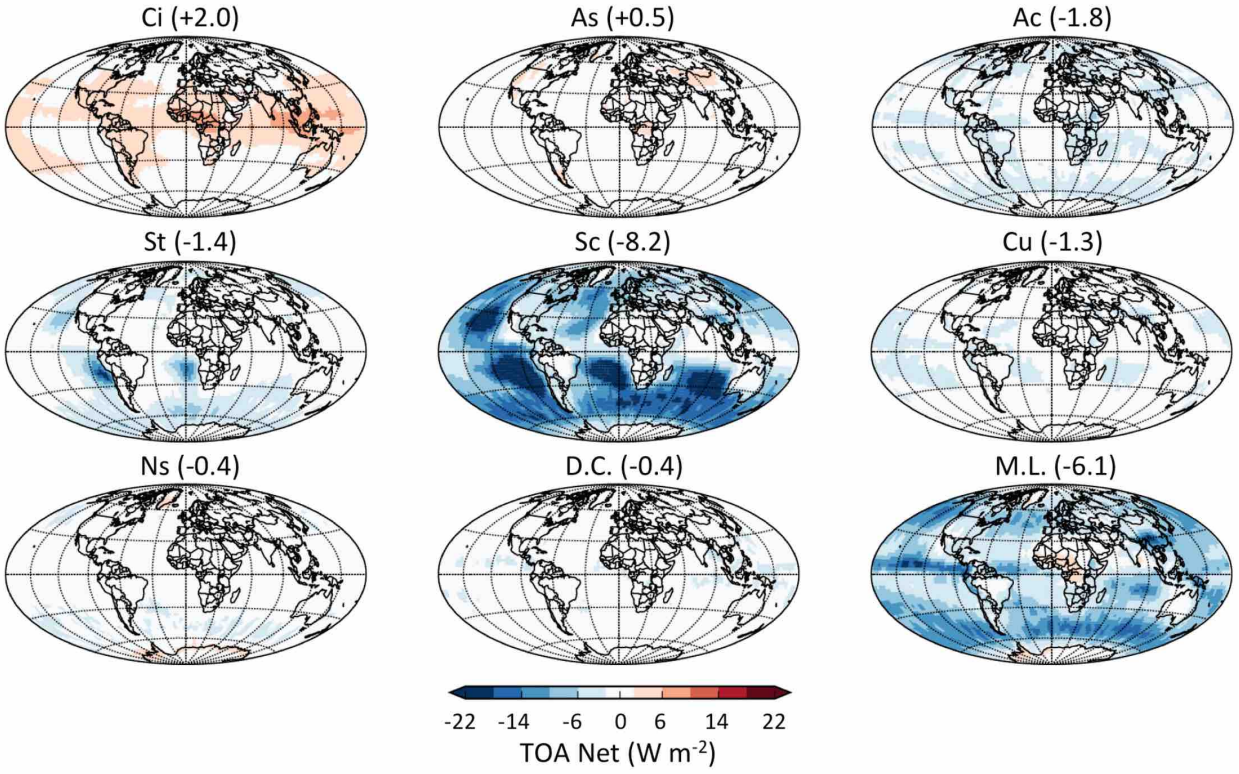

FIGURE 3.6: Annual mean net cloud radiative effects at the top-of-atmosphere (W m^{-2}). Radiative effects are separated by cloud type determined based on 2BCLD classification. All fluxes data presented are from 2BFLX, 2007-2010. The area-weighted global average (in W m^{-2}) is shown in parentheses.

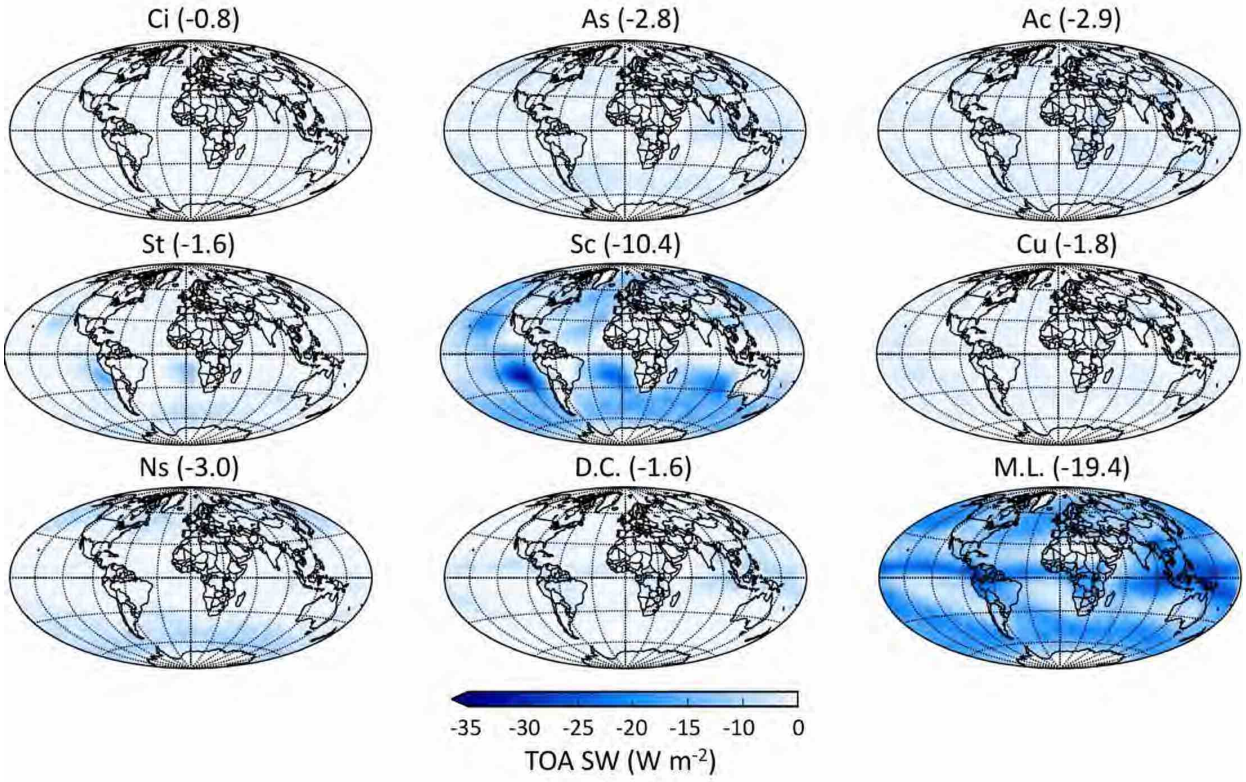

FIGURE 3.7: Same as Figure 3.6, but for shortwave cloud radiative effects at the top-of-atmosphere (W m^{-2}).

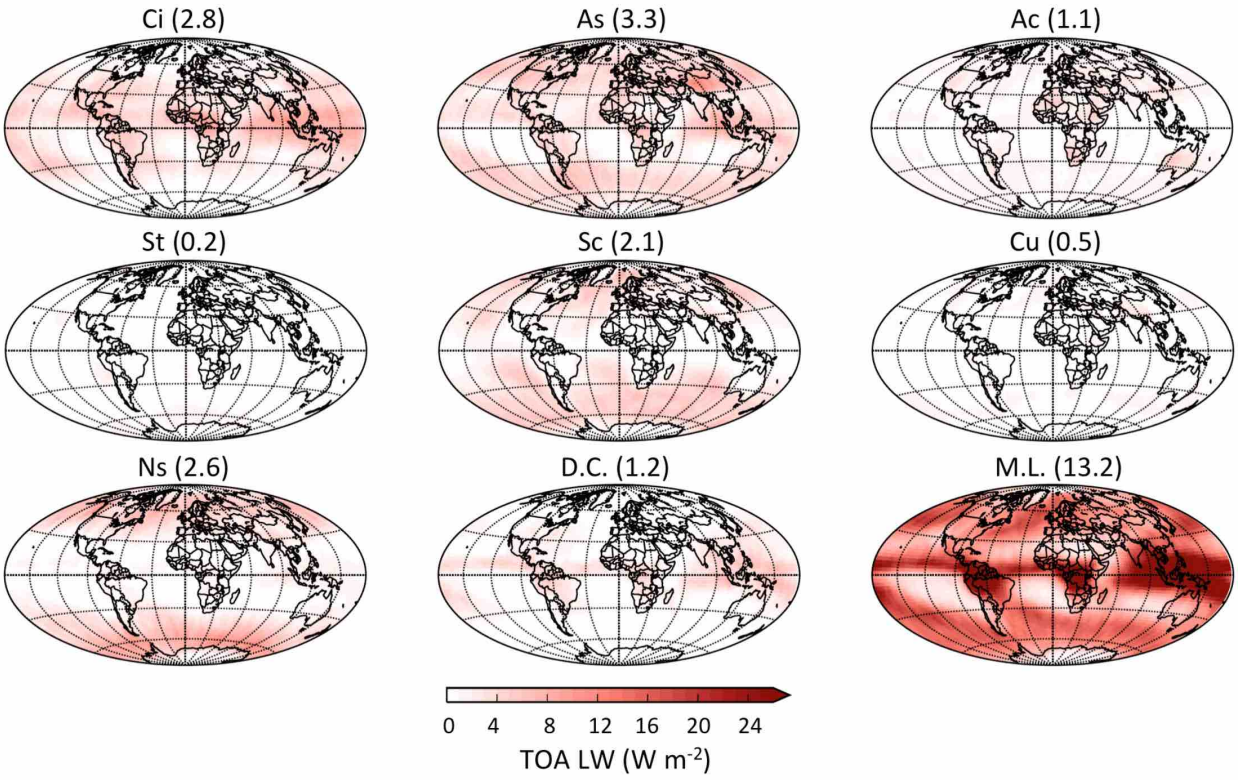

FIGURE 3.8: Same as Figure 3.6, but for longwave cloud radiative effects at the top-of-atmosphere (W m^{-2}).

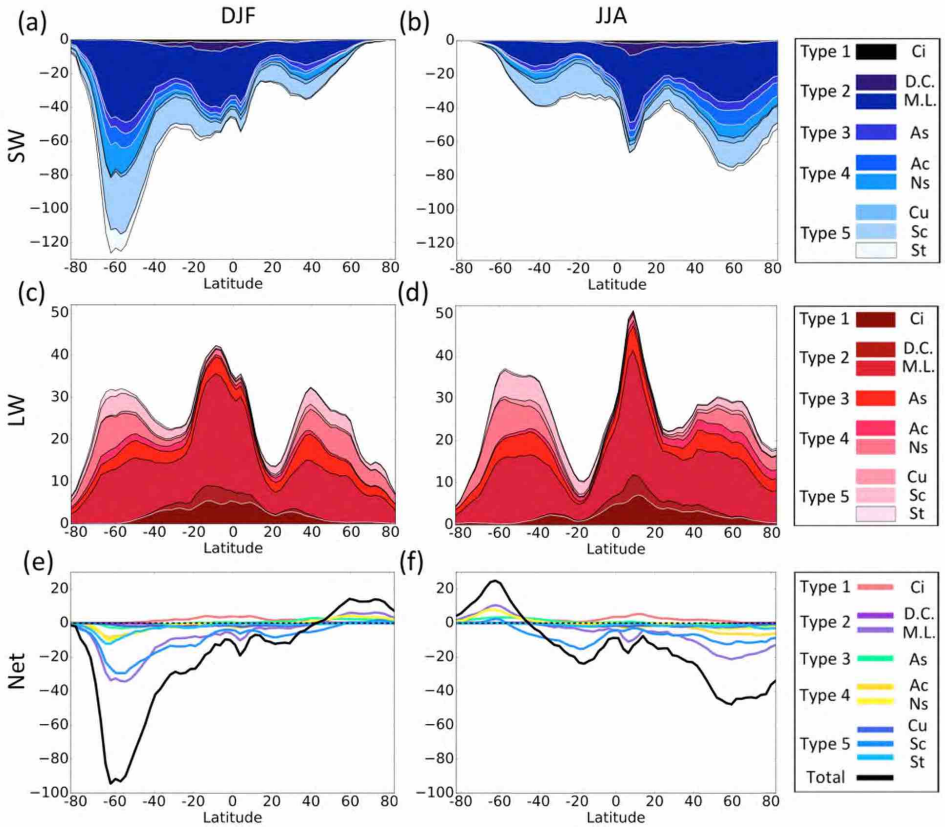

FIGURE 3.9: Seasonal zonal mean cloud radiative effects at the top-of-atmosphere (W m^{-2}). Radiative effects are separated by cloud type determined based on 2BCLD classification. Seasons are defined as December-February (DJF) and June-August (JJA). All fluxes data are from 2BFLX, 2007-2010.

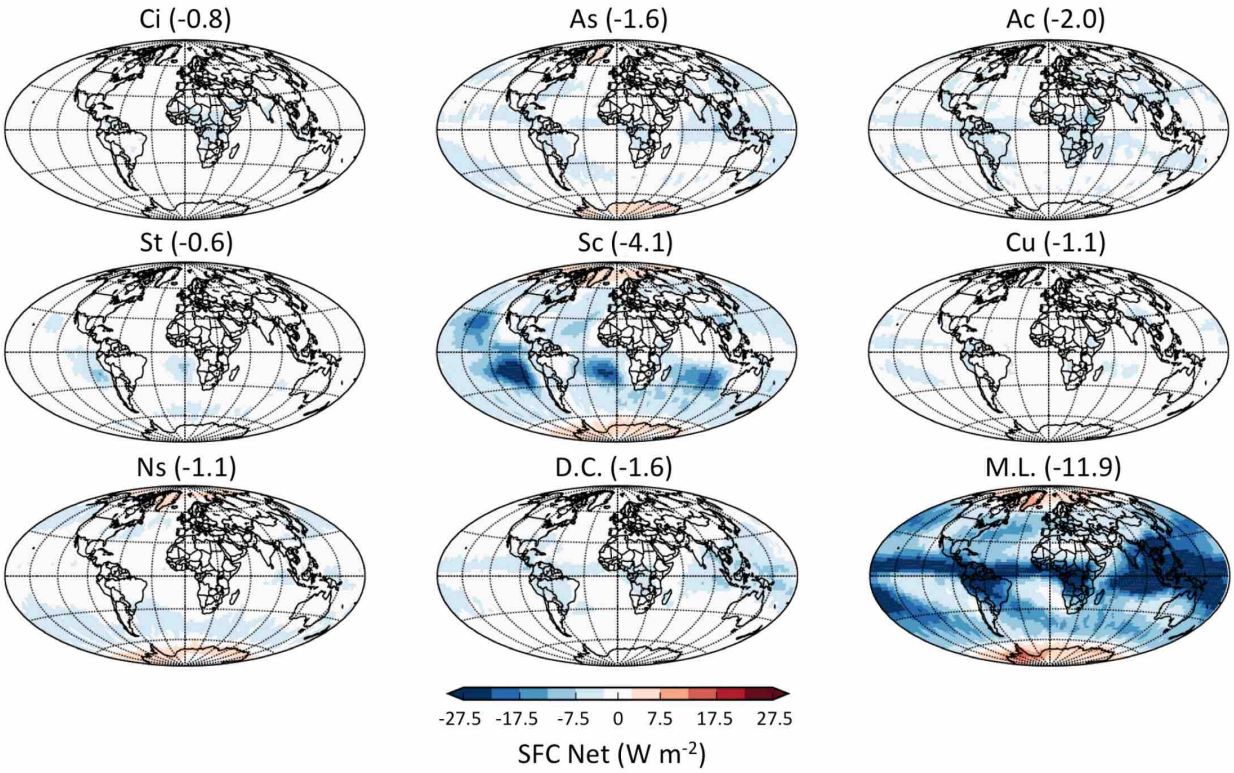

FIGURE 3.10: Same as Figure 3.6, but for net cloud radiative effects at the surface (W m^{-2}).

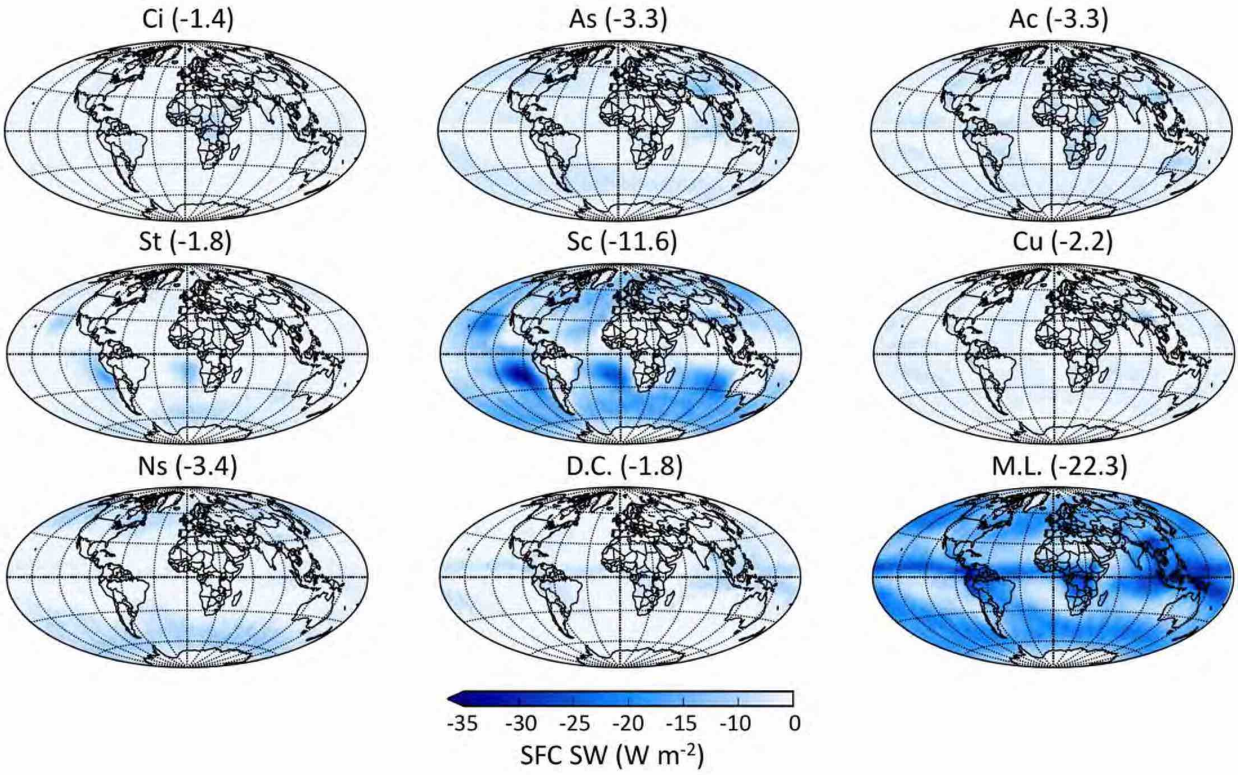

FIGURE 3.11: Same as Figure 3.6, but for shortwave cloud radiative effects at the surface (W m^{-2}).

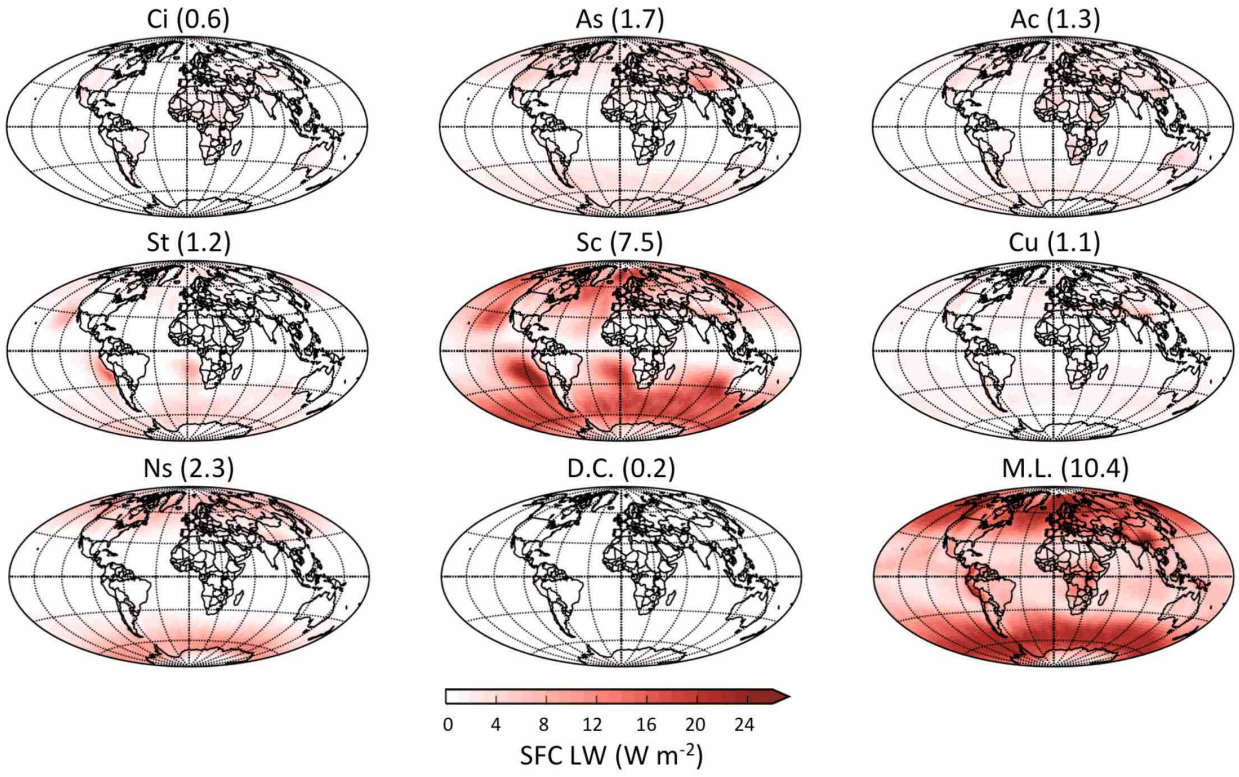

FIGURE 3.12: Same as Figure 3.6, but for longwave cloud radiative effects at the surface (W m^{-2}).

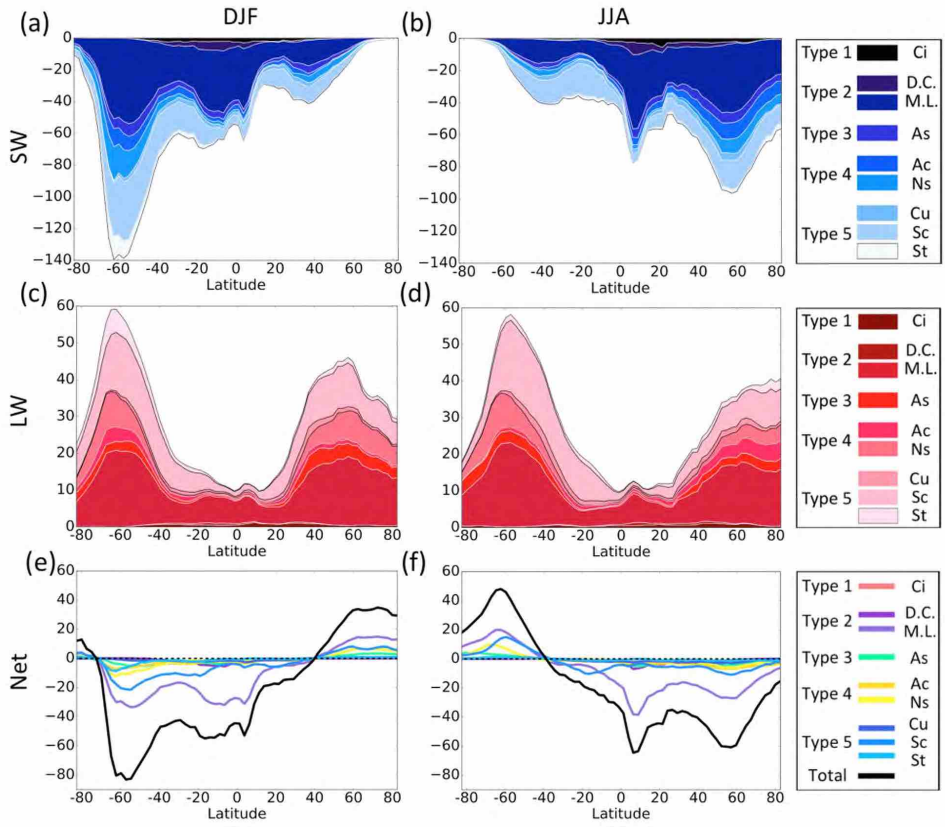

FIGURE 3.13: Same as Figure 3.9, but for seasonal zonal mean cloud radiative effects at the surface (W m^{-2}).

	Global	Ci	As	Ac	St	Sc	Cu	Ns	D.C.	M.L.	Total
TOA	CF	7.9	4.5	3.3	2.3	15.5	3.0	3.7	0.8	29.9	70.8
	CRE_{SW}	-0.8	-2.8	-2.9	-1.6	-10.4	-1.8	-3.0	-1.6	-19.4	-44.2
	CRE_{LW}	2.8	3.3	1.1	0.2	2.1	0.5	2.6	1.2	13.2	27.1
	CRE_{Net}	2.0	0.5	-1.8	-1.4	-8.3	-1.3	-0.4	-0.4	-6.2	-17.1
	NH										
	CF	9.1	5.1	3.5	1.5	12.3	3.0	3.4	0.9	30.5	69.3
	CRE_{SW}	-0.9	-3.0	-3.0	-0.9	-7.5	-1.9	-2.5	-1.8	-19.1	-40.4
	CRE_{LW}	3.2	3.6	1.3	0.2	1.6	0.5	2.3	1.3	13.6	27.6
	CRE_{Net}	2.3	0.6	-1.8	-0.7	-5.9	-1.3	-0.2	-0.4	-5.4	-12.8
	SH										
	CF	6.7	3.9	3.2	3.1	18.6	3.1	4.0	0.6	29.3	72.4
	CRE_{SW}	-0.8	-2.8	-2.6	-2.4	-13.5	-1.9	-3.4	-1.3	-19.5	-48.1
	CRE_{LW}	2.3	3.0	1.0	0.4	2.7	0.6	2.8	1.0	12.9	26.7
	CRE_{Net}	1.6	0.4	-1.7	-2.0	-10.9	-1.3	-0.5	-0.3	-6.7	-21.4

	Global	Ci	As	Ac	St	Sc	Cu	Ns	D.C.	M.L.	All
SFC	CF	7.9	4.5	3.3	2.3	15.5	3.0	3.7	0.8	29.9	70.8
	CRE_{SW}	-1.4	-3.3	-3.3	-1.8	-11.6	-2.2	-3.4	-1.8	-22.3	-51.1
	CRE_{LW}	0.6	1.7	1.3	1.2	7.5	1.1	2.3	0.2	10.4	26.3
	CRE_{Net}	-0.8	-1.6	-2.0	-0.6	-4.1	-1.1	-1.1	-1.6	-11.9	-24.8
	NH										
	CF	9.1	5.1	3.5	1.5	12.3	3.0	3.4	0.9	30.5	69.3
	CRE_{SW}	-2.0	-3.7	-3.5	-1.0	-8.7	-2.3	-3.0	-1.9	-22.8	-49.0
	CRE_{LW}	0.8	1.9	1.4	0.8	5.5	1.1	2.2	0.3	10.1	24.1
	CRE_{Net}	-1.2	-1.8	-2.1	-0.2	-3.3	-1.2	-0.8	-1.6	-12.7	-24.9
	SH										
	CF	6.7	3.9	3.2	3.1	18.6	3.1	4.0	0.6	29.3	72.4
	CRE_{SW}	-1.2	-3.0	-3.1	-2.6	-14.9	-2.2	-3.8	-1.4	-22.0	-54.1
	CRE_{LW}	0.5	1.4	1.1	1.6	9.4	1.1	2.5	0.2	10.6	28.4
	CRE_{Net}	-0.7	-1.6	-1.9	-1.0	-5.5	-1.1	-1.3	-1.2	-11.4	-25.7

FIGURE 3.14: Summary of type-separated global, Northern Hemisphere, and Southern He misphere annual mean cloud fraction (%) and cloud radiative effect (W m^{-2}) at the TOA and surface. All data presented are from 2BFLX, 2007-2010.

Chapter 4

The Effect of Cloud Type on EEB

Part II: Atmospheric Heating

The earliest efforts to quantify radiative heating in the atmosphere began in the mid twentieth century (Manabe and Möller, 1961, Manabe and Strickler, 1964, Manabe and Wetherald, 1967). After entering the satellite era in the 1960s, observations from passive sensors on polar-orbiting satellites revolutionized our understanding of the global top-of-atmosphere radiative fluxes and, through radiative transfer calculations, atmospheric heating in the next several decades (Hartmann and Short, 1980, Kato et al., 2005, Rossow and Zhang, 1995, Sabatini and Suomi, 1962, Vonder Haar and Suomi, 1971, Wielicki et al., 1996b, Zhang et al., 2004). More recently, ground-based active sensors and field campaigns have provided high-quality estimates of the vertical structure of radiative heating in the atmosphere at fixed locations (Johnson and Young, 1983, McFarlane et al., 2007) but extrapolating this information to global scales was challenging until the launch of the CloudSat and CALIPSO

in 2006 (Oreopoulos et al., 2017, Stephens et al., 2002, 2008, Winker et al., 2007). Previous work from Haynes et al. (2013) demonstrated that the active CloudSat and CALIPSO sensors provide the only means for examining profiles of atmospheric heating from space. When integrated vertically, such observations can be used to document the spatial distribution of cloud impacts on radiative heating in the atmosphere.

Chapter 3 provides valuable constraints on TOA and surface energy balance and hint at the different roles distinct cloud types may play in atmospheric radiative heating; however, clouds with similar TOA radiative signatures can have impacts on atmospheric radiative heating in the atmosphere and exert very distinct influences on large scale circulations (Mace and Wrenn, 2013). To help address this issue, this study quantifies the impacts of nine distinct cloud types, defined based explicitly by their vertical structure, on column atmospheric radiative heating. The chapter is organized as follows. Section 1 will describe methods used in this analysis. Section 2 will discuss the cloud impact on column-integrated atmospheric heating and illustrates the dramatically different characteristics of the heating under distinct cloud types. After that, the effects of clouds on atmospheric radiative heating will be further explored by their vertical structures. This study is published in Journal of Climate as Hang et al. (2019).

4.1 Methodology

This study uses 2BCLD and 2BFLX to investigate the impact of clouds on column-integrated atmospheric radiative heating. 2BFLX applies Equation (1.2) to LW and SW flux profiles at the full CloudSat vertical resolution to derive vertical profiles of atmospheric radiative heating in all-sky conditions. A separate set of broadband flux calculations are derived for

each CloudSat profile with all condensate removed to establish clear-sky heating rates from which cloud impacts can be derived. The column-integrated heating is computed by evaluating Equation (1.2) between the top of the atmosphere and the surface. The cloud impact on atmospheric radiative heating Q_{cld} is equivalent to differencing the TOA and surface cloud radiative effect as shown in Equation (1.3). This study investigates the impact of clouds on atmospheric heating using data from the pre-anomaly phase of the CloudSat mission from January 2007 to December 2010 that provided near-global daytime and nighttime coverage from 82.5°S to 82.5°N. All data are gridded to 2.5°×2.5° spatial resolution to ensure adequate sampling on monthly timescales. Since CloudSat and CALIPSO measurements are always collected at 01:30 and 13:30 local time, the estimated SW fluxes are normalized to the diurnally-averaged insolation to approximate the full diurnal cycle. It should be noted, however, that this does not account for diurnal variations in cloud cover other than those directly observed at the two sampling times at 1:30 am/pm.

GPCP-WALRUS data product

To place the cloud impacts derived here in the context of the other main drivers of atmospheric heating, they are compared against clear-sky radiative cooling estimates from 2BFLX and estimates of column-integrated latent heat. Latent heat release from precipitation is estimated primarily using observations from the Global Precipitation Climatology Project (GPCP) augmented in warm rain regions using the CloudSat-based Wisconsin Algorithm for Latent heat and Rainfall Using Satellites (WALRUS) (Nelson et al., 2016). GPCP provides global, monthly rainfall estimates at 2.5°×2.5° resolution derived from merged polar-orbiting and geosynchronous satellite from 1997 to present under the World Climate

Research Program (Huffman et al., 1997). These rainfall estimates include all forms of precipitation but may miss some isolated warm rain in subsidence regions. To account for this small additional source of latent heating, GPCP observations are augmented using WALRUS latent heat estimates in areas where the latter observes more rainfall following the method described in Nelson and L'Ecuyer (2018). WALRUS uses a Bayesian Monte Carlo methodology that couples cloud-resolving model simulations from the Regional Atmospheric Modeling System (RAMS) (Saleeby and Cotton, 2004, Saleeby and van den Heever, 2013) to CloudSat observations to retrieve latent heat profiles at CloudSat's 1.5-km spatial and 240 m vertical resolution (Nelson and L'Ecuyer, 2018). GPCP and WALRUS data from 2007-2010 are adopted to be consistent with the radiative heating estimates.

4.2 Global Distribution of Cloud Impact on Atmospheric Radiative Heating

Cloud impacts on column-integrated atmospheric net, SW, and LW radiative heating are shown in Figure 4.1. Averaged globally, clouds produce a net planetary atmospheric heating of 0.07±0.08 K day^{-1}, increasing SW absorption by 0.06±0.07 K day^{-1} and LW heating by only 0.01±0.04 K day^{-1}. Error bounds are derived using the same methodology in Chapter 3 and are defined using discrepancies between 2BFLX and CERES TOA fluxes, as well as possible shortcomings in the 2BFLX retrieval. The CERES instrument aboard Aqua provides a unique opportunity for evaluating 2BFLX, because of the small temporal gap between the orbits of Aqua satellite and CloudSat. Using the CERES TOA fluxes as a reference, uncertainties in TOA fluxes are derived based on the biases between 2BFLX and CERES presented in Matus and L'Ecuyer (2017) for SW and LW fluxes. At the surface,

sensitivity studies presented in Henderson et al. (2013) suggest that the largest uncertainties 2BFLX surface flux estimates derive from CloudSat liquid water content, surface temperature, and lower-troposphere humidity. Further, significant regional errors in downwelling LW fluxes may arise due to uncertainty in cloud base heights (Mülmenstädt et al., 2018). The total uncertainty at the surface is derived by summing the square of the uncertainties listed in the aforementioned sensitivity analyses and taking the square root of the resultant sum. The overall column integrated net, SW, and LW error bounds are then calculated following Equation (1.3) using the resultant total TOA and surface uncertainty estimates. Since the cloud impact on atmospheric radiative heating is computed as the difference between two large numbers each with non-negligible uncertainties, errors in cloud impacts on top-of-atmosphere and surface fluxes are amplified in atmospheric heating leading to much larger fractional uncertainties.

Despite their relatively small global effects, however, the distinct vertical structures of clouds in different regions leads to substantial variations in LW heating that produce large (primarily zonal) variations in cloud heating (Haynes et al., 2013; Li et al., 2016). Regionally, LW heating ranges from 0.5 K day^{-1} in the Tropical Warm Pool and a minimum cooling of -0.2 K day^{-1} over the sub-tropical oceans. Clouds do not enhance much total column SW absorption compared to LW. Enhancement within cloud is apparently partially compensated by reduced water vapor absorption below the cloud (Oreopoulos et al., 2016). This is especially true over the darker oceans but clouds are observed to enhance SW atmospheric warming over higher albedo land surfaces where they interact with both incoming and reflected radiation. Thus while SW heating over land surfaces is almost entirely responsible for the global mean cloud heating, the large regional variability in LW heating dominates its

spatial distribution. It is clearly shown in the observed zonal distribution of cloud impacts on atmospheric heating that imply that clouds exert a strong influence on large-scale meridional circulations, enhancing equator to pole energy gradients by radiatively warming the tropics and cooling higher latitudes. This requires an increased rate of meridional energy transport in the atmosphere relative to the initial clear-sky radiative cooling imbalances that control the underlying circulation on a global scale (Soden and Held, 2006, Sohn and Smith, 1992). Recent comparisons with climate models have shown that cloud influences on heating is underestimated in convective regimes, while the impact on cooling is underestimated in subsidence regimes because models tend to simulate fewer low clouds (Cesana et al., 2019).

Figure 4.2 decomposes the cloud impact on annual mean column-integrated net atmospheric radiative heating into the contributions from each of the nine CloudSat/CALIPSO cloud types shown in Figure 3.4. By far the most striking feature in Figure 4.2 is the strong contribution from multilayered clouds that bears a strong resemblance to the total $Q_{Net,\ cld}$ (Figure 4.1). For example, the active sensors aboard CloudSat and CALIPSO demonstrate that multilayered cloud systems contribute more than 2.5 times at much global radiative heating as single-layer cirrus clouds. This indicates the fact that cirrus make up the top layer in the vast majority of multilayered clouds, but active sensors suggest that a majority of cirrus cloud radiative effects derive from multilayered cloud scenes rather than single-layer cirrus (Figure 3.4). In some regions such as equatorial Africa, the Sahel, and the Tropical Warm Pool, multilayered clouds warm the atmosphere by more than 0.24 K day^{-1}. Conversely, low cloud types are found to enhance atmospheric radiative cooling. Stratocumulus clouds, in particular, cool the atmosphere by -0.03 K day^{-1}. Over subtropical subsidence regions, the cooling introduced by Peruvian stratocumulus clouds exceeds -0.16 K day^{-1}.

The other major Sc regions off the west coasts of California, Namibia, Australia, and Canary Islands, cool the atmosphere by about -0.12 K day^{-1}. Nimbostratus and altostratus clouds tend to exert a small influence on net atmospheric radiative heating owing to a local cancellation of SW warming and LW cooling effects, even though they are observed somewhat more frequently in the Northern Hemisphere (NH) (Figure 3.4).

Decomposing cloud impacts on atmospheric heating into SW (Figure 4.3) and LW (Figure 4.4) components provides additional insights into the heat budget of the atmosphere. Globally, multilayered cloud systems are found to increase SW atmospheric heating by 0.03 K day^{-1} but exert much larger influences over land regions. The largest impacts are observed in equatorial Africa, the Sahel, and Southeast Asia where SW heating from multilayered clouds exceeds 0.12 K day^{-1}. Cirrus and altostratus clouds exhibit smaller but still significant enhanced SW warming over the Sahel and Western China, respectively.

As noted above, however, the distribution of cloud influences on net atmospheric heating is dominated by the cloud impacts on LW heating. Figure 4.4 suggests that the global pattern of atmospheric LW radiative heating from clouds results primarily from the sum of two cloud types: M.L. and stratocumulus clouds. A predominant warming from multilayered cloud systems is modulated in subsidence regions and over the Southern Oceans by enhanced cooling from marine stratocumulus. Multilayered cloud systems act to substantially enhance the LW heating over Intertropical Convergence Zone (ITCZ), while stratocumulus clouds act to enhance the LW cooling over mid-latitude oceans.

4.3 Role of Cloud Type in Defining Meridional Heating Gradients

L'Ecuyer et al. (2019) suggests that the net cloud impact on global mean atmospheric radiative heating is small, compared to latent heating and sensible heating. However, as shown in Figure 4.1, clouds significantly influence meridional gradients in atmospheric heating. This is further emphasized in Figure 4.5 that displays the annual mean impact of each cloud type on zonal-annual mean atmospheric radiative heating. Clouds significantly enhance tropical atmospheric heating maximizing at 7°N with the majority of heating contributed by cirrus and multilayered clouds. Clouds also substantially cool the atmosphere at high-latitudes owing to cooling from stratocumulus and multilayered clouds. This result is consistent with Chen et al. (2000) who clearly showed the enhancement of the meridional gradient in atmospheric heating by clouds, but mid-level clouds contributed more cooling effects at high-latitudes. One reason for the discrepancy may be that the multilayered clouds containing a combination of high and low cloud are mis-interpreted as mid-level clouds by passive sensors (Mace and Wrenn, 2013, Mace et al., 2009, Marchand et al., 2010).

To understand the significance of these impacts, the magnitudes of these effects are placed in the context of total atmospheric heating, Q_{atm}, defined as:

$$\begin{aligned} Q_{atm} &= f_{clr}\ (< Q_{SW,clr} > + < Q_{LW,clr} >) + \sum_{i=1}^{9} f_i\ (< \overline{Q_{SW,cld_i}} > + < \overline{Q_{LW,cld_i}} >) + LE + SH \\ &= Q_{SW,clr} + Q_{LW,clr} + \sum_{i=1}^{9} (Q_{SW,cld_i} + Q_{LW,cld_i}) + LE_{rain} + LE_{snow} + SH \end{aligned} \tag{4.1}$$

where f_{clr} is the fraction of clear-sky scenes, $< Q_{clr} >$ is the conditional mean atmospheric

cooling of clear-sky. The subscript i, denotes each of the nine cloud types in 2BCLD cloud classification and f_i is the cloud fraction of each cloud type i (Figure 3.4). $< Q_{cld} >$ is the conditional mean cloud impact. Q_{SW,cld_i} or Q_{LW,cld_i} is defined as the cloud impact on SW (Figure 4.3) or LW (Figure 4.4) atmospheric heating, weighted by the cloud fraction of each cloud type i. LE_{rain} or LE_{snow} is the amount of latent heat released from rain or snow and SH is sensible heating.

Figure 4.6 compares the contributions of each term in Equation (4.1) to the global annual mean atmospheric heating. In clear skies, the LW cooling is almost four times stronger than the SW heating, resulting in a net atmospheric cooling of -1.1 K day^{-1}. Despite covering nearly 70% of the sky on average, however, clouds heat the atmosphere by only 0.07 K day^{-1}, or about 6% of the clear sky radiative cooling. Although cirrus, stratocumulus, and multilayered clouds are abundant, they contribute less than 0.05 K day^{-1} to total atmospheric heating when integrated over the globe. This small global mean cloud impact, however, is the result of cancellation of warming and cooling effects of different cloud types in different regions. Such cancellation does not occur in clear-skies where LW radiative cooling dominates or in precipitation where latent heating is always positive. Cloud heating is also much smaller than the latent heat released in precipitation which is estimated to be 0.66 K day^{-1} derived from GPCP-WALRUS and sensible heat which is estimated to be 0.15 K day^{-1} derived from ERA-Interim reanalysis.

To emphasize the potential for clouds to impact atmospheric heating regionally, Figure 4.7 compares zonal averaged distributions of clear-sky atmospheric cooling, cloud impact on atmospheric heating, and latent heat released from precipitation. Zonal mean cloud impact

is greatest at 5°N where it reaches 0.3 K day^{-1}, canceling nearly a quarter of clear-sky radiative cooling. In the polar regions, clouds cool the atmosphere efficiently offsetting all latent heat release poleward of 70°. The balance between radiative cooling and latent heating has been shown to be an important control on precipitation (Stephens and Ellis, 2008). These comparisons reveal that cloud impacts can play an important role in defining this balance zonally with potentially important implications for the general circulation (Slingo and Slingo, 1988).

These strong zonal variations in cloud impacts can, of course, be traced to regional variations in the occurrence of different cloud types. Figure 4.8 decomposes atmospheric radiative heating in four broad latitude bands into contributions from clear-skies and each observed cloud type. Clear-sky atmospheric cooling decreases from tropics to the poles due to the colder emitting temperatures and reduction in LW cooling from water vapor. By contrast, cloud impacts exhibit more regional diversity ranging from net heating in the tropics (0.23 K day^{-1}) to net cooling in the poles (-0.13 K day^{-1}). The regional diversity coincides with large variations in cloud type. Interestingly, in all but the mid-latitude band, the largest contribution to the cloud impact is provided by multilayered cloud systems, which act to heat the tropics but cool the poles primarily through their influences on LW radiation. By contrast, cirrus clouds cause atmospheric LW heating from the equator to the pole, while stratocumulus clouds increase atmospheric LW cooling at all latitudes, dominating the overall cloud impact on atmospheric heating in the mid-latitudes. When considered in the context of the global atmospheric heat transport, these results demonstrate that clouds significantly enhance meridional heating gradients consistent with the suggested two-way coupling between clouds and atmospheric circulations (Harrop and Hartmann, 2016,

Hartmann and Short, 1980, Li et al., 2015, Slingo and Slingo, 1991, Winker et al., 2017).

4.4 Influence of Clouds on Hemispheric Heating Imbalances

Hemispheric energy imbalances and the resulting cross-equatorial heat transport play a key role in establishing the location of the region of large-scale ascending branch of the meridional overturning circulation, or ITCZ, and the associated global precipitation maximum (Donohoe et al., 2013, Frierson et al., 2013, Hwang and Frierson, 2013, Loeb et al., 2016, Stephens et al., 2016). Figure 4.5 clearly indicates that clouds play a role in setting the hemispheric energy imbalances as cloud impacts on atmospheric heating are decidedly asymmetric about the equator. Clouds cool more strongly in the southern high latitudes while the peak in tropical cloud heating resides with the ITCZ north of the equator. The asymmetry in cloud heating is more directly quantified in Figure 4.9 where column-integrated impact of clouds in the Northern Hemisphere and Southern Hemisphere (SH) are summarized separately. Overall cloud heating is three times stronger in the NH (0.1±0.08 K day^{-1} or 3.1±2.5 PW) than in the SH (0.04±0.08 K day^{-1} or 1.1±2.5 PW). As a result, clouds induce a substantial 1.4 PW (shown in Figure 4.10, the difference of hemispheric imbalance in Q_{cld} and LE) of atmospheric heat transport (approximately two thirds of the total heating asymmetry of 2.0±3.5 PW) from the SH to the NH relative to cloud free skies. The decomposition into cloud types presented here support previous assertions that in addition to tropical cloud effects, remote influences from extra-tropical clouds contribute to this imbalance (e.g. Yoshimori and Broccoli (2008) and Frierson and Hwang (2012)). Figure 4.9 indicates that enhanced LW cooling by stratocumulus clouds over the Southern Ocean and excess LW heating from multilayered

clouds in the Northern Hemisphere each contribute approximately one third of this asymmetry. In both cases, cloud impacts on longwave radiation are primarily responsible for the asymmetry. More frequent stratocumulus clouds over the Southern Oceans increase downwelling LW radiation from the atmosphere to the surface, enhancing atmospheric cooling in the SH relative to the NH storm tracks. Conversely, enhanced upper-level cloud cover associated with the asymmetric location of the ITCZ in the Northern Hemisphere leads to an enhanced greenhouse effect that amplifies this hemispheric imbalance.

Figure 4.10 compares the magnitudes of these estimates of cloud-induced hemispheric atmospheric heating imbalances against corresponding imbalances in clear-sky atmospheric cooling, latent heat released in precipitation, and sensible heat exchanges between the surface and the atmosphere. While cloud impacts on atmospheric heating only amount to about 10% of Q_{clr} and LE on the global mean (Figure 4.6), hemispheric asymmetries in cloud heating are larger than those in either clear-sky atmospheric cooling and latent heat. In fact, the hemispheric asymmetry in cloud impacts on atmospheric heating is larger than the other three sources combined. This suggests that hemispheric imbalances in cloud heating, that include both remote influences and those associated with high clouds in the ITCZ itself, play an important role in reinforcing the present-day Northern Hemisphere location of the ITCZ and associated tropical precipitation maximum. Furthermore, the decomposition of this cloud-induced hemispheric atmospheric energy imbalance into components from distinct cloud types supports the assertion that a relatively small bias in SH cloud cover could influence the predicted location of the ITCZ (Hwang and Frierson, 2013). Figures 4.9 and 4.10 thus provide references against which the simulated impacts of distinct cloud types on hemispheric energy imbalances in reanalysis and coupled global models may be compared

(Trenberth and Fasullo, 2010).

As noted in prior studies, cloud radiative effects over the Southern Ocean exhibit a strong seasonal cycle (Haynes et al., 2011, Klein and Hartmann, 1993, Rossow and Lacis, 1990, Trenberth and Fasullo, 2010). As a result, much of the observed asymmetry in cloud heating impacts can be traced to the SH winter months when solar insolation is at a minimum placing a greater emphasis on the longwave radiative cooling effects of the stratocumulus clouds over the southern oceans. Figure 4.11 contrasts the annual cycles of cloud impacts on atmospheric heating in each hemisphere. Global Q_{cld} as well as its SW and LW components are approximately constant throughout the year. Cloud heating in each hemisphere, however, tracks the annual progression of the sun from the SH in Dec, Jan, Feb to the NH in Jun, Jul, Aug. Variations in SW heating are largely symmetric between the hemispheres peaking in the summer hemisphere, but the peak LW cloud heating in the NH summer is considerably stronger than in the SH and remains above the global mean for more than eight months of the year. When combined with the reinforcing effects of a stronger atmospheric greenhouse effect in the NH tropics, this causes the hemispheric imbalance in cloud heating to reach a maximum in the SH winter. When combined with $Q_{SW,\ cld}$, the hemispheric imbalance of $Q_{Net,\ cld}$ reaches a peak of 0.24 K day^{-1} (or 7.3PW) in July (Figure 4.11a).

4.5 Chapter Summary

This work documents the influences of nine vertical structure-based cloud types on atmospheric radiative heating using CloudSat and CALIPSO observations. On the global annual mean, clouds induce a net planetary atmospheric radiative heating of 0.07±0.08 K day^{-1} (0.06±0.07 K day^{-1} in the SW, 0.01±0.04 K day^{-1} in the LW). Multilayered cloud systems,

which are ubiquitous in both hemispheres, are found to exert the strongest influence on the global atmospheric heating. About two thirds of the heating from multilayered clouds is, however, offset by enhanced cooling from stratocumulus clouds that are the most common single-layer cloud type observed. While this leads to a relatively small influence on global, annual mean atmospheric heating (roughly 10 % as large as the clear-sky cooling and latent heat release in precipitation formation), clouds can exert an influence on zonal-mean atmospheric heating that is comparable to clear-sky atmospheric cooling and latent heat release in some regions. It is found that clouds heat the tropics by 0.23 K day^{-1} and cool the poles by -0.13 K day^{-1}, significantly influencing zonal heat redistribution, and supporting stronger poleward energy fluxes (Harrop and Hartmann, 2016).

These zonal variations in cloud heating, in turn, lead to a strong hemispheric asymmetry in atmospheric heating that is driven by both the local effects of multilayered clouds in the ITCZ itself and the remote influence from stratocumulus clouds over the Southern Oceans. This hemispheric asymmetry in cloud heating peaks in the NH summer when the ITCZ is at its northernmost latitude and the effects of SH stratocumulus are dominated by LW cooling. On the annual mean, clouds heat the NH by 0.1$\pm$0.08 K day^{-1}, nearly three times stronger than cloud heating in SH (0.04$\pm$0.08 K day^{-1}). The resulting 2$\pm$3.5 PW imbalance in cloud heating implies that clouds induce more than 1 PW of southward heat transport across the equator relative to clear skies. The decomposition into cloud types presented here suggests that tropical and extra-tropical cloud systems contribute approximately equally to this imbalance.

The magnitude of the cloud-induced atmospheric hemispheric energy imbalance inferred

from CloudSat and CALIPSO observations lies at the upper bound of the total southward atmospheric heat transport (0.33±0.6 PW) estimated by Stephens et al. (2016). One reason for this discrepancy may be that the CERES EBAF product under-estimates downwelling longwave radiation (DLR) by several Wm^{-2} relative to similar products that include active sensor information such as 2BFLX and the CERES-CloudSat-CALIPSO-MODIS (C3M) product (Ham et al., 2017, Kato et al., 2012, Stephens et al., 2012b). Since Chapter 3 demonstrated that cloud impacts on DLR are 4.3 Wm^{-2} larger in the SH, primarily from stratocumulus clouds over the southern oceans, it is plausible that this key source of SH atmospheric cooling is stronger in 2BFLX than EBAF. While there are reasons to believe that active sensors may improve estimates of downwelling fluxes (Henderson et al., 2013, Mülmenstädt et al., 2018, Stephens et al., 2012b), the precise magnitude of cloud impact on DLR in the SH is difficult to estimate and remains uncertain at this time as captured by the large error bars in both the present work and Stephens et al. (2016). However, it is clear that even a small increase in SH downwelling LW radiation of a few Wm^{-2} induces a significant shift in the estimated partitioning of cross-equatorial heat transport from the oceans to the atmosphere.

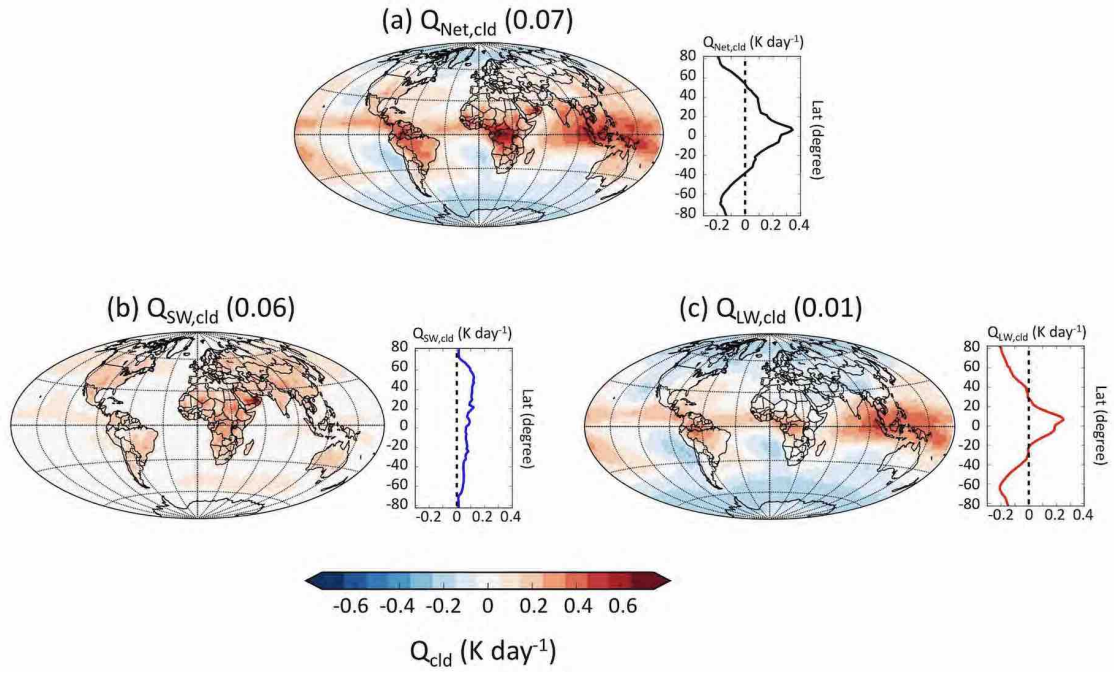

FIGURE 4.1: Annual mean cloud impact on column-integrated (a) net, (b) SW, and (c) LW atmospheric radiative heating (K day^{-1}). The global average is shown in parentheses. Zonal averages are shown on the right.

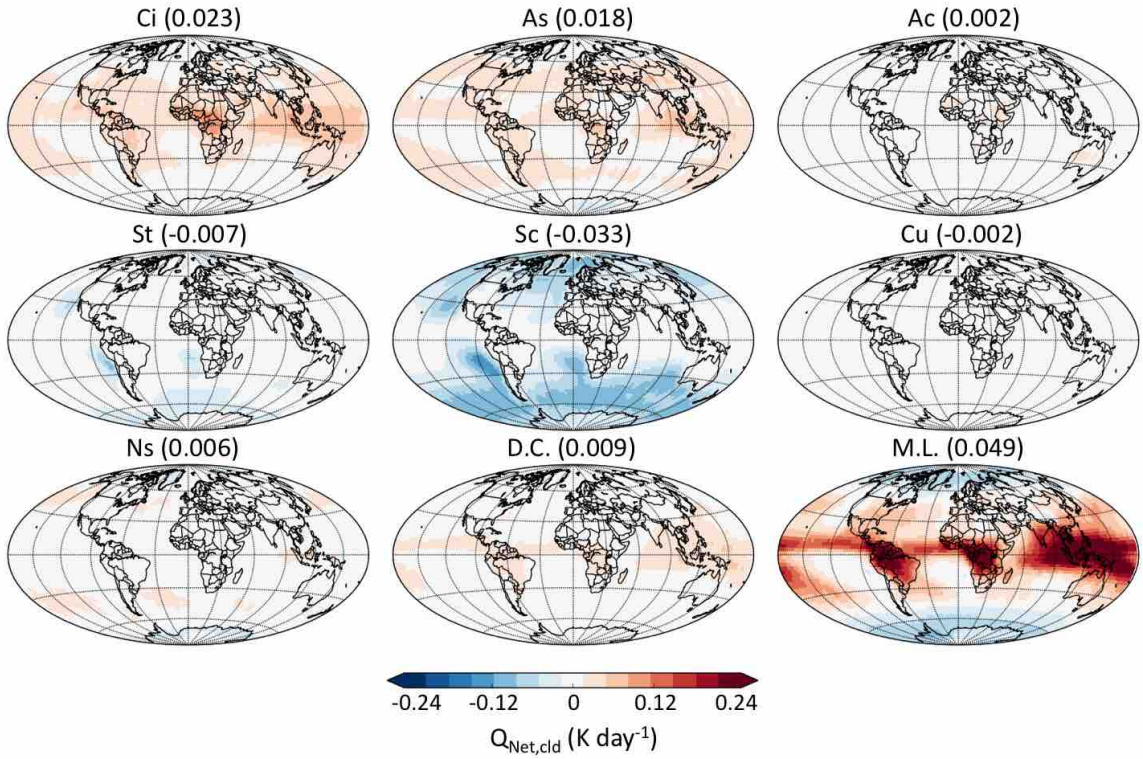

FIGURE 4.2: Annual mean cloud impact on column-integrated atmospheric net radiative heating (K day^{-1}). Cloud types are determined based on 2B-CLDCLASS-LIDAR cloud classification. Global average is shown in parentheses.

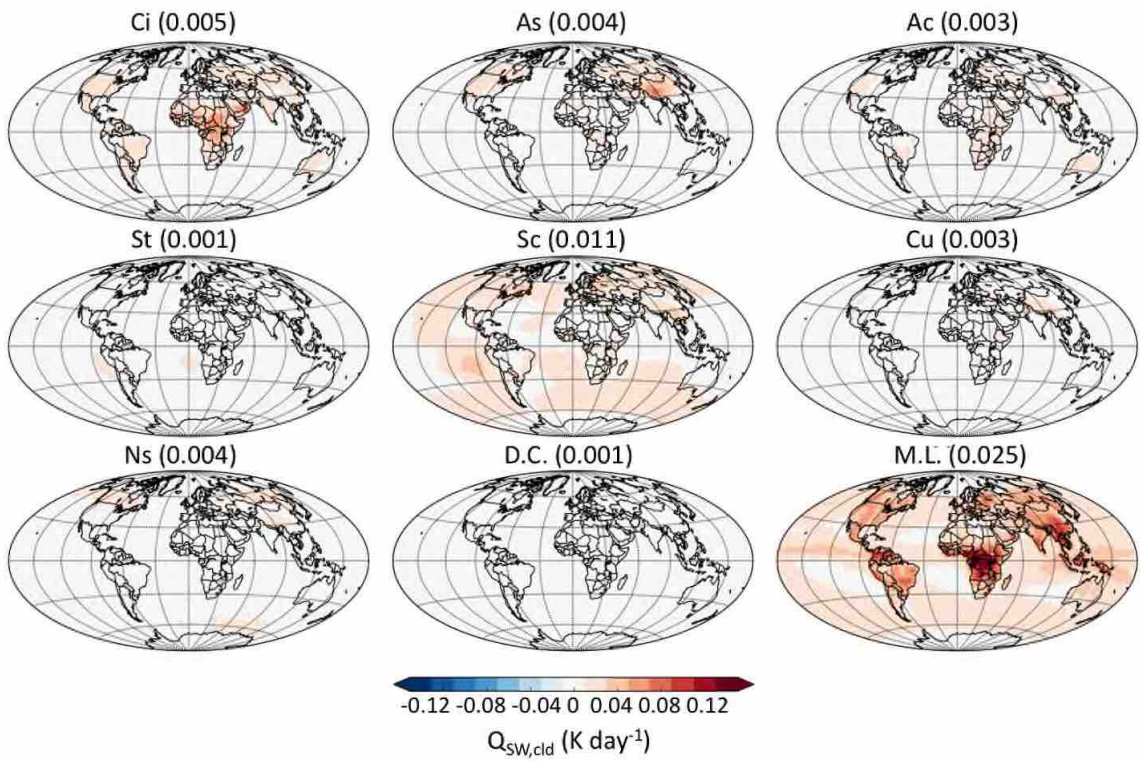

FIGURE 4.3: Same as Figure 4.2, but for cloud impact on SW heating (K day^{-1}).

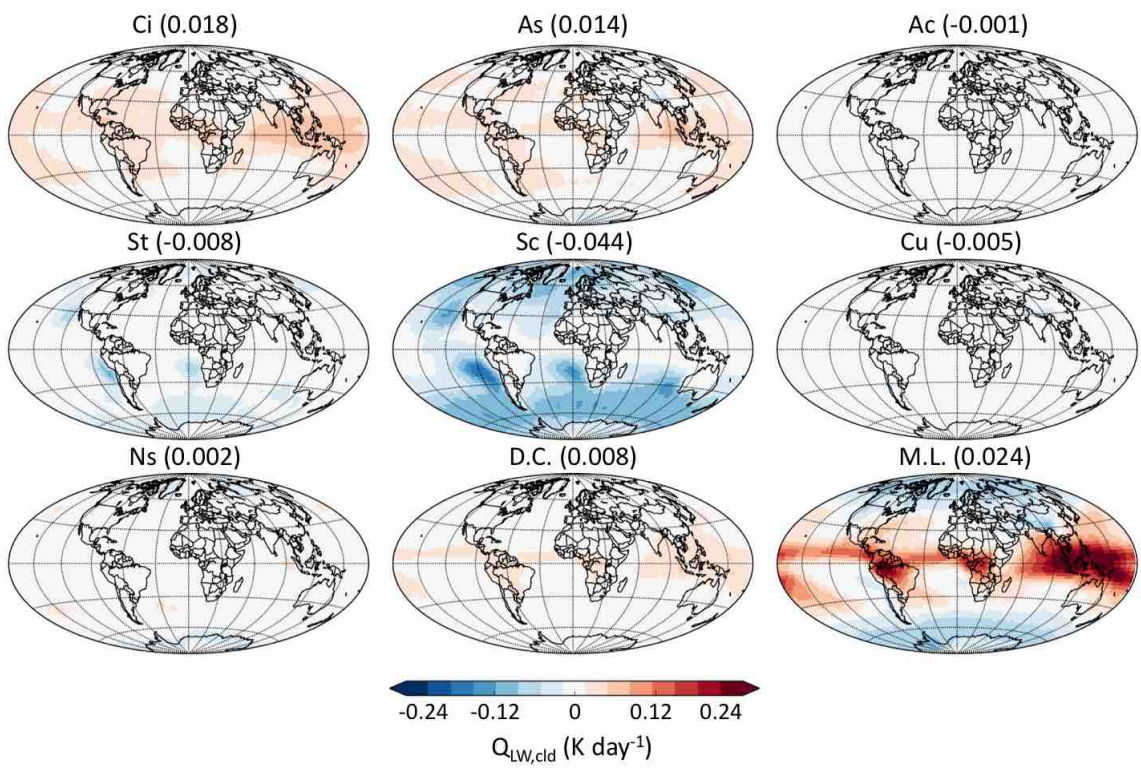

FIGURE 4.4: Same as Figure 4.2, but for cloud impact on LW heating (K day^{-1}).

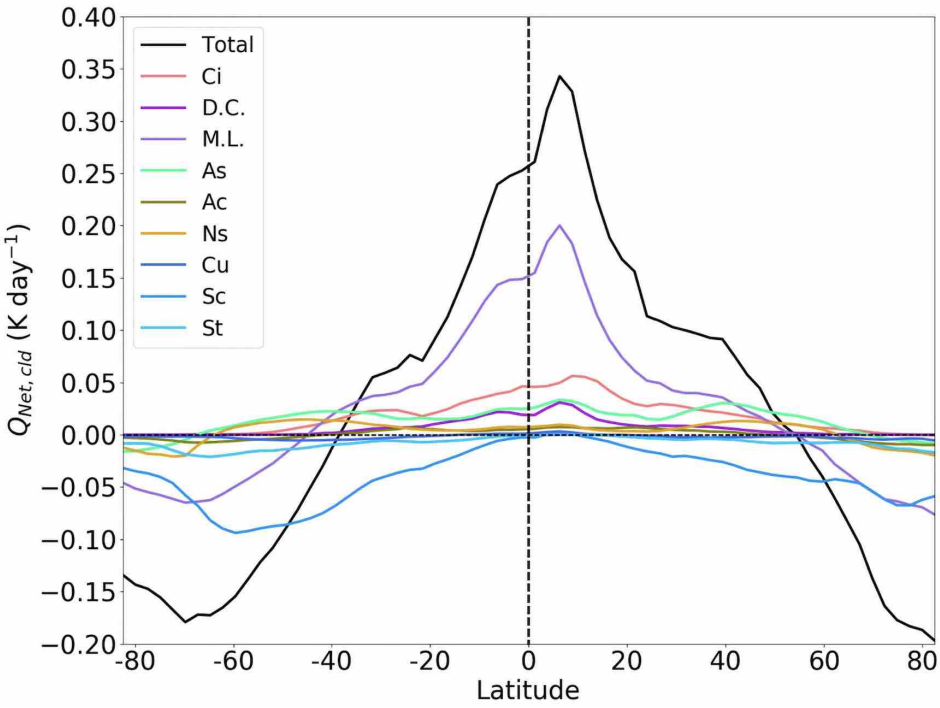

FIGURE 4.5: Zonal mean impact of each cloud type on zonal-annual mean net atmospheric radiative heating (K day^{-1}). Cloud types are determined based on 2B-CLDCLASS-LIDAR cloud classification.

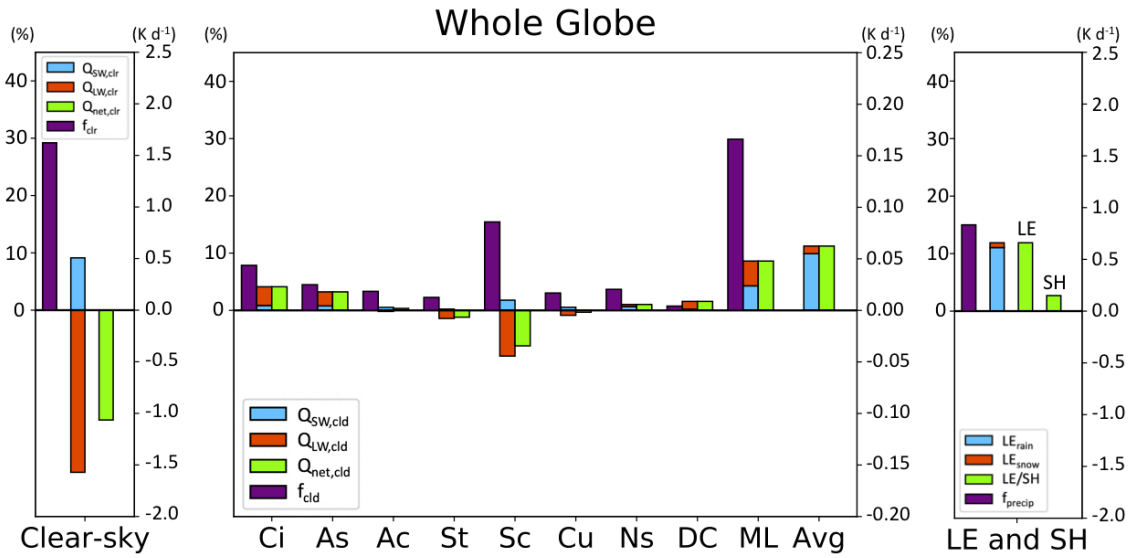

FIGURE 4.6: Global decomposition of net atmospheric heating into its sources (K day^{-1}). Left: the global mean fraction of clear-sky scenes (purple) and their contribution to SW, LW, and net atmospheric cooling (blue, red, and green, respectively). Middle: contribution of each 2BCLD cloud type to global atmospheric heating. Right: global mean latent and sensible heating. Global precipitation fraction (purple) is derived from CloudSat 2C-PRECIP-COLUMN product (Haynes et al., 2009). The global mean latent heating is from GPCP-WALRUS in blue. The small red bar at the top represents an estimate of the fraction of this LE that comes from snow based on the CloudSat 2C-SNOW (7% of the total).

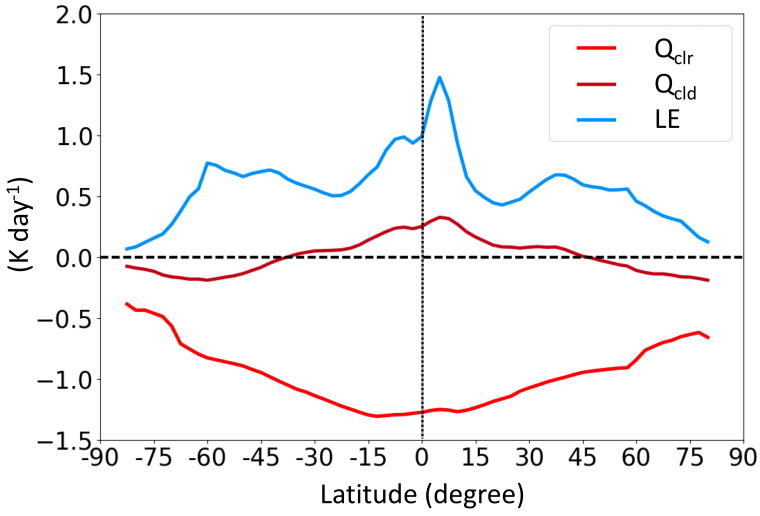

FIGURE 4.7: Zonal mean Q_{clr}, Q_{cld}, and LE (K day^{-1}). Q_{clr} and Q_{cld} are calculated by 2B-FLXHR-LIDAR. LE is calculated using the combination of GPCP and WALRUS.

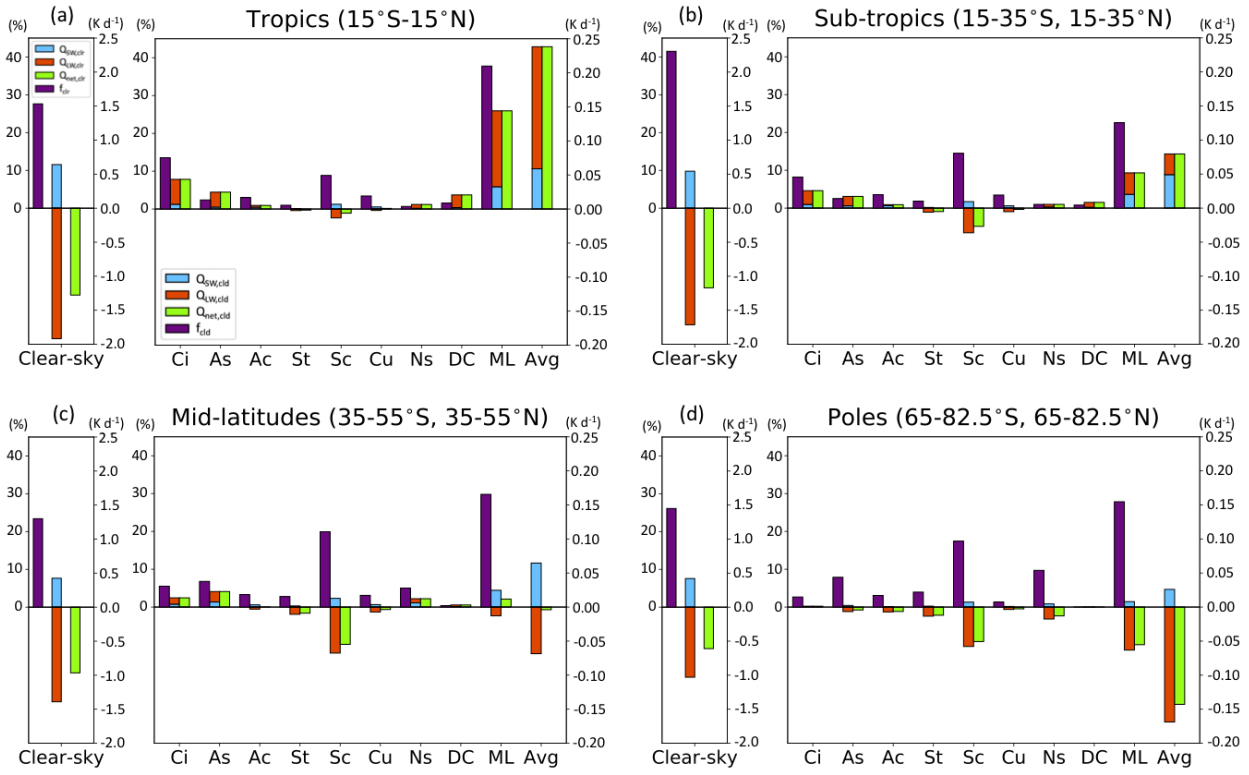

FIGURE 4.8: Same as Figure 4.6, but for four latitude bands: (a) tropics, (b) sub-tropics, (c) mid-latitudes, and (d) poles (K day^{-1}).

Global	Ci	As	Ac	St	Sc	Cu	Ns	D.C.	M.L.	Total
CF	7.9	4.5	3.3	2.3	15.5	3.0	3.7	0.8	29.9	70.8
$Q_{SW,cld}$	0.005	0.004	0.003	0.001	0.011	0.003	0.004	0.001	0.025	0.06
$Q_{LW,cld}$	0.018	0.014	-0.001	-0.008	-0.044	-0.005	0.002	0.008	0.024	0.01
$Q_{Net,cld}$	0.023	0.018	0.002	-0.007	-0.033	-0.002	0.006	0.009	0.049	0.07
NH										
CF	9.1	5.1	3.5	1.5	12.3	3.0	3.4	0.9	30.5	69.3
$Q_{SW,cld}$	0.007	0.006	0.004	0.001	0.010	0.004	0.004	0.001	0.030	0.07
$Q_{LW,cld}$	0.020	0.014	-0.001	-0.005	-0.032	-0.005	0.001	0.009	0.029	0.03
$Q_{Net,cld}$	0.028	0.020	0.003	-0.004	-0.022	-0.001	0.005	0.010	0.059	0.10
SH										
CF	6.7	3.9	3.2	3.1	18.6	3.1	4.0	0.6	29.3	72.4
$Q_{SW,cld}$	0.003	0.003	0.002	0.002	0.011	0.002	0.003	0.001	0.020	0.05
$Q_{LW,cld}$	0.016	0.013	-0.001	-0.010	-0.056	-0.005	0.003	0.007	0.019	-0.01
$Q_{Net,cld}$	0.019	0.016	0.001	-0.008	-0.045	-0.003	0.006	0.008	0.039	0.04
NH-SH										
CF	2.4	1.2	0.3	-1.6	-6.3	-0.1	-0.6	0.3	1.2	-3.1
$Q_{SW,cld}$	0.004	0.003	0.002	-0.001	-0.001	0.002	0.001	0.000	0.010	0.02
$Q_{LW,cld}$	0.004	0.001	0.000	0.005	0.024	0.000	-0.002	0.002	0.010	0.04
$Q_{Net,cld}$	0.008	0.004	0.002	0.004	0.023	0.002	-0.001	0.002	0.020	0.06

FIGURE 4.9: Influence of vertical structure-based cloud types on Global, Northern Hemisphere, and Southern Hemisphere annual mean column-integrated atmospher- ic radiative heating (K day^{-1}). The global fraction of each cloud type, CF (%), is reported in top row.

	$Q_{SW,cld}$	$Q_{LW,cld}$	$Q_{Net,cld}$	$Q_{SW,clr}$	$Q_{LW,clr}$	$Q_{Net,clr}$	LE	SH
Global	0.06	0.01	0.07	0.51	-1.57	-1.07	0.66	0.15±0.01
(PW)	3.5	0.5	3.9	31.2	-96.2	-65.2	40.3	9.2±0.7
NH	0.07	0.03	0.10	0.52	-1.59	-1.07	0.67	0.17±0.01
(PW)	2.2	0.9	3.1	15.9	-48.6	-32.6	20.5	5.2±0.3
SH	0.05	-0.01	0.04	0.49	-1.56	-1.06	0.65	0.12±0.01
(PW)	1.5	-0.4	1.1	15.1	-47.7	-32.5	19.8	3.7±0.4
NH-SH	0.02	0.04	0.06	0.03	-0.03	-0.01	0.02	0.05±0.01
(PW)	0.7	1.3	2.0	0.8	-0.9	-0.1	0.6	1.5±0.2

FIGURE 4.10: Hemispheric differences in cloud impact on atmospheric radiative heating, Q_{cld}, clear-sky atmospheric radiative heating, Q_{clr}, atmospheric latent heating, LE, and sensible heating (K day^{-1}). Q_{clr} and Q_{cld} are derived from 2BFLX. LE is derived from the GPCP and WALRUS while SH is estimated from ERA-Interim reanalysis (error bars are derived from standard deviation of ERA-Interim, JRA-55, MERRA, and MERRA-2). All the values are also reported in PW.

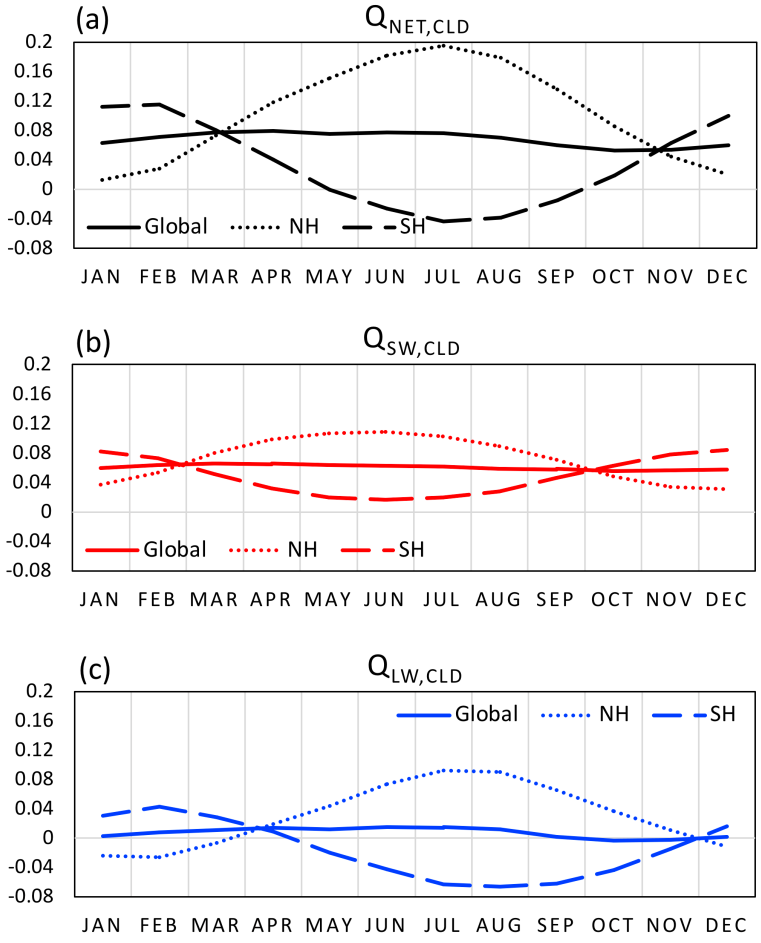

FIGURE 4.11: Annual cycle of (a) $Q_{Net,\ cld}$, (b) $Q_{SW,\ cld}$, and (c) $Q_{LW,\ cld}$ (K day^{-1}). Solid lines represent the global mean while dotted and dashed curves isolate the contributions from the NH and SH, respectively.

Chapter 5

Effect of Upper Tropospheric Clouds on EEB

Observational studies of upper tropospheric cloud (UTC) effects to date have been subject to some important limitations. Surface observations from ships and land stations are adversely affected by the presence of lower clouds and lack global coverage compared to satellites (Comstock et al., 2002, Davis et al., 2007, Hahn and Warren, 1999, Lynch et al., 2002, Sassen and Mace, 2002). Passive sensors on polar-orbiting satellites enable global coverage through algorithms that derive cloud properties from multi-spectral radiometers but have difficulties in detecting optically thin cirrus and distinguishing cirrus from other ice-dominated clouds (Mace et al., 2006b, Minnis, 2002, Rossow and Schiffer, 1999). Also, detecting multiple cloud layers is challenging for passive sensors due to their limited ability to penetrate high thick clouds (Mace and Wrenn, 2013). However, it is found that 29.9% of the globe is characterized by cloudy scenes containing more than one cloud layer (L'Ecuyer et al., 2019). Multilayered

cloud systems are found to exert the strongest influence on the top-of-atmosphere energy balance and significantly affect hemispheric atmospheric heating imbalances that have been shown to drive the location of the Inter-Tropical Convergence Zone (ITCZ) (Hang et al., 2019, L'Ecuyer et al., 2019). It has been demonstrated that the most common multilayered cloud system is a combination of upper tropospheric clouds and lower-level liquid clouds (Christensen et al., 2013).

To provide observational benchmarks of upper tropospheric clouds, this chapter will first assess multilayered cloud systems via CloudSat and CALIPSO satellites data in section 5.1. Then analyze radiative characteristics of convectively-coupled and isolated single- and multilayered upper tropospheric clouds. Section 5.2 will quantify radiative effects of each broad UTC type adopted here at both top-of-atmosphere and surface. The vertical structure information provided by spaceborne active sensors will be further exploited in section 5.3 to document how these clouds influence atmospheric heating and illustrate the dramatically different character of the heating influences of distinct single- and multilayered UTC types. The very distinct radiative impacts of UTCs over land and ocean will be contrasted.

5.1 Multilayered Cloud Systems from Spaceborne Active Sensors Perspective

The profiling capability afforded by CloudSat (Stephens et al., 2002) and Cloud Aerosol Lidar and Infrared Pathfinder Satellite Observation (CALIPSO) (Winker et al., 2003) offers new insights into multilayered cloud systems through their ability to differentiate cloud vertical structures (L'Ecuyer and Jiang, 2010). These data offer an important source of information for distinguishing single- and multilayered UTC systems and re-evaluating the

radiative effects of upper-tropospheric clouds on the climate. The presence of a underlying liquid cloud will substantially modify its upper-level cloud impact. As shown in Figure 5.1a, thick liquid clouds near the surface reflect sunlight, imposing a net cooling effect. In contrast, high-thin clouds, that let most shortwave solar radiation pass through them but trap the upwelling longwave radiation emitted by Earth, generally warm the planet like greenhouse gases (Figure 5.1b). However, between these extremes lie a multitude of cloud states whose net effect depend critically on their vertical structures and microphysical properties. High-thick clouds (Figure 5.1c), for example, can block sunlight and also trap longwave heating from the surface, exerting neutral or slight cooling radiative effects.

Assessing cloud radiative effects is particularly complicated in scenes consisting of more than one layer (Figure 5.1d and 5.1e). Adding a liquid cloud below a high-thin cloud, for instance, reflects more shortwave radiation and mutes the warming effect of the upper-level cloud. As a result, both accurate specification of cloud characters and separation of single- and multilayered cloud scenes are critical for quantifying cloud radiative effects and ultimately evaluating cloud feedbacks (Hang et al., 2019, Oreopoulos et al., 2017). The idea is that these two broad classes of UTCs that have been identified in previous studies (Christensen et al., 2013, Li et al., 2011, Subrahmanyam and Kumar, 2017) likely exhibit significantly different radiative effects owing to differences in their structure, composition, and the presence of underlying low-level clouds. Understanding these differences and quantifying the relative frequencies of these UTC regimes is an important step toward improving their representation in models (Bony et al., 2016, Zhao, 2014).

CloudSat's 2B-CLDCLASS-LIDAR (2BCLD) product is capable to identify multilayered

cloud systems. It groups clouds based on their precipitation presence, cloud-based height, cloud thickness, cloud-top height, cloud-top temperature, and radar reflectivity factor provided by CloudSat, CALIPSO, and MODIS (Wang et al., 2012). An example of the vertically-resolved zonal distributions of the nine cloud types identified in the 2BCLD cloud classification are given in Figure 5.2. In general, the distributions conform to our qualitative understanding of zonal cloud distributions: cirrus and deep convective clouds are most frequently observed at the tropics resulting from the large transport of water vapor into upper levels by persistent convection. The highest frequencies of cirrus are found in the tropical upper troposphere. However, the occurrence of the deep convection category is very low even in the tropics. This is most likely because most deep convection clouds fall into the multilayered case. Altostratus, altocumulus, and nimbostratus clouds are predominantly observed over mid-latitude storm track regions. The high frequency of nimbostratus corresponds to the ascending branches of the Ferrell cell near 60° N/S. Stratus, stratocumulus, and cumulus clouds are prevalent in subsidence regions over mid-latitude oceans. A robust enhancement of stratocumulus cloudiness is observed in the Southern Hemisphere resulting from the increased occurrence of clouds over the Southern Ocean. Note, however, the stratocumulus cloud fraction may be overestimated relative to stratus owing to CloudSat radar detection limits that favor larger cloud and drizzle droplets and low cloud horizontal homogeneity (Wang et al., 2012).

Figure 5.2 reveals two important implications that are generally not captured in passive cloud observations. First, the ability of active sensors to delineate convective cores. From a radiative perspective, it is important to distinguish these convective profiles from the associated cirrus and multilayered clouds even though they may derive from the same storm

system in many instances. This distinction may help improve the understanding of the relationship between convection, detrained cirrus, and isolated cirrus in the upper troposphere. Second, an explicit distinction is observed between single- and multilayered clouds. The cloud fraction of multilayered clouds strongly resembles the pattern of total cloud fraction since the multilayered case occurs frequently and contains all types of clouds (L'Ecuyer et al., 2019, Oreopoulos et al., 2017). It is clear that the multilayered clouds represent the most common cloud conditions on Earth, especially in the middle and upper troposphere. Figure 5.3 illustrates the cloud types that make up the most and the second most frequent top and bottom layers in multilayered cloud pixels. The most frequent bottom layers are altocumulus over the land and stratocumulus over the ocean. Globally, the most frequent top layer is cirrus; the second most frequent top layers are altocumulus over subtropical oceans and altostatus over tropical land and mid-latitude oceans. Over the Southern Oceans, altostratus is the most frequent top layer and cirrus is the second frequent top layer. Figure 5.4 further shows the frequency of single-layered and different types of multilayered clouds. In the tropics, two-layered clouds make up nearly 40% of the total cloud fraction, are found to be as important as the single-layered clouds. Three-layered clouds make up 15% in the tropical regions.

Distinguishing UTCs in multilayered scenarios is often challenging using passive sensors. As a result, the frequency and radiative effects of this more diverse category are enhanced relative to their single-layered counterparts but this is done intentionally to illustrate the importance of accurately characterizing such scenes in both observations and models when assessing global cloud impacts. Figure 5.5 compares the global distribution of annual mean cloud fraction of single-layered cirrus and multilayered clouds containing an upper-level

cirrus cloud layer from CloudSat and CALIPSO observations. Single-layered cirrus clouds are only prevalent over portions of north America, Australia, Saudi Arabia, the Indian Ocean while substantial multilayered cirrus clouds are over the mid-latitude storm tracks. However, many of the multilayered cirrus scenes feature very thin upper-level clouds. Figure 5.6 further separates the multilayered cirrus case according to the optical depth of upper-level cirrus clouds. The cloud layers are defined from 2BCLD and matched to vertically resolved optical depths from visible-band optical depths of BUGSrad (Ritter and Geleyn, 1992, Stephens et al., 2001). A cloud optical depth (COD) threshold of 0.5 is chose due to the tail of thin ice cirrus can extend to an optical depth of that amount (Haladay and Stephens, 2009). Figure 5.6 confirms that a substantial fraction of multilayered UTC systems contain thin cirrus clouds but also highlights the preponderance of multilayered cloud scenes with moderate and thick upper level cirrus clouds consistent with previous studies (Henderson et al., 2013). Passive sensors may lack the ability to penetrate optically thick clouds and measure boundary clouds below thick cirrus. Furthermore, while passive sensors may be capable of detecting lower cloud layers in scenes with thin overlying cirrus, cloud height and properties can be difficult to quantify in such cases for passive sensors (Mace and Wrenn, 2013, Mace et al., 2009). Figure 5.6, therefore, presents a complicated picture that poses a significant challenge for quantifying the radiative effects of UTCs that requires active observations to address.

Correspondingly, CloudSat's 2B-FLXHR-LIDAR (2BFLX) algorithm is used to assign radiative properties to each cloud scene. This chapter uses the full R05 release of the 2BFLX dataset that features numerous improvements in cloud microphysical properties and environmental data relative to earlier versions of the dataset. Many of the new features

incorporated into the R05 release have been previously documented (Matus and L'Ecuyer, 2017, Van Tricht et al., 2016) and include the implementation of explicitly retrieved mixed phase clouds, a more realistic representation of the zenith angle dependence of the surface albedo, and vertically resolved cloud properties in optically thin ice clouds using the CloudSat 2C-ICE data product (Deng et al., 2013). The 2C-ICE data product improves 2BFLX ice contents in upper levels that have been shown previously to be underestimated (Cesana et al., 2019, Ham et al., 2017). Further, R05 CloudSat inputs to 2BFLX provide more accurate cloud water contents and radii (Austin and Wood, 2018), cloud and aerosol detection from CALIPSO V4 products (Kim et al., 2018) and uses R05 2BCLD to better identify low-level CALIPSO detected clouds using single-shot CALIPSO sampling. The R05 2BFLX provides higher confidence in the microphysical representations of observed clouds. While regional biases in radiative fluxes still exist, the R05 release yields better comparisons to TOA fluxes from CERES and surface fluxes at ground validation stations compared to the R04 release (Matus and L'Ecuyer, 2017, McIlhattan et al., 2017).

With the capability to utilize cloud vertical structure information at the full CloudSat resolution, the 2BFLX product is ideally suited for studying the influence of clouds on the vertical structure of atmospheric heating. Figure 5.7 displays vertical profiles of cloud impacts on zonal annual mean atmospheric heating structure. In general, cloud impact on LW heating is about twice as large as SW heating and drives most of the vertical structure of net heating. In the tropical tropopause layer (Fueglistaler et al., 2009), high clouds act to enhance the SW heating and LW cooling by about 0.4 K day^{-1}, which is closely related to the troposphere-to-stratosphere heat transport (Fueglistaler et al., 2009). Although latent

heat dominates the lower troposphere, cloud impact on atmospheric heating becomes increasingly significant in the upper-troposphere-lower-stratosphere region (Johansson et al., 2015); however, global climate models struggle to capture infrared heating occurring in the column below high ice clouds (Cesana et al., 2019).

Figure 5.8 shows the zonally-averaged vertical distribution of cloud radiative heating of individual cloud type estimated by 2BFLX. The multilayered case strongly resembles the pattern of total heating (Figure 5.7), since the multilayered case occurs frequently and contains all types of clouds. The main difference between the multilayered and total case is mainly at 2 km where the cooling is stronger near 2km. This seems to be due to stratocumulus clouds which tend to exist as a single-layered cloud. Although both cirrus and altostratus usually form in the upper troposphere, these two have a significantly different cloud radiative heating signature. Here cirrus is shown to have mostly heating in the tropics above 17 km, while altostratus has a clear cooling/warming vertical pattern. Since altostratus is usually optically thicker compared to cirrus, these clouds have radiative cooling near the top of the cloud due to upwelling longwave radiation into space, and warming inside the cloud mostly from absorbing longwave radiation. Nimbostratus is also shown to have similar cooling and heating pattern, although the cooling by nimbostratus tends to be stronger around 60°-70° N/S. In contrast, optically-thin cirrus often only has radiative heating (McFarlane et al., 2007). As shown by Li et al. (2017b), this pattern of heating in the upper tropical troposphere and cooling in the extratropical upper troposphere increase the meridional temperature gradient, thereby enhancing the eddy kinetic energy and increasing the poleward heat transport. Through the decomposition of radiative heating by cloud types, cirrus clouds are responsible for a large part of the tropical heating, while

altostratus and nimbostratus contribute to the extratropical cooling. Deep convection likely also contributes to some of the high altitude tropical heating, although their effects are hard to separate from the multilayered cloud case.

5.2 Radiative Effects of Upper Tropospheric Clouds

This section will differentiate radiative impacts of convectively-coupled clouds from isolated upper tropospheric clouds as well as multilayered upper tropospheric cloud regimes on radiant energy balance. With CloudSat's capability to capture multilayered cloud scenes, six classes of upper tropospheric clouds are classified as shown in figure 5.9. This grouping is designed to explicitly quantify the importance of underneath liquid clouds, which are defined as either cumulus, stratocumulus, or stratus clouds beneath upper-level high clouds. Observational benchmarks of such scenes are important for evaluating the global models, but have been challenging in conventional passive sensor approaches given their limited ability to measure cloud base or the presence of multiple cloud layers (Mace and Wrenn, 2013, Mace et al., 2009). UTCs are also separated by their proximity to a lower-tropospheric moisture source, namely, whether UTCs are coupled with convection. This classification will advance our understanding of the distinct characteristics of isolated and detrained cirrus. If convection identified in the vicinity of the UTC (within 25 km) but not directly connected to it, then we categorize this UTC type as uncertain since the UTC may still be influenced by convection but a direct connection cannot be established. In the resulting classification (Figure 5.9), UTCs are categorized as single-layered coupled with convective clouds (pink); multilayered coupled with convective clouds (red); isolated single-layered UTCs (light purple); isolated multilayered UTCs (dark purple); single-layered with neighboring convective

clouds within 25 km (yellow); multilayered with neighboring convective clouds within 25 km (orange). An example profile of tropical cloud scenes are categorized according to the UTC classification shown at the bottom of Figure 5.9. It is clear even in this single snapshot that multilayered upper tropospheric clouds are frequently observed in the tropics. Note that UTCs defined in this study includes cirrus and altostratus clouds because these two types of clouds and convective cloud are always closely connected (Sassen et al., 2009). Convective clouds include deep convective and nimbostratus categories from 2BCLD product.

Figure 5.10 shows global distribution of annual mean UTC fraction from CloudSat and CALIPSO observations corresponding to UTC classification in Figure 5.9. The most striking feature of Figure 5.10 is that the global average cloud fraction of multilayered UTCs is 16.1%, nearly six times larger than the cloud fraction of single-layered UTCs. Single- and multilayered convectively-coupled UTCs are found to have similar spatial distribution patterns, but multilayered convectively-coupled UTCs are much more frequent. Over the Tropical Warm Pool, the cloud fraction of multilayered convectively-coupled UTC even exceeds 30%, making the most contributions to the total multilayered clouds system shown in Figure 3.4. In contrast, single- and multilayered isolated UTCs have very distinct spatial distributions. Single-layered isolated UTCs are predominantly observed over land while multilayered isolated UTCs are frequently observed over both land and ocean, especially in the tropics. This can be partially explained by the fact that the strongest and/or longest-lasting convective updrafts are found preferentially over land, spreading sufficient anvil tails and remaining at high altitude (Liu et al., 2007). Also, there are fewer low clouds in general over land may lead to the land-ocean contrast. As a result, single-layered UTCs are more prevalent in the Northern Hemisphere (NH) than in the Southern Hemisphere (SH)

while multilayered UTCs are more evenly distributed between both hemispheres. Figure 5.11 further investigates zonal mean distributions of UTC fraction over land and ocean in Northern Hemisphere winter and summer. The total global annual zonal mean UTC fraction is asymmetric between hemispheres with a maximum tracking migrations of the ITCZ and a distinct minimum contributed by multilayered convectively-coupled UTC in subsidence regions at approximately 20° latitude in the winter hemisphere. Multilayered isolated UTC is found to dominate the zonal distribution of total UTC fraction in both seasons over land and ocean. Single-layered UTC also makes substantial contributions but only over land. Convectively-coupled UTCs are frequently observed in the high latitudes over land. Possibly convectively-coupled UTC almost has no influence on the zonal distribution of total UTC fraction.

To quantify radiative impacts of upper tropospheric clouds, the conditional mean cloud radiative effect (CRE) of each UTC type is calculated in this section. Figure 5.12 displays global maps of annual mean net, SW, and LW CRE of four UTC types at the top-of-atmosphere based on 2BFLX estimates. In general, the spatial pattern of CRE is similar to cloud fraction shown in Figure 5.10, indicating that cloud fraction largely affects CRE from each UTC regime. On the global annual mean, all four UTC regimes together cool the atmosphere by -3.4 W m^{-2} at the TOA, -28.4 W m^{-2} in the shortwave and 25 W m^{-2} in the longwave. In the multilayered cases, liquid clouds are observed to offset the effects of high clouds at the TOA, resulting in a net cooling effect instead of a warming effect. On the global mean, multilayered UTCs contributing -23.4 W m^{-2} to the shortwave cooling and 20.5 W m^{-2} to the longwave warming. The most pronounced influence of multilayered convectively-coupled UTCs occurs over the Tropical Warm Pool where it can exceed -/+30

W m^{-2} in the SW/LW. Multilayered isolated UTC also strongly dominates both SW and LW in the tropics. But single-layered isolated UTC exert a global average net warming effect by 0.4 W m^{-2} that warm the atmosphere over land, especially over the Sahara Desert. Furthermore, Figure 5.13 compares zonal mean distributions of net, SW, and LW CRE of UTC at the TOA. Multilayered UTC regimes strongly enhance hemispheric radiation imbalance at the TOA, especially multilayered isolated UTCs exert pronounced SW cooling in the southern hemisphere during DJF due to enhanced solar reflection from ubiquitous marine clouds in the Southern Ocean. Multilayered convectively-coupled UTCs significantly impact hemispheric radiation imbalance in the poleward of 40°N/s. LW CRE is far more symmetric that is dominated by multilayered UTCs between the hemispheres. This is in contrast to the perspectives from passive sensors that suggest those contributions are made by single-layered high clouds (e.g. Oreopoulos et al. (2011)). But significant asymmetries exist over sub-tropics in the LW component that is mainly introduced by single-layered UTCs and convectively-coupled multilayered UTCs.

UTCs also significantly impact surface energy balance as shown in Figure 5.14, displaying global distributions of net, SW, and LW CRE of each UTC type derived from 2BFLX over 2007-2010. On the global annual mean, each UTC type exert a stronger net cooling effect at the surface (Figure 5.14) compared to TOA (Figure 5.12). Multilayered UTCs represent as a large source of cooling in Earth's surface energy budget with an estimated surface net CRE of -13.7 W m^{-2} (without uncertainty cases). Each multilayered UTC regime is found to exert a net warming effect over polar regions where enhanced longwave emission exceeds impacts on SW absorption owing to the reflective snow and ice surfaces and reduced annual mean solar insolation. It is clear that longwave heating dominates the difference in CRE of

UTC between the TOA and surface. The spatial patterns of SW CRE at the surface and the TOA are very similar even though each UTC type exerts larger shortwave cooling effect at the surface than the TOA owing to additional absorption of SW radiation. The greatest contributions to SW CRE at the surface are from multilayered convectively-coupled UTCs (-12.2 W m^{-2}) and multilayered isolated UTCs (-12.5 W m^{-2}) as at the TOA. But LW CRE at the surface exhibits distinctly different patterns from the TOA (Figure 5.12). Multilayered UTC regimes exert much smaller longwave radiative effects at the surface than at the TOA especially over tropics where upper-level high clouds mute enhanced longwave emission from underlying liquid clouds. Global estimates of the zonal mean CRE of UTCs at the surface are displayed in Figure 5.15. Multilayered UTCs dominate the zonal distribution by strongly cooling the surface in the summer hemisphere while exerting smaller warming effects in the winter hemisphere. The largest annual cycle of net CRE of UTC at the surface occurs over the Southern Oceans where multilayered UTCs exert strong net cooling in DJF and exert warming in JJA. The zonal distribution of SW CRE of UTC at the surface is similar to SW CRE at the TOA, but with a larger magnitude. But the zonal distribution of LW CRE of UTC at the surface is substantially different from LW CRE at the TOA, exhibiting a pronounced minimum in the tropics owing to the effects of water vapor that mask cloud emission to the surface. LW CRE of multilayered UTCs increases at the surface over mid-latitudes especially over the Southern Oceans where underlying liquid clouds enhance LW emission to the surface in both summer and winter.

Figure 5.16 summarizes all the numerical findings from this section and reports the radiative impacts of each vertical structure-based UTC type at the TOA and SFC for land and ocean separately. At the TOA, UTCs warm the land by 1.6 W m^{-2} while cooling the ocean by -2.1

W m^{-2}. This difference is primarily caused by the strong radiative cooling from multilayered UTCs over the Southern Ocean during local summer. Multilayered UTCs are found to exert almost twice as much SW cooling at the TOA (-14.3 W m^{-2}) over the ocean as they do over the land (-6.4 W m^{-2}). At the surface, however, UTCs significantly cool the land and ocean by -4.7 W m^{-2} and -10.2 W m^{-2}, respectively. This suggests that the imbalance in cloud radiative effects is primarily realized in the atmosphere, influencing atmospheric heat transport across from ocean to land. Understanding and modeling this imbalance is critical for accurately representing land-ocean contrast in global models. The results presented here reinforce the need to resolve UTC biases in models and add an imperative to assess and improve the representation of multilayered UTCs using active sensors.

5.3 Influence of Upper Tropospheric Clouds on Atmospheric Radiative Heating

Many existing studies indicate that cloud radiative heating exerts strong influence on the large-scale circulation (Fueglistaler et al., 2009; Hartmann and Short, 1980; McFarlane et al., 2007; Randall et al., 1989b). Under a CO_2 quadrupling experiment, Ceppi and Hartmann (2016) showed that cloud radiative changes are responsible for more than half of the poleward migration of the subtropical jet. In a general circulation modeling experiment with cloud radiative heating on or off, Li et al. (2017b) found that the radiative heating of upper tropospheric clouds enhances the strength of the jet, and intensifies eddy activities in the extratropical troposphere associated with increased baroclinicity. In particular, radiative heating of tropical high clouds are found to contribute to the expansion of the tropics, pushing the extratropical jet further away from the equator (Voigt and Shaw, 2015). Therefore,

it is important to resolve vertical and horizontal distributions of radiative heating induced by UTCs. Vertically-resolved profiles of radiative heating will allow us to diagnose the cloud radiative heating produced in models(Cesana et al., 2019).

Previous work from Haynes et al. (2013) demonstrated that the active CloudSat (Stephens et al., 2002) and CALIPSO (Winker et al., 2003) satellite sensors provide the means for examining profiles of atmospheric heating from space. When integrated vertically, such observations can be used to document the spatial distribution of cloud impacts on radiative heating in the atmosphere. The observed cloud impacts can be used to inform what models are lacking in representing cloud frequency or heating patterns. This section will use CloudSat's 2BCLD and 2BFLX algorithms to investigate the impact of UTCs on atmospheric heating. Figure 5.17 shows vertically resolved cloud radiative heating rates for different hypothetical tropical UTC scenes derived from BUGSrad two-stream, plane-parallel radiative transfer code (Ritter and Geleyn, 1992, Stephens et al., 2001). It can be seen that High-Thin clouds exhibit larger heating rates than High-Thick clouds because of enhanced LW heating. In multilayered UTC cases, cooling from liquid clouds and heating from high clouds cancel each other within the atmosphere. Comparison of the High-Thin case to the High-Thin+Liquid case shows that the underlying cloud acts to reduce heating in the lower portion of the cloud as well as enhance the cooling rate near the top of the cloud. A similar feature is seen by comparing the High-Thick to High-Thick+Liquid case. The cloud-top cooling of the lower liquid cloud is also muted in both multilayered scenarios.

Conditional mean cloud radiative heating of each UTC type before weighting by cloud fraction ($< Q_{cld,i} >$) is presented in Figure 5.18. Single-layered convectively-coupled UTCs have

significantly stronger SW heating than multilayered cases, especially in the tropics between 6 and 15 km. These higher cloud radiative heating might be introduced by very thick clouds with stronger SW heating tend to spread detrained tails. Relative to convectively-coupled UTCs, isolated UTCs have stronger net heating in the tropics above 12 km, which can be attributed to the stronger LW heating of isolated UTCs in this region. This suggests that most of the thin cirrus near the tropical tropopause that cause net heating tends to be independent of convection. The strong net cooling near 2 km in middle and high latitudes also appear only in isolated cases. Heating above 12 km in the tropics is slightly stronger in the single-layered isolated case compared to the multilayered isolated case, which can be explained by the effect of the underlying cloud as shown in Figure 5.17.

Figure 5.19 shows contributions of each UTC regime to net radiative heating after weighing by their cloud fraction. The major contributor to the cooling in the extratropical upper troposphere is convectively-coupled cloud. Additionally, multilayered convectively-coupled UTCs have a stronger cooling effect compared to single-layered convectively-coupled clouds. As mentioned previously, above 12 km isolated UTCs have a stronger heating signature due the effects of cirrus. Below 14 km, the strong heat signature between 8 to 12 km within 15 N/S is more evident in the convectively-coupled case, showing that this bimodal heating distribution is related to convection. In the multilayered convectively-coupled case, these is a cooling in the extratropical upper troposphere, while in the tropics there is heating in the upper troposphere. It have been shown that the pattern of heating in the upper tropical troposphere and cooling in the extratropical upper troposphere increase the meridional temperature gradient, thereby enhancing the eddy kinetic energy and increasing the poleward heat transport (Li et al., 2017b). As shown in Figure 5.19, the extratropical cooling

is mostly associated with convectively-coupled UTC, while both convectively-coupled and isolated UTCs contribute to the tropical warming. The results here show that isolated and convectively-coupled UTCs have distinct effects on three dimensional structures of radiative heating in the atmosphere.

As introduced in chapter 1, cloud impacts on atmospheric heating (Q_{cld}) can be derived as the difference in heating rates between clear-sky and all-sky conditions that is equivalent to differencing the TOA and surface cloud radiative effect. Figure 5.20 decomposes the UTC impact on annual mean column-integrated net atmospheric heating into the contributions from each UTC type. The most striking feature in Figure 5.20 is the strong contribution from multilayered convectively-coupled UTCs that heat the atmosphere by 0.053 K day^{-1}, contributing more than eight times at much global heating as single-layer convectively-coupled UTCs. In some regions such as equatorial Africa and the Tropical Warm Pool, multilayered convectively-coupled UTCs warm the atmosphere by more than 0.21 K day^{-1}. Similarly, isolated UTCs are found to enhance atmospheric radiative heating by 0.062 K day^{-1}, in particular, single-layered isolated UTCs only heat the land by 0.011 K day^{-1} while multilayered isolated UTCs heat tropical regions and subtropical continents by 0.051 K day^{-1}. Decomposing UTC impacts on atmospheric heating into SW and LW components provides additional insights into the heat budget of the atmosphere. Globally, UTCs are found to increase SW atmospheric heating by 0.04 K day^{-1} but exert much larger influences over land regions. The largest impacts are observed in equatorial Africa where SW heating from multilayered isolated UTC exceeds 0.1 K day^{-1}. The distribution of UTC influences on net atmospheric heating is dominated by the cloud impacts on LW heating. As indicated in Figure 5.20, the global pattern of atmospheric LW radiative heating from UTCs results

primarily from multilayered UTCs, acting to substantially enhance the LW heating over the ITCZ.

The land-ocean contrast in UTC heating is more directly quantified in Figure 5.21 where column-integrated impact of each UTC type over land and ocean are summarized separately. Globally, the mean column-integrated cloud radiative heating are positive for both convectively-coupled and isolated UTCs over land and ocean. Although the multilayered isolated case has higher global cloud fraction (8.2%) compared to the multilayered convectively-coupled case (7.9%), the convectively-coupled case has higher net column-integrated heating (0.053 K day^{-1} vs. 0.051 K day^{-1}) due to multilayered convectively-coupled UTCs have a higher LW heating (0.043 K day^{-1} vs 0.031 K day^{-1}). The last row of Figure 5.12 shows the land-ocean difference of cloud fraction and cloud raditive heating of each UTC type. Overall UTC heating is stronger over ocean (0.068 K day^{-1}) than over land (0.053 K day^{-1}). Multilayered convectively-coupled UTC is found to induced a substantial 0.013 K day^{-1} of atmospheric heat transport from the ocean to the land relative to cloud free skies. This ocean-land energy imbalance is partially compensated by the radiative impact of single-layered isolated UTC that only heats the atmosphere over land.

5.4 Chapter Summary

Following chapters 3 and 4 indicating multilayered cloud systems substantially modulate the Earth's energy budget, this chapter further explores compositions and origins of these clouds with observations from active sensors that can detect cloud vertical structure. Multilayered cloud systems are classified according to the optical depth of their upper-level clouds since they exhibit significantly different radiative effects. It is found that over the globe,

most multilayered cloud systems have thin upper-level clouds, but in the tropics and over mid-latitudes, more than 1/3 of the cases contain thick cirrus. Passive sensors may lack the ability to penetrate those thick cirrus and measure the lower level boundary clouds. Quantifying the relative frequencies of these cloud regimes is an important step toward improving their representation in models. Since active sensors can detect deep convective clouds, the radiative effect of single- and multilayered anvil cloud are estimated in addition to isolated upper-level clouds. This helps provide evidence for hypotheses debating cold cloud climate feedbacks.

In this chapter, the global annual mean cloud fraction of UTCs with underlying liquid clouds is found to be 16.1% (7.9% in convectively-coupled clouds and 8.2% in isolated cirrus clouds), which is almost six times larger than single-layered UTCs (2.8%). On the global annual mean, UTC regimes cool the atmosphere by -3.4 W m^{-2} at the TOA, -28.4 W m^{-2} in the shortwave and 25 W m^{-2} in the longwave. In the multilayered cases, liquid clouds are observed to offset the effects of high clouds at the TOA, resulting in a net cooling effect instead of a warming effect. At the surface, each UTC type exert a stronger net cooling effect compared to TOA. Multilayered UTCs represent as a large source of cooling in Earth's surface energy budget with an estimated surface net CRE of -13.7 W m^{-2}. This chapter also documents the influences of UTCs on atmospheric radiative heating using CloudSat and CALIPSO observations. Multilayered anvil clouds are found to contribute a contrast of heating in the upper tropical troposphere and cooling in the extratropical upper troposphere that increase the meridional temperature gradient. Multilayered UTCs are found to exert strong influence on the Earth's radiation budget, inducing a net atmospheric heating of 0.11 K day^{-1} on a global average. A clear land-ocean contrast in cloud radiative heating

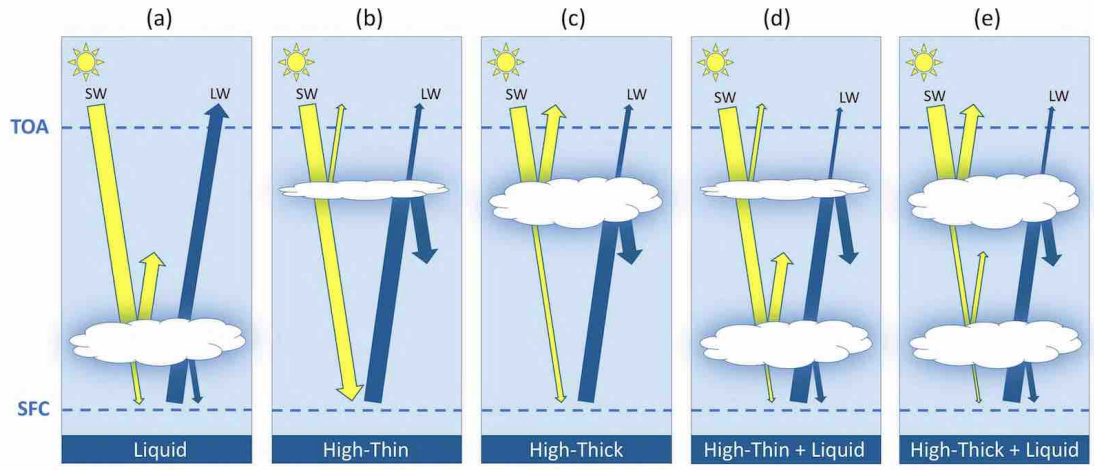

FIGURE 5.1: Radiative mechanisms under five cloudy scenes: (a) single-layered liquid cloud; (b) single-layered thin ice cloud; (c) single-layered thick ice cloud; (d) multilayered thin ice cloud with a liquid cloud underneath; (e) multilayered thick ice cloud with a liquid cloud underneath. The yellow arrows represent shortwave radiation while the deep blue arrows represent longwave radiation.

is observed, contributed by enhanced single-layered UTC heating over land and enhanced multi-layered UTC heating over ocean.

Note that in this chapter, the definition of possibly convectively-coupled UTCs are high clouds that have convective clouds neighbours with a distance less than 25 km. If the distance changes, all estimates of isolated UTCs will change correspondingly. Figure 5.22 compares area-weighted global average net cloud radiative effects at the TOA and SFC, net cloud radiative heating, and cloud fraction of UTCs with different possibly convectively-coupled distance at 10km, 25km, and 50 km in January and July, 2007-2010. As indicated in Figure 5.22, the uncertainty ranges are 0.25 W m^{-2} for CRE at the TOA, 1.5 W m^{-2} for CRE at the surface, 0.1 K day^{-1} for net cloud radiative heating, 0.4% for cloud fraction. No significant seasonal change is observed.

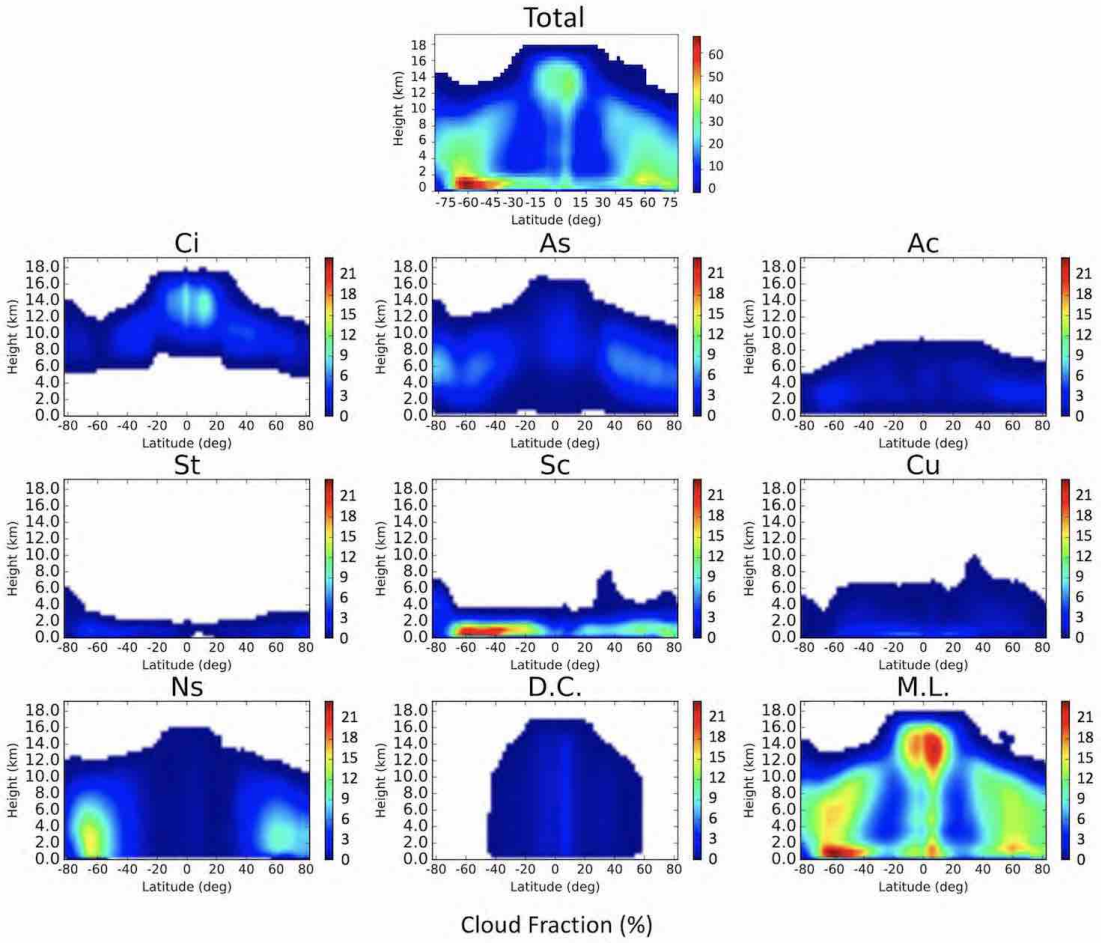

FIGURE 5.2: Breakdown of annual zonal mean cloud fraction by cloud type determined based on 2BCLD classification, 2007-2010 (%). Ci=cirrus, As=altostratus, Ac=altocumulus, St=stratus, Sc=stratocumulus, Cu=cumulus, Ns=nimbost ratus, D.C.=deep convection and M.L.=multilayered cloud system.

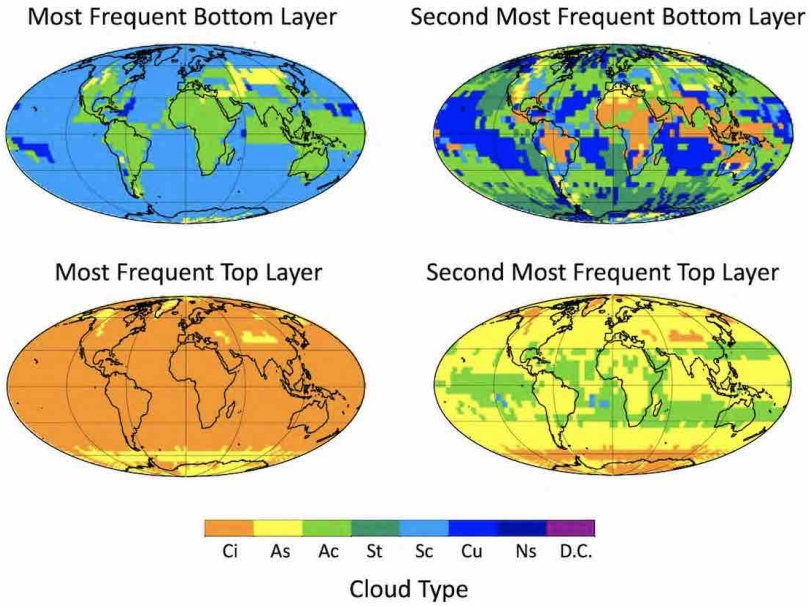

FIGURE 5.3: The most frequent and the second frequent cloud types identified as the bottom and top layers of multilayered clouds.

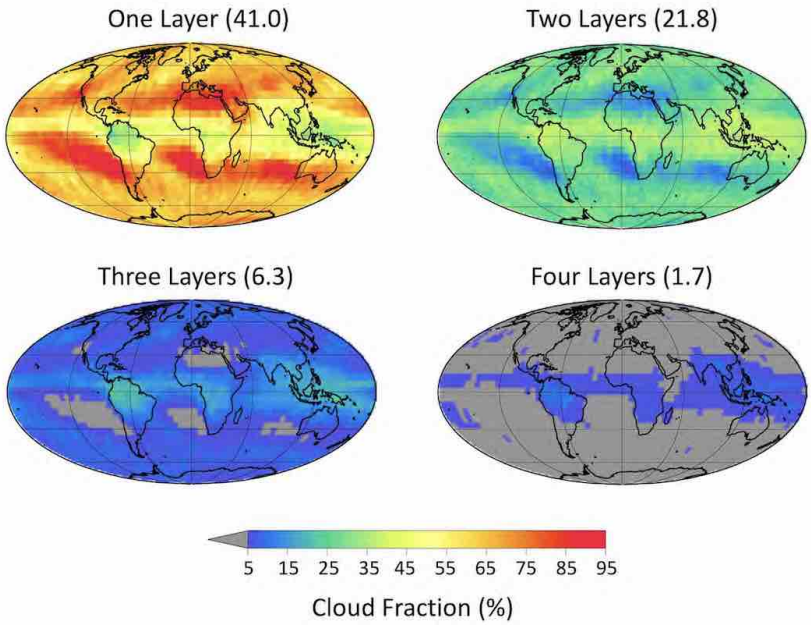

FIGURE 5.4: The frequency of single-layered and multilayered clouds (%). The multilayered clouds are classified as two layers, three layers, and four layers.

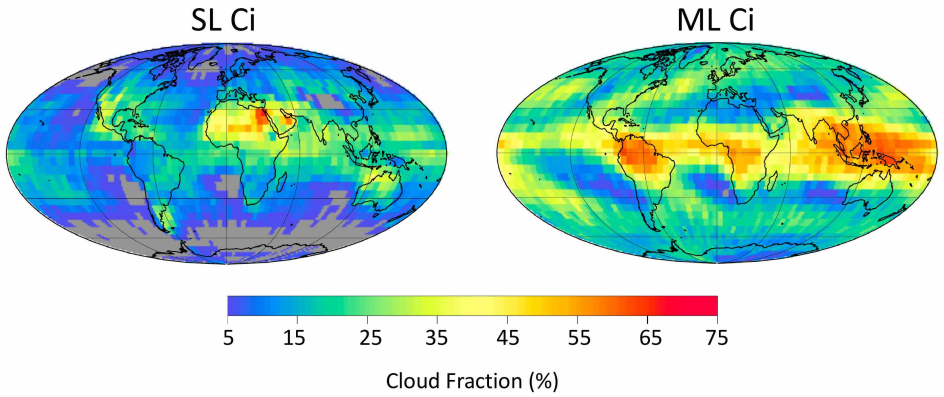

FIGURE 5.5: Annual mean cloud fraction of single-layered cirrus clouds and multilayered cirrus clouds using CloudSat and CALIPSO observations from 2009 (%).

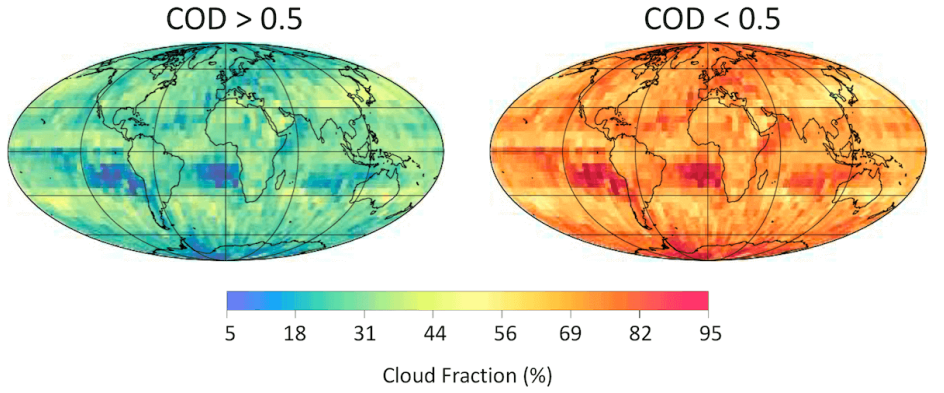

FIGURE 5.6: Annual mean cloud fraction of multilayered cirrus clouds using CloudSat and CALIPSO observations from 2009 (%). The multilayered cirrus clouds are separated into thin cirrus and thick cirrus categories by a cloud depth threshold of 0.5.

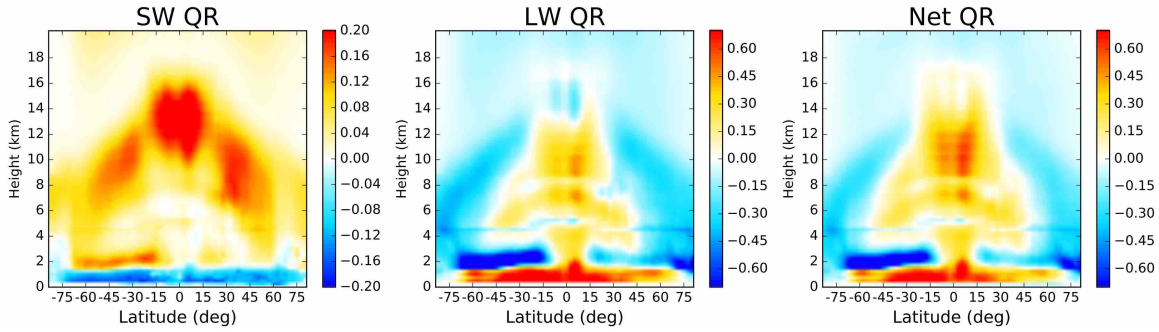

FIGURE 5.7: Annual zonal mean cloud impact on column-integrated shortwave, longwave, and net atmospheric radiative heating (K day^{-1}). All fluxes data presented are from CloudSat's level 2 radiative flux and heating rate product, 2007-2010.

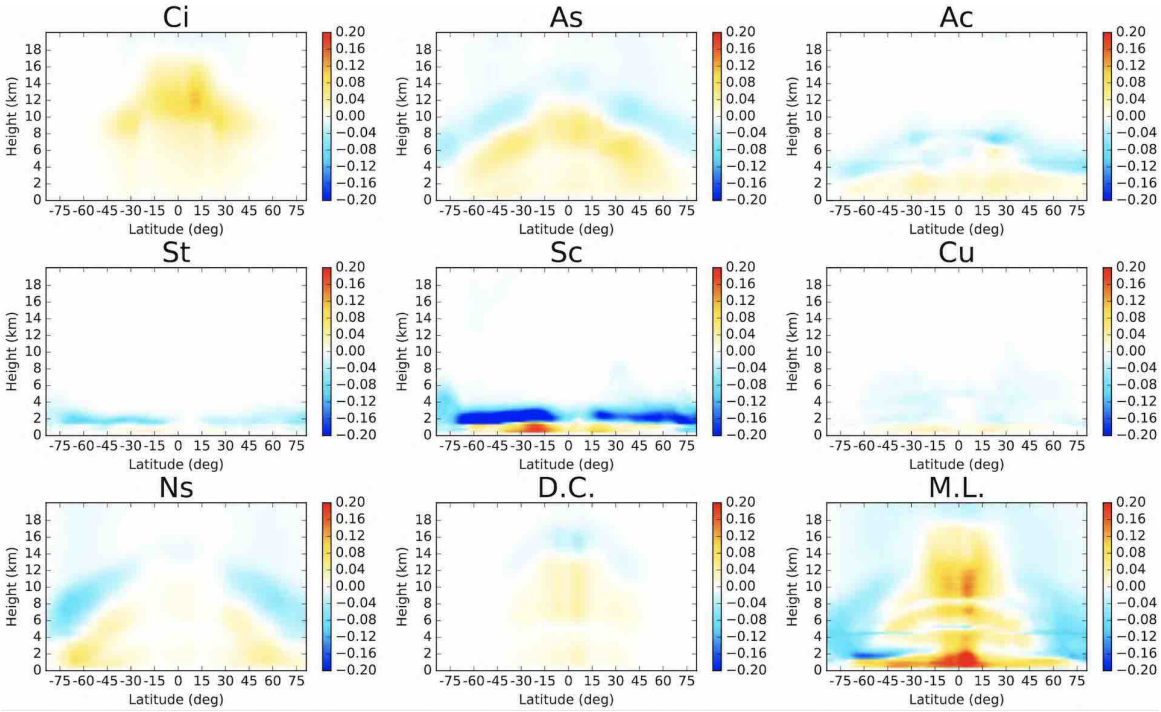

FIGURE 5.8: Annual zonal mean net cloud radiative heating (K day^{-1}), separated by cloud type determined based on 2BCLD classification. All fluxes data presented are from CloudSat's level 2 radiative flux and heating rate product, 2007-2010. Ci=cirrus, As=altostratus, Ac=altocumulus, St=stratus, Sc=stratocumulus, Cu=cumulus, Ns=nimbostratus, D.C.=deep convection and M.L.=multilayered cloud system.

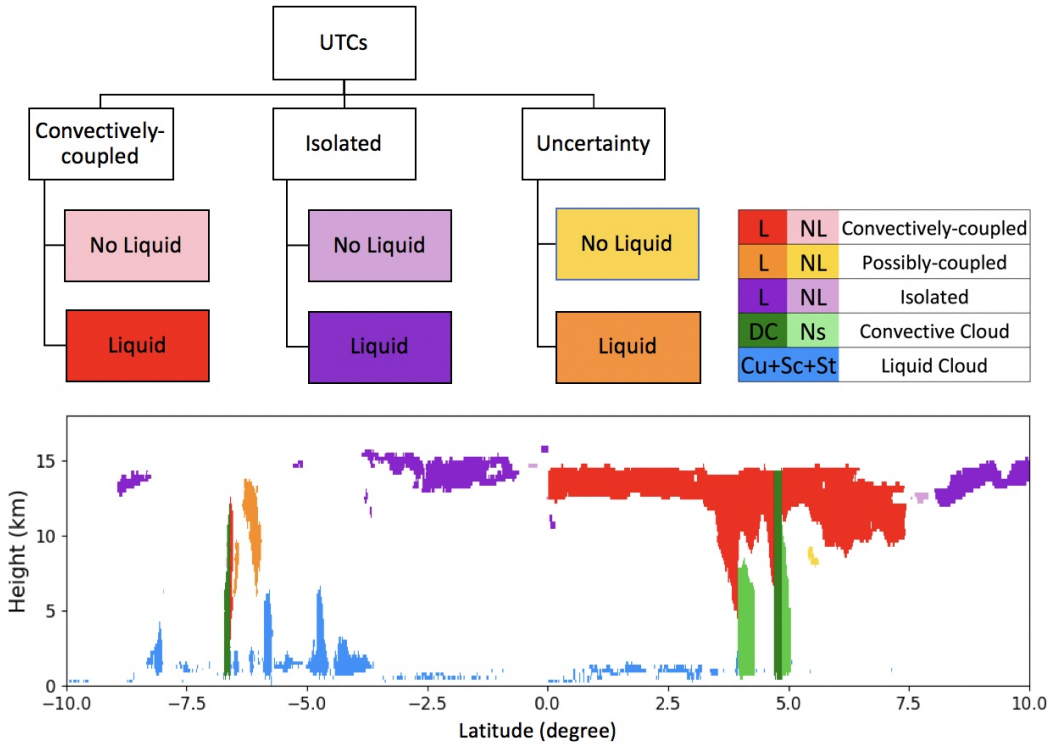

FIGURE 5.9: Six classes of upper tropospheric clouds (UTCs) defined according to clouds spatial locations from a portion of granule 05806 between 10°S and 10°N. Pink: single-layered UTCs that coupled with convective clouds; red: multilayered UTCs that coupled with convective clouds and with liquid clouds underneath; light purple: isolated single-layered UTCs; dark purple: isolated multilayered UTCs with liquid clouds underneath; yellow: single-layered UTCs with convective clouds neighbours (the distance between UTCs and convective clouds is smaller than 25 km); orange: multilayered UTCs with convective clouds neighbours and has liquid clouds underneath. We note that underlying liquid clouds are present from 5.0N to 7.5N; however, they are small and sparsely distributed, and therefore difficult to depict in the figure shown.

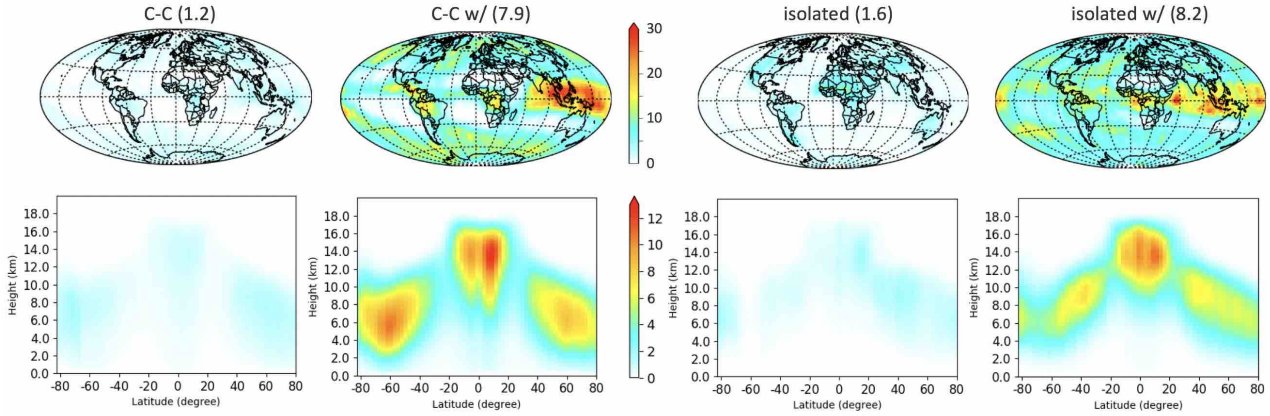

FIGURE 5.10: Breakdown of annual mean and zonal mean UTC fraction based on classifications in Figure 5.9, 2007-2010 (%). The area-weighted global average (in %) is shown in parentheses. C-C = convectively-coupled, C-C w/ = convectively-coupled and with liquid clouds underneath, isolated = isolated, isolated w/ = isolated and with liquid clouds underneath.

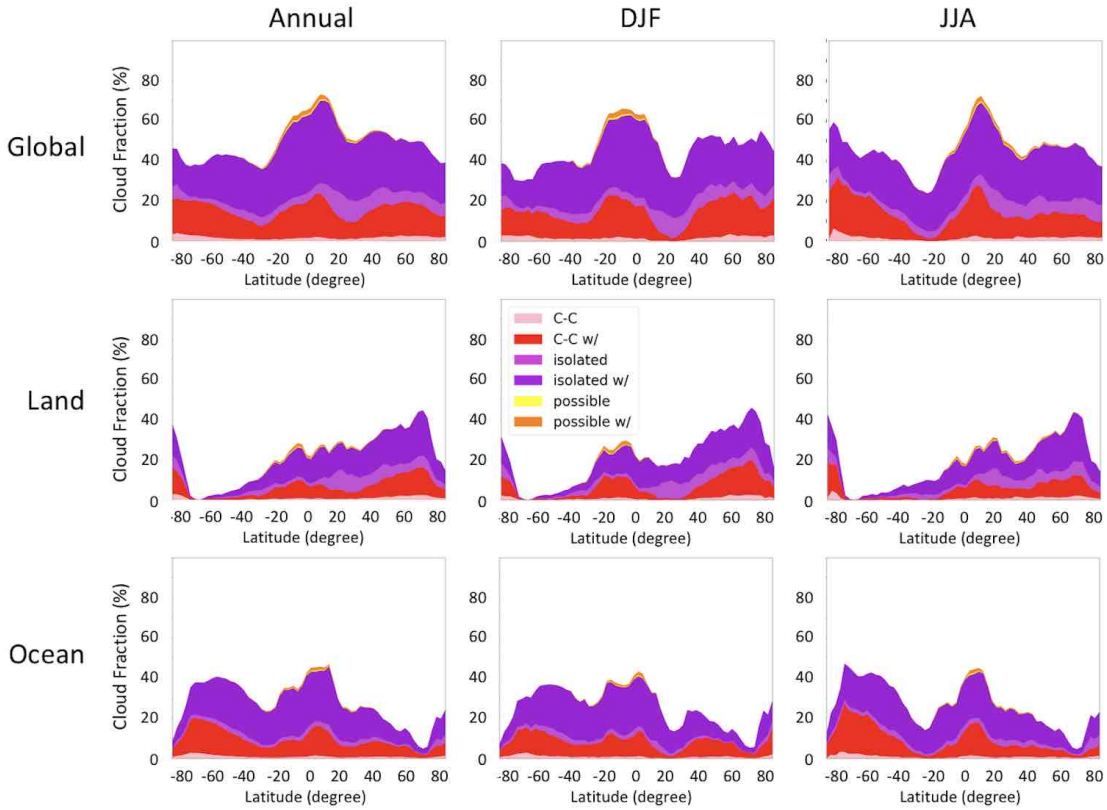

FIGURE 5.11: Global annual zonal mean cloud fraction of UTCs (top), and seasonal zonal mean cloud fraction of UTCs over land (middle) and ocean (bottom) (%). Seasons are defined as December-February (DJF) and June-August (JJA). All cloud data are from 2BCLD, 2007-2010.

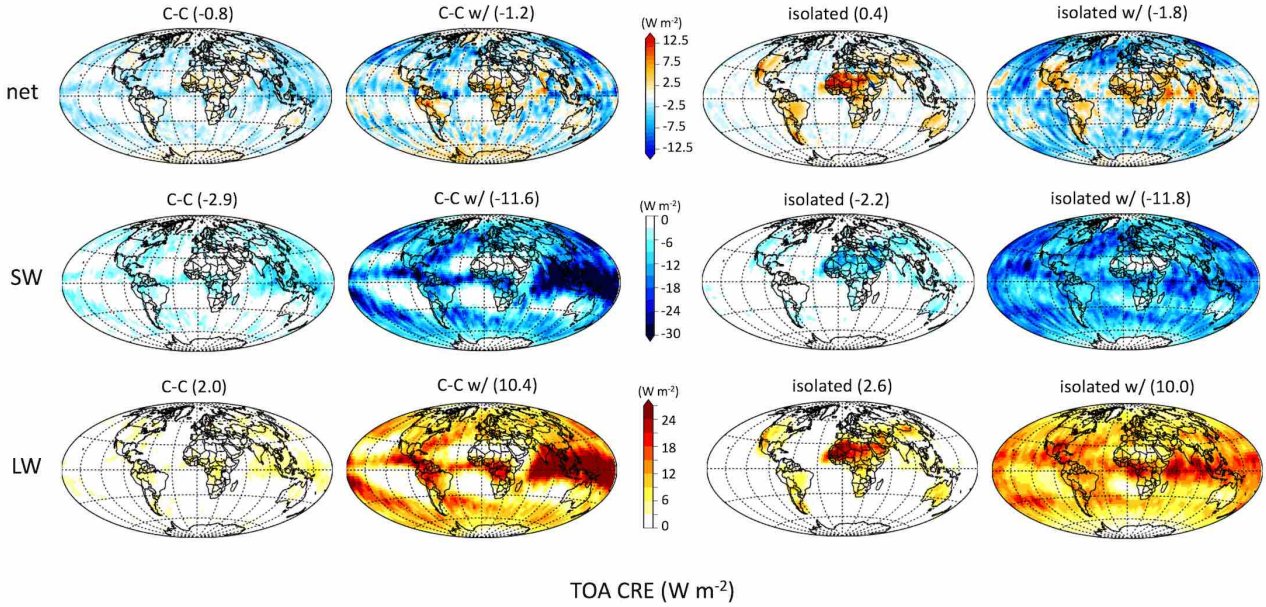

FIGURE 5.12: Annual mean net, SW, and LW cloud radiative effects of UTCs at the top-of-atmosphere (W m^{-2}). All fluxes data presented are from 2BFLX, 2007-2010. The area-weighted global average (in W m^{-2}) is shown in parentheses.

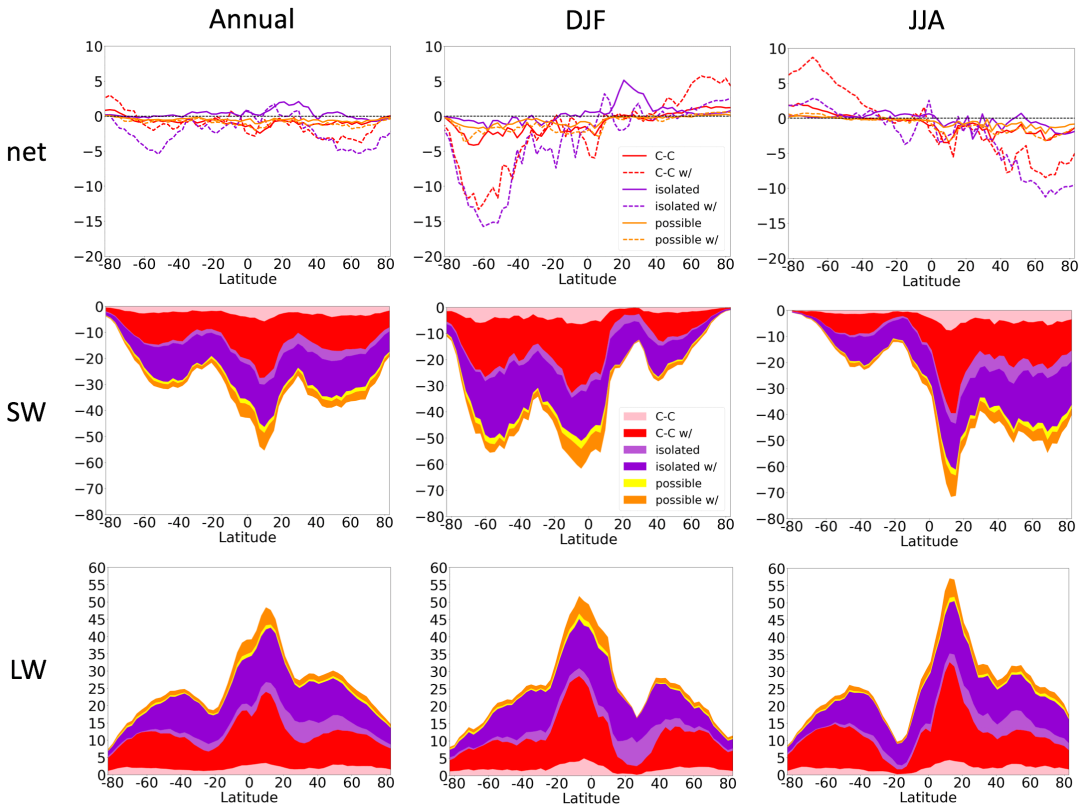

FIGURE 5.13: Seasonal zonal mean net, SW, and LW cloud radiative effects of UTCs at the top-of-atmosphere (W m^{-2}). Seasons are defined as DJF and JJA. All fluxes data are from 2BFLX, 2007-2010.

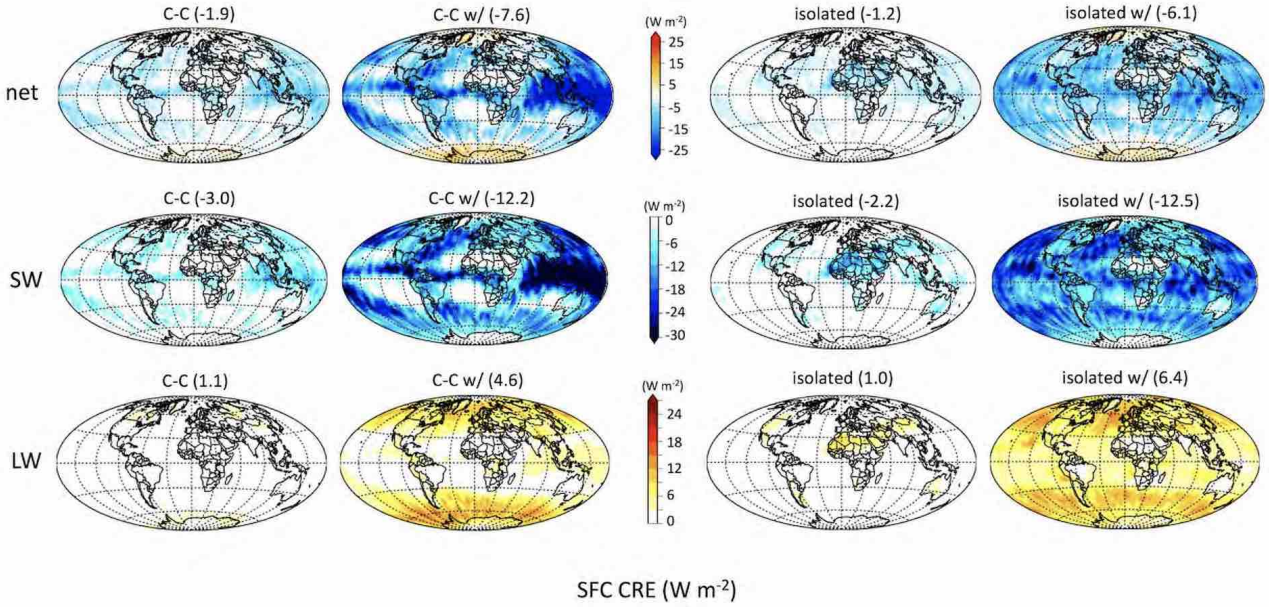

FIGURE 5.14: Same as Figure 5.12, but for cloud radiative effects at the surface (W m^{-2}).

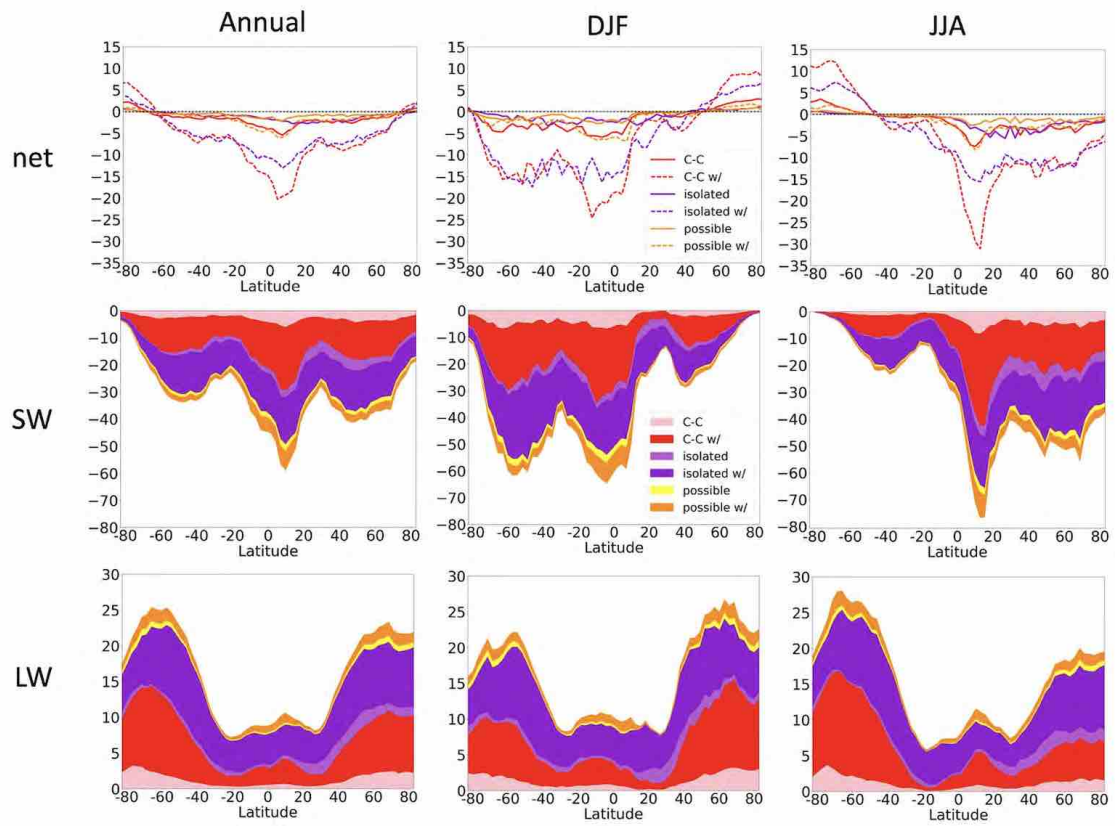

FIGURE 5.15: Same as Figure 5.13, but for cloud radiative effects at the surface (W m^{-2}).

CRE_{TOA}

Global	C-C	C-C w/	isolated	isolated w/	Total	Uncertainty
CF	1.2	7.9	1.6	8.2	18.9	1.4
CRE_{SW}	-1.5	-9.2	-1.6	-11.4	-23.7	-1
CRE_{LW}	1.2	9.8	1.8	10.7	23.5	0.6
CRE_{net}	-0.3	0.5	0.1	-0.7	-0.4	-0.3
Land						
CF	0.6	2.9	1.1	2.8	7.4	0.5
CRE_{SW}	-0.5	-2.9	-0.8	-3.5	-7.7	-0.4
CRE_{LW}	0.5	3.6	1.2	4.1	9.4	0.3
CRE_{net}	0	0.8	0.3	0.5	1.6	-0.1
Ocean						
CF	0.6	4.9	0.5	5.5	11.5	0.7
CRE_{SW}	-0.9	-6.4	-0.8	-7.9	-16	-0.5
CRE_{LW}	0.7	6.1	0.6	6.6	14	0.3
CRE_{net}	-0.3	-0.3	-0.2	-1.3	-2.1	-0.2
Land-Ocean						
CF	0	-2	0.6	-2.7	-4.1	-0.2
CRE_{SW}	0.4	3.5	0	4.4	8.3	0.1
CRE_{LW}	-0.2	-2.5	0.6	-2.5	-4.6	0
CRE_{net}	0.3	1.1	0.5	1.8	3.7	0.1

CRE_{SFC}

Global	C-C	C-C w/	isolated	isolated w/	Total	Uncertainty
CF	1.2	7.9	1.6	8.2	18.9	1.4
CRE_{SW}	-1.7	-10.6	-2.3	-13.8	-28.4	-1.1
CRE_{LW}	0.7	4.6	1.2	7.1	13.6	0.1
CRE_{net}	-1	-5.9	-1.1	-6.8	-14.8	-0.9
Land						
CF	0.6	2.9	1.1	2.8	7.4	0.5
CRE_{SW}	-0.6	-3.6	-1.4	-5.2	-10.8	-0.5
CRE_{LW}	0.3	1.9	0.9	3	6.1	0.1
CRE_{net}	-0.3	-1.6	-0.6	-2.2	-4.7	-0.4
Ocean						
CF	0.6	4.9	0.5	5.5	11.5	0.2
CRE_{SW}	-1	-7	-0.9	-8.6	-17.5	-0.6
CRE_{LW}	0.4	2.7	0.3	4.1	7.5	0.1
CRE_{net}	-0.7	-4.3	-0.6	-4.6	-10.2	-0.4
Land-Ocean						
CF	0	-2	0.6	-2.7	-4.1	0.3
CRE_{SW}	0.4	3.4	-0.5	3.4	6.7	0.1
CRE_{LW}	-0.1	-0.8	0.6	-1.1	-1.4	0
CRE_{net}	0.4	2.7	0	2.4	5.5	0

FIGURE 5.16: Influence of UTCs on global, land, and ocean annual mean CRE at the top-of-atmosphere and surface (W m^{-2}). The global fraction of each UTC type, CF (%), is reported in top row.

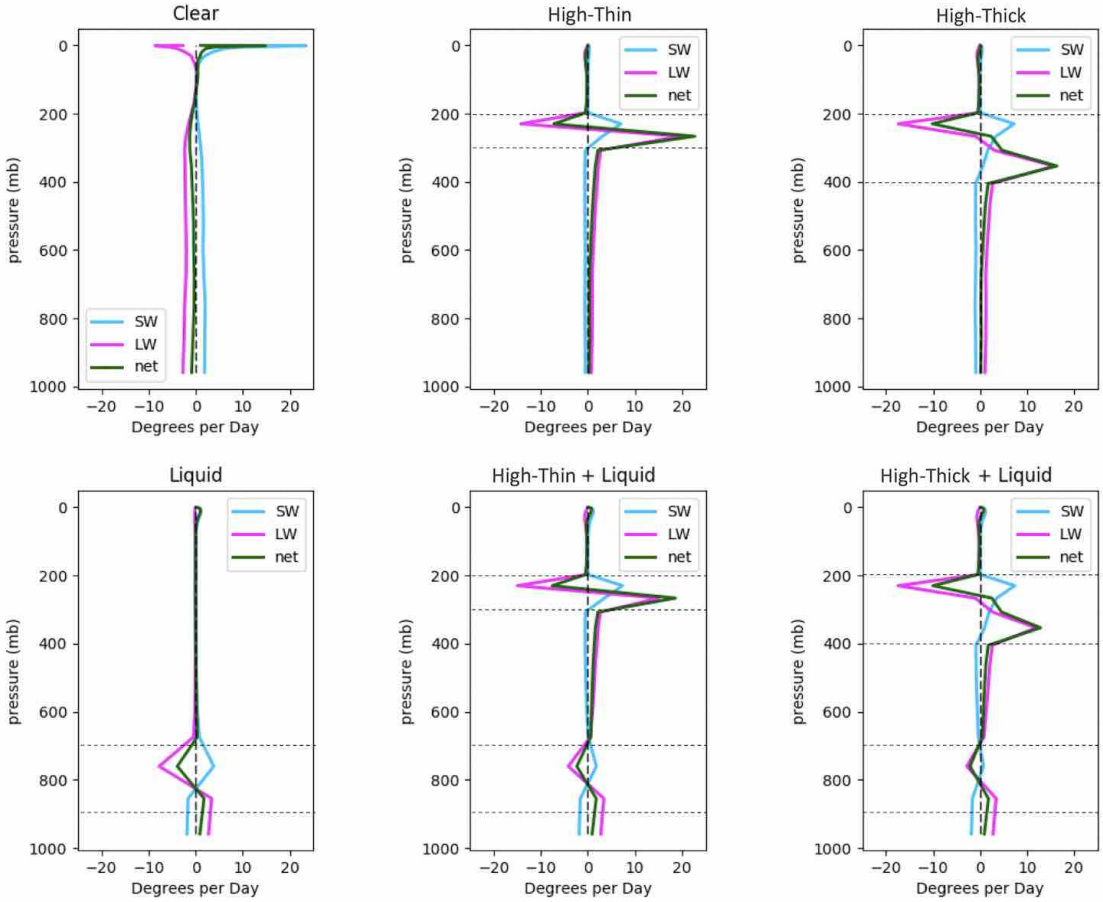

FIGURE 5.17: Cloud radiative heating rates for hypothetical tropical UTCs derived from BUGSrad. Thin ice cloud is defined as: cloud base = 300 mb, cloud top = 200 mb, ice mixing ratio = 0.1 g/kg, cloud fraction = 100%; thick ice cloud is same as thin ice cloud but with a cloud base at 400 mb. Liquid cloud is defined as: cloud base = 900 mb, cloud top = 700 mb, water mixing ratio = 1 g/kg, cloud fraction = 100%.

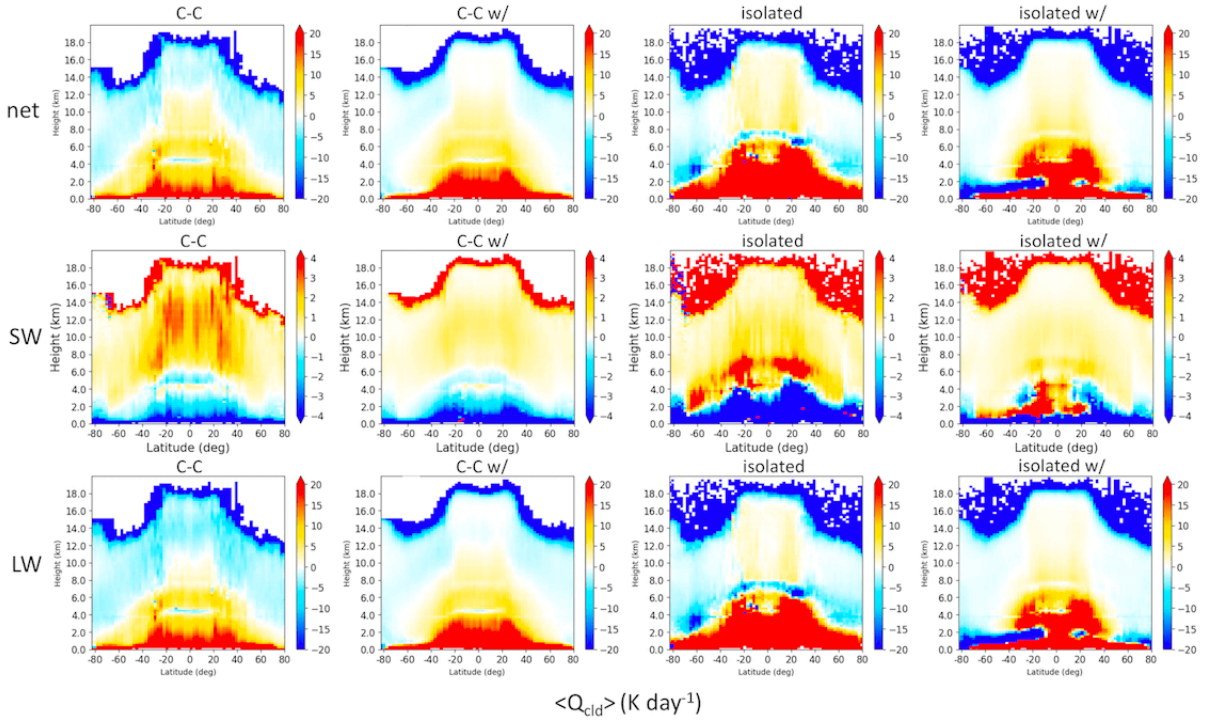

FIGURE 5.18: Annual zonal mean net, SW, and LW $< Q_{cld,i} >$ of UTCs (K day^{-1}). All fluxes data presented are from 2BFLX, 2007-2010.

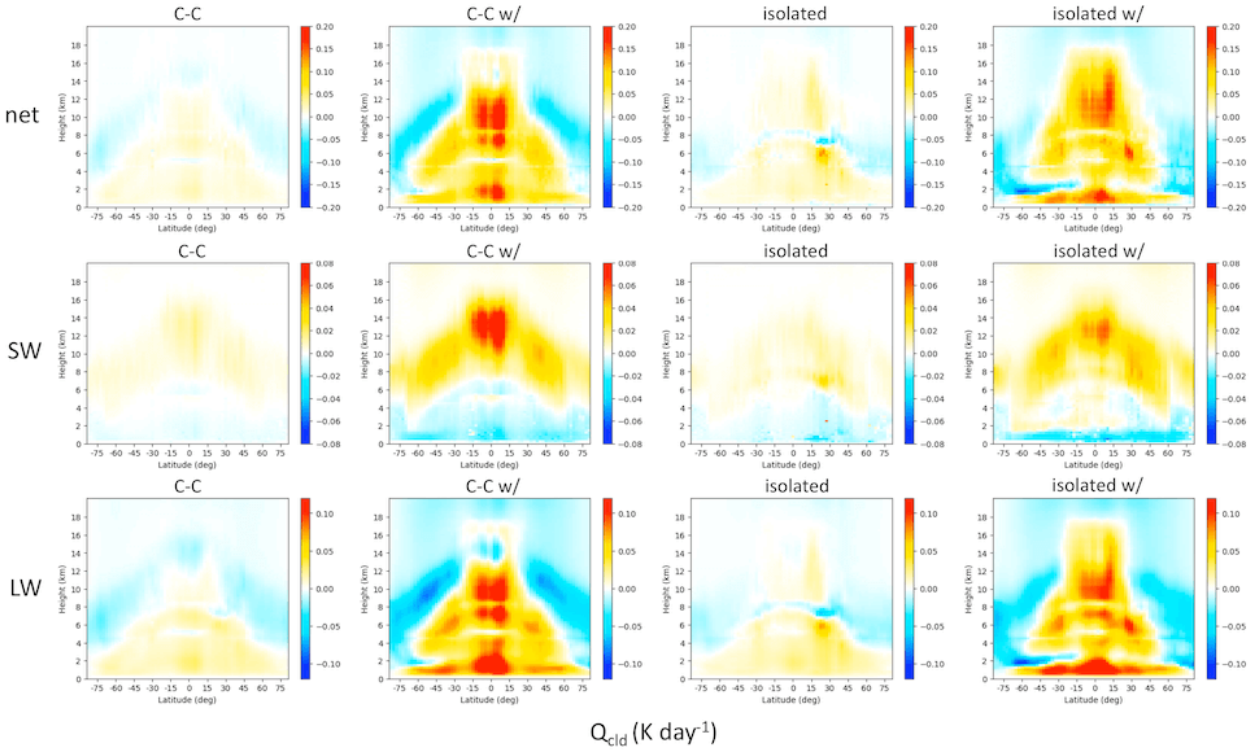

FIGURE 5.19: Same as Figure 5.18, but for $Q_{cld,i}$ (K day^{-1}).

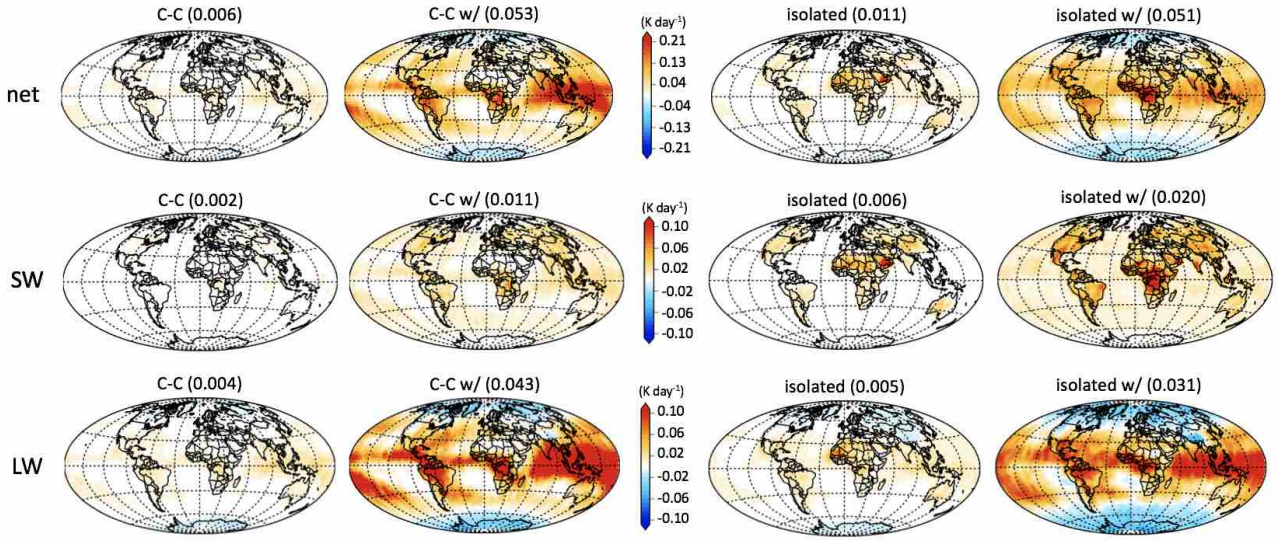

FIGURE 5.20: Annual mean net, SW, and LW cloud radiative heating of UTCs (K day^{-1}). All fluxes data presented are from 2BFLX, 2007-2010. The area-weighted global average (in K day^{-1}) is shown in parentheses.

Q_{cld}

Global	C-C	C-C w/	isolated	isolated w/	Total	Uncertainty
CF	1.2	7.9	1.6	8.2	18.9	1.4
$Q_{SW,cld}$	0.002	0.011	0.006	0.020	0.038	0.001
$Q_{LW,cld}$	0.004	0.043	0.005	0.031	0.083	0.003
$Q_{net,cld}$	0.006	0.053	0.011	0.051	0.121	0.005
Land						
CF	0.6	2.9	1.1	2.8	7.4	0.5
$Q_{SW,cld}$	0.001	0.006	0.005	0.013	0.025	0.001
$Q_{LW,cld}$	0.002	0.014	0.003	0.009	0.028	0.002
$Q_{net,cld}$	0.003	0.020	0.008	0.023	0.053	0.003
Ocean						
CF	0.6	4.9	0.5	5.5	11.5	0.2
$Q_{SW,cld}$	0.001	0.005	0.001	0.006	0.013	0.000
$Q_{LW,cld}$	0.003	0.028	0.003	0.022	0.055	0.003
$Q_{net,cld}$	0.003	0.033	0.003	0.028	0.068	0.003
Land-Ocean						
CF	0	-2	0.6	-2.7	-4.1	0.3
$Q_{SW,cld}$	0.000	0.001	0.004	0.008	0.013	0.001
$Q_{LW,cld}$	-0.001	-0.014	0.000	-0.013	-0.028	-0.001
$Q_{net,cld}$	-0.001	-0.013	0.004	-0.005	-0.015	0.000

FIGURE 5.21: Same as Figure 5.16, but for cloud radiative heating (K day^{-1})

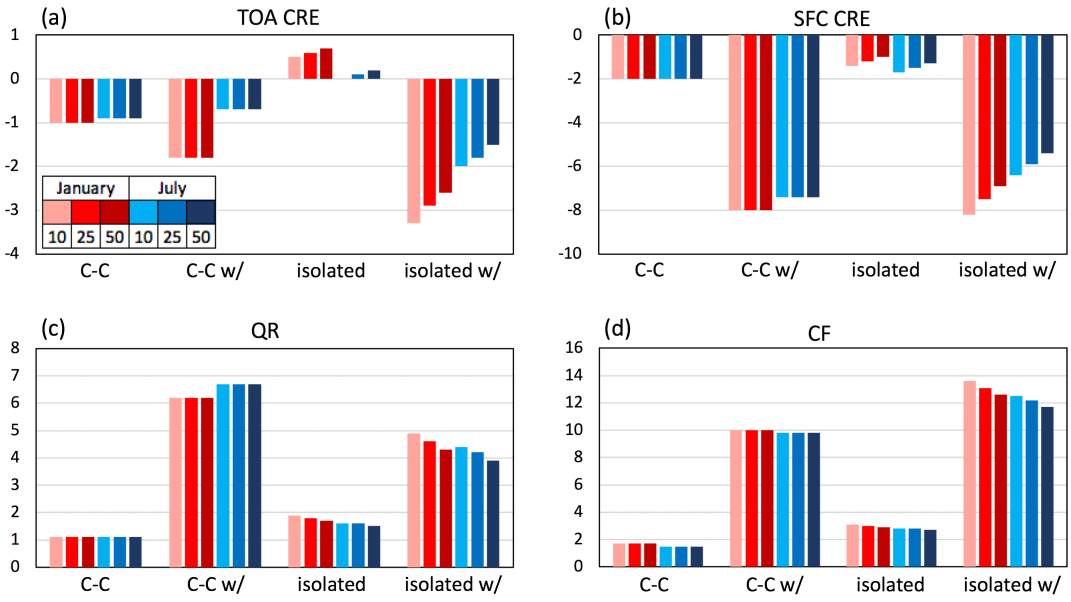

FIGURE 5.22: The area-weighted global average net cloud radiative effect (W m^{-2}) at the TOA (a) and SFC (b), net cloud radiative heating (c, K day^{-1}), and cloud fraction (d, %) of UTCs with different possibly convectively-coupled distance at 10km, 25km, and 50 km in January and July, 2007-2010.

Chapter 6

Influence of Aerosol on Solar Energy Potential

Solar energy, as a clean energy resource has attracted exponentially increased attentions during past two decades (Kannan and Vakeesan, 2016). In particular, solar energy targets of Asian countries are getting ambitious over the years. Ten years ago, China's domestic solar power capacity was virtually non-exist, but now, China owns or operates nine of the world's top 10 solar panel manufacturers. Current solar capacity target of China is 213 GW that is three times larger than the US solar capacity in 2019 (https://unearthed.greenpeace.org/2017/08/25/china-raises-solar-power-target/). According to India's energy minister, India is on track for achieving its solar capacity target of 100GW by 2022 (https://ieefa.org/india-on-track-to-meet-100gw-solar-target-by-2022-minister-says/). Southeast Asian countries are also accelerating their solar power projects to triple current solar power capacity by 2024 (https://www.reuters.com/article/us-singapore-energy-solar/cheaper-solar-power-gains

-ground-in-southeast-asia-idUSKBN1XA1KJ). So far, Thailand has lead the pack that it has more solar power capacity than all the rest of Southeast Asian countries combined.

Although solar power market in Asia is prosperous, observed high aerosol concentrations over many regions including China and India has imposed risks on regional solar electricity generation (Aayog, 2015). Combining both aerosol-radiation and aerosol-cloud interactions, aerosols exert a negative radiative forcing that results in energy loss in Earth's systems, especially over regions where are highly polluted (IPCC AR5). Also, dust aerosols that cover the surface of solar collectors significantly reduce the efficiency of producing electricity, adding maintenance expenses to the whole solar energy system (Sweerts et al., 2019). Thus, it is important to monitor and quantify influences of individual aerosol type on regional solar energy potential.

Many studies have discussed the impact of inter-annual and monthly variations of aerosol optical depth (AOD) on solar radiation with ground-based measurement, satellite observations, and numerical models (Jinhuan and Liquan, 2000, López-Solano et al., 2018, Ruiz-Arias et al., 2013). For example, Si-Ya and Jing (2015) shows that there is a strong negative correlation between AOD and radiation change. AOD is a good indicator of loacal solar resource availability. However, surface measurements are usually limited in spatial coverage whereas the temporal resolution of satellite measurements is low. Also, without accurate observations, model simulations alone are inadequate for characterizing wide diversity of aerosol properties. Reanalyses such as the second Modern-Era Retrospective analysis for Research and Applications (MERRA-2) (Randles et al., 2017) attempts to fill the gap between observations and models. It can effectively combine the continuity of a model with

real-world observations.

This chapter will utilize the start-of-art MERRA-2 reanalysis aerosol data that has high spatial and temporal resolutions to document hourly variations of regional AOD. The seasonal changes of AOD derived from MERRA-2 aerosol reanalysis will be compared with observation-based measurements derived from CALIPSO satellite. Considering CALIPSO version 4 (V4) aerosol classification (Kim et al., 2018) and MERRA-2 aerosol classification (Randles et al., 2017) are very different, aerosol types are generally separated into three categories as shown in Figure 6.1.. The "pollution" category includes all human-made aerosol types such as sulfate, organic carbon, black carbon, and polluted dust. Finally, the "marine" category includes clean marine from CALIPSO V4 and sea salt from MERRA-2. In addition to AOD, estimates of regional aerosol direct raditive effect (DRE) under clear-sky condition will be provided by CloudSat's level 2 radiative flux and heating rate (2B-FLXHR-LIDAR, hereafter, 2BFLX) algorithm (L'Ecuyer et al., 2008).

6.1 Estimating Regional AOD and Aerosol DRE with Spaceborne Observations

In this section, observation-based estimates of AOD and aerosol DRE are derived using collocated satellite retrievals from CloudSat and CALIPSO observation. Aerosol types are identified with CALIPSO V4 aerosol classification that detects aerosol layers between the surface and 30 km altitude (Kim et al., 2018). There are seven aerosol types in CALIPSO V4 includes clean marine, dust, clean continental, polluted continental, polluted dust, smoke, and dusty marine. In order to compare satellite observations with MERRA-2 modeled results, aerosol types are simplified in three categories: dust, pollution, and marine aerosol

(Figure 6.1). To quantify aerosol direct radiative effect of each aerosol category, radiative fluxes are derived using CloudSat's 2BFLX product. This study only focuses on aerosol DRE under clear-sky condition at the TOA to isolate the radiative influence of cloud cover.

Aerosol optical depth, as one of the most important properties to access aerosol radiative characters, measuring column-integrated magnitude of light extinction from aerosols. Therefore, AOD is a great indicator to access the influence of aerosol on solar radiation that successfully arrives at solar photovoltaic panels at the surface. Ground-based AOD measurements are more accurate than satellite measurements because air mass factors and surface albedo corrections add uncertainties to satellite retrievals. But to quantify AOD for large countries like China and India, spaceborne observations are more suitable due to their broad spatial coverage. Figure 6.2 displays annual mean CALIPSO AOD separated by three aerosol categories determined based on aerosol classification in Figure 6.1 Over China, strong dust AOD is found to exist over Taklimakan Desert located at Southwest Xinjiang. Dust AOD is also relatively large in western and central Inner Mongolia Plateau. But over eastern China, AOD of polluted aerosol is much higher than dust and marine aerosols. This is because economy over eastern China has been developing rapidly that requires abundant conventional energy resources such as coal and oil. The growth of economy also brings population growth resulting in increased vehicle emissions. Over India, thick AOD of pollution aerosol is observed in industrialized regions especially in the northeast where the Himalaya Mountain blocks the spread of human-made pollution. Dust AOD is large in the west India that has the Great India Desert and close to the Arabian desert. Pollution AOD also dominates the total AOD of Southeast Asia where biomass burning is a major source of air pollution in addition to vehicle and industrial emissions. Marine AOD is very thin and

evenly distributed over ocean regions.

Figure 6.3 correspondingly shows estimates of annual mean aerosol net direct radiative effect at the TOA under clear-sky condition with CloudSat's 2BFLX algorithm. Not surprisingly, pollution aerosol significantly cools eastern China and northeastern India by more than -12 W m^{-2}. Compared with Figure 3.6 annual mean net cloud radiative effects at the TOA derived from the same satellite product, the DRE of pollution aerosol is much stronger than cloud radiative effect over land. At the same time, dust aerosol substantially cools western India, Inner Mongolia Plateau, and western China by more than -4 W m^{-2}.

To further interpret seasonal variability of aerosol radiative effect on solar resources, Figure 6.4 compares total aerosol DRE at the TOA under clear-sky condition for each season. Aerosol DRE over India is mainly influenced by human activity, Himalayan mountains, and the South Asian Monsoon (Padma Kumari et al., 2007). In densely populated regions that produce high emission of anthropogenic aerosols, for example in Mumbai and Delhi areas, DRE of aerosol exceeds -16 W m^{-2} resulting in a significant cooling effect. This situation is aggravated over northern India because Himalayan Mountains prevent southerly and westerly winds to dissipating polluted air (Pant et al., 2006). But India experiences a light aerosol DRE during summer rainfall season since the strong South Asian monsoon brings moist wind from the India Ocean to the Indian subcontinent that might let pollutants sink or transport to other regions (Lau and Kim, 2006). Together, topography, seasonal wind, and precipitation dominate the temporal and spatial distributions of aerosol DRE over India. Over China, high anthropogenic emissions play a dominant role in regional aerosol DRE as well, especially during winter and autumn. One of the main reasons for this seasonal

change might be chinese “heating policy” that regulates central heating systems to provide heat to local homes starting from November to early March (Xiao et al., 2015). The bulk of residential and industrial energy needs in China have long been met by coal, so the late autumn and winter is marked by a spike in air pollution. Another reason for the strong DRE in winter is temperature inversion that traps pollutants beneath clouds, acting as a lid to block pollution at the ground (Xu et al., 2019).

Figure 6.5 compares seasonal shortwave cloud radiative effect and clear-sky DRE at TOA estimated from 2B-FLXHR-LIDAR, 2007-2010. In general, clouds are the dominant factor that results in solar resources intermittency. Clouds strongly reduce solar radiation in summer, while aerosols have the largest influence in winter. During winter and autumn, aerosols largely attenuate solar radiation over northern and eastern China. Note that aerosol indirect effect that increases cloud amount is attributed to clouds rather than aerosols, therefore, the real aerosol impact on solar resources is larger.

Following the seasonal changes of total aerosol DRE, Figures 6.6 and 6.7 show seasonal aerosol DRE of dust aerosol and pollution aerosol defined in Figure 6.1 at the TOA under clear-sky condition. In general, dust and pollution aerosol DRE are much stronger than marine aerosol DRE, but they have distinct seasonal variations. As shown in Figure 6.6, yellow dust severely influences northern China that results in a cooling effect during late winter and springtime (Zhao et al., 2006). Then start from late spring, pre-monsoon dust storms significant threaten northern India since local weather is dry to allow dust to be picked up by passing winds (Kumar et al., 2013). The strongest pollution aerosol DRE exists in autumn and winter over India and China (Figure 6.7). The reason of the distribution

pattern over China has been explained previously that includes winter temperature inversion and the Chinese "central heat policy". But over India, the strong DRE of pollution aerosol during autumn and winter is due to biomass burning that tons of crop residue are burnt, and winds blow from India's north and northwest towards east, resulting in human-made smoke and air pollution (Rastogi et al., 2016).

6.2 Accessing Regional Aerosol DRE with MERRA-2 Aerosol Reanalysis

One unique strength of MERRA-2 aerosol reanalysis is it uses an upgraded GEOS-5 data assimilation system that includes assimilation of AOD from various ground- and space-based remote sensing platforms such as AEROsol Robotic Network (AERONET), Advanced Very High Resolution Radiometer (AVHRR), multi-angle Imaging SpectroRadiometer (MISR), and MODerate resolution Imaging Spectroradiometer (MODIS) (Randles et al., 2017). The spatial resolution of MERRA-2 aerosol reanalysis is as high as $0.625^\circ \times 0.5^\circ$ with a fine temporal resolution of 1 hour (Randles et al., 2017). Also additional meteorological fields such as winds, temperature, and pressure are assimilated in MERRA-2. This section will document AOD separated by three aerosol categories determined based on aerosol classification in Figure 6.1 with MERRA-2 aerosol reanalysis data in 2008.

Figure 6.8 displays annual mean total AOD separated by three aerosol categories with MERRA-2 aerosol reanalysis data. Compare Figure 6.8 with previous observational AOD derived from CALIPSO shown in Figure 6.2, the main discrepancy comes from pollution AOD over eastern China and Sichuan Basin. A recent study Feng and Wang (2019) shows that the reason for the large discrepancy is that MERRA-2 overestimates atmospheric aerosols

loading and underestimates cloud fraction, especially for multiyear cloud fraction. At the same time, other studies have also shown that CALIPSO may misclassify dense aerosol layers as clouds and may fail to detect aerosols with low AOD (Kacenelenbogen et al., 2014, Schuster et al., 2012), which add more disparities between AOD derived from CALIPSO and MERRA-2. Also, higher MERRA-2 AOD may also be from boundary layer aerosols under thick clouds that would not be detected by CALIPSO.

In addition, Figures 6.9, 6.10, and 6.11 provide more insights on seasonal change of AOD of each aerosol category with MERRA-2 reanalysis. Considering MERRA-2's strength on assimilated meteorological fields, Figure 6.12 displays seasonal mean wind field at the surface to explain spatial distributions of AOD during different seasons. Combining Figures 6.9 and 6.12, it is found that thick dust AOD over western China during spring and summer is generated from local Taklamakan desert, but dust AOD over western India during Summer is contributed by fine sand blowing from northwest India and the central Asian region (Maharana et al., 2019). Figure 6.10 shows seasonal mean AOD of pollution aerosol with MERRA-2 aerosol reanalysis. The most striking feature is a layer of very thick AOD covers Chengdu-Chongqing region that locates at Sichuan Basin in China. Sichuan Basin is a lowland region that is surrounded by mountains on all sides, therefore, air pollution generated from heavy oil refining industries in the Chengdu-Chongqing region is easy to accumulate rather than disperse. It is evident that wind speed over Chengdu-Chongqing region is fairly small (less than 1 m/s) during every season (Figure 6.12). Even the strong summer East Asian monsoon is blocked by the surrounding mountains. Another reason is that the populous Chengdu-Chongqing region has a large amount of automobile emissions, only Beijing has higher emissions in China (Yao et al., 2007). Also, the Chengdu-Chongqing

region is rapidly developing. Over eastern Russia, a thick layer of pollution AOD is found due to spring fires and smoke in the Amur forest region. Finally, Figure 6.11 compares AOD of marine aerosol for each season. With surface wind speed and direction information provided in Figure 6.12, it is found that oceanic regions with large wind speed have thick marine AOD, such as the west coast of India in summer when the summer India monsoon is very strong (O'Dowd et al., 2010). Surface water temperature also determines marine AOD (Mårtensson et al., 2003). Although northern Indian Ocean experiences relatively high wind speed in winter, its surface water temperature is low, resulting in low AOD in the region.

As introduced earlier in this section, MERRA-2 aerosol reanalysis provides valuable information to track daily variations of AOD at high spatial resolution. For example, MERRA-2 aerosol reanalysis is capable to capture regional AOD changes in Beijing during and after Summer Olympics in 2008. In order to make sure air quality is healthy for athletes and tourists who came to Beijing during 2008 Summer Olympics, chinese government implemented a "Air Quality Guarantee Plan" in Beijing and surrounding regions starting from June to September in 2008. This plan has four goals including reducing construction dust, limiting industrial pollution, decreasing coal burning pollution, and controlling traffic flow (http://www.gov.cn/xwfb/2008-02/27/content_903668.htm). Figures 6.13 shows regional daily average AOD separated by three aerosol categories on August 16, 2008 - one day during Beijing Summer Olympics. Obviously, Beijing enjoyed very low aerosol concentrations on that day with MERRA-2 reanalysis data. Both pollution and dust AODs over Beijing area were lower than 0.25 on August 16. Figure 6.14 is similar to Figure 6.13 but for the day of September 6, 2008 - one day after Beijing Summer Olympics. By contrast, there was a very thick layer of pollution AOD covers Beijing and its surrounding areas, but

dust and marine AODs were at a similar level to AODs during Olympics.

More importantly, MERRA-2 aerosol reanalysis has unprecedented ability to identify hourly changes in AOD as well. Figure 6.15 compares 72-hour pollution AOD change in Beijing during (August 15-17 UTC, orange line) and after (September 5-7 UTC, blue line) 2008 Olympics. It is clear that during 2008 Olympics, pollution AOD was always lower than 1. But after Olympics, starting from 8am Beijing time on September 8, aerosol AOD rose very sharply. On September 7, 2008, the pollution AOD was even approaching 14 at 2pm Beijing time. This is because the restrictions came to an end without formal government announcement. Factories were allowed to resume normal work, so they increased output to make up for losses caused by emission policies during Olympics. Local meteorological situation could also contribute to the extremely high concentration of pollution AOD in the afternoon of September 7.

Historical weather observations of Beijing from September 5-7, 2008 is displayed in Figure 6.16. It is shown that the humidity of Beijing was very high at around 80% on September 7 and the local wind speed was dramatically decreasing from 8 mph at 6am to 2 mph at 5pm. The wind direction was reported as ENE on September 7 and the weather was cloudy according to Weather Underground. There is a Taihang Mountain locates at west side of Beijing that blocks east wind. So, there was no chance for pollutants generated from Beijing area to be either transported and dissipate. Meteorological and geographical conditions catalyze air pollution in Beijing, enhancing local aerosol radiative influence.Note that those information on hourly changes of AOD are particular useful to quantify the influence of aerosol on solar energy's intermittency challenge.

6.3 Quantifying Influence of Aerosol on Solar Energy Potential over South Asia

Although solar resource is clean and renewable, solar power generators only convert solar radiation when the sun is shining. This intermittency challenge makes solar energy less attractive in electricity generation market. An example is given in Figure 6.17 that compares electricity system load (the total electric power consumed by all users connected to the distribution network of a system) with and without a large solar PV system during summer and spring days. It is shown that adding a solar PV system to a normal electricity system load during summer substantially reduce diurnal electricity peak demand (Figure 6.17a). But in cool spring (Figure 6.17b), when there is less demand during daylight hours, the net load with PV is actually less than the base load power capacity. Since base load power stations are normally supported by nuclear or coal, so, their output cannot be varied easily. Thus investors would probably rather reject solar power than reduce output from its base load stations, meaning that solar power could not be sold even if it has been produced. If investors continue integrating solar energy, it will hit their dispatchable energy resources directly. The more solar energy is integrated, the more base-load resources will be attacked. In contrast, dispatchable technologies such as coal combustion can continuously generate units with its capability to vary output following energy demand from market. Dispatchable technologies have more values in adjusting energy system than less flexible non-dispatchable technologies such as solar PV. Therefore, quantifying seasonal and hourly changes of solar resources is beneficial to mitigate the intermittency challenge.

Aerosol largely influences solar resources by aerosol deposition and atmospheric attenuation.

Dust aerosol that covers the surface of PV modules can reduce power production by more than 50% if no cleaning is performed on modules for a period of time that exceeds half a year (Adinoyi and Said, 2013). Li et al. (2017a) evaluates the impact of aerosol on solar PV generation in China and finds that aerosol-related annual average reductions in solar energy have comparable impacts to clouds over eastern China in winter. It is found that aerosols reduce annual average point-of-array irradiance by up to 35% northern and eastern China polluted regions relative to pollution-free conditions (Li et al., 2017a).

AOD is a good indicator of solar resources availability. There is a strong negative correlation between AOD and radiation change. According to Si-Ya and Jing (2015), if AOD equals to 1, the shortwave radiation reaching at the surface will decrease by 30%, if AOD equals to 2, the radiation will decrease by even 50%. Therefore, the ability to quantify regional AOD change at fine resolution is beneficial to study the intermittent change in order to make solar energy more reliable. Figure 6.18 shows solar farm locations and capacities from India and Thailand who are leaders in South Asia solar energy market. Three solar farms with large energy capacities are selected to study their regional AOD of dust and pollution aerosols with MERRA-2 aerosol reanalysis from 2008. All solar farm data are derived from Global Power Plant Database (https://www.wri.org/publication/global-power-plant-database).

Figure 6.19 displays boxplots of AOD from dust and pollution aerosols over three solar farms A, B, and C as labeled in Figure 6.18. Dust aerosol is found to significantly reduce solar radiation at solar farm A. During summer, the median dust AOD over solar farm A is around 1, indicating substantial solar radiation has been blocked (Si-Ya and Jing, 2015). These dust can also potentially cover the surface of solar PV panels that largely reduce

power production (Adinoyi and Said, 2013). One striking feature of dust AOD over solar farm A is that the maximum can even reach 3.5 in June, which means the power output is almost zero. Also, the third quartile of dust AOD over solar farm A in June is large, ranging from 0.6-1.7. These AOD values might be caused by pre-monsoon dust storms (Prasad and Singh, 2007). At solar park B, AOD of pollution aerosol is large during November-May (around 0.5). This is influenced by winter monsoon that blows from the northeast in winter (Padma Kumari et al., 2007). Ramachandran (2004) found that anthropogenic aerosols generated from India are transported to downwind zones during northeast winter monsoon season. Both anthropogenic activities and monsoon dominate the variability of aerosols in India (Pal and Devara, 2012). AOD of pollution aerosol is also large at solar farm C from January-April. In March, the median even exceeds 1 and the maximum is almost up to 2. This is because crop residue burning of rice and sugarcane in central Thailand starting from January to April (Phairuang et al., 2017).

6.4 Chapter Summary

This chapter documents regional aerosol optical depth and direct radiative effect of individual aerosol categories with CALIPSO and CloudSat spaceborne observations. These information are useful to understand regional anthropogenic aerosol forcing, offering a great opportunity to investigate research questions difficult to address with data from conventional passive sensors. This study also highlights the unique strength of MERRA-2 aerosol reanalysis to quantify regional change of AOD at fine spatial and temporal resolutions. Considering solar resource's intermittency problem making solar energy face the risk of rejection

	CALIPSO V4	MERRA-2 Aerosol
Dust	Dust Clean continental Dusty marine	Dust
Pollution	Polluted continental Polluted dust Elevated smoke	Sulfate Organic carbon Black carbon
Marine	Clean marine	Sea salt

FIGURE 6.1: Three classes of aerosol defined according to CALIPSO version 4 (V4) aerosol classification (Kim et al., 2018) and MERRA-2 aerosol classification (Randles et al., 2017).

from investors. A better understanding of seasonal, daily, hourly variations of aerosol concentration of individual aerosol type over local solar parks will help investors decide how many solar energy and base-load energy need to be integrated in the whole energy system, which makes solar energy more attractive in electricity generation market. Note that this study only uses MERRA-2 data from 2008. 2008 is a La Niña year that influences Asia monsoon and brings strong precipitation. More data will be calculated in a future paper.

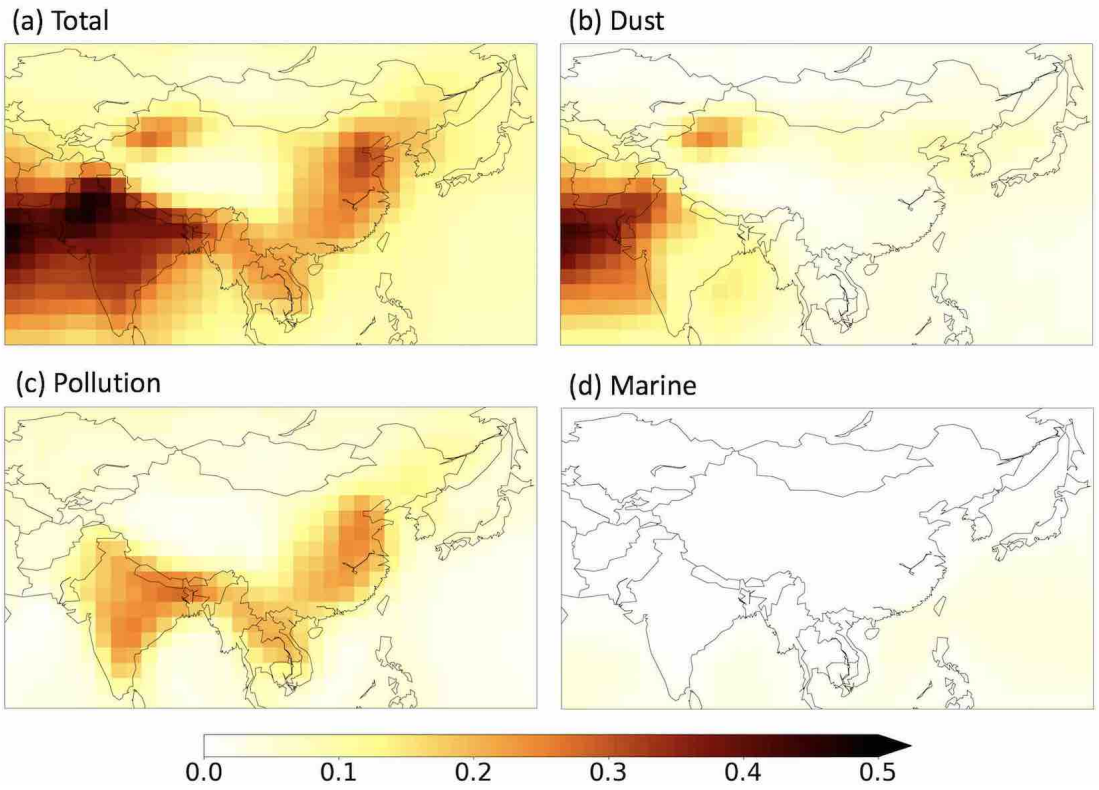

FIGURE 6.2: Annual mean aerosol optical depth (AOD) separated by three aerosol categories determined based on aerosol classification in Figure 6.1. All AOD data presented are from CALIPSO V4, 2007-2010.

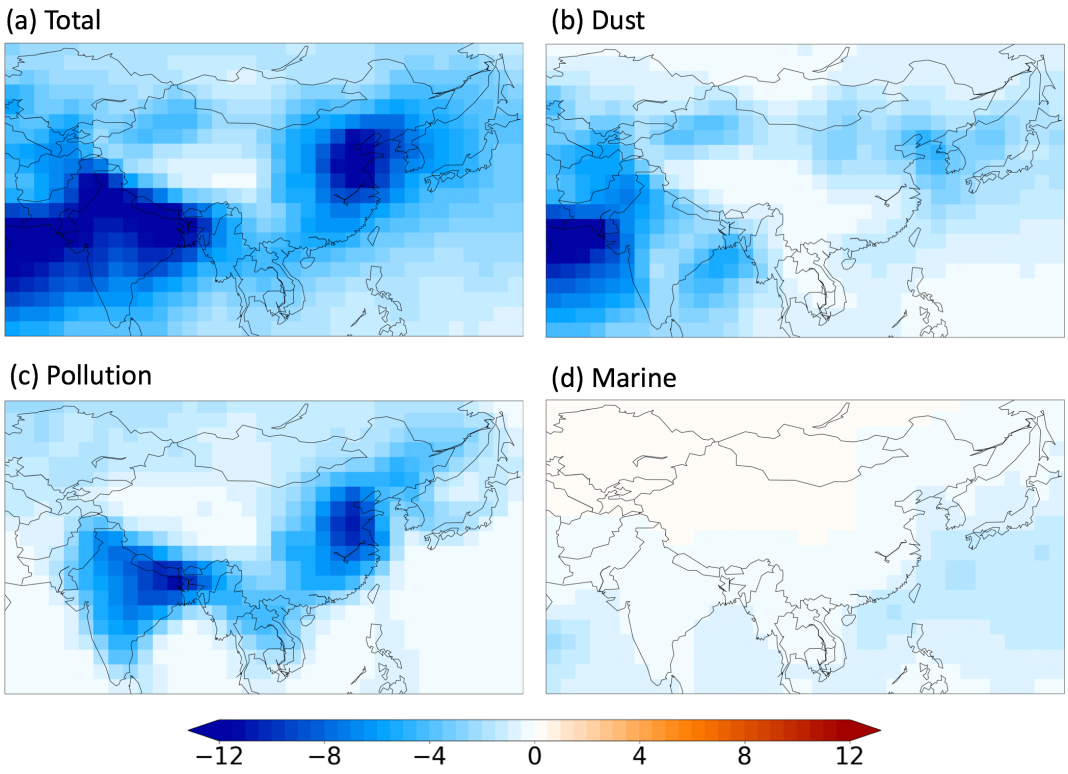

FIGURE 6.3: Annual mean aerosol net direct radiative effect (DRE, in W m^{-2}) at TOA under clear-sky condition, separated by three aerosol categories determined based on aerosol classification in Figure 6.1. All flux data presented are from 2BFLX, 2007-2010.

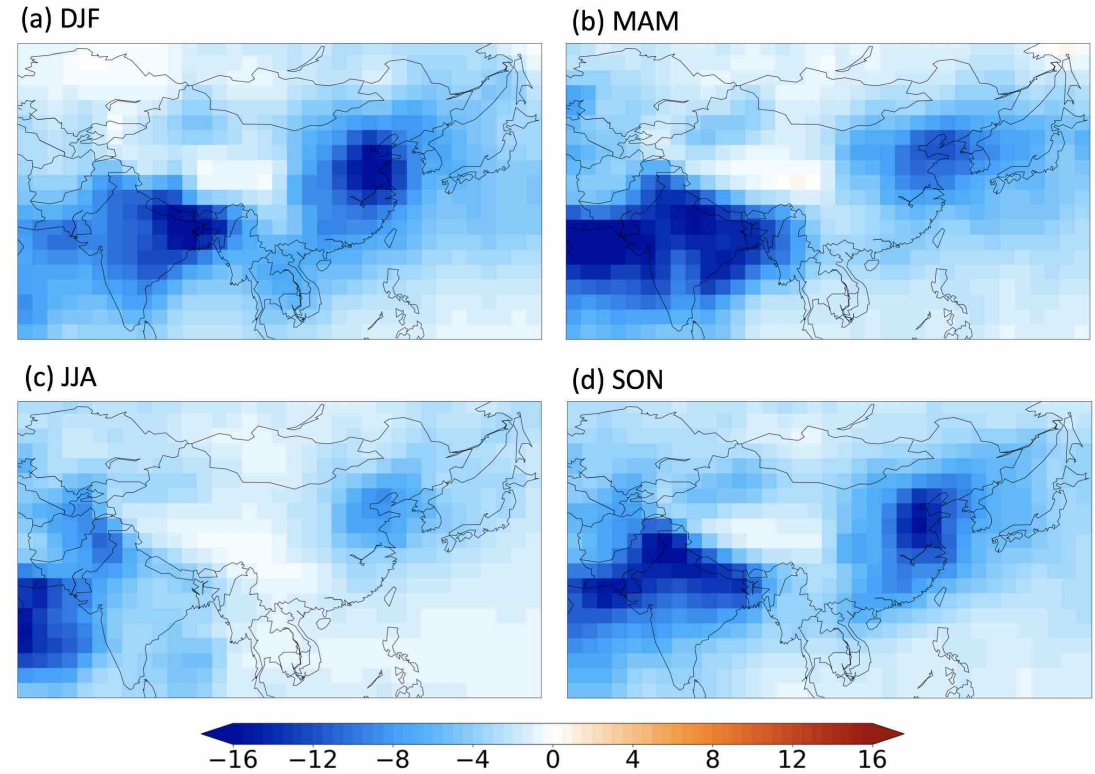

FIGURE 6.4: Seasonal mean DRE of total aerosol (W m^{-2}) at the TOA under clear-sky condition. All flux data presented are from 2BFLX, 2007-2010.

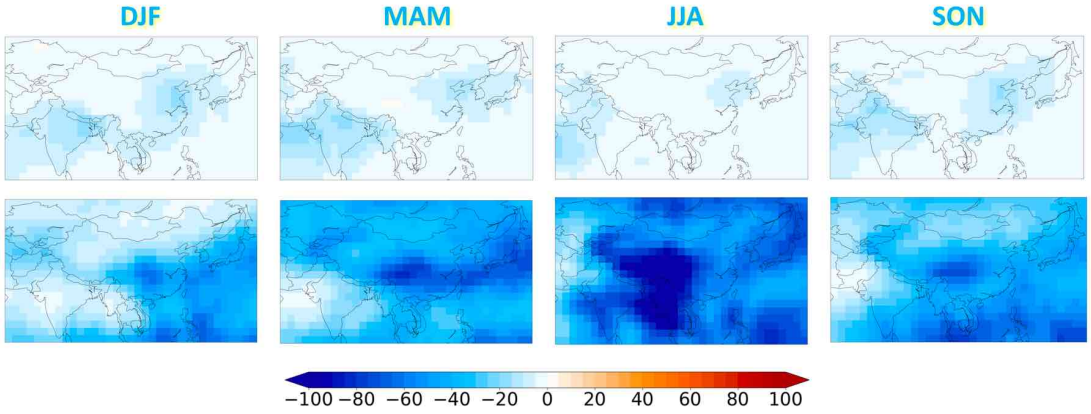

FIGURE 6.5: Net cloud radiative effect (first line) and clear-sky DRE (second line, in W m-2) at TOA estimated from 2B-FLXHR-LIDAR, 2007-2010.

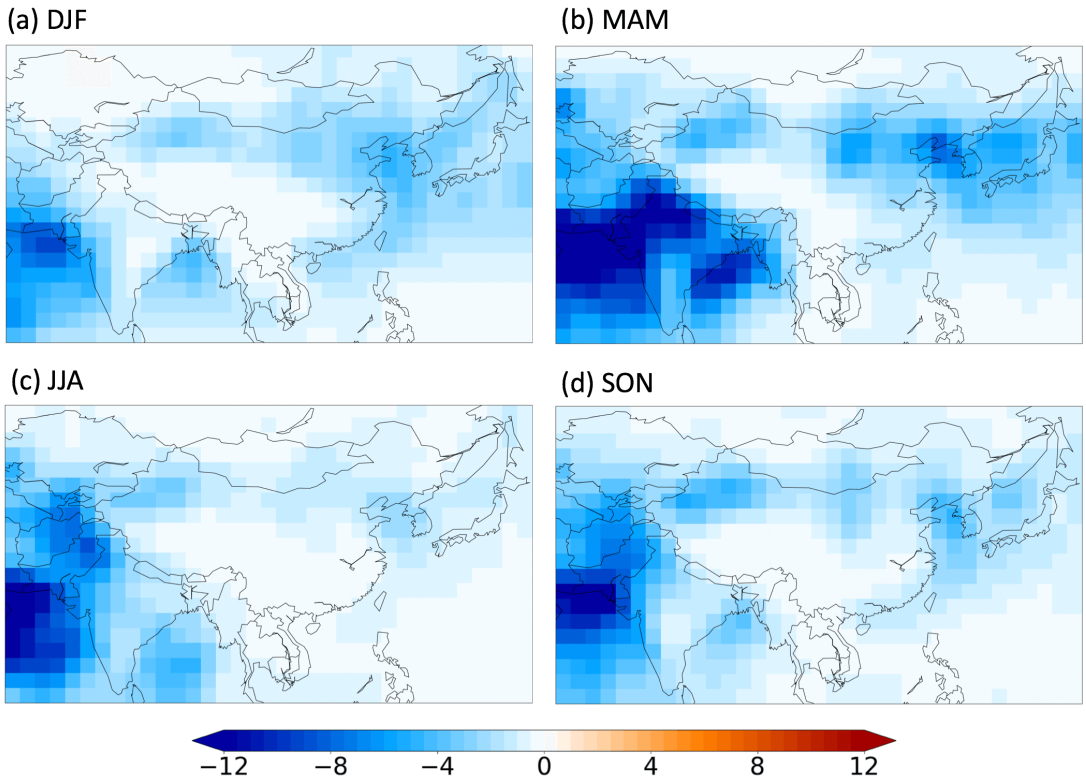

FIGURE 6.6: Seasonal mean DRE of dust aerosol (W m^{-2}) at the TOA under clear-sky condition. All flux data presented are from 2BFLX, 2007-2010.

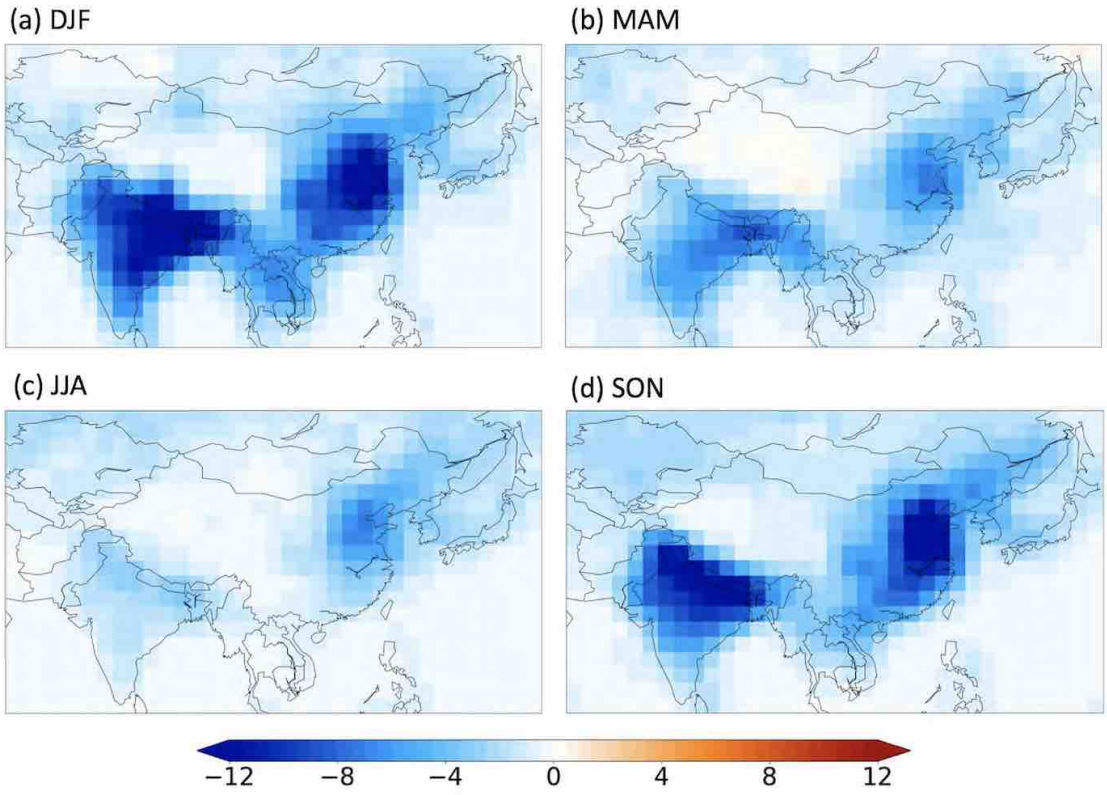

FIGURE 6.7: Seasonal mean DRE of pollution aerosol (W m^{-2}) at the TOA under clear-sky condition. All flux data presented are from 2BFLX, 2007-2010.

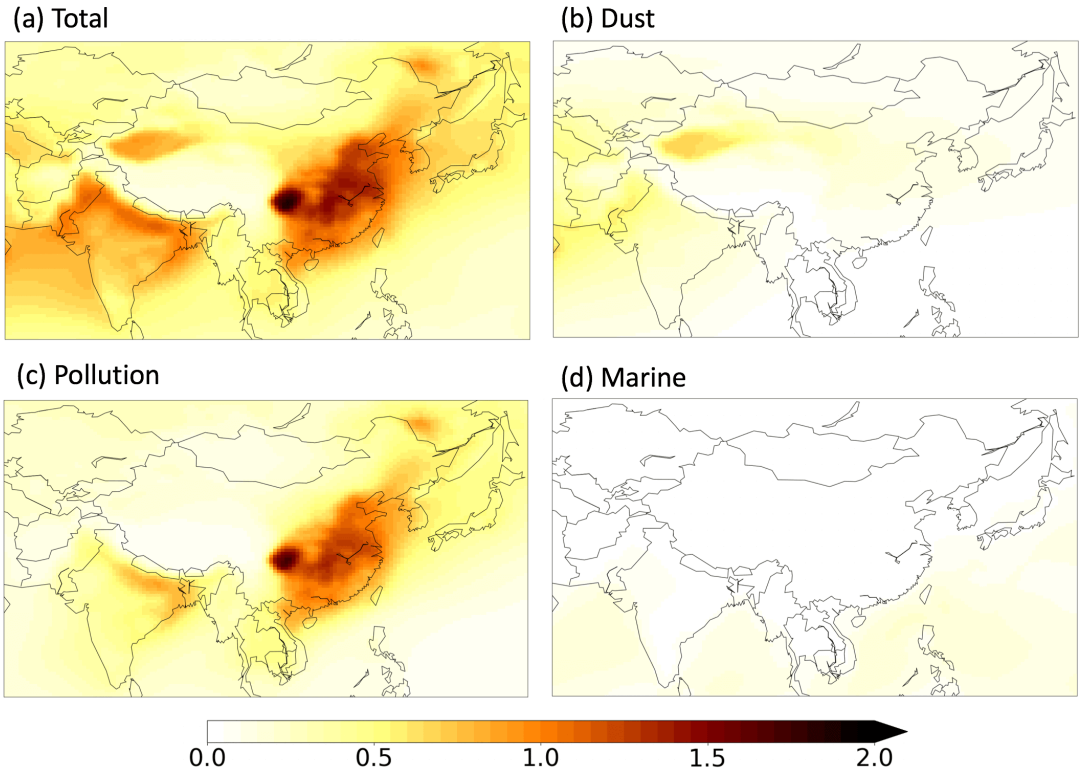

FIGURE 6.8: Annual mean AOD separated by three aerosol categories determined based on aerosol classification in Figure 6.1 with MERRA-2 aerosol reanalysis data in 2008.

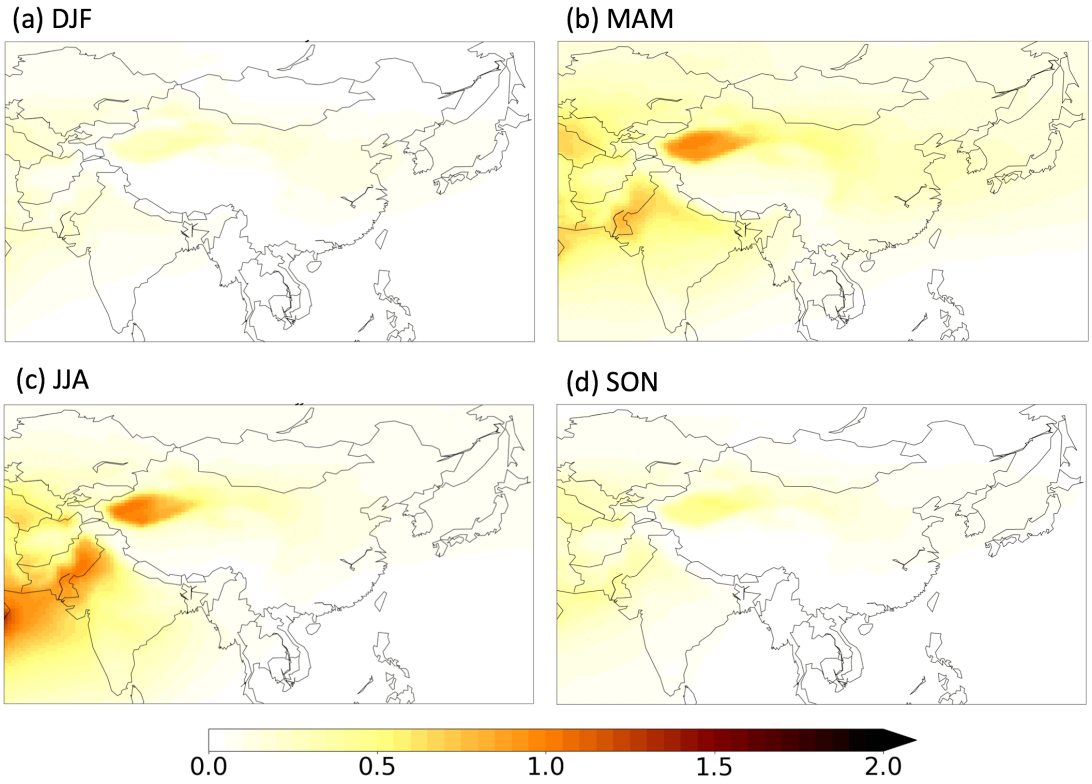

FIGURE 6.9: Seasonal mean AOD of dust aerosol. All data presented are from MERRA-2 aerosol reanalysis, 2008.

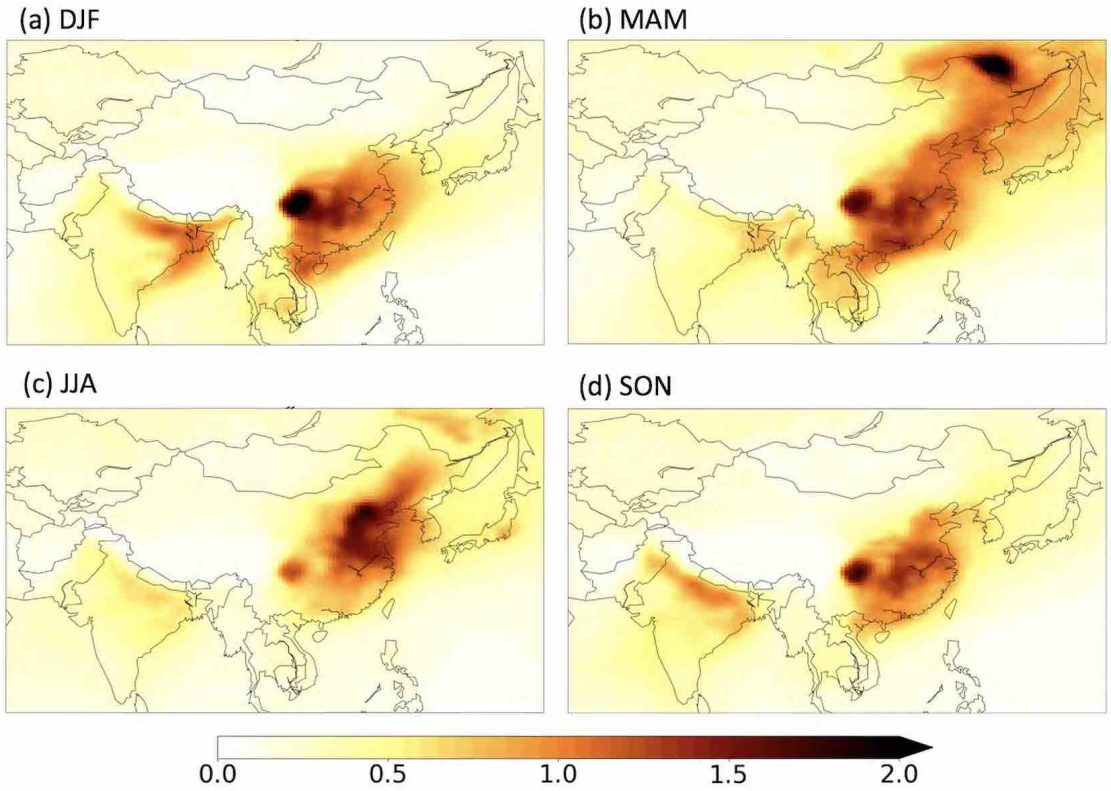

FIGURE 6.10: Seasonal mean AOD of pollution aerosol. All data presented are from ME -RRA-2 aerosol reanalysis, 2008.

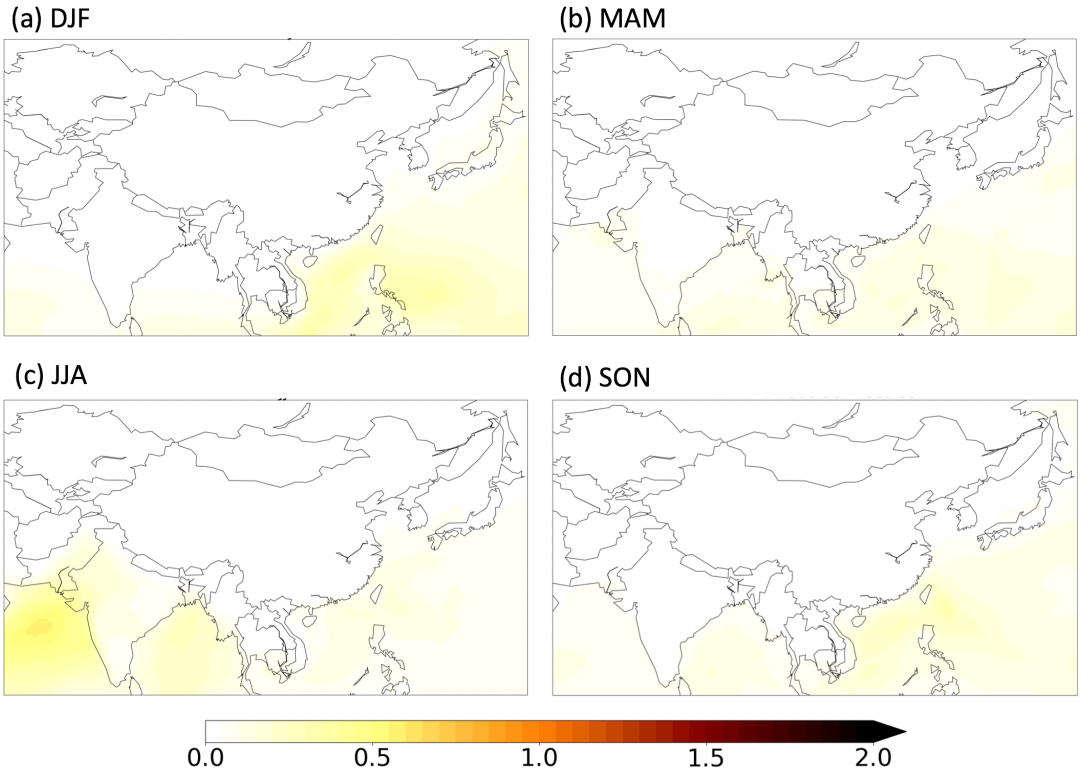

FIGURE 6.11: Seasonal mean AOD of marine aerosol. All data presented are from MERRA-2 aerosol reanalysis, 2008.

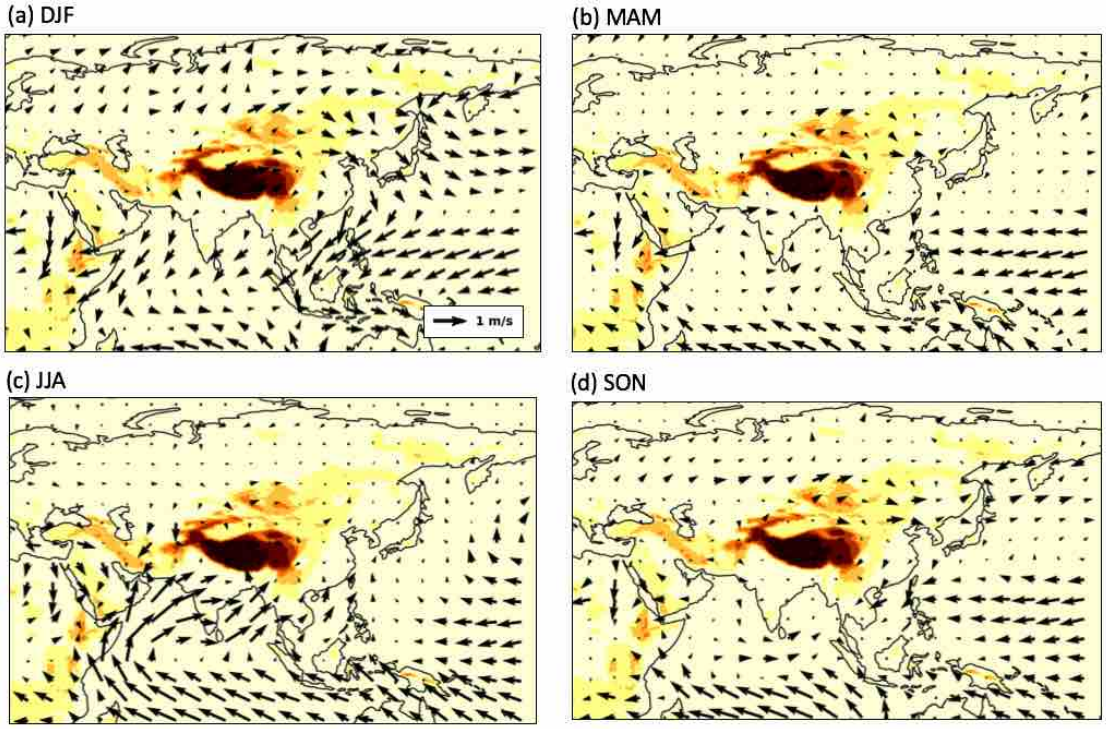

FIGURE 6.12: Seasonal mean wind field at the surface. All data presented are from MERRA-2 aerosol reanalysis, 2008.

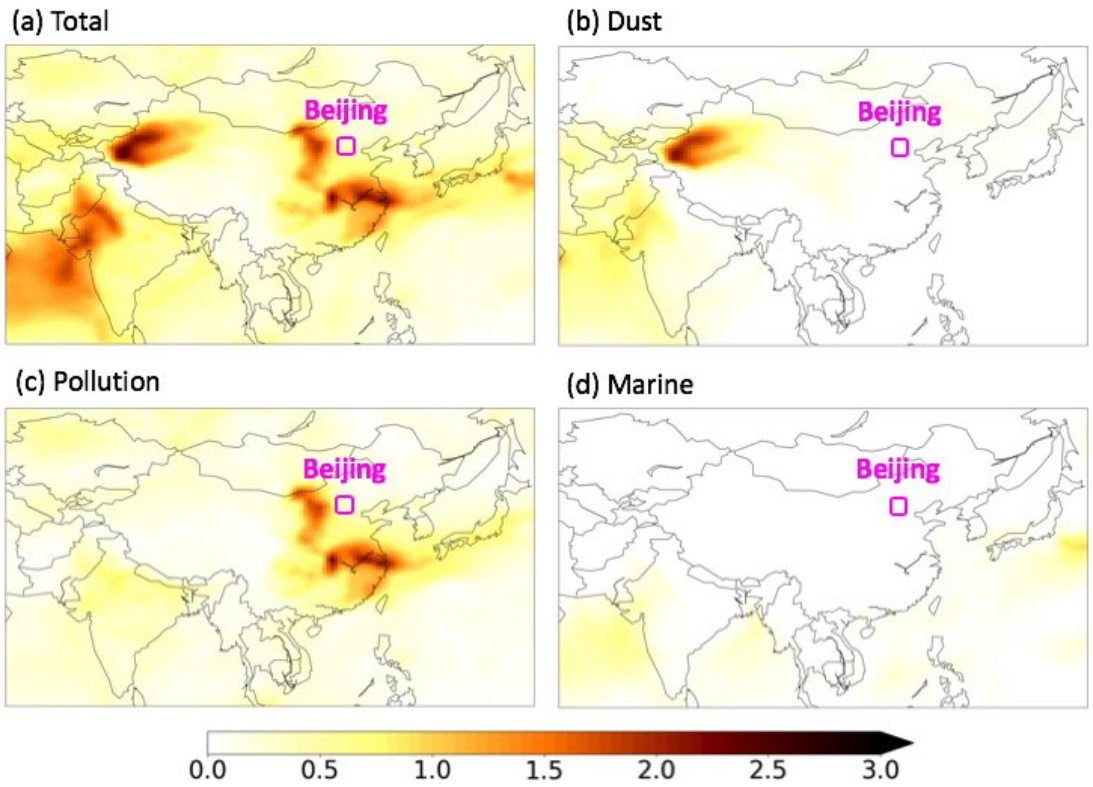

FIGURE 6.13: Daily average AOD separated by three aerosol categories during 2008 Summer Olympics. All data presented are from MERRA-2 aerosol reanalysis, August 16, 2008.

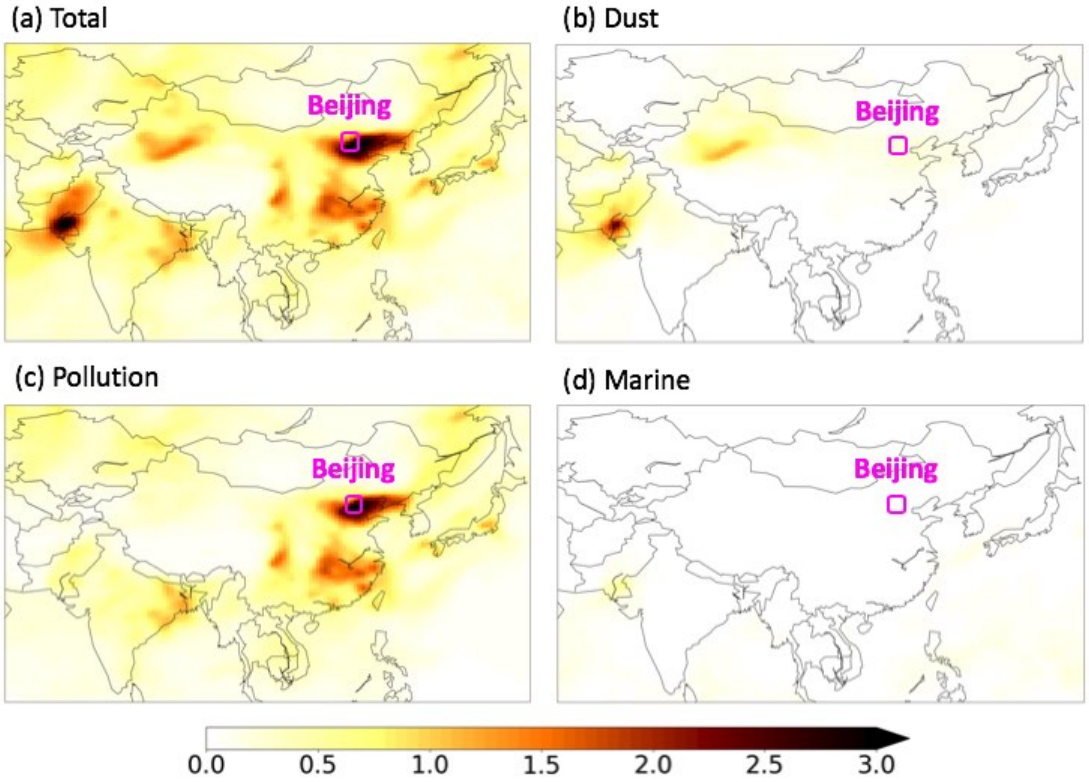

FIGURE 6.14: Daily average AOD separated by three aerosol categories after 2008 Summer Olympics. All data presented are from MERRA-2 aerosol reanalysis, September 6, 2008.

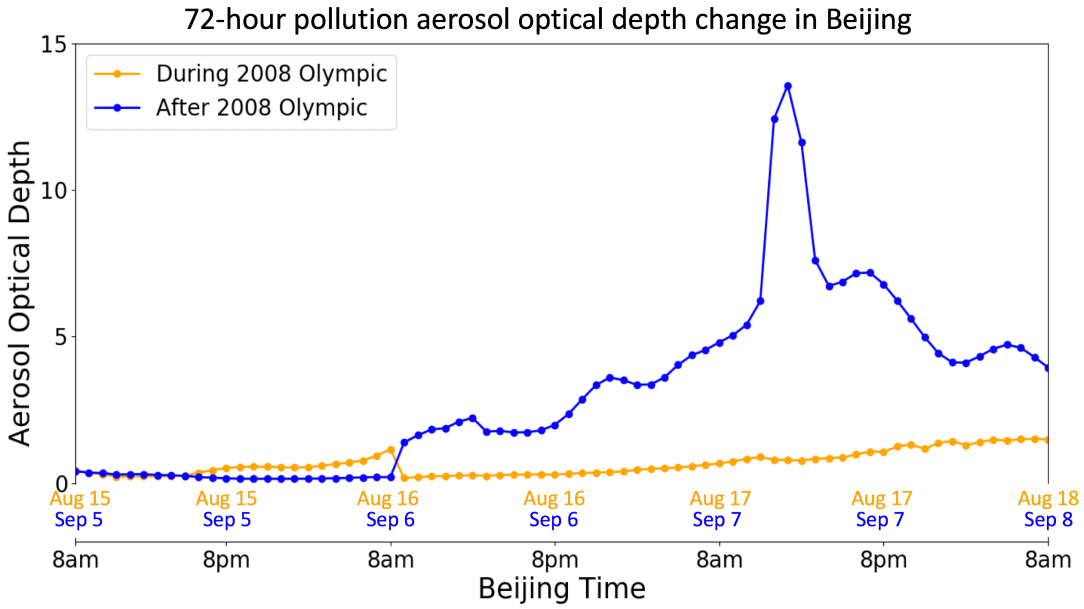

FIGURE 6.15: 72-hour AOD change of pollution aerosol in Beijing during (orange line) and after (blue line) 2008 Summer Olympics. All data presented are from MERRA-2 aerosol reanalysis.

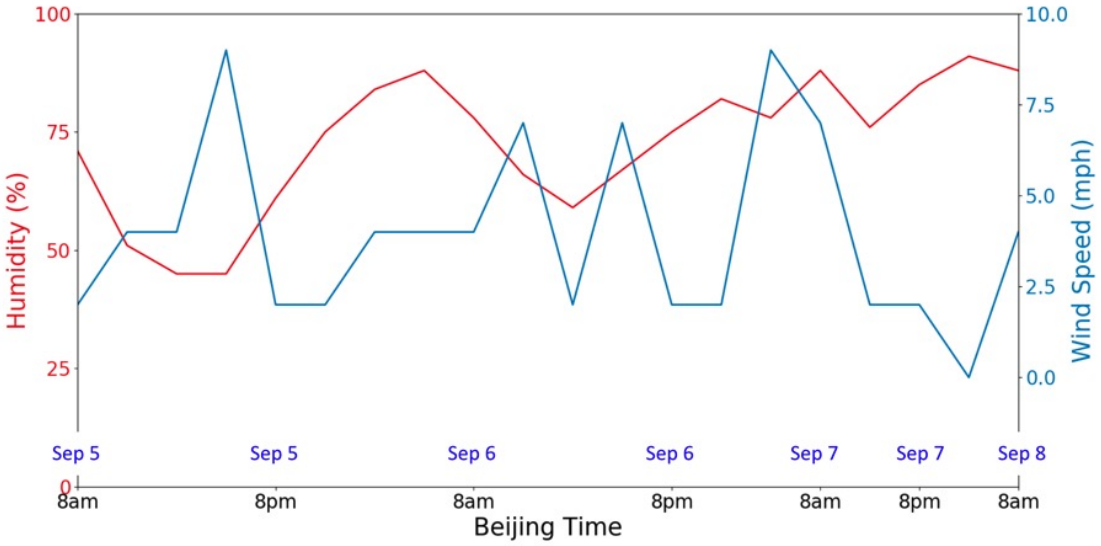

FIGURE 6.16: Historical weather of Beijing from September 5-7, 2008. All date are measured at Beijing Nanyuan Airport Station (Source: Weather Underground).

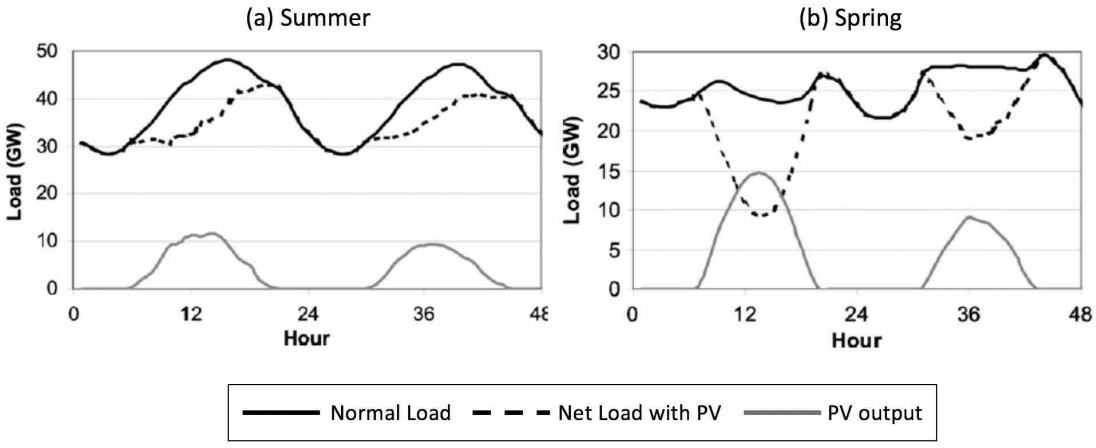

FIGURE 6.17: System load with and without a large (16GW) PV system for (a) two summer days and (b) two spring days (Heal, 2010).

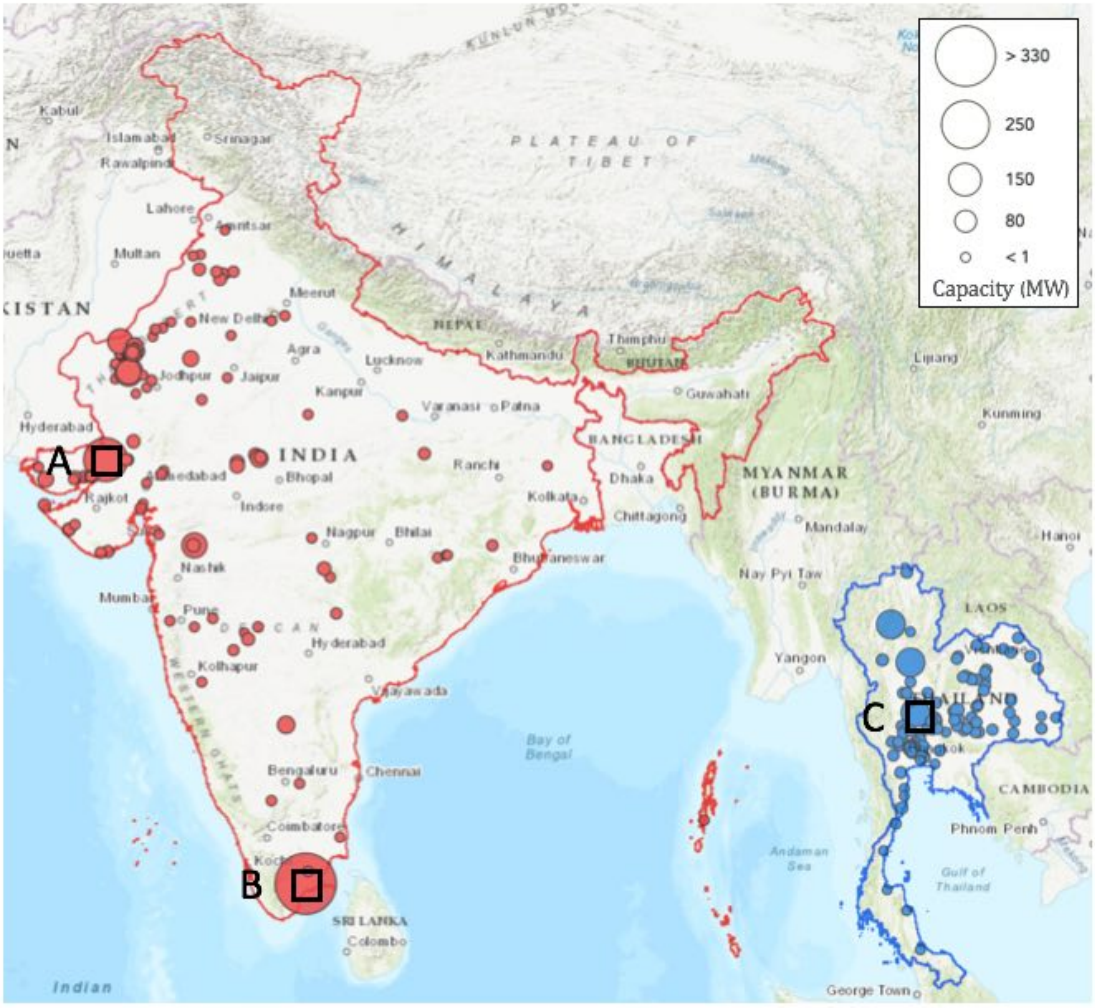

FIGURE 6.18: Solar power plants over India and Thailand. Selected three solar parks: (A) Charanka Solar Park, India; (B) Kamuthi Solar Park, India; (C) Nakhon Sawan Solar Park, Thailand. All data presented are from Global Power Plant Database.

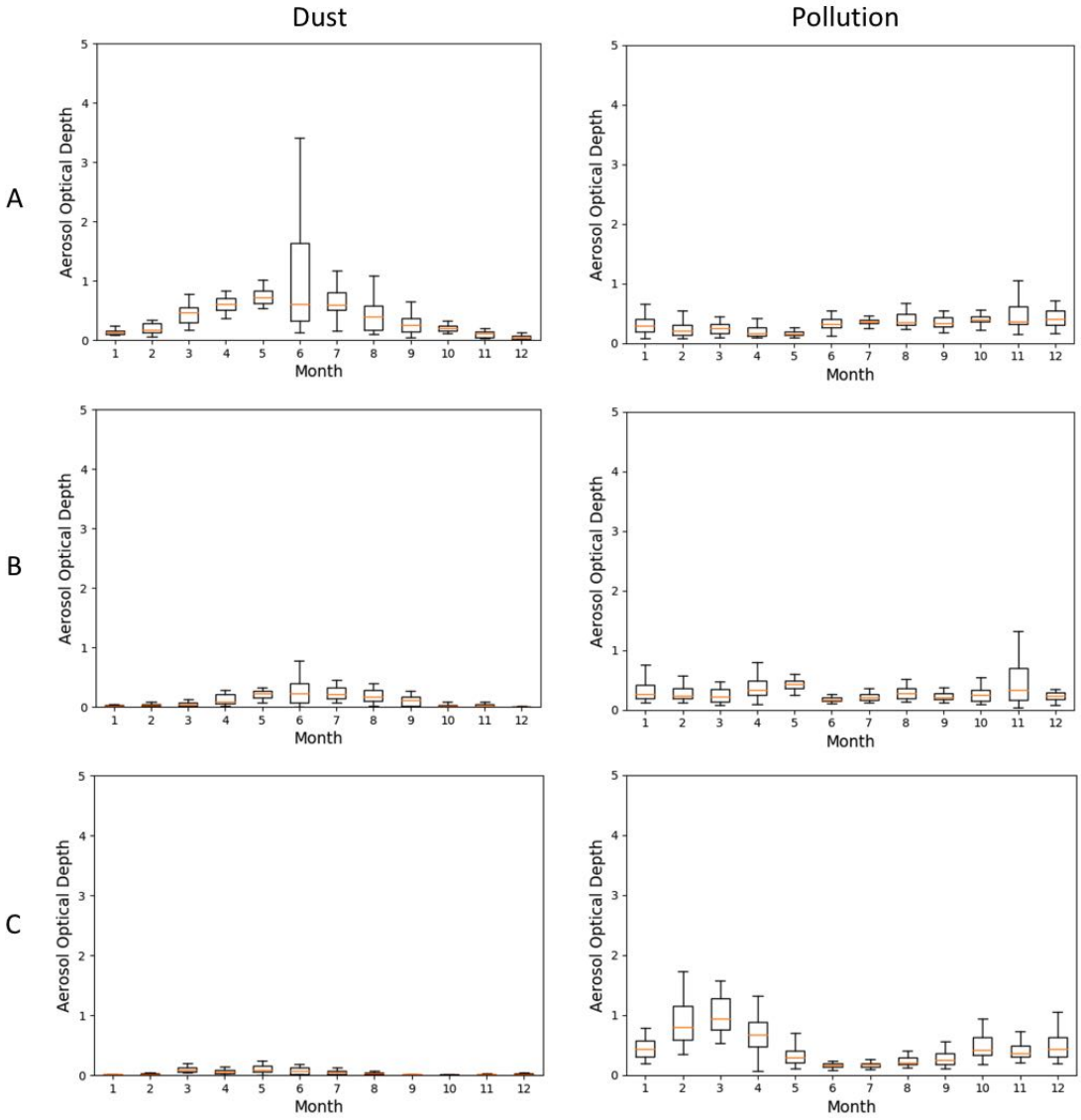

FIGURE 6.19: Monthly AOD of dust and pollution aerosols over three selected solar farms. All data presented are from MERRA-2 aerosol reanalysis, 2008.

Chapter 7

Conclusions and Future Work

This dissertation centers on the role of cloud and aerosol in Earth's energy budget and its implication to realize the full potential of solar energy. Specifically, chapters 3, 4, 5 quantify the effect of cloud type on Earth's energy balance and its radiative influences on atmospheric circulation. Beyond that, chapter 6 focuses on the influence of aerosols on solar energy potential in Asia and its economic impact on solar intermittency. This dissertation addresses these questions primarily through analyzing complimentary satellite data and atmospheric reanalysis. In the following sections, I would first review my dissertation work and then introduce a proposed research plan on estimating rooftop solar energy potential in the United Sates.

7.1 Dissertation Summary

The Earth is a solar powered system that maintains a balance between solar energy reaching the Earth and energy emitted from the Earth back to space. If an energy imbalance situation

occurs, the sea surface temperature will change correspondingly to restore an energy balance. Thus, keeping an eye on Earth's energy budget is important for understanding the link between climate change and global warming. Variations in the Earth's energy budget are associated with clouds because cloud phase, height, thickness, and vertical structure all modulate the way clouds influence the propagation of solar and thermal radiation through the atmosphere. Accurately modeling the sensitivity of Earth's temperature to external forcing, therefore, requires a precise accounting of the radiative feedbacks owing to cloud changes. However, it is challenging for models to represent radiative effects of distinct cloud types, their spatial distributions, and their temporal variability (Calisto et al., 2014).

To provide observational benchmarks for Earth's energy budget in climate models, chapters 3 and 4 quantify radiative influences of nine cloud types distinguished based on their vertical structure defined by spaceborne active observations from CloudSat and CALIPSO satellites. With accurate cloud base information provided by active sensors, chapter 3 goes beyond the top of atmosphere to establish how clouds influence the partitioning of the earth's energy imbalance between the atmosphere and surface (Figure 7.1) that is poorly resolved by passive sensors and models. In fact, more than 90% of the excess energy in the climate system due to increased greenhouse gas concentrations is absorbed at the surface where clouds play a critical role in modulating radiative fluxes. Those estimations on global, annual mean cloud radiative effect at the surface allow more robust insights of how clouds influence the surface energy balance. In addition, chapter 4 explicitly diagnoses radiative contributions from multilayered cloud systems that are often misclassified as thick mid-level clouds in approaches that using passive sensors alone. It is shown that multilayered cloud systems exert the strongest cloud-induced influence on Earth's global energy budget and dominate

atmosphere heating imbalance between the hemispheres.

As multilayered cloud systems substantially modulate the Earth's energy budget, chapter 5 further explores compositions and origins of these clouds with observations from active sensors that can detect cloud vertical structure. Multilayered cloud systems are classified according to the optical depth of their upper-level clouds since they exhibit significantly different radiative effects. It is found that over the globe, most multilayered cloud systems have thin upper-level clouds, but in the tropics and over mid-latitudes, more than 1/3 of the cases contain thick cirrus. Passive sensors may lack the ability to penetrate those thick cirrus and measure the lower level boundary clouds. Quantifying the relative frequencies of these cloud regimes is an important step toward improving their representation in models. Because active sensors can detect deep convective clouds, the radiative effect of single- and multilayered anvil cloud are estimated in addition to isolated upper-level clouds. This helps provide evidence for hypotheses debating cold cloud climate feedbacks. Multilayered anvil clouds are found to contribute a contrast of heating in the upper tropical troposphere and cooling in the extratropical upper troposphere that increase the meridional temperature gradient, thereby enhancing the eddy kinetic energy and increasing the poleward heat transport.

Based on previous chapters on global Earth's energy budget (EEB), chapter 6 focuses on the implication of regional EEB to realize the full potential of solar energy. Similar to clouds, aerosols are associated with attenuation in the atmosphere by scattering and absorbing sunlight. Rapid variations in local aerosol optical depth and aerosol direct radiative effect directly influence solar energy generations from solar farms. This problem is particularly

severe in Asia that has world's largest solar farms but faces atmospheric dimming from fuel combustion and industrial activities (Wild et al., 2005). Li et al. (2017a) evaluates the impact of aerosols on solar photovoltaic (PV) generation in China and finds that aerosol-related annual average reductions have strong impacts in winter. Thus, estimating radiative influences of aerosols on solar farms provides reference for evaluating solar energy output.

Chapter 6 assesses aerosol radiative impacts on solar energy potential in Asia with CloudSat and CALIPSO space-borne observations. It is found that clouds are the dominant factor that modulate solar resources, causing intermittency. But aerosols largely attenuate solar radiation over northern and eastern China during winter and autumn by nearly -20 Wm^{-2} that can be comparable with the impact from clouds. Also, aerosol indirect effect that increases cloud amount is attributed to clouds rather than aerosols, so the real aerosol impact is even larger. Note that this study only calculates aerosol direct radiative effects under clear-sky conditions, aerosols over different types of clouds that weaken the cooling effect from aerosol or cause warming effect over land need to be considered (Matus et al., 2015).

Chapter 6 particularly diagnoses hourly variation of aerosol optical depth over Beijing during and after 2008 Olympic games with MERRA-2 high resolution data. In the case study, the MERRA-2 aerosol reanalysis is able to capture short-term location-based aerosol loadings, indicating hourly solar power availability. Meteorological conditions are found to catalyze air pollution in Beijing, enhancing local aerosol radiative influence. Geographical condition also intensifies the influence of aerosol on solar power over Beijing. In addition, the influence of aerosol on three selected solar farms in India and Thailand is investigated. Both

anthropogenic activities and monsoon dominate the variability of aerosols that decrease solar radiation in India (Pal and Devara, 2012). Crop residue burning significantly reduces solar radiation received at the surface in Thailand (Phairuang et al., 2017). Further studies are needed to access hourly variations of aerosol optical depth over these solar farms to better understand how many base load powers are needed for every hour to compensate the solar intermittency. Base load powers are normally from nuclear or large coal stations, so their outputs cannot be varied easily. Investors would rather reject the solar power than reduce redundant output from its base load stations, meaning that solar power could not be sold even if it were produced. These work on hourly aerosol influences over solar farms will offer new thoughts on saving base load energy resources and decreasing the rejection risk of solar power in electricity market.

7.1.1 Uncertainties

For observation-based results in chapters 3-6, while the vertical structure information provided by spaceborne active sensors provides significant new insights into the role of distinct cloud types in the global energy budget, these data are not without their limitations. The spatial and temporal characteristics of CloudSat and CALIPSO may introduce sampling biases in the results. For example, the diurnal variations in cloud cover are not properly accounted for by the limited twice-daily sampling of the A-Train. Some multilayered clouds may be missed, especially in the tropics, due to the CPR ground-clutter issues and attenuation of the lidar (Protat et al., 2014). Also, these datasets do not provide full global coverage, omitting regions of 82.5°-90°. Uncertainties may also be present in the radiative effects estimated from 2B-FLXHR-LIDAR (2BFLX) owing to cloud detection and cloud microphysical

property retrievals. Liquid water content, surface temperature, and lower-troposphere humidity, in particular, exert strong influences on surface flux estimates (Henderson et al., 2013). In addition, Mülmenstädt et al. (2018) recently reported that significant regional errors may exist in downwelling LW fluxes due to uncertainty in cloud base heights. Comprehensive set of sensitivity studies can be found in Henderson et al. (2013) and Matus and L'Ecuyer (2017).

Model-based results shown in chapter 6 also have limitations. Comparison of MERRA-2 to observations shows that AOD and its vertical distribution agree well with satellite and aircraft observations (Buchard et al., 2017). However, the assimilation only constrains AOD and does not constrain other aspects like speciation. The emission inventory causes uncertainty over regions like Asia where anthropogenic contributions are large. Due to the uncertainty in anthropogenic aerosols in MERRA-2, it is limited for estimating the aerosol forcing. Also, the coupled GOCART model only has limited aerosol species, unlike the Model for Simulating Aerosol Interactions and Chemistry (MOSAIC) with a dynamic gas-particle partitioning module that can treat detailed aerosol species including sulfate, methanesulfonate, nitrate, chloride, carbonate, ammonium, sodium, calcium, black carbon, primary organic mass, liquid water and other inorganic mass (Zaveri et al., 2008). The comparison on AOD derived from CALIPSO observations and MERRA-2 reanalysis is too general and provides very limited information. More detailed aerosol classification need to be considered into future research.

7.2 Future Work

For future work, I am interested in accessing the influence of urban emission on rooftop solar energy potential with Geographic Information Systems (GIS) technology. Renewable energy plays an important role in providing energy service in a sustainable manner. Across the world, solar energy capacity has increased dramatically due to falling prices, governmental regulations, and environmental concerns over greenhouse gas emissions from fossil fuel generators. The United States, as a large and populous country with abundant solar resources, is experiencing an increasing demand of electricity that requires rooftop solar energy capacity to help meet peak electricity demand and reduce delivery cost of energy transmission and distribution. As reported by Gagnon et al. (2016), most states in the U.S. are suitable for rooftop solar PV due to less tree canopy coverage, but solar energy market in some states still remains untapped due to gaps in public perceptions and information (Rai and Beck, 2015). The goal of this future research is to bridge the gap by offering insights into rooftop solar energy potential in the United Sates.

7.2.1 Assessing the influence of polluted aerosols on solar radiation in the U.S. with satellite data

Solar energy received at a particular place is intermittent: solar generators only produce energy when the sun is shining. Rapid variations in local aerosol substantially reduce the amount of irradiance reaching the Earth's surface. Thus, estimating the radiative influence of aerosols on solar energy potential has emerged as a challenge to make solar energy more reliable. To approach this challenge, I will use complementary satellite observations from CloudSat and CALIPSO that provide unprecedented information on aerosol vertical

structures. Aerosol types matter for regions with large rooftop space but facing different air pollutants. Aerosol particles like black carbon directly absorb sunlight while sulfate aerosols scatter sunlight. CloudSat and CALIPSO satellite data allow more robust estimates of how aerosols influence surface solar radiation under both clear-sky and cloudy-sky conditions (Matus et al., 2015). Note that this study can make the most of the CloudSat data that are often unused in atmospheric science research since CloudSat only operates during daytime after 2011 due to battery malfunction. Considering spatial and temporal limitations of polar-orbit satellites, ground observation and geostationary satellite data from GOES will be used to estimate uncertainties (Xia et al., 2018, 2017). The main outcome of this first aim is to provide observational estimates of surface solar radiation in the United States. Meanwhile, investigate the role of aerosol type on surface energy budget.

7.2.2 Estimating rooftop solar energy potential in the U.S. with GIS technology

The second aim focuses on extracting solar energy potential derived from the first aim to the U.S. building footprints provided by Microsoft open data with GIS technology. I will classify the U.S. building footprints into nine categories according to buildings heights (low, middle, high) and densities (low, middle, high). The reason to separate building heights is that new photovoltaic technology is very likely to make "solar windows" generating solar energy a reality in the future (Luo et al., 2018). Also, solar PV panels can be installed on the sides of buildings. Different building densities are separated is because building shade substantially affects light environment compared to fully exposed conditions (Tan and Ismail, 2014). In this proposed study I will be able to estimate nation-wide rooftop PV potential in the United States. The outcome will be used to identify optimal PV rooftops with considering spatial

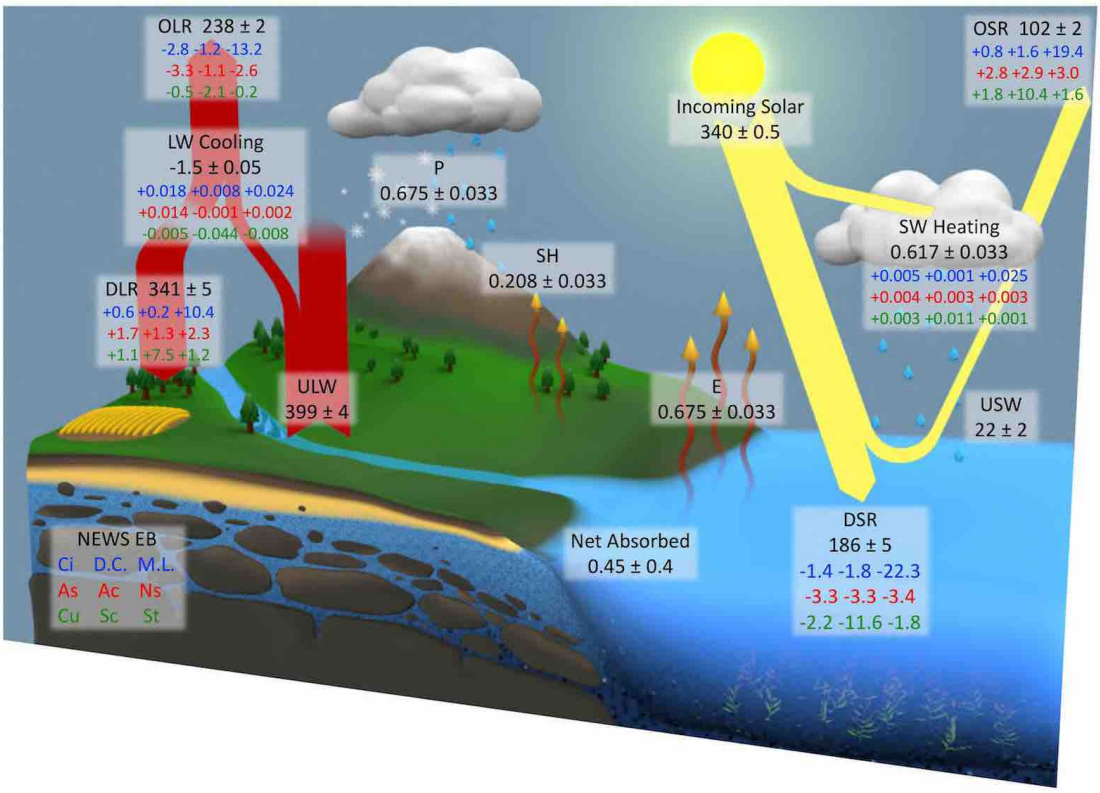

FIGURE 7.1: The observed annual mean global energy budget of Earth after applying relevant energy and water cycle balance constraints adapted from L'Ecuyer et al. (2015). The radiative effects of nine 2BCLD vertical cloud types are super-imposed in colored text based on the results of Chapter 3. All fluxes are reported in W m^{-2} while heating due to precipitation, P, evaporation, E, sensible heating, SH, and radiation (LW&SW) are reported in K day^{-1}. Heating rate in all subsequent figures are similarly reported in K day^{-1} but can be converted to W m^{-2} by multiplying by 120.

variation of aerosol. The ultimate goal of the second aim is to offer new thoughts for future energy planning from an atmospheric science perspective. The methodologies and findings can be expanded to multi-scale spatial analysis from country-state-county-city-neighborhood to assist policy-decision processes on the use of renewable energy in the United States.

Bibliography

Aayog, N., 2015: Report on india's renewable electricity roadmap 2030: Toward accelerated renewable electricity deployment. *NITI Ayog. Government of India, Tech. Rep*.

Ackerman, A. S., O. Toon, D. Stevens, A. Heymsfield, V. Ramanathan, and E. Welton, 2000: Reduction of tropical cloudiness by soot. *Science*, **288**, 1042–1047.

Ackerman, S., R. Holz, R. Frey, E. Eloranta, B. Maddux, and M. McGill, 2008: Cloud detection with modis. part ii: validation. *Journal of Atmospheric and Oceanic Technology*, **25**, 1073–1086.

Ackerman, T. P. and G. M. Stokes, 2003: The atmospheric radiation measurement program. *Physics Today*, **56**, doi:10.1063/1.1554135.

Adinoyi, M. J. and S. A. Said, 2013: Effect of dust accumulation on the power outputs of solar photovoltaic modules. *Renewable energy*, **60**, 633–636.

Albrecht, B. A., 1989: Aerosols, cloud microphysics, and fractional cloudiness. *Science*, **245**, 1227–1230.

Allan, R. P., 2011: Combining satellite data and models to estimate cloud radiative effect at the surface and in the atmosphere. *Meteorological applications*, **18**, 324–333.

Arakawa, A., 1975: Modelling clouds and cloud processes for use in climate models. *WMO The Phys. Basis of Climate and Climate Modelling p 183-197(SEE N 76-19675 10-47)*.

Atwater, M. A., 1970: Planetary albedo changes due to aerosols. *Science*, **170**, 64–66.

Austin, R. and N. Wood, 2018: Level 2b radar-only cloud water content (2b-cwc-ro) process description and interface control document, product version p1 r05. *NASA JPL CloudSat project document revision*.

Balkanski, Y., M. Schulz, T. Claquin, and S. Guibert, 2007: Reevaluation of mineral aerosol radiative forcings suggests a better agreement with satellite and aeronet data. *Atmospheric Chemistry and Physics*, **7**, 81–95.

Bell, T. L., D. Rosenfeld, K.-M. Kim, J.-M. Yoo, M.-I. Lee, and M. Hahnenberger, 2008: Midweek increase in us summer rain and storm heights suggests air pollution invigorates rainstorms. *Journal of Geophysical Research: Atmospheres*, **113**.

Bellouin, N., J. Quaas, J.-J. Morcrette, and O. Boucher, 2013: Estimates of aerosol radiative forcing from the macc re-analysis. *Atmospheric Chemistry and Physics*, **13**, 2045–2062.

Bony, S., K.-M. Lau, and Y. C. Sud, 1997: Sea surface temperature and large-scale circulation influences on tropical greenhouse effect and cloud radiative forcing. *Journal of Climate*, **10**, 2055–2077, doi:10.1175/1520-0442(1997)010¡2055:SSTALS¿2.0.CO;2.

Bony, S., B. Stevens, D. Coppin, T. Becker, K. A. Reed, A. Voigt, and B. Medeiros, 2016: Thermodynamic control of anvil cloud amount. *Proceedings of the National Academy of Sciences*, **113**, 8927–8932.

Bony, S., B. Stevens, D. M. Frierson, C. Jakob, M. Kageyama, R. Pincus, T. G. Shepherd, S. C. Sherwood, A. P. Siebesma, A. H. Sobel, et al., 2015: Clouds, circulation and climate sensitivity. *Nature Geoscience*, **8**, 261.

Booth, B. B., N. J. Dunstone, P. R. Halloran, T. Andrews, and N. Bellouin, 2012: Aerosols implicated as a prime driver of twentieth-century north atlantic climate variability. *Nature*, **484**, 228.

Boucher, O., D. Randall, P. Artaxo, C. Bretherton, G. Feingold, P. Forster, V.-M. Kerminen, Y. Kondo, H. Liao, U. Lohmann, et al., 2013: Clouds and aerosols. *Climate change 2013: the physical science basis. Contribution of Working Group I to the Fifth Assessment Report of the Intergovernmental Panel on Climate Change*, Cambridge University Press, 571–657.

Buchard, V., C. Randles, A. Da Silva, A. Darmenov, P. Colarco, R. Govindaraju, R. Ferrare, J. Hair, A. Beyersdorf, L. Ziemba, et al., 2017: The merra-2 aerosol reanalysis, 1980 onward. part ii: Evaluation and case studies. *Journal of Climate*, **30**, 6851–6872.

Calisto, M., D. Folini, M. Wild, and L. Bengtsson, 2014: Cloud radiative forcing intercomparison between fully coupled cmip5 models and ceres satellite data. *Ann. Geophys*, **32**, 793–807.

Cao, C., F. J. De Luccia, X. Xiong, R. Wolfe, and F. Weng, 2013: Early on-orbit performance of the visible infrared imaging radiometer suite onboard the suomi national polar-orbiting partnership (s-npp) satellite. *IEEE Transactions on Geoscience and Remote Sensing*, **52**, 1142–1156.

Ceppi, P. and D. L. Hartmann, 2016: Clouds and the atmospheric circulation response to warming. *Journal of Climate*, **29**, 783–799.

Ceppi, P., Y.-T. Hwang, D. M. Frierson, and D. L. Hartmann, 2012: Southern hemisphere jet latitude biases in cmip5 models linked to shortwave cloud forcing. *Geophysical Research Letters*, **39**.

Cesana, G., D. Waliser, D. Henderson, T. L'Ecuyer, X. Jiang, and J.-L. Li, 2019: The vertical structure of radiative heating rates: A multimodel evaluation using a-train satellite observations. *Journal of Climate*, **32**, 1573–1590.

Cess, R. D., G. Potter, J. Blanchet, G. Boer, A. Del Genio, M. Deque, V. Dymnikov, V. Galin, W. Gates, S. Ghan, et al., 1990: Intercomparison and interpretation of climate feedback processes in 19 atmospheric general circulation models. *Journal of Geophysical Research: Atmospheres*, **95**, 16601–16615.

Cess, R. D., G. Potter, J. Blanchet, G. Boer, S. Ghan, J. Kiehl, H. Le Treut, Z.-X. Li, X.-Z. Liang, J. Mitchell, et al., 1989: Interpretation of cloud-climate feedback as produced by 14 atmospheric general circulation models. *Science*, **245**, 513–516.

Chan, M. A. and J. C. Comiso, 2011: Cloud features detected by modis but not by cloudsat and caliop. *Geophysical Research Letters*, **38**.

Chand, D., R. Wood, T. Anderson, S. Satheesh, and R. Charlson, 2009: Satellite-derived direct radiative effect of aerosols dependent on cloud cover. *Nature Geoscience*, **2**, 181.

Chen, T., W. B. Rossow, and Y. Zhang, 2000: Radiative effects of cloud-type variations. *Journal of climate*, **13**, 264–286.

Chepfer, H., S. Bony, D. Winker, M. Chiriaco, J.-L. Dufresne, and G. Sèze, 2008: Use of calipso lidar observations to evaluate the cloudiness simulated by a climate model. *Geophysical Research Letters*, **35**.

Chin, M., P. Ginoux, S. Kinne, O. Torres, B. N. Holben, B. N. Duncan, R. V. Martin, J. A. Logan, A. Higurashi, and T. Nakajima, 2002: Tropospheric aerosol optical thickness from the gocart model and comparisons with satellite and sun photometer measurements. *Journal of the atmospheric sciences*, **59**, 461–483.

Chin, M., R. B. Rood, S.-J. Lin, J.-F. Müller, and A. M. Thompson, 2000: Atmospheric sulfur cycle simulated in the global model gocart: Model description and global properties. *Journal of Geophysical Research: Atmospheres*, **105**, 24671–24687.

Choi, Y.-S., W. Kim, S.-W. Yeh, H. Masunaga, M.-J. Kwon, H.-S. Jo, and L. Huang, 2017: Revisiting the iris effect of tropical cirrus clouds with trmm and a-train satellite data. *Journal of Geophysical Research: Atmospheres*, **122**, 5917–5931.

Christensen, M. W., G. G. Carrió, G. L. Stephens, and W. R. Cotton, 2013: Radiative impacts of free-tropospheric clouds on the properties of marine stratocumulus. *Journal of the atmospheric sciences*, **70**, 3102–3118.

Chung, E.-S. and B. J. Soden, 2017: Hemispheric climate shifts driven by anthropogenic aerosol–cloud interactions. *Nature Geoscience*, **10**, 566.

Comstock, J. M., T. P. Ackerman, and G. G. Mace, 2002: Ground-based lidar and radar remote sensing of tropical cirrus clouds at nauru island: Cloud statistics and radiative impacts. *Journal of Geophysical Research: Atmospheres*, **107**, AAC–16.

Daloz, A., E. Nelson, T. L'Ecuyer, A. Rapp, and L. Sun, 2018: Assessing the coupled influences of clouds on the atmospheric energy and water cycles in reanalyses with a-train observations. *Journal of Climate*, **31**, 8241–8264.

Davis, S. M., L. M. Avallone, E. M. Weinstock, C. H. Twohy, J. B. Smith, and G. L. Kok, 2007: Comparisons of in situ measurements of cirrus cloud ice water content. *Journal of Geophysical Research: Atmospheres*, **112**.

Deng, M., G. G. Mace, Z. Wang, and R. P. Lawson, 2013: Evaluation of several a-train ice cloud retrieval products with in situ measurements collected during the sparticus campaign. *Journal of Applied Meteorology and Climatology*, **52**, 1014–1030.

Dessler, A., 2013: Observations of climate feedbacks over 2000–10 and comparisons to climate models. *Journal of Climate*, **26**, 333–342.

Diner, D. J., J. C. Beckert, T. H. Reilly, C. J. Bruegge, J. E. Conel, R. A. Kahn, J. V. Martonchik, T. P. Ackerman, R. Davies, S. A. Gerstl, et al., 1998: Multi-angle imaging spectroradiometer (misr) instrument description and experiment overview. *IEEE Transactions on Geoscience and Remote Sensing*, **36**, 1072–1087.

Donohoe, A., J. Marshall, D. Ferreira, and D. Mcgee, 2013: The relationship between itcz location and cross-equatorial atmospheric heat transport: From the seasonal cycle to the last glacial maximum. *Journal of Climate*, **26**, 3597–3618.

Dubovik, O., B. Holben, T. F. Eck, A. Smirnov, Y. J. Kaufman, M. D. King, D. Tanré, and I. Slutsker, 2002: Variability of absorption and optical properties of key aerosol types observed in worldwide locations. *Journal of the atmospheric sciences*, **59**, 590–608.

Dubovik, O., A. Smirnov, B. Holben, M. King, Y. Kaufman, T. Eck, and I. Slutsker, 2000: Accuracy assessments of aerosol optical properties retrieved from aerosol robotic network (aeronet) sun and sky radiance measurements. *Journal of Geophysical Research: Atmospheres*, **105**, 9791–9806.

Dufresne, J.-L. and S. Bony, 2008: An assessment of the primary sources of spread of global warming estimates from coupled atmosphere–ocean models. *Journal of Climate*, **21**, 5135–5144.

Fasullo, J. T. and K. E. Trenberth, 2008: The annual cycle of the energy budget. part ii: Meridional structures and poleward transports. *Journal of Climate*, **21**, 2313–2325.

Feng, F. and K. Wang, 2019: Does the modern-era retrospective analysis for research and applications-2 aerosol reanalysis introduce an improvement in the simulation of surface solar radiation over china? *International Journal of Climatology*, **39**, 1305–1318.

Forster, P., V. Ramaswamy, P. Artaxo, T. Berntsen, R. Betts, D. W. Fahey, J. Haywood, J. Lean, D. C. Lowe, G. Myhre, et al., 2007: Changes in atmospheric constituents and in radiative forcing. chapter 2. *Climate Change 2007. The Physical Science Basis*, Cambridge University Press, 129–234.

Frierson, D. M. and Y.-T. Hwang, 2012: Extratropical influence on itcz shifts in slab ocean simulations of global warming. *Journal of Climate*, **25**, 720–733.

Frierson, D. M., Y.-T. Hwang, N. S. Fučkar, R. Seager, S. M. Kang, A. Donohoe, E. A. Maroon, X. Liu, and D. S. Battisti, 2013: Contribution of ocean overturning circulation to tropical rainfall peak in the northern hemisphere. *Nature Geoscience*, **6**, 940–944.

Fu, R., A. D. Del Genio, W. B. Rossow, and W. T. Liu, 1992: Cirrus-cloud thermostat for tropical sea surface temperatures tested using satellite data. *Nature*, **358**, 394.

Fueglistaler, S., A. Dessler, T. Dunkerton, I. Folkins, Q. Fu, and P. W. Mote, 2009: Tropical tropopause layer. *Reviews of Geophysics*, **47**.

Gagnon, P., R. Margolis, J. Melius, C. Phillips, and R. Elmore, 2016: Rooftop solar photovoltaic technical potential in the united states. a detailed assessment. Technical report, National Renewable Energy Lab.(NREL), Golden, CO (United States).

Garratt, J., 2001: Clear-sky longwave irradiance at the earth's surface—evaluation of climate models. *Journal of climate*, **14**, 1647–1670.

Ginoux, P., M. Chin, I. Tegen, J. M. Prospero, B. Holben, O. Dubovik, and S.-J. Lin, 2001: Sources and distributions of dust aerosols simulated with the gocart model. *Journal of Geophysical Research: Atmospheres*, **106**, 20255–20273.

Ginoux, P., L. Clarisse, C. Clerbaux, P.-F. Coheur, O. Dubovik, N. Hsu, and M. V. Damme, 2012: Mixing of dust and nh 3 observed globally over anthropogenic dust sources. *Atmospheric chemistry and physics*, **12**, 7351–7363.

Gleckler, P., D. Randall, G. Boer, R. Colman, M. Dix, V. Galin, M. Helfand, J. Kiehl, A. Kitoh, W. Lau, et al., 1995: Cloud-radiative effects on implied oceanic energy transports as simulated by atmospheric general circulation models. *Geophysical research letters*, **22**, 791–794.

Gupta, S. K., N. A. Ritchey, A. C. Wilber, C. H. Whitlock, G. G. Gibson, and P. W. Stackhouse Jr, 1999: A climatology of surface radiation budget derived from satellite data. *Journal of Climate*, **12**, 2691–2710.

Hahn, C. J. and S. G. Warren, 1999: *Extended edited synoptic cloud reports from ships and land stations over the globe, 1952-1996*. Environmental Sciences Division, Office of Biological and Environmental Research, US Department of Energy.

Haladay, T. and G. Stephens, 2009: Characteristics of tropical thin cirrus clouds deduced from joint cloudsat and calipso observations. *Journal of Geophysical Research: Atmospheres*, **114**.

Ham, S.-H., S. Kato, F. G. Rose, D. Winker, T. L'Ecuyer, G. G. Mace, D. Painemal, S. Sun-Mack, Y. Chen, and W. F. Miller, 2017: Cloud occurrences and cloud radiative effects (cres) from ceres-calipso-cloudsat-modis (cccm) and cloudsat radar-lidar (rl) products. *Journal of Geophysical Research: Atmospheres*, **122**, 8852–8884.

Hang, Y., T. S. L'Ecuyer, D. S. Henderson, A. V. Matus, and Z. Wang, 2019: Reassessing the role of cloud type in earth's energy balance after a decade of active spaceborne observations. part ii: Atmospheric heating. *Journal of Climate*.

Harrison, E. F., P. Minnis, B. R. Barkstrom, V. Ramanathan, R. D. Cess, and G. G. Gibson, 1990: Seasonal variation of cloud radiative forcing derived from the earth radiation budget experiment. *Journal of Geophysical Research: Atmospheres*, **95**, 18687–18703, doi:10.1029/JD095iD11p18687.

Harrop, B. E. and D. L. Hartmann, 2012: Testing the role of radiation in determining tropical cloud-top temperature. *Journal of Climate*, **25**, 5731–5747.

— 2016: The role of cloud radiative heating in determining the location of the itcz in aquaplanet simulations. *Journal of Climate*, **29**, 2741–2763.

Hartmann, D., V. Ramanathan, A. Berroir, and G. Hunt, 1986: Earth radiation budget data and climate research. *Reviews of Geophysics*, **24**, 439–468.

Hartmann, D. L. and K. Larson, 2002: An important constraint on tropical cloud-climate feedback. *Geophysical Research Letters*, **29**, 12–1.

Hartmann, D. L. and M. L. Michelsen, 1993: Large-scale effects on the regulation of tropical sea surface temperature. *Journal of Climate*, **6**, 2049–2062.

— 2002: No evidence for iris. *Bulletin of the American Meteorological Society*, **83**, 249–254.

Hartmann, D. L., M. E. Ockert-Bell, and M. L. Michelsen, 1992: The effect of cloud type on earth's energy balance: Global analysis. *Journal of Climate*, **5**, 1281–1304.

Hartmann, D. L. and D. A. Short, 1980: On the use of earth radiation budget statistics for studies of clouds and climate. *Journal of the Atmospheric Sciences*, **37**, 1233–1250.

Haynes, J. M., C. Jakob, W. B. Rossow, G. Tselioudis, and J. Brown, 2011: Major characteristics of southern ocean cloud regimes and their effects on the energy budget. *Journal of Climate*, **24**, 5061–5080.

Haynes, J. M., T. S. L'Ecuyer, G. L. Stephens, S. D. Miller, C. Mitrescu, N. B. Wood, and S. Tanelli, 2009: Rainfall retrieval over the ocean with spaceborne w-band radar. *Journal of Geophysical Research: Atmospheres*, **114**.

Haynes, J. M., T. H. Vonder Haar, T. L'Ecuyer, and D. Henderson, 2013: Radiative heating characteristics of earth's cloudy atmosphere from vertically resolved active sensors. *Geophysical Research Letters*, **40**, 624–630.

Heal, G., 2010: Reflections—the economics of renewable energy in the united states. *Review of Environmental Economics and Policy*, **4**, 139–154.

Henderson, D. S., T. L'Ecuyer, G. Stephens, P. Partain, and M. Sekiguchi, 2013: A multisensor perspective on the radiative impacts of clouds and aerosols. *Journal of Applied Meteorology and Climatology*, **52**, 853–871.

Herman, J., P. Bhartia, O. Torres, C. Hsu, C. Seftor, and E. Celarier, 1997: Global distribution of uv-absorbing aerosols from nimbus 7/toms data. *Journal of Geophysical Research: Atmospheres*, **102**, 16911–16922.

Hoff, T., C. Lenox, N. Miller, Y. huei Wan, R. George, J. Stein, B. Kroposki, A. D. Mills, M. Ahlstrom, M. Brower, and A. Ellis, 2009: Understanding variability and uncertainty of photovoltaics for integration with the electric power system. Technical report, LBNL, Berkeley.

Holben, B. N., T. F. Eck, I. Slutsker, D. Tanre, J. Buis, A. Setzer, E. Vermote, J. A. Reagan, Y. Kaufman, T. Nakajima, et al., 1998: Aeronet—a federated instrument network and data archive for aerosol characterization. *Remote sensing of environment*, **66**, 1–16.

Houghton, J. T., L. Meiro Filho, B. A. Callander, N. Harris, A. Kattenburg, and K. Maskell, 1996: Climate change 1995: the science of climate change. *Climatic Change*, 584.

Huffman, G. J., R. F. Adler, P. Arkin, A. Chang, R. Ferraro, A. Gruber, J. Janowiak, A. McNab, B. Rudolf, and U. Schneider, 1997: The global precipitation climatology project (gpcp) combined precipitation dataset. *Bulletin of the American Meteorological Society*, **78**, 5–20.

Hwang, Y.-T. and D. M. Frierson, 2013: Link between the double-intertropical convergence zone problem and cloud biases over the southern ocean. *Proceedings of the National Academy of Sciences*, **110**, 4935–4940.

Jakub, F. and B. Mayer, 2015: A three-dimensional parallel radiative transfer model for atmospheric heating rates for use in cloud resolving models—the tenstream solver. *Journal of Quantitative Spectroscopy and Radiative Transfer*, **163**, 63–71.

Jiang, X., D. E. Waliser, P. K. Xavier, J. Petch, N. P. Klingaman, S. J. Woolnough, B. Guan, G. Bellon, T. Crueger, C. DeMott, et al., 2015: Vertical structure and physical processes of the madden-julian oscillation: Exploring key model physics in climate simulations. *Journal of Geophysical Research: Atmospheres*, **120**, 4718–4748.

Jinhuan, Q. and Y. Liquan, 2000: Variation characteristics of atmospheric aerosol optical depths and visibility in north china during 1980–1994. *Atmospheric Environment*, **34**, 603–609.

Johansson, E., A. Devasthale, T. L'Ecuyer, A. M. Ekman, and M. Tjernström, 2015: The vertical structure of cloud radiative heating over the indian subcontinent during summer monsoon. *Atmospheric Chemistry and Physics*, **15**, 11557–11570.

Johnson, R. H. and G. S. Young, 1983: Heat and moisture budgets of tropical mesoscale anvil clouds. *Journal of the Atmospheric Sciences*, **40**, 2138–2147.

Kacenelenbogen, M., J. Redemann, M. Vaughan, A. Omar, P. Russell, S. Burton, R. Rogers, R. Ferrare, and C. Hostetler, 2014: An evaluation of caliop/calipso's aerosol-above-cloud detection and retrieval capability over north america. *Journal of Geophysical Research: Atmospheres*, **119**, 230–244.

Kahn, R. A., B. J. Gaitley, J. V. Martonchik, D. J. Diner, K. A. Crean, and B. Holben, 2005: Multiangle imaging spectroradiometer (misr) global aerosol optical depth validation based on 2 years of coincident aerosol robotic network (aeronet) observations. *Journal of Geophysical Research: Atmospheres*, **110**.

Kannan, N. and D. Vakeesan, 2016: Solar energy for future world:-a review. *Renewable and Sustainable Energy Reviews*, **62**, 1092–1105.

Kato, S., N. G. Loeb, D. A. Rutan, F. G. Rose, S. Sun-Mack, W. F. Miller, and Y. Chen, 2012: Uncertainty estimate of surface irradiances computed with modis-, calipso-, and cloudsat-derived cloud and aerosol properties. *Surveys in geophysics*, **33**, 395–412.

Kato, S., F. G. Rose, and T. P. Charlock, 2005: Computation of domain-averaged irradiance using satellite-derived cloud properties. *Journal of Atmospheric and Oceanic Technology*, **22**, 146–164.

Kato, S., S. Sun-Mack, W. F. Miller, F. G. Rose, Y. Chen, P. Minnis, and B. A. Wielicki, 2010: Relationships among cloud occurrence frequency, overlap, and effective thickness derived from calipso and cloudsat merged cloud vertical profiles. *Journal of Geophysical Research: Atmospheres*, **115**.

Kay, J., B. Hillman, S. Klein, Y. Zhang, B. Medeiros, R. Pincus, A. Gettelman, B. Eaton, J. Boyle, R. Marchand, et al., 2012: Exposing global cloud biases in the community atmosphere model (cam) using satellite observations and their corresponding instrument simulators. *Journal of Climate*, **25**, 5190–5207.

Keil, A. and J. M. Haywood, 2003: Solar radiative forcing by biomass burning aerosol particles during safari 2000: A case study based on measured aerosol and cloud properties. *Journal of Geophysical Research: Atmospheres*, **108**.

Khairoutdinov, M. and K. Emanuel, 2013: Rotating radiative-convective equilibrium simulated by a cloud-resolving model. *Journal of Advances in Modeling Earth Systems*, **5**, 816–825.

Kiehl, J. and B. Briegleb, 1993: The relative roles of sulfate aerosols and greenhouse gases in climate forcing. *Science*, **260**, 311–314.

Kiehl, J. T., 1994: Clouds and their effects on the climate system. *Physics Today*, **47**, 36–42.

Kim, M.-H., A. H. Omar, J. L. Tackett, M. A. Vaughan, D. M. Winker, C. R. Trepte, Y. Hu, Z. Liu, L. R. Poole, M. C. Pitts, et al., 2018: The calipso version 4 automated aerosol classification and lidar ratio selection algorithm. *Atmospheric Measurement Techniques*, **11**.

King, M. D., Y. J. Kaufman, D. Tanré, and T. Nakajima, 1999: Remote sensing of tropospheric aerosols from space: Past, present, and future. *Bulletin of the American Meteorological society*, **80**, 2229–2260.

Klein, S. A. and D. L. Hartmann, 1993: The seasonal cycle of low stratiform clouds. *Journal of Climate*, **6**, 1587–1606.

Koren, I., Y. J. Kaufman, L. A. Remer, and J. V. Martins, 2004: Measurement of the effect of amazon smoke on inhibition of cloud formation. *Science*, **303**, 1342–1345.

Kuang, Z. and D. L. Hartmann, 2007: Testing the fixed anvil temperature hypothesis in a cloud-resolving model. *Journal of Climate*, **20**, 2051–2057.

Kubar, T. L., D. L. Hartmann, and R. Wood, 2007: Radiative and convective driving of tropical high clouds. *Journal of Climate*, **20**, 5510–5526.

Kumar, R., M. Barth, G. Pfister, M. Naja, and G. Brasseur, 2013: Wrf-chem simulations of a typical pre-monsoon dust storm in northern india: influences on aerosol optical properties and radiation budget. *Atmospheric Chemistry & Physics Discussions*, **13**.

Lau, K.-M. and K.-M. Kim, 2006: Observational relationships between aerosol and asian monsoon rainfall, and circulation. *Geophysical research letters*, **33**.

L'Ecuyer, T. S., H. K. Beaudoing, M. Rodell, W. Olson, B. Lin, S. Kato, C. A. Clayson, E. Wood, J. Sheffield, R. Adler, et al., 2015: The observed state of the energy budget in the early twenty-first century. *Journal of Climate*, **28**, 8319–8346.

L'Ecuyer, T. S., W. Berg, J. Haynes, M. Lebsock, and T. Takemura, 2009: Global observations of aerosol impacts on precipitation occurrence in warm maritime clouds. *Journal of Geophysical Research: Atmospheres*, **114**.

L'Ecuyer, T. S., Y. Hang, A. V. Matus, and Z. Wang, 2019: Reassessing the role of cloud type in earth's energy balance after a decade of active spaceborne observations. part i: Top of atmosphere and surface. *Journal of Climate*.

L'Ecuyer, T. S. and J. H. Jiang, 2010: Touring the atmosphere aboard the a-train. *Phys. Today*, **63**, 36–41.

L'Ecuyer, T. S. and G. L. Stephens, 2003: The tropical oceanic energy budget from the trmm perspective. part i: Algorithm and uncertainties. *Journal of climate*, **16**, 1967–1985.

L'Ecuyer, T. S., N. B. Wood, T. Haladay, G. L. Stephens, and P. W. Stackhouse, 2008: Impact of clouds on atmospheric heating based on the r04 cloudsat fluxes and heating rates data set. *Journal of Geophysical Research: Atmospheres*, **113**.

Lee, M.-I., I.-S. Kang, J.-K. Kim, and B. E. Mapes, 2001: Influence of cloud-radiation interaction on simulating tropical intraseasonal oscillation with an atmospheric general circulation model. *Journal of Geophysical Research: Atmospheres*, **106**, 14219–14233.

Lee, S. J., M.-H. Ahn, and S.-R. Chung, 2017: Atmospheric profile retrieval algorithm for next generation geostationary satellite of korea and its application to the advanced himawari imager. *Remote Sensing*, **9**, 1294.

Li, J., Y. Yi, P. Minnis, J. Huang, H. Yan, Y. Ma, W. Wang, and J. K. Ayers, 2011: Radiative effect differences between multi-layered and single-layer clouds derived from ceres, calipso, and cloudsat data. *Journal of Quantitative Spectroscopy and Radiative Transfer*, **112**, 361–375.

Li, J.-L., W.-L. Lee, D. Waliser, Y.-H. Wang, J.-Y. Yu, X. Jiang, T. L'Ecuyer, Y.-C. Chen, T. Kubar, E. Fetzer, et al., 2016: Considering the radiative effects of snow on tropical pacific ocean radiative heating profiles in contemporary gcms using a-train observations. *Journal of Geophysical Research: Atmospheres*, **121**, 1621–1636.

Li, J.-L., D. Waliser, G. Stephens, S. Lee, T. L'Ecuyer, S. Kato, N. Loeb, and H.-Y. Ma, 2013: Characterizing and understanding radiation budget biases in cmip3/cmip5 gcms, contemporary gcm, and reanalysis. *Journal of Geophysical Research: Atmospheres*, **118**, 8166–8184.

Li, X., F. Wagner, W. Peng, J. Yang, and D. L. Mauzerall, 2017a: Reduction of solar photovoltaic resources due to air pollution in china. *Proceedings of the National Academy of Sciences*, **114**, 11867–11872.

Li, Y., D. W. Thompson, and S. Bony, 2015: The influence of atmospheric cloud radiative effects on the large-scale atmospheric circulation. *Journal of Climate*, **28**, 7263–7278.

Li, Y., D. W. J. Thompson, and S. Bony, 2017b: The influence of atmospheric cloud radiative effects on the large-scale atmospheric circulation. *Journal of Climate*, **30**, 5621–5635.

Lindzen, R. S. and Y.-S. Choi, 2011: On the observational determination of climate sensitivity and its implications. *Asia-Pacific Journal of Atmospheric Sciences*, **47**, 377.

Lindzen, R. S., M.-D. Chou, and A. Y. Hou, 2001: Does the earth have an adaptive infrared iris? *Bulletin of the American Meteorological Society*, **82**, 417–432.

Liu, C., E. J. Zipser, and S. W. Nesbitt, 2007: Global distribution of tropical deep convection: Different perspectives from trmm infrared and radar data. *Journal of climate*, **20**, 489–503.

Loeb, N. G., D. R. Doelling, H. Wang, W. Su, C. Nguyen, J. G. Corbett, L. Liang, C. Mitrescu, F. G. Rose, and S. Kato, 2018: Clouds and the earth's radiant energy system (ceres) energy balanced and filled (ebaf) top-of-atmosphere (toa) edition-4.0 data product. *Journal of Climate*, **31**, 895–918.

Loeb, N. G., H. Wang, A. Cheng, S. Kato, J. T. Fasullo, K.-M. Xu, and R. P. Allan, 2016: Observational constraints on atmospheric and oceanic cross-equatorial heat transports: revisiting the precipitation asymmetry problem in climate models. *Climate Dynamics*, **46**, 3239–3257.

Loeb, N. G., B. A. Wielicki, D. R. Doelling, G. L. Smith, D. F. Keyes, S. Kato, N. Manalo-Smith, and T. Wong, 2009: Toward optimal closure of the earth's top-of-atmosphere radiation budget. *Journal of Climate*, **22**, 748–766.

López-Solano, J., A. Redondas, T. Carlund, J. J. Rodriguez-Franco, H. Diémoz, S. F. León-Luis, B. Hernández-Cruz, C. Guirado-Fuentes, N. Kouremeti, J. Grobner, et al., 2018: Aerosol optical depth in the european brewer network. *Atmospheric Chemistry and Physics*, **18**, 3885–3902.

Luo, X., T. Ding, X. Liu, Y. Liu, and K. Wu, 2018: Quantum-cutting luminescent solar concentrators using ytterbium-doped perovskite nanocrystals. *Nano letters*, **19**, 338–341.

Lynch, D. K., K. Sassen, D. O. Starr, and G. Stephens, 2002: *Cirrus*. Oxford University Press.

Ma, X., F. Yu, and G. Luo, 2012: Aerosol direct radiative forcing based on geos-chem-apm and uncertainties. *Atmospheric Chemistry and Physics*, **12**, 5563–5581.

Mace, G. G., S. Benson, K. L. Sonntag, S. Kato, Q. Min, P. Minnis, C. H. Twohy, M. Poellot, X. Dong, C. Long, et al., 2006a: Cloud radiative forcing at the atmospheric radiation measurement program climate research facility: 1. technique, validation, and comparison to satellite-derived diagnostic quantities. *Journal of Geophysical Research: Atmospheres*, **111**.

Mace, G. G., S. Benson, and E. Vernon, 2006b: Cirrus clouds and the large-scale atmospheric state: Relationships revealed by six years of ground-based data. *Journal of climate*, **19**, 3257–3278.

Mace, G. G. and F. J. Wrenn, 2013: Evaluation of the hydrometeor layers in the east and west pacific within isccp cloud-top pressure–optical depth bins using merged cloudsat and calipso data. *Journal of Climate*, **26**, 9429–9444.

Mace, G. G., Q. Zhang, M. Vaughan, R. Marchand, G. Stephens, C. Trepte, and D. Winker, 2009: A description of hydrometeor layer occurrence statistics derived from the first year of merged cloudsat and calipso data. *Journal of Geophysical Research: Atmospheres*, **114**.

Maharana, P., A. Dimri, and A. Choudhary, 2019: Redistribution of indian summer monsoon by dust aerosol forcing. *Meteorological Applications*, **26**, 584–596.

Manabe, S. and F. Möller, 1961: *On the radiative equilibrium and heat balance of the atmosphere*. Monthly Weather Review.

Manabe, S. and R. F. Strickler, 1964: Thermal equilibrium of the atmosphere with a convective adjustment. *Journal of the Atmospheric Sciences*, **21**, 361–385.

Manabe, S. and R. T. Wetherald, 1967: Thermal equilibrium of the atmosphere with a given distribution of relative humidity. *Journal of the Atmospheric Sciences*, **24**, 241–259.

Marchand, R., T. Ackerman, M. Smyth, and W. B. Rossow, 2010: A review of cloud top height and optical depth histograms from misr, isccp, and modis. *Journal of Geophysical Research: Atmospheres*, **115**.

Mårtensson, E., E. Nilsson, G. de Leeuw, L. Cohen, and H.-C. Hansson, 2003: Laboratory simulations and parameterization of the primary marine aerosol production. *Journal of Geophysical Research: Atmospheres*, **108**.

Mather, J. H. and S. A. McFarlane, 2009: Cloud classes and radiative heating profiles at the manus and nauru atmospheric radiation measurement (arm) sites. *Journal of Geophysical Research: Atmospheres*, **114**.

Matus, A. V. and T. S. L'Ecuyer, 2017: The role of cloud phase in earth's radiation budget. *Journal of Geophysical Research: Atmospheres*, **122**, 2559–2578.

Matus, A. V., T. S. L'Ecuyer, and D. S. Henderson, 2019: New estimates of aerosol direct radiative effects and forcing from a-train satellite observations. *Geophysical Research Letters*.

Matus, A. V., T. S. L'Ecuyer, J. E. Kay, C. Hannay, and J.-F. Lamarque, 2015: The role of clouds in modulating global aerosol direct radiative effects in spaceborne active observations and the community earth system model. *Journal of Climate*, **28**, 2986–3003.

Mauritsen, T. and B. Stevens, 2015: Missing iris effect as a possible cause of muted hydrological change and high climate sensitivity in models. *Nature Geoscience*, **8**, 346.

McFarlane, S. A., J. H. Mather, and T. P. Ackerman, 2007: Analysis of tropical radiative heating profiles: A comparison of models and observations. *Journal of Geophysical Research: Atmospheres*, **112**.

McGill, M. J., M. A. Vaughan, C. R. Trepte, W. D. Hart, D. L. Hlavka, D. M. Winker, and R. Kuehn, 2007: Airborne validation of spatial properties measured by the calipso lidar. *Journal of Geophysical Research: Atmospheres*, **112**.

McIlhattan, E. A., T. S. L'Ecuyer, and N. B. Miller, 2017: Observational evidence linking arctic supercooled liquid cloud biases in cesm to snowfall processes. *Journal of Climate*, **30**, 4477–4495.

Ming, Y. and V. Ramaswamy, 2011: A model investigation of aerosol-induced changes in tropical circulation. *Journal of Climate*, **24**, 5125–5133.

Minnis, P., 2002: Satellite remote sensing of cirrus. *Oxford Univ. Press, Oxford, UK, 2002), chp*, **7**, 147–167.

Mülmenstädt, J., O. Sourdeval, D. S. Henderson, T. S. L'Ecuyer, C. Unglaub, L. Jungandreas, C. Böhm, L. M. Russell, and J. Quaas, 2018: Using caliop to estimate cloud-field base height and its uncertainty: the cloud base altitude spatial extrapolator (cbase) algorithm and dataset. *Earth System Science Data*.

Myhre, G., 2009: Consistency between satellite-derived and modeled estimates of the direct aerosol effect. *Science*, **325**, 187–190.

Myhre, G., A. Myhre, and F. Stordal, 2001: Historical evolution of radiative forcing of climate. *Atmospheric Environment*, **35**, 2361–2373.

Myhre, G., B. H. Samset, M. Schulz, Y. Balkanski, S. Bauer, T. K. Berntsen, H. Bian, N. Bellouin, M. Chin, T. Diehl, et al., 2013: Radiative forcing of the direct aerosol effect from aerocom phase ii simulations. *Atmospheric Chemistry and Physics*, **13**, 1853.

Naud, C. M., A. Del Genio, G. G. Mace, S. Benson, E. E. Clothiaux, and P. Kollias, 2008: Impact of dynamics and atmospheric state on cloud vertical overlap. *Journal of Climate*, **21**, 1758–1770.

Naud, C. M., A. D. Del Genio, M. Bauer, and W. Kovari, 2010: Cloud vertical distribution across warm and cold fronts in cloudsat–calipso data and a general circulation model. *Journal of Climate*, **23**, 3397–3415.

Nelson, E. L. and T. S. L'Ecuyer, 2018: Global character of latent heat release in oceanic warm rain systems. *Journal of Geophysical Research: Atmospheres*, **123**, 4797–4817.

Nelson, E. L., T. S. L'Ecuyer, S. M. Saleeby, W. Berg, S. R. Herbener, and S. C. van den Heever, 2016: Toward an algorithm for estimating latent heat release in warm rain systems. *Journal of Atmospheric and Oceanic Technology*, **33**, 1309–1329.

Norris, J. R., R. J. Allen, A. T. Evan, M. D. Zelinka, C. W. O'Dell, and S. A. Klein, 2016: Evidence for climate change in the satellite cloud record. *Nature*, **536**, 72–75.

Norris, J. R. and M. Wild, 2009: Trends in aerosol radiative effects over china and japan inferred from observed cloud cover, solar "dimming," and solar "brightening". *Journal of Geophysical Research: Atmospheres*, **114**.

Ockert-Bell, M. E. and D. L. Hartmann, 1992: The effect of cloud type on earth's energy balance: Results for selected regions. *Journal of Climate*, **5**, 1157–1171, doi:10.1175/1520-0442(1992)005¡1157:TEOCTO¿2.0.CO;2.

O'Dowd, C., C. Scannell, J. Mulcahy, and S. G. Jennings, 2010: Wind speed influences on marine aerosol optical depth. *Advances in Meteorology*, **2010**.

Omar, A., D. Winker, J. Tackett, D. Giles, J. Kar, Z. Liu, M. Vaughan, K. Powell, and C. Trepte, 2013: Caliop and aeronet aerosol optical depth comparisons: One size fits none. *Journal of Geophysical Research: Atmospheres*, **118**, 4748–4766.

Oreopoulos, L., N. Cho, and D. Lee, 2017: New insights about cloud vertical structure from cloudsat and calipso observations. *Journal of Geophysical Research: Atmospheres*.

Oreopoulos, L., N. Cho, D. Lee, and S. Kato, 2016: Radiative effects of global modis cloud regimes. *Journal of Geophysical Research: Atmospheres*, **121**, 2299–2317, doi:10.1002/2015JD024502.

Oreopoulos, L., W. Rossow, et al., 2011: The cloud radiative effects of international satellite cloud climatology project weather states. *Journal of Geophysical Research: Atmospheres*, **116**.

Padma Kumari, B., A. L. Londhe, S. Daniel, and D. B. Jadhav, 2007: Observational evidence of solar dimming: Offsetting surface warming over india. *Geophysical Research Letters*, **34**.

Pal, S. and P. Devara, 2012: A wavelet-based spectral analysis of long-term time series of optical properties of aerosols obtained by lidar and radiometer measurements over an

urban station in western india. *Journal of atmospheric and solar-terrestrial physics*, **84**, 75–87.

Pant, P., P. Hegde, U. Dumka, R. Sagar, S. Satheesh, K. K. Moorthy, A. Saha, and M. Srivastava, 2006: Aerosol characteristics at a high-altitude location in central himalayas: Optical properties and radiative forcing. *Journal of Geophysical Research: Atmospheres*, **111**.

Pavolonis, M. J. and J. R. Key, 2003: Antarctic cloud radiative forcing at the surface estimated from the avhrr polar pathfinder and isccp d1 datasets, 1985–93. *Journal of Applied Meteorology*, **42**, 827–840.

Phairuang, W., M. Hata, and M. Furuuchi, 2017: Influence of agricultural activities, forest fires and agro-industries on air quality in thailand. *Journal of Environmental Sciences*, **52**, 85–97.

Pierrehumbert, R. T., 1995: Thermostats, radiator fins, and the local runaway greenhouse. *Journal of the atmospheric sciences*, **52**, 1784–1806.

Pincus, R., R. Hemler, and S. A. Klein, 2006: Using stochastically generated subcolumns to represent cloud structure in a large-scale model. *Monthly weather review*, **134**, 3644–3656.

Platnick, S., M. D. King, S. A. Ackerman, W. P. Menzel, B. A. Baum, J. C. Riédi, and R. A. Frey, 2003: The modis cloud products: Algorithms and examples from terra. *IEEE Transactions on Geoscience and Remote Sensing*, **41**, 459–473.

Powell, K. M. and T. F. Edgar, 2012: Modeling and control of a solar thermal power plant with thermal energy storage. *Chemical Engineering Science*, **71**, 138–145.

Prasad, A. A., R. A. Taylor, and M. Kay, 2015: Assessment of direct normal irradiance and cloud connections using satellite data over australia. *Applied energy*, **143**, 301–311.

Prasad, A. K. and R. P. Singh, 2007: Changes in aerosol parameters during major dust storm events (2001–2005) over the indo-gangetic plains using aeronet and modis data. *Journal of Geophysical Research: Atmospheres*, **112**.

Protat, A., S. Young, S. A. McFarlane, T. L'Ecuyer, G. G. Mace, J. M. Comstock, C. N. Long, E. Berry, and J. Delanoë, 2014: Reconciling ground-based and space-based estimates of the frequency of occurrence and radiative effect of clouds around darwin, australia. *Journal of Applied Meteorology and Climatology*, **53**, 456–478.

Rai, V. and A. L. Beck, 2015: Public perceptions and information gaps in solar energy in texas. *Environmental Research Letters*, **10**, 074011.

Ramachandran, S., 2004: Spectral aerosol optical characteristics during the northeast monsoon over the arabian sea and the tropical indian ocean: 2. ångström parameters and anthropogenic influence. *Journal of Geophysical Research: Atmospheres*, **109**.

Ramanathan, V., 1987: The role of earth radiation budget studies in climate and general circulation research. *Journal of Geophysical Research: Atmospheres*, **92**, 4075–4095.

Ramanathan, V., R. Cess, E. Harrison, P. Minnis, B. Barkstrom, E. Ahmad, and D. Hartmann, 1989: Cloud-radiative forcing and climate: Results from the earth radiation budget experiment. *Science*, **243**, 57–63.

Ramanathan, V., C. Chung, D. Kim, T. Bettge, L. Buja, J. Kiehl, W. Washington, Q. Fu, D. Sikka, and M. Wild, 2005: Atmospheric brown clouds: Impacts on south asian climate and hydrological cycle. *Proceedings of the National Academy of Sciences*, **102**, 5326–5333.

Ramanathan, V. and W. Collins, 1991: Thermodynamic regulation of ocean warming by cirrus clouds deduced from observations of the 1987 el nino. *Nature*, **351**, 27.

Randall, D. A., D. A. Dazlich, and T. G. Corsetti, 1989a: Interactions among radiation, convection, and large-scale dynamics in a general circulation model. *Journal of the Atmospheric sciences*, **46**, 1943–1970.

— 1989b: Interactions among radiation, convection, and large-scale dynamics in a general circulation model. *Journal of the Atmospheric sciences*, **46**, 1943–1970.

Randles, C., A. Da Silva, V. Buchard, P. Colarco, A. Darmenov, R. Govindaraju, A. Smirnov, B. Holben, R. Ferrare, J. Hair, et al., 2017: The merra-2 aerosol reanalysis, 1980 onward. part i: System description and data assimilation evaluation. *Journal of climate*, **30**, 6823–6850.

Raschke, E., S. Kinne, W. B. Rossow, P. W. Stackhouse Jr, and M. Wild, 2016: Comparison of radiative energy flows in observational datasets and climate modeling. *Journal of Applied Meteorology and Climatology*, **55**, 93–117.

Rastogi, N., A. Singh, M. Sarin, and D. Singh, 2016: Temporal variability of primary and secondary aerosols over northern india: Impact of biomass burning emissions. *Atmospheric Environment*, **125**, 396–403.

Remer, L. A., Y. Kaufman, D. Tanré, S. Mattoo, D. Chu, J. V. Martins, R.-R. Li, C. Ichoku, R. Levy, R. Kleidman, et al., 2005: The modis aerosol algorithm, products, and validation. *Journal of the atmospheric sciences*, **62**, 947–973.

Ritter, B. and J.-F. Geleyn, 1992: A comprehensive radiation scheme for numerical weather prediction models with potential applications in climate simulations. *Monthly Weather Review*, **120**, 303–325.

Rossow, W., F. Mosher, E. Kinsella, A. Arking, M. Desbois, E. Harrison, P. Minnis, E. Ruprecht, G. Seze, C. Simmer, et al., 1985: Isccp cloud algorithm intercomparison. *Journal of Climate and Applied Meteorology*, **24**, 877–903.

Rossow, W. and Y.-C. Zhang, 1995: Calculation of surface and top of atmosphere radiative fluxes from physical quantities based on isccp data sets: 2. validation and first results. *Journal of Geophysical Research: Atmospheres*, **100**, 1167–1197.

Rossow, W. B. and A. A. Lacis, 1990: Global, seasonal cloud variations from satellite radiance measurements. part ii. cloud properties and radiative effects. *Journal of Climate*, **3**, 1204–1253.

Rossow, W. B. and R. A. Schiffer, 1999: Advances in understanding clouds from isccp. *Bulletin of the American Meteorological Society*, **80**, 2261–2287.

Ruiz-Arias, J., J. Dudhia, C. Gueymard, and D. Pozo-Vázquez, 2013: Assessment of the level-3 modis daily aerosol optical depth in the context of surface solar radiation and numerical weather modeling. *Atmos. Chem. Phys*, **13**, 675–692.

Sabatini, R. R. and V. E. Suomi, 1962: On the possibility of atmospheric infrared cooling estimates from satellite observations. *Journal of the Atmospheric Sciences*, **19**, 349–350.

Saide, P., S. Spak, R. Pierce, J. Otkin, T. Schaack, A. Heidinger, A. da Silva, M. Kacenelenbogen, J. Redemann, and G. Carmichael, 2015: Central american biomass burning smoke can increase tornado severity in the us. *Geophysical research letters*, **42**, 956–965.

Saleeby, S. M. and W. R. Cotton, 2004: A large-droplet mode and prognostic number concentration of cloud droplets in the colorado state university regional atmospheric modeling system (rams). part i: Module descriptions and supercell test simulations. *Journal of Applied Meteorology*, **43**, 182–195.

Saleeby, S. M. and S. C. van den Heever, 2013: Developments in the csu-rams aerosol model: Emissions, nucleation, regeneration, deposition, and radiation. *Journal of Applied Meteorology and Climatology*, **52**, 2601–2622.

Sassen, K. and G. G. Mace, 2002: *Ground based remote sensing of cirrus clouds*. Oxford, New York, NY.

Sassen, K. and Z. Wang, 2008: Classifying clouds around the globe with the cloudsat radar: 1-year of results. *Geophysical research letters*, **35**.

— 2012: The clouds of the middle troposphere: composition, radiative impact, and global distribution. *Surveys in geophysics*, **33**, 677–691.

Sassen, K., Z. Wang, and D. Liu, 2008: Global distribution of cirrus clouds from cloudsat/cloud-aerosol lidar and infrared pathfinder satellite observations (calipso) measurements. *Journal of Geophysical Research: Atmospheres*, **113**.

— 2009: Cirrus clouds and deep convection in the tropics: Insights from calipso and cloudsat. *Journal of Geophysical Research: Atmospheres*, **114**.

Schmit, T. J., M. M. Gunshor, W. P. Menzel, J. J. Gurka, J. Li, and A. S. Bachmeier, 2005: Introducing the next-generation advanced baseline imager on goes-r. *Bulletin of the American Meteorological Society*, **86**, 1079–1096.

Schneider, S. H., 1972: Cloudiness as a global climatic feedback mechanism: The effects on the radiation balance and surface temperature of variations in cloudiness. *Journal of the Atmospheric Sciences*, **29**, 1413–1422.

Schubert, S. D., R. B. Rood, and J. Pfaendtner, 1993: An assimilated dataset for earth science applications. *Bulletin of the American meteorological Society*, **74**, 2331–2342.

Schuster, G. L., M. Vaughan, D. MacDonnell, W. Su, D. Winker, O. Dubovik, T. Lapyonok, and C. Trepte, 2012: Comparison of calipso aerosol optical depth retrievals to aeronet measurements, and a climatology for the lidar ratio of dust. *Atmos. Chem. Phys*, **12**, 7431–7452.

Seidel, D. J., Q. Fu, W. J. Randel, and T. J. Reichler, 2008: Widening of the tropical belt in a changing climate. *Nature geoscience*, **1**, 21.

Sena, E., P. Artaxo, and A. Correia, 2013: Spatial variability of the direct radiative forcing of biomass burning aerosols and the effects of land use change in amazonia. *Atmospheric Chemistry and Physics*, **13**, 1261–1275.

Senior, C. and J. Mitchell, 1993: Carbon dioxide and climate. the impact of cloud parameterization. *Journal of Climate*, **6**, 393–418.

Sherwood, S. C., V. Ramanathan, T. P. Barnett, M. K. Tyree, and E. Roeckner, 1994: Response of an atmospheric general circulation model to radiative forcing of tropical clouds. *Journal of Geophysical Research: Atmospheres*, **99**, 20829–20845.

Shonk, J. K., R. J. Hogan, and J. Manners, 2012: Impact of improved representation of horizontal and vertical cloud structure in a climate model. *Climate dynamics*, **38**, 2365–2376.

Si-Ya, S. and Z. Jing, 2015: All-sky direct radiative effects of urban aerosols in beijing and shanghai, china. *Atmospheric and Oceanic Science Letters*, **8**, 295–300.

Slingo, A. and J. Slingo, 1988: The response of a general circulation model to cloud longwave radiative forcing. i: Introduction and initial experiments. *Quarterly Journal of the Royal Meteorological Society*, **114**, 1027–1062.

Slingo, J. and A. Slingo, 1991: The response of a general circulation model to cloud longwave radiative forcing. ii: Further studies. *Quarterly Journal of the Royal Meteorological Society*, **117**, 333–364.

Smirnov, A., B. Holben, T. Eck, O. Dubovik, and I. Slutsker, 2000: Cloud-screening and quality control algorithms for the aeronet database. *Remote sensing of environment*, **73**, 337–349.

Soden, B. J. and I. M. Held, 2006: An assessment of climate feedbacks in coupled ocean–atmosphere models. *Journal of Climate*, **19**, 3354–3360.

Sohn, B.-J. and E. A. Smith, 1992: The significance of cloud–radiative forcing to the general circulation on climate time scales—a satellite interpretation. *Journal of the atmospheric sciences*, **49**, 845–860.

Spencer, R. W., W. D. Braswell, J. R. Christy, and J. Hnilo, 2007: Cloud and radiation budget changes associated with tropical intraseasonal oscillations. *Geophysical Research Letters*, **34**.

Stackhouse Jr, P. W., S. K. Gupta, S. J. Cox, T. Zhang, J. C. Mikovitz, and L. M. Hinkelman, 2011: The nasa/gewex surface radiation budget release 3.0: 24.5-year dataset. *GEWEX News*, **21**, 10–12.

Stephens, G., D. Winker, J. Pelon, C. Trepte, D. Vane, C. Yuhas, T. L'ecuyer, and M. Lebsock, 2018: Cloudsat and calipso within the a-train: ten years of actively observing the earth system. *Bulletin of the American Meteorological Society*, **99**, 569–581.

Stephens, G. L., 2005: Cloud feedbacks in the climate system: A critical review. *Journal of climate*, **18**, 237–273.

Stephens, G. L. and T. D. Ellis, 2008: Controls of global-mean precipitation increases in global warming gcm experiments. *Journal of Climate*, **21**, 6141–6155.

Stephens, G. L., P. M. Gabriel, and P. T. Partain, 2001: Parameterization of atmospheric radiative transfer. part i: Validity of simple models. *Journal of the atmospheric sciences*, **58**, 3391–3409.

Stephens, G. L. and T. J. Greenwald, 1991: The earth's radiation budget and its relation to atmospheric hydrology 2: Observations of cloud effects. *J. Geophys. Res.*, **15**, 15325–15340.

Stephens, G. L., M. Z. Hakuba, M. Hawcroft, J. M. Haywood, A. Behrangi, J. E. Kay, and P. J. Webster, 2016: The curious nature of the hemispheric symmetry of the earth's water and energy balances. *Current Climate Change Reports*, **2**, 135–147.

Stephens, G. L., J. Li, M. Wild, C. A. Clayson, N. Loeb, S. Kato, T. L'ecuyer, P. W. Stackhouse, M. Lebsock, and T. Andrews, 2012a: An update on earth's energy balance in light of the latest global observations. *Nature Geoscience*, **5**, 691–696.

Stephens, G. L., D. G. Vane, R. J. Boain, G. G. Mace, K. Sassen, Z. Wang, A. J. Illingworth, E. J. O'connor, W. B. Rossow, S. L. Durden, et al., 2002: The cloudsat mission and the

a-train: A new dimension of space-based observations of clouds and precipitation. *Bulletin of the American Meteorological Society*, **83**, 1771–1790, doi:10.1175/BAMS-83-12-1771.

Stephens, G. L., D. G. Vane, S. Tanelli, E. Im, S. Durden, M. Rokey, D. Reinke, P. Partain, G. G. Mace, R. Austin, et al., 2008: Cloudsat mission: Performance and early science after the first year of operation. *Journal of Geophysical Research: Atmospheres*, **113**.

Stephens, G. L. and P. J. Webster, 1981: Clouds and climate: Sensitivity of simple systems. *Journal of the Atmospheric Sciences*, **38**, 235–247.

Stephens, G. L., M. Wild, P. W. Stackhouse Jr, T. L'Ecuyer, S. Kato, and D. S. Henderson, 2012b: The global character of the flux of downward longwave radiation. *Journal of Climate*, **25**, 2329–2340.

Stephens, G. L. and N. B. Wood, 2007: Properties of tropical convection observed by millimeter-wave radar systems. *Monthly weather review*, **135**, 821–842.

Su, H., J. H. Jiang, Y. Gu, J. D. Neelin, B. H. Kahn, D. Feldman, Y. L. Yung, J. W. Waters, N. J. Livesey, M. L. Santee, et al., 2008: Variations of tropical upper tropospheric clouds with sea surface temperature and implications for radiative effects. *Journal of Geophysical Research: Atmospheres*, **113**.

Su, H., J. H. Jiang, J. D. Neelin, T. J. Shen, C. Zhai, Q. Yue, Z. Wang, L. Huang, Y.-S. Choi, G. L. Stephens, et al., 2017: Tightening of tropical ascent and high clouds key to precipitation change in a warmer climate. *Nature communications*, **8**, 15771.

Su, H., J. H. Jiang, C. Zhai, V. S. Perun, J. T. Shen, A. Del Genio, L. S. Nazarenko, L. J. Donner, L. Horowitz, C. Seman, et al., 2013: Diagnosis of regime-dependent cloud

simulation errors in cmip5 models using "a-train" satellite observations and reanalysis data. *Journal of Geophysical Research: Atmospheres*, **118**, 2762–2780.

Subrahmanyam, K. V. and K. K. Kumar, 2017: Cloudsat observations of multi layered clouds across the globe. *Climate Dynamics*, **49**, 327–341.

Sun, D.-Z. and Z. Liu, 1996: Dynamic ocean-atmosphere coupling: A thermostat for the tropics. *Science*, **272**, 1148–1150.

Sweerts, B., S. Pfenninger, S. Yang, D. Folini, B. Van der Zwaan, and M. Wild, 2019: Estimation of losses in solar energy production from air pollution in china since 1960 using surface radiation data. *Nature Energy*, **4**, 657–663.

Tan, P. Y. and M. R. B. Ismail, 2014: Building shade affects light environment and urban greenery in high-density residential estates in singapore. *Urban Forestry & Urban Greening*, **13**, 771–784.

Tanelli, S., S. L. Durden, E. Im, K. S. Pak, D. G. Reinke, P. Partain, J. M. Haynes, and R. T. Marchand, 2008: CloudSat's Cloud Profiling Radar After Two Years in Orbit: Performance, Calibration, and Processing. *IEEE Transactions on Geoscience and Remote Sensing*, **46**, 3560–3573, doi:10.1109/TGRS.2008.2002030.

Tompkins, A. M. and G. C. Craig, 1999: Sensitivity of tropical convection to sea surface temperature in the absence of large-scale flow. *Journal of climate*, **12**, 462–476.

Trenberth, K. E. and J. T. Fasullo, 2010: Simulation of present-day and twenty-first-century energy budgets of the southern oceans. *Journal of Climate*, **23**, 440–454.

Trenberth, K. E., J. T. Fasullo, and M. A. Balmaseda, 2014: Earth's energy imbalance. *Journal of Climate*, **27**, 3129–3144.

Trenberth, K. E., J. T. Fasullo, and J. Kiehl, 2009: Earth's global energy budget. *Bulletin of the American Meteorological Society*, **90**, 319–323, doi:10.1175/2008BAMS2634.1.

Troccoli, A. and J.-J. Morcrette, 2014: Skill of direct solar radiation predicted by the ecmwf global atmospheric model over australia. *Journal of Applied Meteorology and Climatology*, **53**, 2571–2588.

Tselioudis, G. and C. Jakob, 2002: Evaluation of midlatitude cloud properties in a weather and a climate model: Dependence on dynamic regime and spatial resolution. *Journal of Geophysical Research: Atmospheres*, **107**, AAC–14.

Twomey, S., 1977: The influence of pollution on the shortwave albedo of clouds. *Journal of the atmospheric sciences*, **34**, 1149–1152.

Van Tricht, K., S. Lhermitte, J. T. Lenaerts, I. V. Gorodetskaya, T. S. L'Ecuyer, B. Noël, M. R. van den Broeke, D. D. Turner, and N. P. Van Lipzig, 2016: Clouds enhance greenland ice sheet meltwater runoff. *Nature communications*, **7**, 10266.

Voigt, A. and T. A. Shaw, 2015: Circulation response to warming shaped by radiative changes of clouds and water vapour. *Nature Geoscience*, **8**, 102.

Vonder Haar, T. H. and V. E. Suomi, 1971: Measurements of the earth's radiation budget from satellites during a five-year period. part i: Extended time and space means. *Journal of the Atmospheric Sciences*, **28**, 305–314.

Wallace, J. M., 1992: Effect of deep convection on the regulation of tropical sea surface temperature. *Nature*, **357**, 230.

Wang, Z. and K. Sassen, 2001: Cloud type and macrophysical property retrieval using multiple remote sensors. *Journal of Applied Meteorology*, **40**, 1665–1682, doi:10.1175/1520-0450(2001)040¡1665:CTAMPR¿2.0.CO;2.

Wang, Z., D. Vane, G. Stephens, and D. Reinke, 2012: Level 2 combined radar and lidar cloud scenario classification product process description and interface control document. *JPL Rep*, **22**.

Webb, M., C. Senior, S. Bony, and J.-J. Morcrette, 2001: Combining erbe and isccp data to assess clouds in the hadley centre, ecmwf and lmd atmospheric climate models. *Climate Dynamics*, **17**, 905–922.

Webster, P. and G. Stephens, 1984: Cloud-radiation interaction and the climate problem.

Wei, J., Y. Peng, R. Mahmood, L. Sun, and J. Guo, 2019: Intercomparison in spatial distributions and temporal trends derived from multi-source satellite aerosol products. *Atmospheric Chemistry and Physics*, **19**, 7183–7207.

Wielicki, B. A., B. R. Barkstrom, E. F. Harrison, R. B. Lee III, G. Louis Smith, and J. E. Cooper, 1996a: Clouds and the earth's radiant energy system (ceres): An earth observing system experiment. *Bulletin of the American Meteorological Society*, **77**, 853–868.

Wielicki, B. A., B. R. Barkstrom, E. F. Harrison, R. B. Lee III, G. L. Smith, and J. E. Cooper, 1996b: Clouds and the earth's radiant energy system (ceres): An earth observing system experiment. *Bulletin of the American Meteorological Society*, **77**, 853–868.

Wielicki, B. A., R. D. Cess, M. D. King, D. A. Randall, and E. F. Harrison, 1995: Mission to planet earth: Role of clouds and radiation in climate. *Bulletin of the American Meteorological Society*, **76**, 2125–2154.

Wild, M., 2005: Solar radiation budgets in atmospheric model intercomparisons from a surface perspective. *Geophysical research letters*, **32**.

— 2008: Short-wave and long-wave surface radiation budgets in gcms: A review based on the ipcc-ar4/cmip3 models. *Tellus A*, **60**, 932–945.

Wild, M., D. Folini, C. Schär, N. Loeb, E. G. Dutton, and G. König-Langlo, 2013: The global energy balance from a surface perspective. *Climate dynamics*, **40**, 3107–3134.

Wild, M., H. Gilgen, A. Roesch, A. Ohmura, C. N. Long, E. G. Dutton, B. Forgan, A. Kallis, V. Russak, and A. Tsvetkov, 2005: From dimming to brightening: Decadal changes in solar radiation at earth's surface. *Science*, **308**, 847–850.

Wild, M., A. Ohmura, H. Gilgen, J.-J. Morcrette, and A. Slingo, 2001: Evaluation of downward longwave radiation in general circulation models. *Journal of Climate*, **14**, 3227–3239.

Wing, A. A. and T. W. Cronin, 2016: Self-aggregation of convection in long channel geometry. *Quarterly Journal of the Royal Meteorological Society*, **142**, 1–15.

Winker, D., H. Chepfer, V. Noel, and X. Cai, 2017: Observational constraints on cloud feedbacks: The role of active satellite sensors. *Surveys in Geophysics*, **38**, 1483–1508.

Winker, D., J. Pelon, J. Coakley Jr, S. Ackerman, R. Charlson, P. Colarco, P. Flamant, Q. Fu, R. Hoff, C. Kittaka, et al., 2010: The calipso mission: A global 3d view of aerosols and clouds. *Bulletin of the American Meteorological Society*, **91**, 1211–1230.

Winker, D. M., W. H. Hunt, and M. J. McGill, 2007: Initial performance assessment of caliop. *Geophysical Research Letters*, **34**.

Winker, D. M., J. R. Pelon, and M. P. McCormick, 2003: The calipso mission: Spaceborne lidar for observation of aerosols and clouds. *Lidar Remote Sensing for Industry and Environment Monitoring III*, International Society for Optics and Photonics, volume 4893, 1–12.

Wyant, M. C., C. S. Bretherton, J. T. Bacmeister, J. T. Kiehl, I. M. Held, M. Zhao, S. A. Klein, and B. J. Soden, 2006: A comparison of low-latitude cloud properties and their response to climate change in three agcms sorted into regimes using mid-tropospheric vertical velocity. *Climate Dynamics*, **27**, 261–279.

Xia, S., A. M. Mestas-Nuñez, H. Xie, J. Tang, and R. Vega, 2018: Characterizing variability of solar irradiance in san antonio, texas using satellite observations of cloudiness. *Remote Sensing*, **10**, 2016.

Xia, S., A. M. Mestas-Nuñez, H. Xie, and R. Vega, 2017: An evaluation of satellite estimates of solar surface irradiance using ground observations in san antonio, texas, usa. *Remote Sensing*, **9**, 1268.

Xiao, Q., Z. Ma, S. Li, and Y. Liu, 2015: The impact of winter heating on air pollution in china. *PloS one*, **10**.

Xu, T., Y. Song, M. Liu, X. Cai, H. Zhang, J. Guo, and T. Zhu, 2019: Temperature inversions in severe polluted days derived from radiosonde data in north china from 2011 to 2016. *Science of the Total Environment*, **647**, 1011–1020.

Yang, X. and Z. Li, 2014: Increases in thunderstorm activity and relationships with air pollution in southeast china. *Journal of Geophysical Research: Atmospheres*, **119**, 1835–1844.

Yao, Z., Q. Wang, K. He, H. Huo, Y. Ma, and Q. Zhang, 2007: Characteristics of real-world vehicular emissions in chinese cities. *Journal of the Air & Waste Management Association*, **57**, 1379–1386.

Yoshimori, M. and A. J. Broccoli, 2008: Equilibrium response of an atmosphere–mixed layer ocean model to different radiative forcing agents: Global and zonal mean response. *Journal of Climate*, **21**, 4399–4423.

Yu, H., Y. Kaufman, M. Chin, G. Feingold, L. Remer, T. Anderson, Y. Balkanski, N. Bellouin, O. Boucher, S. Christopher, et al., 2006: A review of measurement-based assessments of the aerosol direct radiative effect and forcing. *Atmospheric Chemistry and Physics*, **6**, 613–666.

Yue, Q., B. H. Kahn, E. J. Fetzer, S. Wong, X. Huang, and M. Schreier, 2019: Temporal and spatial characteristics of short-term cloud feedback on global and local interannual climate fluctuations from a-train observations. *Journal of Climate*, **32**, 1875–1893.

Zaveri, R. A., R. C. Easter, J. D. Fast, and L. K. Peters, 2008: Model for simulating aerosol interactions and chemistry (mosaic). *Journal of Geophysical Research: Atmospheres*, **113**.

Zelinka, M. D. and D. L. Hartmann, 2010: Why is longwave cloud feedback positive? *Journal of Geophysical Research: Atmospheres*, **115**.

— 2011: The observed sensitivity of high clouds to mean surface temperature anomalies in the tropics. *Journal of Geophysical Research: Atmospheres*, **116**.

Zelinka, M. D., S. A. Klein, K. E. Taylor, T. Andrews, M. J. Webb, J. M. Gregory, and P. M. Forster, 2013: Contributions of different cloud types to feedbacks and rapid adjustments in cmip5. *Journal of Climate*, **26**, 5007–5027.

Zhang, D., Z. Wang, and D. Liu, 2010: A global view of midlevel liquid-layer topped stratiform cloud distribution and phase partition from calipso and cloudsat measurements. *Journal of Geophysical Research: Atmospheres*, **115**.

Zhang, J. and S. A. Christopher, 2003: Longwave radiative forcing of saharan dust aerosols estimated from modis, misr, and ceres observations on terra. *Geophysical Research Letters*, **30**.

Zhang, M., W. Lin, S. Klein, J. Bacmeister, S. Bony, R. Cederwall, A. Del Genio, J. Hack, N. Loeb, U. Lohmann, et al., 2005: Comparing clouds and their seasonal variations in 10 atmospheric general circulation models with satellite measurements. *Journal of Geophysical Research: Atmospheres*, **110**.

Zhang, T., P. W. Stackhouse Jr, S. K. Gupta, S. J. Cox, J. C. Mikovitz, and L. M. Hinkelman, 2013: The validation of the gewex srb surface shortwave flux data products using bsrn measurements: A systematic quality control, production and application approach. *Journal of Quantitative Spectroscopy and Radiative Transfer*, **122**, 127–140.

Zhang, Y., W. B. Rossow, A. A. Lacis, V. Oinas, and M. I. Mishchenko, 2004: Calculation of radiative fluxes from the surface to top of atmosphere based on isccp and other global data sets: Refinements of the radiative transfer model and the input data. *Journal of Geophysical Research: Atmospheres*, **109**, D19105, doi:10.1029/2003JD004457.

Zhang, Y.-C., W. Rossow, and A. Lacis, 1995: Calculation of surface and top of atmosphere radiative fluxes from physical quantities based on isccp data sets: 1. method and sensitivity to input data uncertainties. *Journal of Geophysical Research: Atmospheres*, **100**, 1149–1165.

Zhao, M., 2014: An investigation of the connections among convection, clouds, and climate sensitivity in a global climate model. *Journal of Climate*, **27**, 1845–1862.

Zhao, P., Y. Feng, T. Zhu, and J. Wu, 2006: Characterizations of resuspended dust in six cities of north china. *Atmospheric Environment*, **40**, 5807–5814.